THE INTERACTION OF A HIGH-CURRENT, RELATIVISTIC ELECTRON BEAM WITH A PLASMA

by

John Pace VanDevender

Thesis submitted for the Degree of Ph.D.
in Physics of the University of London.

Imperial College of Science and Technology,
London, June 1974.

ABSTRACT

The energy transfer from a high-current, relativistic electron beam to a dense hydrogen plasma without an external magnetic field is investigated experimentally. The electron beam consists of 3.6×10^4 amperes of 3.8×10^5 eV electrons and has a duration of 100 ns. The average electron number density is 5×10^{12} cm^{-3}. The plasma is produced by either a z-discharge (with electron number density between 5×10^{13} and 3×10^{15} cm^{-3} and with initial electron temperature between 0.2 to 2.0 eV) or by the beam propagating into neutral hydrogen (at a pressure of 5×10^{-3} to 10 Torr).

The first measurements of the plasma electrons' number density and velocity distribution in such a beam-plasma system are reported using 90° ruby-laser scattering. These results are interpreted to show that the energy density of the plasma electrons is consistent with anomalous heating through the ion-acoustic instability.

Energy transfer from the beam to the plasma ions is also effected by the $\underline{j}_p \times \underline{B}$ force, on the plasma, where $\underline{j}_p$ is the plasma current density and $\underline{B}$ is the magnetic field of the net current. Evidence for this energy transfer is presented through the interpretation of the net-current waveforms and the image-converter streak-photographs of the plasma channel.

The electrons' velocity distribution was found to be non-Maxwellian and can be interpreted as arising from an azimuthal current density in the plasma.

CONTENTS

LIST OF FIGURES

TABLES

NOTE ON UNITS

Unless otherwise noted, rationalised MKS units will be used throughout the thesis. However, results will often be quoted in the most convenient units, for example, number densities in cm^{-3} and kinetic temperatures in electron volts. In such cases, the units will be clearly marked. The co-ordinate system used throughout the text is right handed cylindrical co-ordinates with the relativistic electrons in the beam moving in the positive z direction.

CHAPTER 1

INTRODUCTION

1.1 The Application of High-Current, Relativistic Electron Beams to Plasma Heating

In 1964, J.C. Martin and his associates at AWRE, Aldermaston, began the development of the technology for relativistic electron beams with currents between 10^4 and 10^6 amperes. These beams were designed as radiation sources for material studies, and subsequent developments have been directed toward problems relevant to this application, i.e., beam production, focusing, transport, and combination. However, these beams also offer an efficient source of energy to heat a plasma since typically 30% to 50% of the energy in the capacitor bank is extracted as beam energy. This compares favorably with the corresponding efficiency of approximately 1% for Nd:glass laser systems.

1.2 Theoretical Motivation for the Present Experiment

To heat a plasma with these beams, the energy must be transferred from the beam electrons to the plasma particles. The classical energy and momentum-transfer process of electron-ion collisions is inadequate for efficient energy transfer.

The mean free path for classical, non-relativistic electron-ion collisions is given by Spitzer (1962) as

$$\lambda \doteq w t_D = 6.2 \times 10^{-20} \frac{w^4}{n_i} \text{ cm.}$$

for an electron with velocity w cm/sec and an ion density n_i cm^{-3}. For $w \simeq 1.5 \times 10^{10}$ cm/sec and $n_i \approx 10^{15}$ cm^{-3}, $\lambda \sim 3 \times 10^{6}$ cm. Consequently, a beam electron loses very little energy to the plasma by classical electron-ion collisions in its passage through the experimental chamber. However, theoretical work by Fainberg, et al. (1969) indicates that the anomalous collision frequency arising from the two-stream instability between the plasma electrons and the beam electrons may efficiently transfer energy from the beam to the plasma. Lovelace and Sudan (1971) have suggested that the energy could be transferred to the plasma through the ion-acoustic instability excited with the plasma current induced in the plasma by the beam. In both cases, electron temperatures of approximately 1 keV at $n_e = 10^{14}$ cm^{-3} were optimistically expected.

1.3 Experimental Evidence for Energy Transfer in 1971

When the present experiment began, one paper had been published on the observation of heating by such a beam. Altyntsev, et al. (1971) injected a 10 kA, 4 MeV, and 50 ns electron beam into a magnetized plasma and found that the signal from a diamagnetic pick-up coil increased as the initial plasma number density was decreased. They also observed very high energy electrons travelling in the opposite direction from the beam and interpreted these as electrons scattered by the turbulence. The authors interpreted these results as evidence of anomalous heating of the plasma via the two-stream instability.

1.4 Purpose of the Present Experiment

The purpose of the present experiment was to seek direct evidence for the energy transfer from the electron beam to the plasma particles through the streaming instabilities. The present experiment was designed to use a higher current electron beam than Altyntsev, et al. used and to diagnose the heating with ruby laser scattering. The use of laser scattering is important because it measures the energy distribution of the plasma electrons directly. The diagnostic can be used to determine whether the energy is in the plasma electrons as opposed to the ions or trapped beam electrons.

1.5 Results of the Present Experiment

The present experiment yielded the first measurements of the plasma-electron number density and temperature during and shortly after a high-current, relativistic electron beam. The energy density of the plasma electrons was measured to be approximately twice that expected from classical electron-ion and electron-neutral collisions alone. The additional electron energy was consistent with the heating expected from the ion-acoustic instability. There was no evidence for energy transfer from the beam to the plasma through the electron-electron two stream instability.

In addition, the experiment provided evidence of significant energy transfer from the beam electrons to the plasma ions. The experimental evidence supports the hypothesis that the ions gained significant energy through acceleration by the $\underline{j} \times \underline{B}$ force characteristic of the beam-plasma system. Under some conditions, the ion energy was very much greater than the measured electron energy.

1.6 Special Nature of "High-Current" Relativistic Electron Beams

The fundamental difference between experiments in the high-current regime and other beam experiments is the dominance of the self-magnetic field of the beam in all phenomena. The criterion for "high-current" was first derived by Alfvén (1939) in relation to the transport of proton currents in inter-stellar space. The limiting current in an electrostatically neutralized plasma was found to be the current which produced a magnetic field sufficient to deflect its own beam particles through 180°. Particles in such a magnetic field cannot propagate, which limits the total current to I_A, the Alfvén current.

Alfvén derived I_A for a homogeneous, electrostatically neutralized beam by finding the current at which the Larmor radius r_L at the beam radius r_b equaled $r_b/2$. Under this condition, if an electron at the beam edge experienced the same magnetic field throughout its trajectory as it did at the beam's edge, it would be travelling in the opposite direction at the center of the beam.

An electron with mass m, charge e, velocity βc, moving in the magnetic field B_θ has a Larmor radius r_L given by

$$r_L = \frac{\gamma m \beta c}{e B_\theta}$$

in which β and γ are the usual relativistic factors, and c is the speed of light. The self-magnetic field B_θ of the beam is

$$B_\theta = \frac{\mu_o I}{2\pi r_b}$$

at the beam radius r_b. I is the current within a distance r_b of the center of the uniform current distribution. The condition for

deflection of an electron at the beam edge by 180° can be written as

$$r_L = r_b/2$$

$$r_L = \left(\frac{\gamma m \beta c}{e\,\mu_o\, I_A}\, 2\pi\right) r_b = \tfrac{1}{2}\, r_b \qquad \text{for the limiting current } I_A.$$

Solving for I_A gives

$$I_A = \left(\frac{4\pi mc}{e\,\mu_o}\right) \beta\,\gamma \qquad (1\text{-}1)$$

$$= 17{,}000\ \beta\gamma \text{ amperes.}$$

Thus, for a 350 keV electron beam, I_A = 23 kA. No one has ever reported propagating a beam with a net current greater than its Alfvén current.

However, when a high-current beam is injected into a plasma, a return current is induced in the plasma. The plasma current partially cancels the beam current. If the resulting net current $I_{net} = I_{beam} - I_{plasma}$ is very much less than I_A, the beam can still propagate even for $I_{beam} \gg I_A$. However, the non-relativistic plasma electrons experience a large magnetic field from I_{net} perpendicular to their drift velocity and in such a direction as to accelerate them out of the beam channel. This field also alters the usual dispersion relation for plasma waves in a beam-plasma system. The physics that arises from this magnetic field justifies the study of the high-current, relativistic, electron beam-plasma interaction.

CHAPTER 2

THEORY

2.1 General Description of the Beam-Plasma System

The physical picture that will be discussed can be summarized as follows: A beam of electrons is injected at time t = 0 through a conducting plane (the anode foil of the diode) into a drift tube with conducting walls at r_w. The beam electrons each have a kinetic energy eV_b and a velocity βc in the z direction, (perpendicular to the entrance foil). The total beam current rises linearly to its maximum value I_b in a time t_r and remains at I_b until time t_b. The current then decreases linearly to zero at $t = t_b + t_r$. The beam density n_b is uniform to a radius r_b and is zero for $r > r_b$. The plasma frequency associated with the beam number density ω_{pb} is given by

$$\omega_{pb}^2 = \frac{n_b e^2}{\epsilon_o m \gamma^3} \qquad (2\text{-}1)$$

where $e = 1.6 \times 10^{-19}$ coulombs, $m = 9.1 \times 10^{-31}$ kg, $\epsilon_o = 8.85 \times 10^{-12}$ farad/m, and γ is the usual relativistic factor.

The drift tube may contain either a preformed plasma or a neutral gas at time t = 0. If a plasma is initially present, the electron number density and electron temperature are n_e and T_e. The ion number density is $n_i = n_e + n_b$ and the ion temperature is T_i. If there is a neutral gas present initially, the beam creates its own plasma through direct ionization by the beam (primary) electrons and by Townsend avalance of the plasma (secondary) electrons.

The concepts that have been developed to describe the injection process can now be defined to identify the main features of the beam plasma model before they are discussed in greater detail.

1. Primary ionization: the ionization of a neutral gas by the primary (beam) electrons to produce ions and secondary (plasma) electrons.

2. Electrostatic neutralization: the expulsion of the secondary electrons from the beam channel by the electric field from the space charge. When the ion number density equals the beam number density in the lab frame, the system is said to be electrostatically neutralized.

3. Induced electric field E_z: the inductive electric field caused by the change in the azimuthal magnetic field B_θ with time during the rise of the beam current.

4. Gas Breakdown: Townsend avalanching of the secondary electrons in the induced electric field, which causes a rapid increase in the plasma number density. The avalanching continues until the plasma becomes sufficiently conductive for the plasma current to be comparable to the beam current. After this time (t_{bd}) the increase in the plasma current cancels the increase in the beam current and dI/dt decreases. The induced electric field E_z which is proportional to dI/dt also decreases after t_{bd} and becomes too small to drive additional avalanching. The time t_{bd} is called the breakdown time.

5. Plasma return current: the plasma current that is induced in the plasma by the rising beam current after breakdown. I_p is in the opposite direction from the beam current and is called the plasma return current.

6. Electron drift velocity of the plasma electrons in the axial direction is given by

$$v_{ez} = -j_p/ne$$

where j_p is the current density of the plasma current I_p.

7. Net current I_{net}: the vector sum of the beam current I_b and the plasma current I_p. It is always in the direction of the current driving the system, i.e. in the direction of the beam current.

8. Magnetic neutralization: the fractional magnetic neutralization f_m is the ratio of the I_p to I_b, and is effectively the fraction of the beam's magnetic field that is neutralized by the plasma current.

9. ν/γ : the ratio of the line number density of the electron beam per classical electron radius to the relativistic factor γ of the beam electrons:

$$r_e \equiv \frac{e^2}{4\pi\varepsilon_o mc^2} = \frac{e^2 \mu_o}{4\pi m}$$

$$\nu \equiv (n_b \pi r_b^2) r_e = \frac{n_b \pi r_b^2 e^2 \mu_o}{4 \pi m} .$$

Since $I_b = n_b \pi r_b^2 e \beta c$,

$$\frac{\nu}{\gamma} = \frac{I_b}{(\frac{4\pi mc}{e\mu_o}) \beta\gamma} = \frac{I_b}{I_A} \qquad (2\text{-}2)$$

from equation (1-1) for I_A. Therefore, the ratio of the beam current to the Alfven current appropriate to the beam electron energy is ν/γ . The expression is used in the literature as a strength parameter for high current relativistic electron beams.

Many of the processes and concepts defined above occur simultaneously in the beam-plasma system. However, to make the discussion intelligible, they will be discussed separately.

2.2 The Beam-Plasma Model

The phenomena defined in Section 2.1 and associated with the injection of a high-current, relativistic electron beam into a neutral gas will now be described in greater detail.

2.2a Electrostatic neutralization

For an intense electron beam, injected along a strong magnetic field into a hard vacuum, the space charge of the beam is sufficient to stop the beam electrons in a distance c/ω_{pb} as shown by Poukey and Rostoker (1971). At this distance the potential from the space charge relative to that of the anode entrance foil is $-V_b$ and is sufficient to stop the electrons with an initial kinetic energy eV_b. Unless the beam produces secondary electrons and unless those electrons escape to the walls leaving the positive ions to neutralize the space charge, the beam is electrostatically stopped.

For injection into a vacuum without a strong magnetic field, the one-dimensional problem described by Poukey and Rostoker is altered. The net radial force on a beam electron is the difference between the radially outward electrostatic force F_e and the radially inward magnetic force F_m. The ratio of F_e/F_m is

$$\frac{F_e}{F_m} = \frac{eE_r}{e\beta cB_\theta} = \frac{E_r}{\beta cB_\theta} = \frac{(1-f_e)(I/2\pi r\beta c\varepsilon_o)}{(\beta c\, \mu_o I/2\pi\, r)} = \frac{(1-f_e)}{\beta^2 c^2 \varepsilon_o \mu_o} = \frac{(1-f_e)}{\beta^2} \qquad (2\text{-}3)$$

where $f_e = \frac{n_i}{n_b}$, the fractional charge neutralization. For $f_e < 1-\beta^2$, the electrostatic force dominates and the beam defocuses. Thus, for the beam to propagate, the space charge must be neutralized by ionization and by the escape of secondary electrons from the beam channel. In a low pressure gas, the mean free path of the secondary electrons is sufficiently large for them to escape quickly to the walls once they are produced by ionization. Thus, the time taken for charge neutralization t_{cn} is the time required for f_e to equal 1. For a linearly rising beam number density n_b in a gas with an ionization crossection Q and a neutral number density n_o, the charge neutralization time t_{cn} is derived as follows:

$$\frac{\partial n_i}{\partial t} = n_o \beta c Q n_{beam}$$

$$n_i = \int_o^t n_{beam} n_o \beta c Q dt = n_o \beta c Q \int_o^t n_{beam} dt$$

$$n_{beam} = \frac{n_b t}{t_r}, \text{ for } t < t_r$$

$$= n_b, \text{for } t > t_r.$$

After integrating and solving for $t_{cn} = t$ at which $n_i = n_b$, one has

$$t_{cn} = \frac{2}{n_o \beta c Q} \quad \text{for } t < t_r$$

$$= \frac{1}{n_o \beta c Q} + \frac{t_r}{2} \quad \text{for } t > t_r.$$

For 400 keV electrons in hydrogen, Q is given by McClure (1953) as 4×10^{-19} cm^2. Therefore, for a pressure of P Torr, $n_o = 3.5 \times 10^{16}$ P cm^{-3} and t_{cn} is

$$t_{cn} = 4.7/\beta P \text{ ns, for } t_{cn} < t_r$$

$$= 2.4/\beta P + t_r/2 \text{ ns for } t_{cn} > t_r. \qquad (2\text{-}4)$$

Since one expects the beam to defocus for $f_e = \frac{n_i}{n_{beam}} < 1-\beta^2$, the beam defocuses until $t \approx t_f$ for

$$t_f = \frac{2(1-\beta^2)}{n_o \beta c Q} = 4.7 \frac{(1-\beta^2)}{\beta P} \text{ ns for } t_f < t_r$$

$$t_f = \frac{(1-\beta^2)}{n_o \beta c Q} + \frac{t_r}{2} \qquad (2\text{-}5)$$

$$= \frac{2.4(1-\beta^2)}{\beta P} + \frac{t_r}{2} \text{ ns for } t_f > t_r$$

from $n_i/n_e = 1-\beta^2$ in the derrivation for t_{cn}. Thus, the energy transported to the end of the experimental chamber should vary as

$$\int_{t_f}^{t_b} I_b(t)\, V_b(t)\, dt \qquad (2\text{-}6)$$

For a 350 keV beam with t_r = 30ns and t_b = 100 ns, $t_f = t_r$ for P = 94 mTorr H_2 and $t_f = t_b$ for P = 17 mTorr H_2. Thus the energy transported is expected to be reduced for P < 94 mTorr H_2.

2.2b Electron Avalanching

Once the beam is sufficiently neutralized electrostatically, it pinches under the net radial E-M forces and propagates. If $t_f \ll t_r$, the rising beam current $\frac{\partial I_b}{\partial t}$ produces an axial electric field E_z in the drift tube. Since the walls of the drift tube are conducting, the boundary condition on E_z is E_z=0 at $r=r_w$. For an axially independent problem $\frac{\partial}{\partial z} E_r = 0$ and the application of Faraday's law

$$\nabla \times \underline{E} = -\frac{\partial \underline{B}}{\partial t}$$

along a path of integration shown in Figure 1 gives

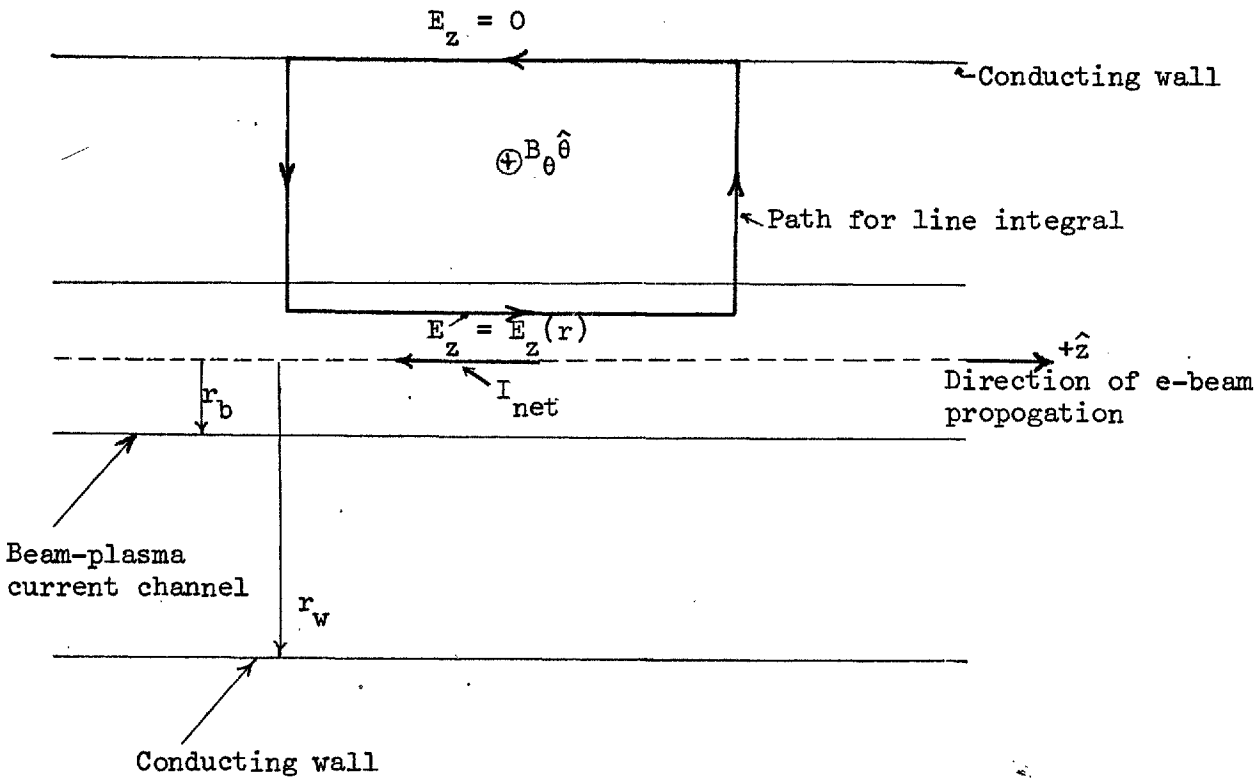

Figure 1. Path of the line integral for the calculation of the induced axial electric field E_z.

$$1\ E_z(r) = -\frac{\partial}{\partial t}\int \underline{B}\cdot d\underline{A}$$

$$= -\frac{\partial}{\partial t}\int_{r_w}^{r} B_\theta(-1)\, dr$$

$$E_z(r) = \frac{\partial}{\partial t}\int_{r_w}^{r} B_\theta\, dr$$

$$B_\theta = -\frac{\mu_o I}{2\pi r}\,\hat{\theta}, \text{for } r > r_b \qquad (2\text{-}7)$$

$$= -\frac{\mu_o I}{2\pi r_b^2}\, r\,\hat{\theta}, \text{for } r < r_b$$

$$E_z(r) = \frac{\mu_o}{2\pi}\cdot\frac{\partial I}{\partial t}\cdot \ln\left(\frac{r_w}{r}\right),\ r > r_b$$

$$\doteq \frac{\mu_o}{2\pi}\,\frac{\partial I}{\partial t}\left[\ln\left(\frac{r_w}{r_b}\right) + \tfrac{1}{2}\left(1-\frac{r^2}{r_b^2}\right)\right], \text{for } r < r_b$$

For $\dfrac{\partial I}{\partial t} = \dfrac{I_b}{t_r} = \dfrac{3 \times 10^4 \text{ amps}}{3 \times 10^{-8} \text{sec.}}$,

and for a drift tube with r_w = 4 cm with a beam radius r_b = 1 cm, the axial electric field at r=0 is 3.8×10^5 V/m. This field accelerates the plasma electrons to sufficient energies for avalanching. The plasma number density increases until the plasma is sufficiently conductive to short circuit E_z; the electrons are no longer accelerated to sufficient energies for ionization and the avalanching stops. The time at which the field is shorted is called the breakdown time t_{bd}. For $t > t_{bd}$ electrons emerging through the anode see a plasma, and the analysis for the injection into a plasma is appropriate to this case also.

2.2c Induced Plasma Current and Magnetic Neutralization

The formation of the plasma current for injection of a high current, relativistic electron beam into a plasma has been studied theoretically by Hammer and Rostoker (1969), Cox and Bennett (1970), Lee and Sudan (1971), and Rukhadze and Rukhlin (1971). Their calculations are appropriate for injection into neutral gas after $t = t_{bd}$, (i.e. after the plasma is formed) and for injection into a preformed plasma at $t = 0$. All of these papers show that if $n_b << n_e$, if the plasma electrons' collision frequency for momentum transfer ν_m is very much less than ω_p, and if the beam channel radius r_o is very much greater than c/ω_p, then the induced plasma current I_p is nearly equal and opposite to the beam current I_b and flows almost entirely within the beam channel.

Thus, for injection into a preformed plasma, the net current I_{net} defined as $I_b - I_p$ is approximately zero, and the plasma current density j_p is almost equal to minus the beam current density j_b inside the beam channel, as shown in Figure 2. The fractional magnetic neutralization f_m is defined as $f_m = I_p/I_b$.

For injection into a neutral gas, the self-magnetic field at $t = t_{bd}$ is "frozen in" after break-down. For $t > t_{bd}$, the plasma current increases to counter the increase in the beam current as shown in Figure 2. The value of I_{net} at $t = t_{bd}$ is $I_{beam}(t=t_{bd})$ since the plasma current is zero at that time. Thus if the plasma current is not dissipated through the finite resistivity of the plasma channel, I_{net} remains constant and the fractional magnetic neutralization is

$$f_m \equiv \frac{I_p}{I_b} = \frac{I_b - I_{net}}{I_b} = 1 - \frac{I_{beam}\,(t=t_{bd})}{I_b} \qquad (2\text{-}8)$$

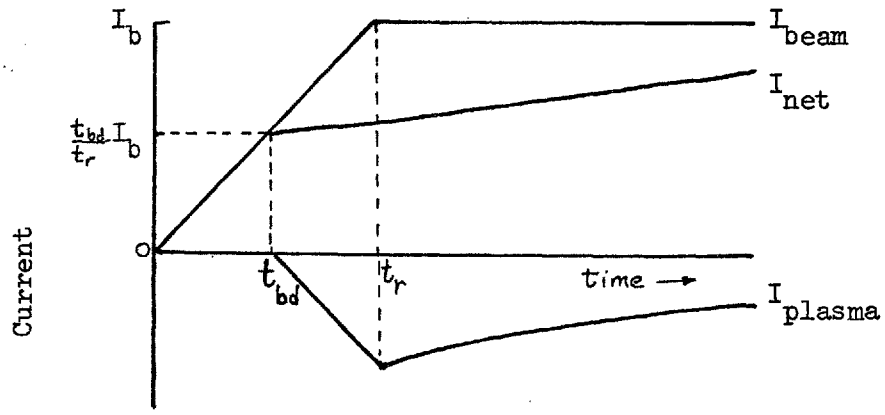

a) Injection into neutral gas

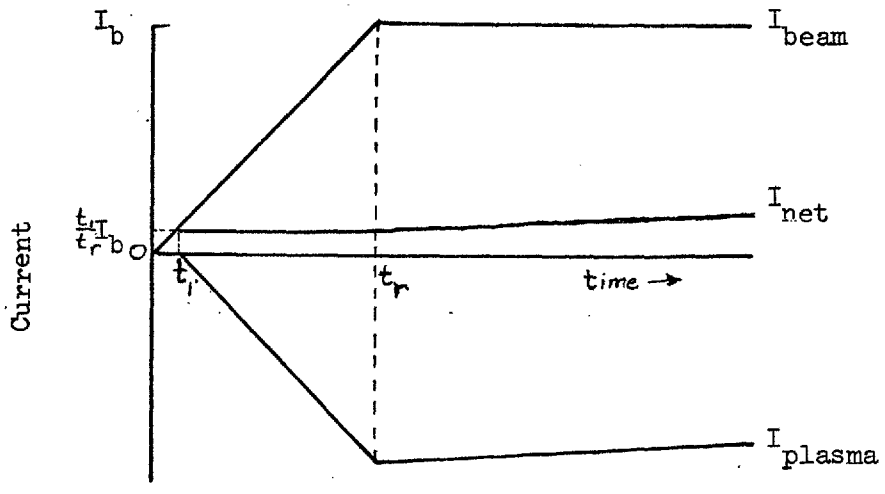

b) Injection into a plasma

Figure 2. Magnetic neutralization of the return current. Until $t=t_1$, the resistance of the plasma channel is large and the plasma current is very small. Thus the net current equals the beam current for $t<t_1$. After $t=t_1$, the plasma resistance drops to a very low value, and the plasma current is induced to counter the additional increase in the beam current. In the neutral gas case (a), the gas must be ionized by the beam, and then must avalanche to produce a dense plasma at $t_1=t_{bd} \lesssim t_r$. Thus, the net current at $t=t_1$ is comparable to the final beam current. In contrast, for the case (b) with a preformed plasma, the plasma is already present at $t=0$, so it must simply be heated to increase its conductivity, which happens for $t_1 \ll t_r$. Thus the net current at $t=t_1$ is much less than the final beam current for injection into a plasma. After $t=t_1$, the additional increase in the net current is governed by the resistive decay of the plasma current.

Consequently, the net current is expected to be nearly zero for injection into a preformed plasma and somewhat larger for injection into a neutral gas. Roberts and Bennett (1968) and Levine, et al., (1971) measured I_{net} for injection into a neutral gas and into a plasma, and their results supported the theory.

After the plasma current is formed, it decays with an L/R time from the inductance L and resistance R associated with the beam-plasma current channel, as proposed by Yonas, et al. (1969). They assumed that the product $\omega_{ce}\tau$ of the electron cyclotron frequency ω_{ce} and the collision time τ for electron momentum transfer was very much less than one. Thus the axial electric field was proportional to the scalar resistivity η. For a uniform beam and plasma channel extending from r = 0 to r = r_o and lying in the center of a conducting drift tube of radius r_w, the induced axial electric field E_z equals ηj_{pz}, i.e.

$$\eta j_{pz} = E_z = -\frac{\partial}{\partial t}\int_r^{r_w} B_\theta\,(r')\,dr' \tag{2-9}$$

For $r \ll r_w$; $E_z(r) \approx E_z(0)$

$$E_z = -\frac{\partial}{\partial t}\left[\int_o^{r_o}\frac{\mu_o j_{net}\, r}{2}\,dr + \int_{r_o}^{r_w}\frac{\eta_o I_{net}}{2\pi r}\,dr\right]$$

$$= -\frac{\mu_o}{2\pi}\left(\tfrac{1}{4} + \ln\left(\frac{r_w}{r_b}\right)\right)\frac{\partial I_{net}}{\partial t}\,.$$

Thus for a uniform beam

$$\eta j_p = \frac{\eta}{\pi r^2} I_p = -\frac{\mu_o}{2\pi}\left(\tfrac{1}{4} + \ln\left(\frac{r_w}{r_b}\right)\right)\frac{\partial I_{net}}{\partial t} \tag{2-10}$$

For an axial length l of the current channel, the inductance L defined by

$$\tfrac{1}{2} L I_{net}^2 = \int_V \frac{\underline{B}\cdot\underline{H}}{2}\,d^3R$$

is $$L = \frac{1\ \mu_o}{2\pi}\left(\frac{1}{4} + \ln(r_w/r_b)\right) \qquad (2\text{-}11)$$

For $\underline{j}_p = j_p \hat{z}$ and $\underline{j}_b = -j_b \hat{z}$, equation (2-10) becomes

$$\frac{nl}{\pi r_o^2} I_p = RI_p = -L \frac{\partial I_{net}}{\partial t} = -L \frac{\partial I_p}{\partial t}$$

$$\frac{\partial I_p}{I_p} = -\frac{R}{L}\,\partial t$$

$$I_p(t) = I_p\,(t=t_r)\ e^{\left(-(t-t_r)/(L/R)\right)} \qquad (2\text{-}12)$$

Yonas and Spence report that this expression gives an adequate description for their data in air at a pressure above 1 Torr. Levine, et al. (1971) used the same analysis to find R and [with the Spitzer (1962) conductivity] inferred an electron temperature T_e. Their data implied T_e was 0.35 eV for injection into a CH_4 plasma (P = 150 mTorr) and into neutral air at 880 mTorr.

More recently, the analysis of I_{net} has been extended by McArthur and Poukey (1973). They used a computer solution of Ohm's law, Maxwell's equation, and the rate equations for ionization to calculate I_{net} (t) for injection of a beam into neutral nitrogen. Their calculations matched their experimental waveform to 20% for P $\geq$ 1 Torr N_2. Their computer solution gave $\omega_{ce}\tau > 1$ for P < 1 Torr. Below 1 Torr they were not able to obtain agreement between theory and experiment for I_{net} (t). No one has presented a theory for the low pressure case with $\omega_{ce}\tau < 1$ and no one has reported measuring n_e and T_e to find $\omega_{ce}\tau$ experimentally.

2.2d Additional Ionization after Breakdown

After breakdown, the high energy tail of the electron velocity distribution $f(\underline{w})$ causes additional ionization.

$$\frac{\partial n_i}{\partial t} = \int_o^\infty 4\pi w^3 f(\underline{w})\, Q_{ioniz}\, n_o\, dw \qquad (2\text{-}13)$$

for an isotropic velocity distribution $f(\underline{w})$, and a neutral number density n_o with an ionization cross-section $Q_{ioniz}(w)$.

2.2e Plasma Heating

If there is no additional ionization and if the expansion velocity of the plasma is zero, the rate of increase of the particle energy per unit volume W_p is

$$\frac{\partial W_p}{\partial t} = \frac{3}{2} n k \frac{\partial T_e}{\partial t} = \eta j_p^2, \qquad (2\text{-}14)$$

where j_p is the plasma current density and η is the plasma resistivity. Equation (2-14) is valid if the heating takes place on a time scale short compared to the electron-ion energy equilibration time, and long compared to the electrons' energy relaxation time. The energy is then deposited in the three degrees of freedom of the electron distribution. The resistivity is given by

$$\eta = \frac{m}{n_p e^2} \nu_{eff} \qquad (2\text{-}15)$$

The effective collision frequency ν_{eff} for momentum transfer to the electrons is given by

$$\nu_{eff} = \nu_{e-i} + \nu_{e-n} + \nu_{anom}$$

where the terms correspond to electron-ion collisions, electron-neutral collisions, and anomalous collisions arising from streaming instabilities, respectively.

2.3 Heating via Streaming Instabilities

2.3a Heating via Electron-Electron (e-e) Modes

Buneman (1959) has shown that when two streams of charged particles pass through each other, an electrostatic instability grows, and energy is exchanged between the two streams. If the plasma frequencies of the two streams are very different, the wave is nearly at rest in the frame of the species with the smaller plasma frequency. In this frame one sees a particle of the other stream approaching a small perturbation in charge density. The electrostatic field of the perturbation accelerates the particle (e.g. a negatively charged particle approaching a negatively charged perturbation slows down). As it is accelerated, it contributes to the local electric field of the perturbation. The particles behind it see a larger retarding field, and the perturbation grows in time. The electric field of the wave has the effect of slowing the particles in one stream and accelerating particles in the other stream, and energy is transferred from one to the other.

Excitation of the instability requires a double-humped velocity distribution with significant energy in the "bump in the tail". The quasi-linear, relativistic theory by Fainberg, et al. (1969) shows that the saturation level of the field energy of the instability is

proportional to $\gamma(\frac{n_b}{n_p})^{1/3}$, where the two streams are the beam electrons and the plasma electrons with densities n_b and n_p respectively, and γ is the usual relativistic factor for the beam electrons. It is assumed that a large field energy in the instability would be correlated with a large energy transfer to the plasma electrons. Consequently, it is desirable to have n_b/n_p large and to have γ large. Since high-current, relativistic electron beams can provide n_b up to 10^{14} cm^{-3} and $\gamma = 10\text{-}20$, the prospect of using these beams to heat a plasma for thermonuclear fusion appears very attractive.

The excitation of this instability requires that (1) the relative velocity of the two streams be much larger than the thermal velocities of the particles in their respective stream frames and (2) the electron collision frequency be sufficiently small, as described by Singhaus (1964). Since one stream is relativistic, the first criterion is easily satisfied. The second criterion can be expressed as

$$\nu_{eff} < 0.7\,\omega_p \frac{n_b}{\gamma n_p} \frac{V_o}{\Delta V_o} \equiv \nu_{Singhaus} \qquad (2\text{-}16)$$

where ν_{eff} is the effective collision frequency for the plasma electrons, V_o is the axial beam velocity, and ΔV_o is the axial spread in the beam velocity. The physical picture contained in this expression is that if the spread in the velocities of the beam particles is too large, there are few particles with the phase velocity of the fastest growing wave, so few beam particles couple to the wave. If the collision frequency of the plasma electrons is too large, the plasma electrons do not stay in phase with the electrostatic field of the wave. Either effect would reduce the

correlation of $\langle \delta E \cdot \delta n_p \rangle$ and hence reduce the strength of the instability. The expression was derived by finding the ν_{eff} which caused the growth rate of the instability to go to zero for a given ΔV_o.

Since the present experiment began, numerical studies have been published on the non-linear development of the instability. Thode and Sudan (1973) included the effects of finite wave-energy and of particle trapping. In addition to these effects, Toepfer and Poukey (1973) included the effect of ion density fluctuations. Thode and Sudan found that the growth of the instability ceases when the wave energy density W_{field} reaches a fraction f of the beam energy density W_{beam} given by

$$f = \frac{W_{field}}{W_{beam}} = \frac{\sum_k \frac{\varepsilon_o}{2} E_k^2}{n_b \gamma mc^2} = 0.158\ S \qquad (2\text{-}17)$$

for $S < .5$, where S is a strength parameter given by

$$S \equiv \beta_o^2 \gamma \left(\frac{n_b}{2n_p}\right)^{1/3} \qquad (2\text{-}18)$$

After a transition region for $0.5 < S < 0.66$, f decreases as S increases. Consequently, for a given ratio n_b/n_p, there is an optimum value of γ defined by $S = 0.66$ for the maximum field energy in contrast to the quasi-linear result in which f increased monatonically with γ.

In addition, the calculations of Thode and Sudan (1973) showed that the particle energy density at saturation is a weak function of the strength parameter and is 20% to 30% of the initial kinetic energy density of the beam. The "numerical experiments" of Toepfer and Poukey (1973) gave this fraction as 10 to 20%. The second

figure includes the effect of the ion density fluctuations. In the present state of the theory, it seems best to take the value of

$$W_{plasma} = 0.2\, W_{beam} \qquad (2\text{-}19)$$

to compare with experiment for energy transfer to the plasma via the electron-electron instability.

It should also be noted that Toepfer and Poukey (1973) found that the saturation level of the particle energy dropped by 37% as the initial plasma temperature was raised from 0 to 660 eV. Consequently, it appears that the efficiency of the interaction drops as the plasma is heated.

2.3b Heating via the Ion-Acoustic (e-i) Mode

When the thermal velocity of the plasma electrons exceeds their drift velocity V_{ez} relative to the ions, the ion acoustic instability may develop when V_{ez} exceeds the sound speed, as discussed by Kadomstev (1965) and others. In contrast to the case treated above, in which the two streams were the beam electrons and the plasma electrons, this instability develops between the plasma electrons and the plasma ions. The beam is a source of energy to drive the return current in the plasma and imparts a drift velocity V_{ez} to the plasma electrons relative to the ions.

The increased collision frequency between the plasma electrons and the electrostatic fluctuations associated with the instability produces an anomalous resistivity and increases the energy dissipated in the plasma.

When the experiment began, the prevailing theory for the ion-acoustic instability was based on the saturation of the instability by ion trapping, as developed by Sagdeev (1967). This leads to an effective collision frequency

$$\nu_{Sagdeev} \approx .01 \frac{T_e}{T_i} \left(\frac{V_{ze}}{V_{th}}\right)^2 \omega_{pe}, \; T_e >> T_i \qquad (2\text{-}20)$$

where T_e and T_i are the electron and ion temperatures, V_{ze} and V_{th} are the electron drift velocity and thermal velocity respectively, and ω_{pe} is the plasma frequency.

Caponi and Davidson (1973) suggested that the saturation mechanism is dominated by ion-resosnance broadening, thus producing a different collision frequency:

$$\nu_{c+D} = \frac{1}{4\sqrt{2\pi}} \left[\frac{T_i}{T_e}\right]^{3/2} \omega_{pe}, \quad \text{for} \quad \frac{T_i}{T_e} << 1 \qquad (2\text{-}21)$$

for the approximations chosen by the authors, i.e. $(\Delta k)\lambda_D = 1$, $k_o^2 \cdot \lambda_D^2 = \frac{1}{2}$ and $\frac{\omega_{pi}\lambda_D}{V_{ze}} = \frac{1}{2}$ where k is the width of the excited spectrum in momentum space, λ_D is the Debye length, k_o is the center of the excited spectrum, and ω_{pi} is the ion plasma frequency. In contrast to the Sagdeev value, the Caponi and Davidson resistivity is only weakly dependent on the ratio of the $\frac{V_{ze}}{V_{th}}$. Caponi and Davidson compare the resistivity from their treatment with several experiments, and the agreement is quite good. Their value of the anomalous resistivity may differ from that of Sagdeev by more than two orders of magnitude and is generally smaller than the Sagdeev value. Since the detailed kinetic treatment of the instability and the agreement with experiments favour the Caponi and Davidson

resistivity, it will be used in the comparison of this experiment with the theory.

If the ion-acoustic instability is excited, the effective collision frequency of the plasma electrons must be added to the electron-ion and electron-neutral collision frequencies in the Singhaus criterion for the electron-electron mode. Consequently, if the ion-acoustic mode is excited, the e-e mode may be suppressed.

2.3c Application of the Theory to One Example

The heating that is expected from (1) the e-e mode, (2) the ion-acoustic mode, (3) classical electron-ion collisions, and (4) electron-neutral collisions as a function of the initial plasma number density is shown in Figure 3. The beam in this example has a current density of 2.5×10^{8} A/m^2, an electron energy of 350 keV, and a duration of 100 ns. The beam's number density is, therefore, $n_b = 6.3 \times 10^{12}/cm^{-3}$ and the beam's energy density is $W_{beam} = 2.2 \times 10^{24}$ eV/cm^3. The initial plasma temperature is 1 eV.

The final temperatures for the various heating mechanisms are calculated as described below:

<u>E-E Mode</u> - at saturation, the plasma energy density $nkT \approx 0.2\ W_b$. Therefore,

$$kT_f = \frac{0.2\ W_b}{n_e} \approx \frac{4.4 \times 10^{23}}{n_e}\ eV \qquad (2\text{-}22)$$

with n_e in m^{-3} for the post-1972 theory. The pre-1972 theory of Fainberg, et al., (1969) assumed the particle energy nkT equaled the field energy at saturation. Thus

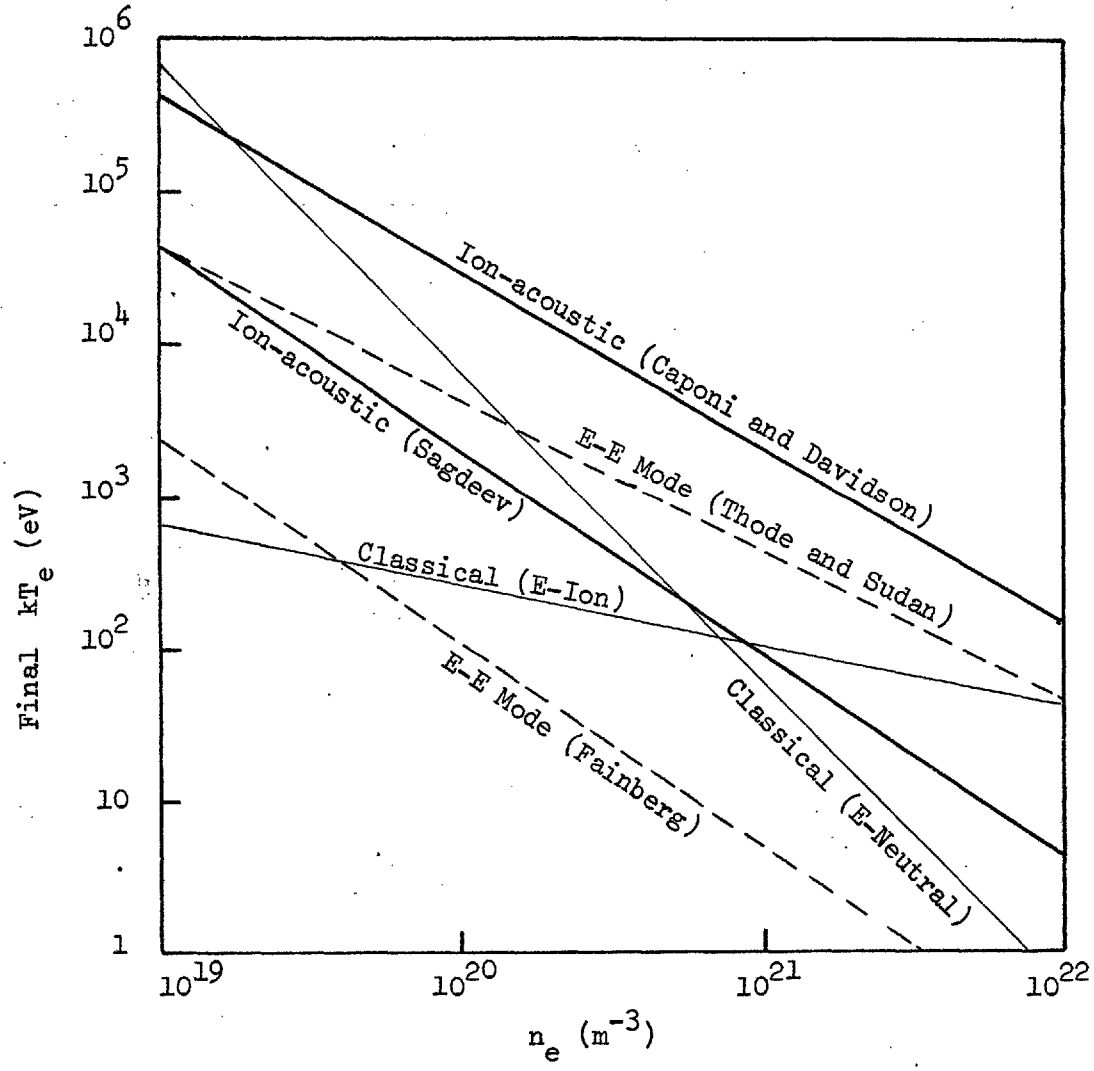

Figure 3. Estimates of plasma heating as a function of the plasma number density n_e. The graph gives the final electron energy kT_e expected from heating a plasma with a number density n_e by a beam of 350 keV electrons with a current density of 2.5×10^8 amperes/m^2 for 100 ns. As explained in Section 2.3c, the calculations were done for a) heating by the e-e mode as described by Thode and Sudan(1973), b) heating by the e-e mode as described by Fainberg, et al. (1971), c) heating by the ion-acoustic mode as described by Caponi and Davidson (1973), d) heating by the ion-acoustic mode as described by Sagdeev (1967), e) heating by the classical electron-ion collisions, and f) heating by the classical electron-neutral collisions with a neutral gas pressure of 10 mTorr H_2.

$$kT_f = \frac{0.158\ S\ W_b}{n_e} = \frac{0.158\ \beta_o^2\ \gamma\ (\frac{n_b}{2})^{1/3}}{n_e^{4/3}} \qquad (2\text{-}23)$$

$$= \frac{5.4 \times 10^{29}}{n_e^{4/3}} \quad eV$$

and is shown for comparison.

Ion-Acoustic Mode - The resistivity that arises from the anomalous collision frequency given by Caponi and Davidson (1973) is

$$\eta_{c\text{-}D} = \frac{5 \times 10^6}{n_e^{1/2}} \quad \text{ohm-m}, \qquad (2\text{-}24)$$

with n_e in m^{-3} and $T_e/T_i = 10$. The increase in the electron energy is given by

$$\Delta \frac{3}{2}\ nkT = \int_o^{10^{-7}} \eta\ j_p^2\ dt$$

$$= \frac{3.1 \times 10^{16}}{n_e^{1/2}} \quad \text{joules/m}^3 .$$

$$k\ T_{f_{c\text{-}d}} = 1\ eV + \frac{1.3 \times 10^{35}}{n_e^{3/2}} \quad eV \qquad (2\text{-}25)$$

The resistivity that arises from the anomalous collision frequency given by Sagdeev (1967) is

$$\eta_{Sag} = \frac{1.6 \times 10^{22}}{n_e^{\frac{1}{2}}\ T_e(eV)^{\frac{1}{2}}} \quad \text{ohm-m} \qquad (2\text{-}26)$$

for $\frac{T_e}{T_i} = 10, \quad V_d = \frac{j_p}{ne}.$

From $\frac{3}{2}\ n\ k\ \frac{\partial T}{\partial t} = \eta\ j_p^2$,

$$\int_{T_o}^{T_f} T^{\frac{1}{2}}\, dT = \frac{2}{3}\,\frac{(1.6 \times 10^{22})}{(1.6 \times 10^{-19})\, n_e^{\frac{3}{2}}} \int_0^{10^{-7}} dt$$

$$kT_f \underset{\text{Sag}}{\approx} \frac{4.6 \times 10^{22}}{n_e} \text{ eV} . \qquad (2\text{-}27)$$

Classical Electron-Ion Resistivity - The classical electron-ion collisions in strong magnetic field produce a resistivity given by Spitzer (1962) as

$$\eta_{\text{Spitzer}} = \frac{1.75 \times 10^{-3}}{T_e^{3/2}(\text{eV})} \text{ ohm-m for } \ln \Lambda = 10. \qquad (2\text{-}28)$$

Integrating the equation for $\frac{\partial T}{\partial t}$ from zero to 100 ns, gives

$$^3/_2\, nk \int_{T_o}^{T_f} T^{3/2}\, dT = 1.75 \times 10^{-3} \int_0^{10^{-7}} (2.5 \times 10^8)^2\, dt$$

$$T_f^{5/2} - 1 = \frac{1.1 \times 10^{26}}{n_e}$$

$$kT_f \underset{\text{Spitzer}}{=} \frac{2.6 \times 10^{10}}{n_e^{2/5}} \text{ eV.} \qquad (2\text{-}29)$$

Classical Electron-Neutral Resistivity - The electron-neutral resistivity for collisions with H_2 molecules is given by

$$\eta_{en} = \frac{6.6 \times 10^{-6}\ n_o}{n_e} \text{ ohm-m} \qquad (2\text{-}30)$$

from the data for the momentum transfer cross section for electrons in H_2 given by Delacroix (1960). The cross section varies as $(Ve)^{-1}$ QV_e was taken from the value of QV_e for 10 eV electrons. For $n_o = 3.5 \times 10^{22}$ P m^{-3} and P in Torr, integration of $\frac{\partial T}{\partial t}$ gives

$$kT_{f_{en}} = \frac{6 \times 10^{45}}{n_e^2} P \quad eV \tag{2-31}$$

In the example, the neutral number density is taken to be 3.5×10^{20} m^{-3} which corresponds to P = 0.01. For large values of kT_f, additional ionization would certainly lower the actual value of the electron temperature. Nevertheless, the heating via electron-neutral collisions must be included in a comparison of theory with an experimentally measured value.

CHAPTER 3

APPARATUS

3.1 General Description of the Apparatus

A brief description of the major items of the apparatus and of their purpose will give a perspective for the more detailed discussion that follows. A block diagram of the apparatus is given in Figure 4. The various items of hardware are divided into two categories according to their function as follows:

I. Generation and handling of the electron beam
   - A. High voltage generator
     1. D.C. power supply
     2. Marx generator
     3. Blumlein transmission line
   - B. Beam production and focusing
     1. Vacuum diode
     2. Cone focusing chamber

II. Plasma source
   - A. Z-discharge chamber
   - B. Experimental chamber.

The desired characteristics of the apparatus were partially determined by the capabilities of the diagnostics that were used to study the plasma. The primary diagnostic in the present experiment was laser scattering, which measured the number density and velocity distribution of the plasma electrons. The power available from the

Figure 4. Block diagram of the experimental apparatus.

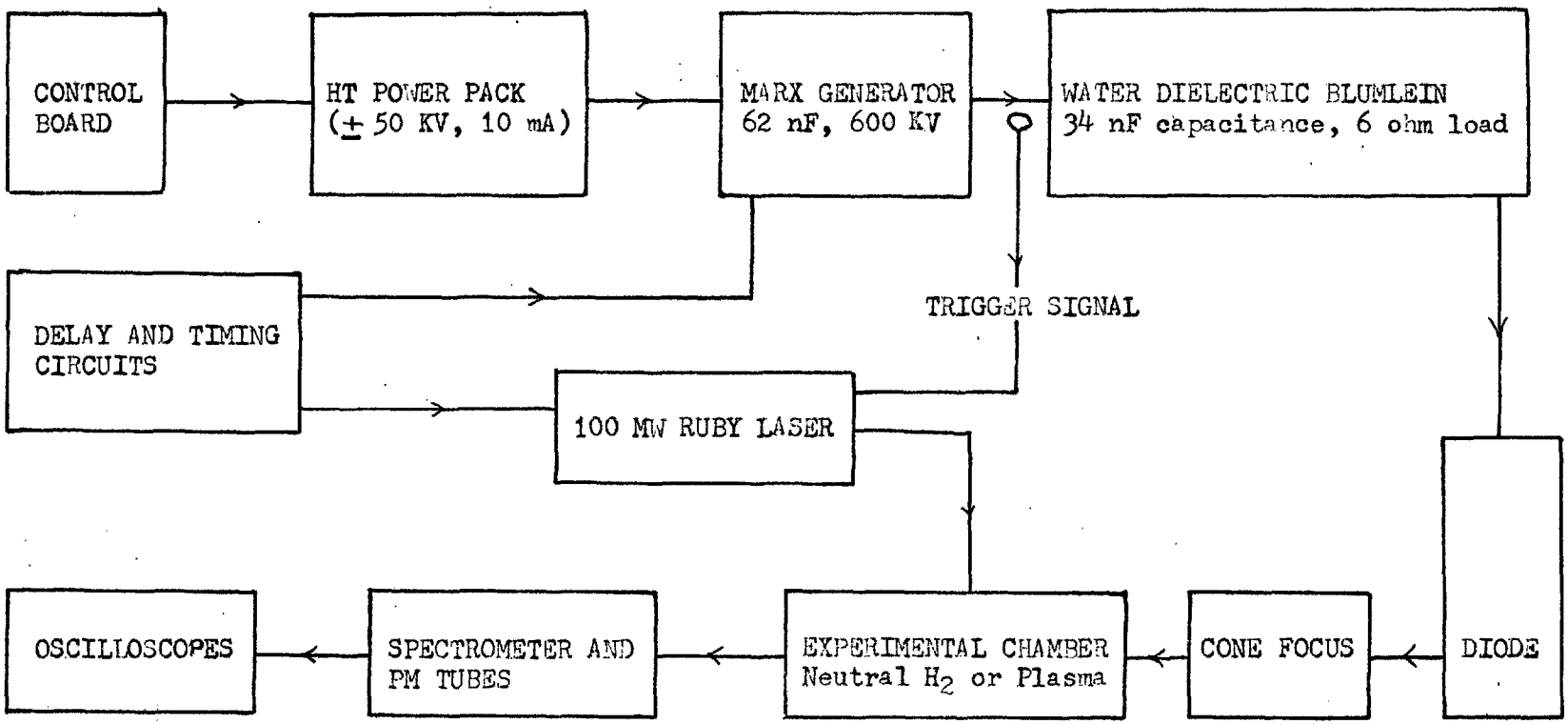

laser (100 MW) placed a lower limit on the plasma number density of $n_e \geq 10^{14}$ cm^{-3}, which in turn placed a lower limit on the beam number density $n_b \geq 10^{12}$ cm^{-3} to obtain a measurable effect. The basic experimental requirements were (1) as dense an electron beam as practical, and (2) a homogeneous plasma with as high a percentage ionization as practical with an electron number density between 10^{14} and 10^{16} cm^{-3}.

3.1a Generation and Handling of the Electron Beam

High voltage generator

The first problem of producing a high-current, relativistic electron beam was to produce a voltage pulse of several hundred kilovolts from a generator of a few ohms and for a duration of approximately 100 ns. A DC power supply charged a set of N capacitors in parallel. The capacitors were then switched to series, which resulted in a transient voltage multiplication of approximately N. The capacitor network that was charged in parallel and discharged in series is called a Marx generator (hereafter called the Marx for brevity). The Marx pulse charged a fast storage capacitor, which was in the form of a transmission line.

In general, an additional voltage multiplication of less than 2 can be achieved by charging a load capacitor through an inductor from another capacitor. This technique is commonly called resonant charging and was employed to charge the transmission line from the Marx.

The transmission line was the pulse forming network and the impedance matching element for the voltage generator. Since the transmission line was pulsed charged, it had to maintain the high

voltage for only a short time. The time dependence of breakdown phenomena could then be used to reduce the dimensions of the fast storage system (the transmission line as a capacitor while it was being charged) which lowered its inductance and its output impedance.

However, it is well known that an ordinary transmission line of impedance Z_o delivers the maximum energy to a load when the load impedance is also Z_o. Unfortunately, the output voltage at the maximum output energy is only half the charging voltage on the line. After working so hard to achieve a high voltage, one would regret having to use only half the charging voltage. The type of transmission line known as the Blumlein transmission line (hereafter called the Blumlein for brevity) avoids this difficulty. The Blumlein is composed of two transmission lines, each charged to a voltage V_o, with one common conductor and with the load impedance inserted between the two lines in the other conductor as shown in Figure 5. The impedance of the two lines need not be equal, but maximum power output is achieved if each line has an impedance Z_o and if the load impedance is $2Z_o$. When one end of the first line is shorted by a spark gap (commonly called the fast switch), a pulse travels down the line into an impedance Z_{total} (from the second line in series with the load). The transmitted voltage is given by the usual expression

$$V = V_o \frac{2\,Z_{total}}{Z_o+Z_{total}} = V_o \frac{2\,(3Z_o)}{Z_o+3Z_o} = \frac{3}{2} V_o$$

with 2/3 of that voltage(i.e. $\frac{2}{3} \times \frac{3}{2} V_o = V_o$) dropped across the load. The duration t_b of the voltage across the load is the double transit time of each of the two lines. At $t = t_b$, the reflected wave in the first line and the transmitted wave in the second line return

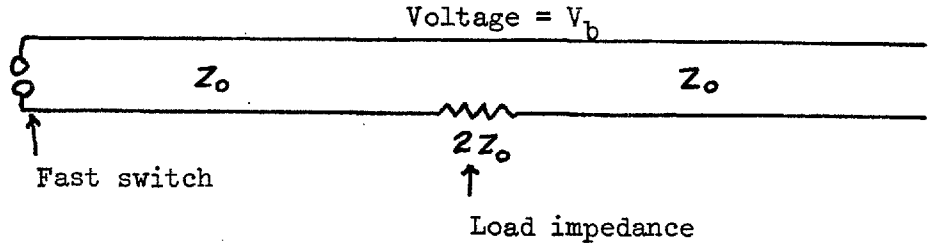

a) Blumlein configuration

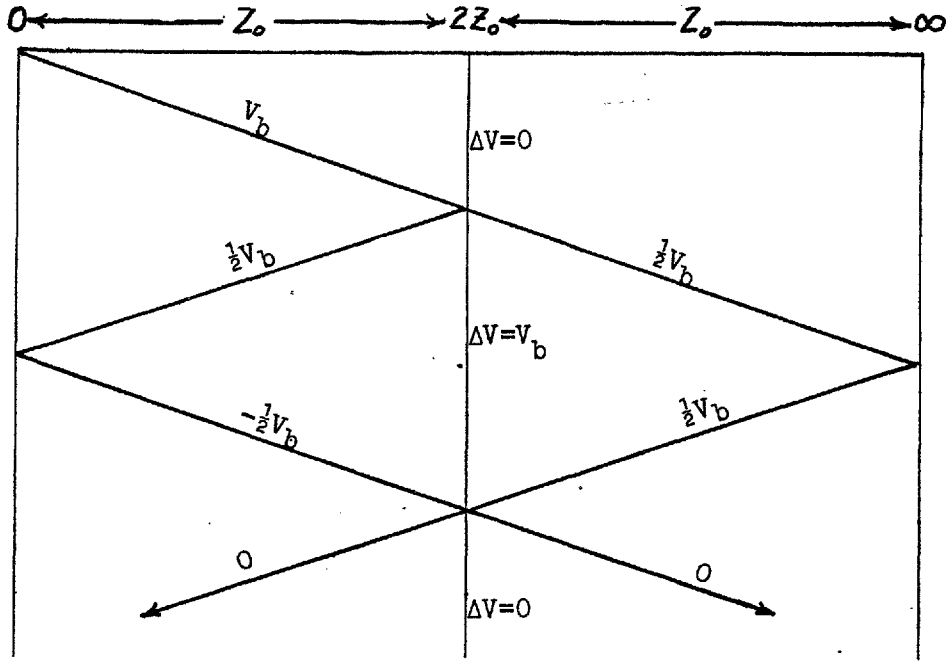

b) Voltage distribution

Figure 5. Schematic diagram of a Blumlein. The Blumlein configuration is shown in (a) and the voltage distribution in the line as a function of time is shown in (b). The horizontal position corresponds to the position along the line as shown in (a); the impedance in the circuit at that position is shown on the top scale. Time increases down the page. The wave begins at the fast switch and moves with the velocity of the E-M wave in the dielectric. The locus of each electromagnetic wave is shown with the amplitude of the wave (the voltage across the line in front of the wave minus the voltage across the line behind the wave). The full charging voltage V_b develops across the load for the double transit time of each half of the Blumlein.

to the load and the voltage across the load becomes zero. The output into the load is then a square pulse at the full charging voltage. During the pulse all of the energy that is stored in the Blumlein is dissipated in the load.

Beam Production and Focusing

The load impedance of the Blumlein was the diode, which contained a cold cathode as the source of electrons and a thin anode foil as an output window for the relativistic electrons. The voltage pulse V is applied across the gap between the anode and the cathode. Electrons are accelerated across the gap and acquire an energy eV. The impedance of the diode is determined by the Child-Langmuir Law for space charge limited current. This law for plane and parallel anode and cathode surfaces is

$$Z = \frac{136\ d^2}{V^{\frac{1}{2}}\ r^2} \quad \text{ohms} \qquad (3\text{-}1)$$

for a cathode of radius r in cm, an anode-cathode gap of d cm, and an applied voltage V in mega-volts (10^6 volts). Since the diode impedance scales as $(d/r)^2$, the area of the beam (πr^2) can be reduced and the beam particle density increased without changing the diode impedance if the gap separation is also reduced. However, the anode-cathode gap closes with a velocity of 1 to 3 cm/μsec, depending on the current density at the cathode. If the gap is too small or if the current density in the diode is too high, the impedance will change significantly during the pulse. Consequently, there is a limit to the beam density that can be produced in the diode. To increase the beam density beyond that

limit without losing control of the beam (i.e. without having a tightly pinched beam that is difficult to control) one requires a focusing system, external to the diode. Converging magnetic fields reflect the electrons as well as focus the beam. A converging metal cone filled with an optimum pressure of gas focuses the beam. Olson (1973) describes the process: The converging sides of the cone causes the induced electric field E_z from the rise of the beam current (Equation 2-7) to decrease with distance from the anode. Since the breakdown time t_{bd} depends on E_z, the beam current $I_b(t_{bd}(z))$ is therefore different for different axial positions. The axially dependent, gas breakdown produces a net current that increases with distance from the anode. The beam is then focused by its own net current. The cone-focusing mechanism was used in the present experiment to increase the beam density.

3.1b Plasma Source

The plasma number density must be sufficiently high to scatter a significant number of photons from the laser into the collection system. The required number density depends on the intensity of the plasma light and on the electron temperature, but is generally greater than 5×10^{14} cm^{-3} for a typical scattering system. If the density is too large, or the temperature of the plasma is too low, the scattered spectrum is dominated by collective effects (scattering from plasma waves) rather than by free electron scattering. Free electron scattering places an upper limit on the electron number density for the target plasma of $\sim 10^{16}$ cm^{-3}. The electron momentum transfer cross section must be sufficiently low to satisfy

the Singhaus criterion (Eq. 2-16) for excitation of the two-stream instability. The initial electron temperature should then be greater than or equal to a few tenths of an electron volt. Such a plasma is easily produced in a z-pinch, which was the plasma source for the present experiment.

If the electron beam is injected into a neutral gas, it will produce a plasma. This method was also used, although it had the disadvantage that the initial plasma parameters after breakdown were not known.

The walls of the plasma source contained ports for the laser input, the laser output, a light dump for the main laser pulse, and a viewing dump to accommodate the laser scattering experiment. In the final version of the experimental chamber, the plasma source was attached to a brass chamber containing the four ports to facilitate replacement of the glass z-pinch, which frequently shattered under the high voltages produced during the experiment and under direct bombardment by the beam electrons.

3.2 Marx Generator

J.C. Martin and his colleagues kindly arranged the loan of a Marx from A.W.R.E., Aldermaston, for the present experiment. Since the Marx was supplied, rather than developed for the experiment, a detailed description of the design features would be inappropriate in this thesis. General information about Marx generators is available in standard references, such as Craggs and Meek (1954). The technology employed in building the Marx for the present experiment is given in Storr (1969).

The schematic diagram of the Marx used in the present experiment is given in Figure 6. It is composed of eight ICSE, 0.5 μF, 100 kV capacitors which are charged in parallel and discharged in series with a pressurized column of ten spark gaps. The eight capacitors were each charged to 75 kV to give 600 kV across a capacitance of 0.062 μF when the Marx was switched to series.

3.3 The Blumlein

3.3a The Water Dielectric Blumlein

The Marx charged the Blumlein, the particular configuration of a transmission line described in Section 3.1. The Blumlein was composed of two parallel plate transmission lines folded together with a common plate at high voltage, as shown in Figure 7. The outer lines remained near ground potential during charging and the centerline was charged to the full negative voltage V_b. When the full voltage was reached the fast switch broke down, and the high voltage pulse was delivered to the diode.

The lines in the present experiment used de-ionized water as the dielectric between the plates. The water had a resistivity greater than 5×10^6 ohm-cm, which gave a resistance of approximately 1000 ohms through the water in parallel with the Blumlein capacitance. The RC time to discharge the Blumlein was, therefore, 27 μsecs compared to a charging time of 1.5 μsecs. The advantages of using water included: (1) water was inexpensive, (2) the high dielectric constant of water gave a low velocity for electromagnetic radiation at these frequencies, which allowed a long duration beam pulse to be produced with a short length of transmission line, (3) the energy stored per

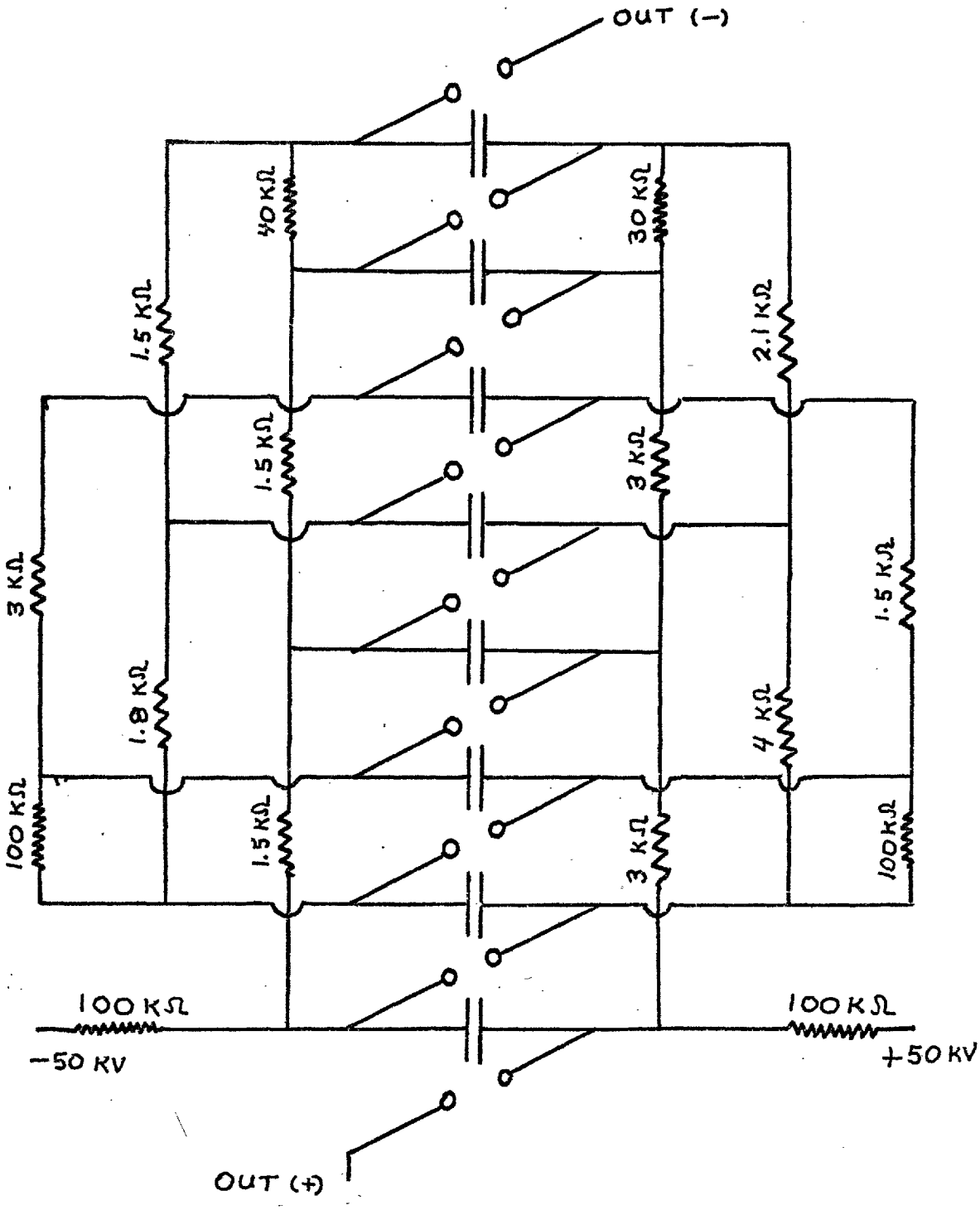

Figure 6. Schematic diagram of the Marx generator. The capacitors are 0.5 μF, 100 kV, low inductance capacitors.

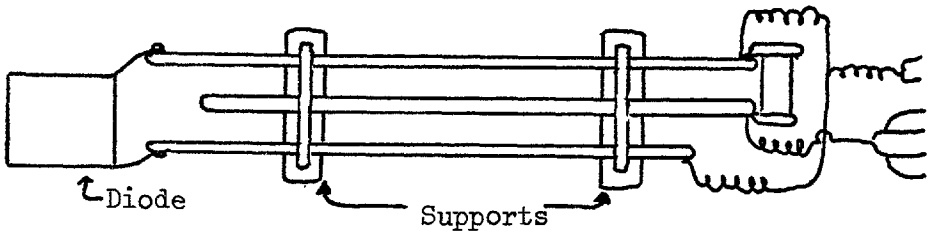

Top view of Blumlein

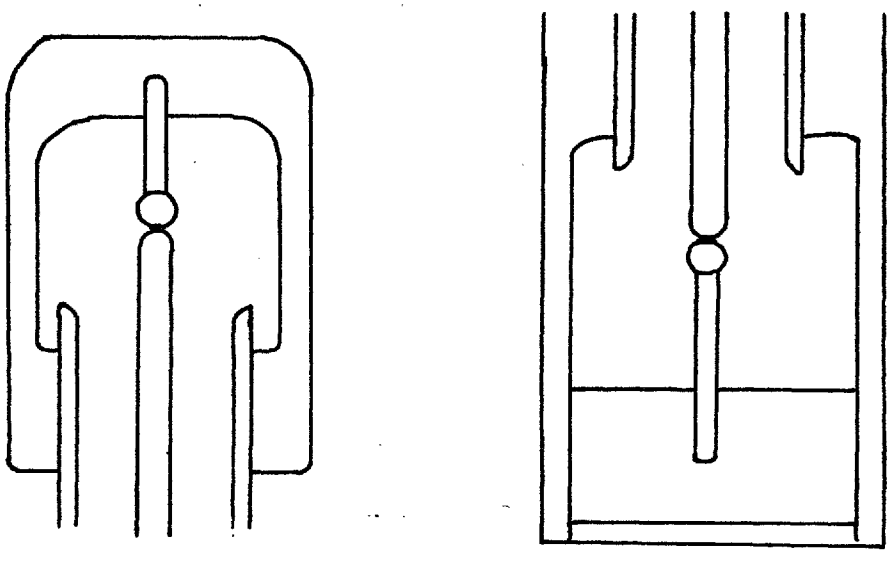

Top support

Bottom support

Figure 7. Construction of the Blumlein supports. The center line rests on a metal ball which is held by the molded socket in the nylon stalk. The rest of the support is polypropylene.

unit volume ($\epsilon E^2/2$) was large, so the spatial dimensions of the low impedance Blumlein were small, (4) the breakdown strength of water was quite acceptable for short times, and (5) water, like all fluids, was self-healing after the occasional breakdown in the stressed volume.

However, the high dielectric constant of water produced severe high-voltage tracking problems at interfaces. Since the boundary condition perpendicular to a dielectric interface is $\epsilon_1 E_1 = \epsilon_2 E_2$, and the relative dielectric constant of water is 80, the small stray electric fields at the water-air interface are multiplied by 80 in air and cause breakdown. The problem is illustrated by the breakdown around a perspex cylinder with a 40 cm tracking distance rather than through a 1 cm water gap shown in Figure 8.

3.3b Construction of the Blumlein

In spite of these difficulties, water was used for each of the three Blumlein systems that were built during the course of the present experiment.

Each of the three systems was balanced, i.e., the impedance of each of the two lines was Z_o and was half the load impedance $Z_L = 2Z_o$. The first lines were for a 20 ohm system (20 ohm load) and produced a 30 kA beam of 600 keV electrons for 100 ns. These lines were loaned by AWRE and had been used with an oil dielectric. The supports for the center (high voltage) line were inadequate to withstand the electrical stresses of a water system, and oil leaked from the inside of the lines. These two problems ensured that they were temporary lines for use until I learned enough to build a permanent set of lines.

Figure 8. High voltage breakdown at the water-air interface. The streamer ran 40 cm along the surface of the water, over the perspex edge, down the side, around the chamber, and across to the opposite side, rather than breakdown the 1 cm water gap.

The next two sets of lines were for 6 ohm systems to produce 100 kA at 600 kV for 100 ns. The first of these was constructed of chipboard which was sealed in araldite and covered with copper, a standard construction. The lines quickly absorbed water and split along the seams. For the final set, the wood was replaced by poly-propelene. It was clad with copper, which was soldered and smoothed on the edges. This construction did not prove completely satisfactory either, since the electrolytic action between the lead-tin solder and the copper and aluminum in the tank deteriorated the soldered joint. The EM forces on the copper (from the currents) then ripped the joints apart. If another system were to be built, a better construction technique would be to turn the copper over the rounded edge of the poly-propelene, fasten the copper to the poly-propelene with screws in the field-free regions, and recess the heads in the high-field regions.

Various methods of supporting the center lines were tried, and the final system is shown in Figure 7 with drawings of the Blumlein. The phosphor-bronze balls mated to the nylon stalks worked well. A simpler design of poly-propelene directly touching the center line was found to be inadequate, as shown in Figure 9b. The support was destroyed.

The design of the Blumlein was relatively simple. The length of the Blumlein was determined by the length of the pulse required. The separation was determined by the breakdown time for a given electric field, and the width was then determined by the required impedance for the desired load. The empirical formula for a water breakdown is given by Martin (1970) as

(a) (View into Blumlein tank) (b)

Figure 9. High voltage fault modes in water. High voltage breakdown through the support for the center line is shown in Figure 9a; the discharge destroyed the support. Tracking along the creases in the PVC liner at the rear of the tank is also evident in 9a. Discharges between the center line and an outer line and from the ground conductor towards the Marx are shown in Figure 9b.

$$F = \frac{k}{t_{eff}^{1/3} A^{1/10}} \quad \text{MV/cm} \qquad (3\text{-}2)$$

where k = 0.3 for positive streamers and 0.6 for negative streamers, t_{eff} is in μsecs, and A is the electrode area in cm^2. The appropriate time t_{eff} is approximately the charging time divided by π. For V = 0.6 MV, t = 0.4 μsecs, and A = 3.2×10^4 cm^2, the minimum separation is 2.1 cm for breakdown. The separation of 7 cm used in the experiment gives a safety factor of 3.5.

The impedance of a strip transmission line is

$$Z = \frac{377}{\sqrt{\epsilon_r}} \frac{d}{w} \quad \text{ohms} \qquad (3\text{-}3)$$

with d = the plate separation, w = the plate width, and ϵ_r is the relative dielectric constant. The impedance is 3 ohms for the present system. For a plate separation of 7 cm, the impedance determines the mean width to be 1.05 meters. The center line is wider than the side lines by twice the gap separation to lessen the likelihood of edge-edge breakdown.

For a pulse length of 100 ns, each line is required to have a 50 ns single transit time. In water this makes the line 1.6 meters long. In oil, the length would be six times that.

3.3c The Fast Switch

The fast switch was a pressurized SF_6 over-volted gap, shown in Figure 10. The current path was along the axis of the cylinder. The electric field along the water-perspex boundary was predominately tangential to the interface, which reduced the likelihood of tracking along the interface (since the local field in the perspex is not

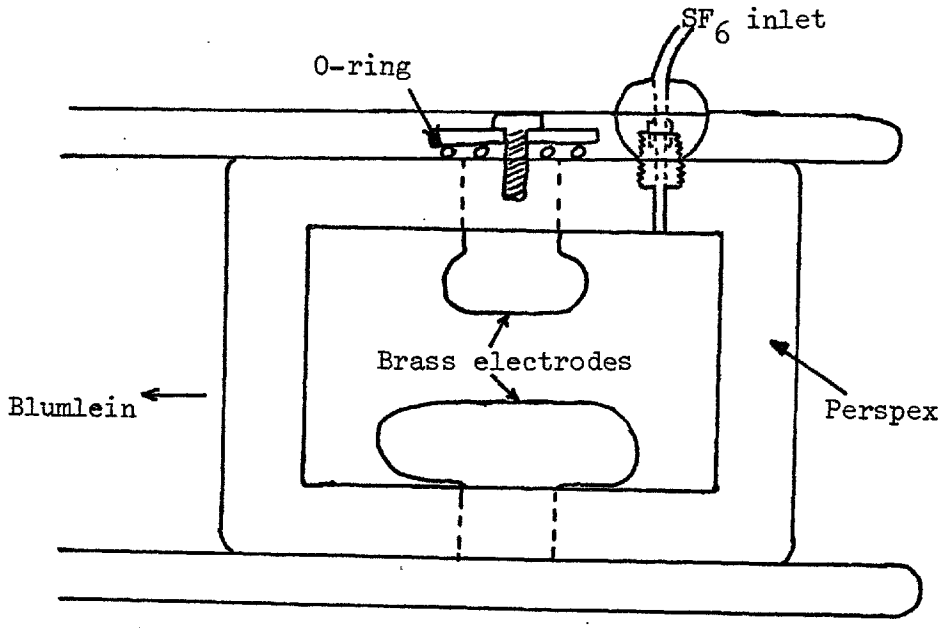

Figure 10. Self-breaking, pressurized SF_6 spark gap for the Blumlein. The design featured 1) large diameter feeds that reduced the V/R field in the perspex, 2) a perspex-water interface that was parallel to the electric field in order to reduce the effect of the dielectric mismatch, 3) an input for the SF_6 that was located in a region with a nearly uniform electric field, and 4) a gap separation that was small compared to the tracking length along the walls to prevent contamination from wall breakdown.

enhanced if $E_{\perp} = 0$). The brass feeds were 1" diameter to reduce the field enhancement in the perspex. The disadvantage of this design was thatatrack would run down the side, across the bottom, and up the other side of the gap when the discharge debris collected on the bottom. Consequently, the gap required cleaning with alcohol and drying under vacuum about every 100 shots. The gap was completely sealed with Simplex, which is a cold-setting acrylic cement for perspex. It was important that no bubbles were caught in the interface since the irregularities increased the likelihood of tracking. This design was developed for the present experiment. After the gap had been conditioned by several shots which removed whiskers from the electrodes, the breakdown was reproducible. The breakdown voltage versus SF_6 pressure is given in Figure 11.

The rise time of the pulse delivered to the load by the Blumlein is determined by the rise of current in the fast switch. The rise time as discussed by Martin (1970) is the sum of a resistive term t'_r (the time taken to establish the current channel) and the usual inductive term $t_L = L/Z$ where Z is the impedance of the generator feeding the line. The resistive term is given by

$$t'_r = \frac{88\ (\rho/\rho_o)^{1/2}}{Z^{1/3} E^{4/3}} \quad \text{ns} \qquad (3\text{-}4)$$

where E is the field along the channel at its closure in units of 10 kV/cm, ρ/ρ_o is the ratio of the density of the gas to air at NTP, and Z is the impedance of the generator driving the channel. In the present experiment, t'_r is 4 ns and is small compared to t_L.

For a disk feeding a spark channel of length l and radius r_o at the center of the disk, the inductance is

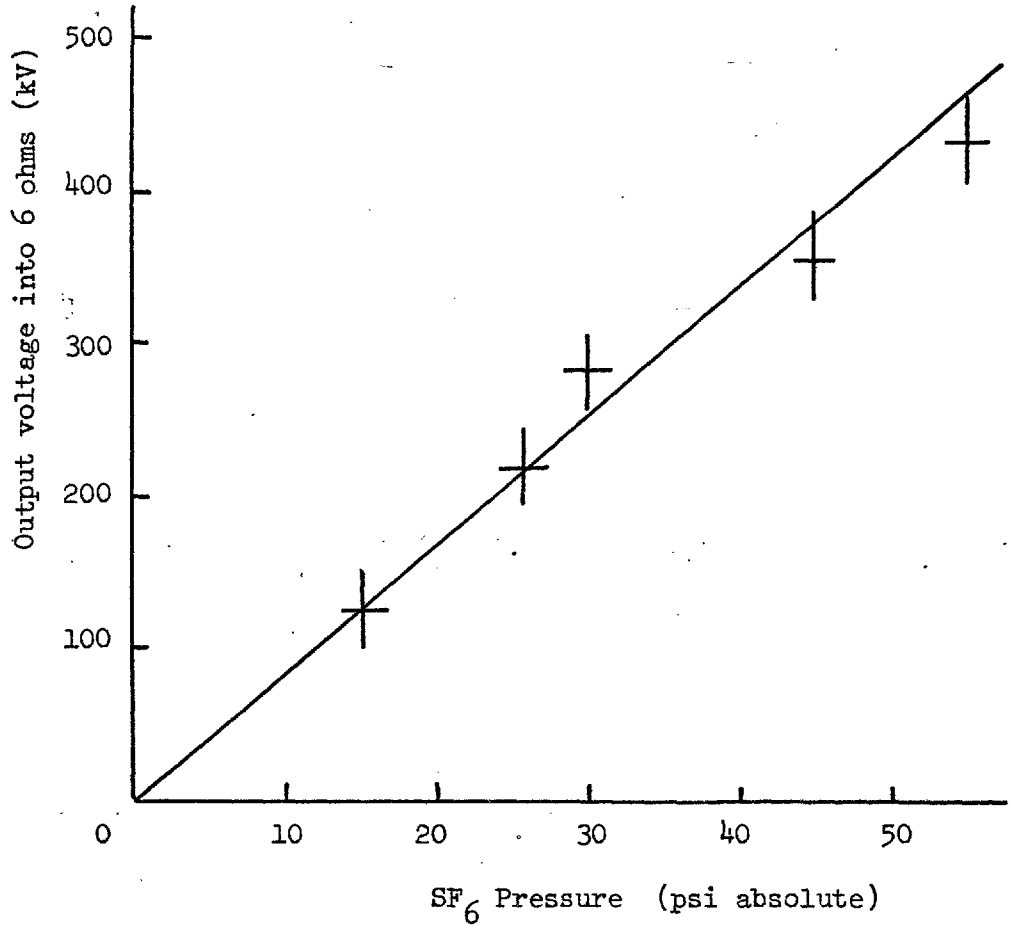

Figure 11. Calibration curve for the Blumlein switch after conditioning with several shots at low voltage.

$$L = 2 \times l(\text{cm}) \times \ln(R/r_o) \quad \text{nano-henries}, \qquad (3\text{-}5)$$

This expression neglects the reduction of the effective inductance caused by the velocity of light in the medium. The finite velocity of light in the medium also increases the effective impedance feeding the channel for times short compared to the width of the strip transmission line divided by the local speed of light. The usual approximation over estimates L and under estimates Z, so it over-estimates t_L. The rule of thumb is to take $\ln (R/r_o)$ as 6 or 7 and not rely on the answer.

For our gap of l = 10 cm fed by an impedance of 3 ohms

$$t_L = \frac{2(10)(6)}{3} = 40 \text{ ns}$$

The 10% to 90% risetime is then ≈ 80 ns compared to the observed rise time of 30 ns.

3.4 Charging the Blumlein with the Marx

The Marx charged the Blumlein. Since the charging time was much longer than the time required for the electromagnetic wave to travel the length of the Blumlein and back, the Blumlein behaved like a simple capacitor during the charging. The schematic diagram of the charging circuit is shown in Figure 12 and the location of the circuit elements relative to the Blumlein are shown in Figure 13.

The Blumlein was charged through a resistor R_s and through inductors to the center line (L_3) and to the side lines (L_1 and L_2). The resistor helped dissipate the energy left in the Marx after the

Figure 12. Marx-Blumlein charging circuit.

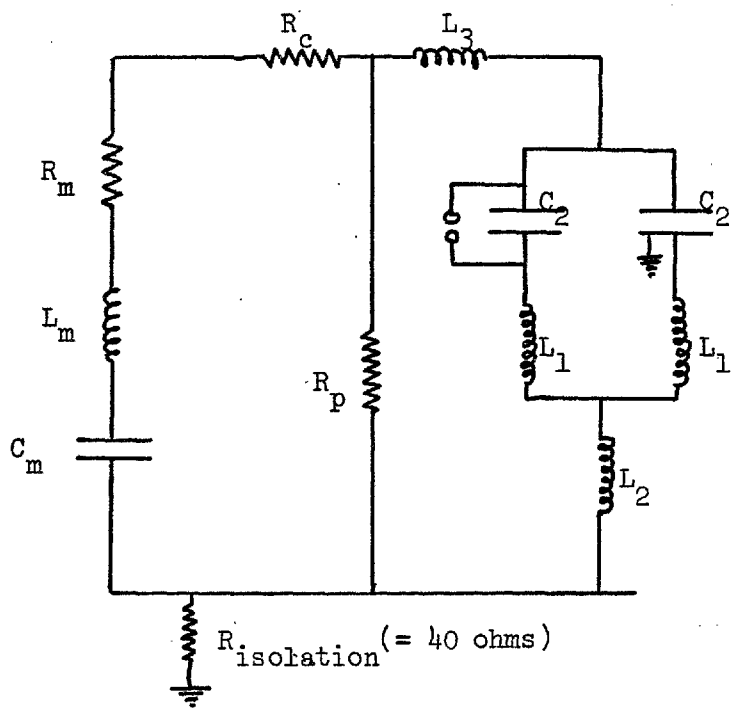

V_o = the charging voltage

p = the number of stages in the Marx with C' per stage

$C_m = C'/p$, the capacitance of the erected Marx

$C_b = 2 \times C_2$, the capacitance of the Blumlein

$R_s = R_m + R_c$, the series resistance in the Marx plus the resistance in the charging resistor

R_p = the resistance in parallel with the Marx from the Marx charging resistors, the voltage monitor, and the water

L_t = the total inductance in the circuit

$$Z = \sqrt{L_t(C_m+C_b)/C_mC_b}$$

$$V = p\,V_o\,\frac{C_m}{C_m + C_b}\left(\exp\left(-\frac{\pi R_s}{2Z}\right) + \exp\left(\frac{-\pi Z}{2R_p}\right)\right),$$ the Blumlein voltage

$$T = \pi\sqrt{L_tC_mC_b/(C_m+C_b)}$$, the time to charge the Blumlein to peak voltage V

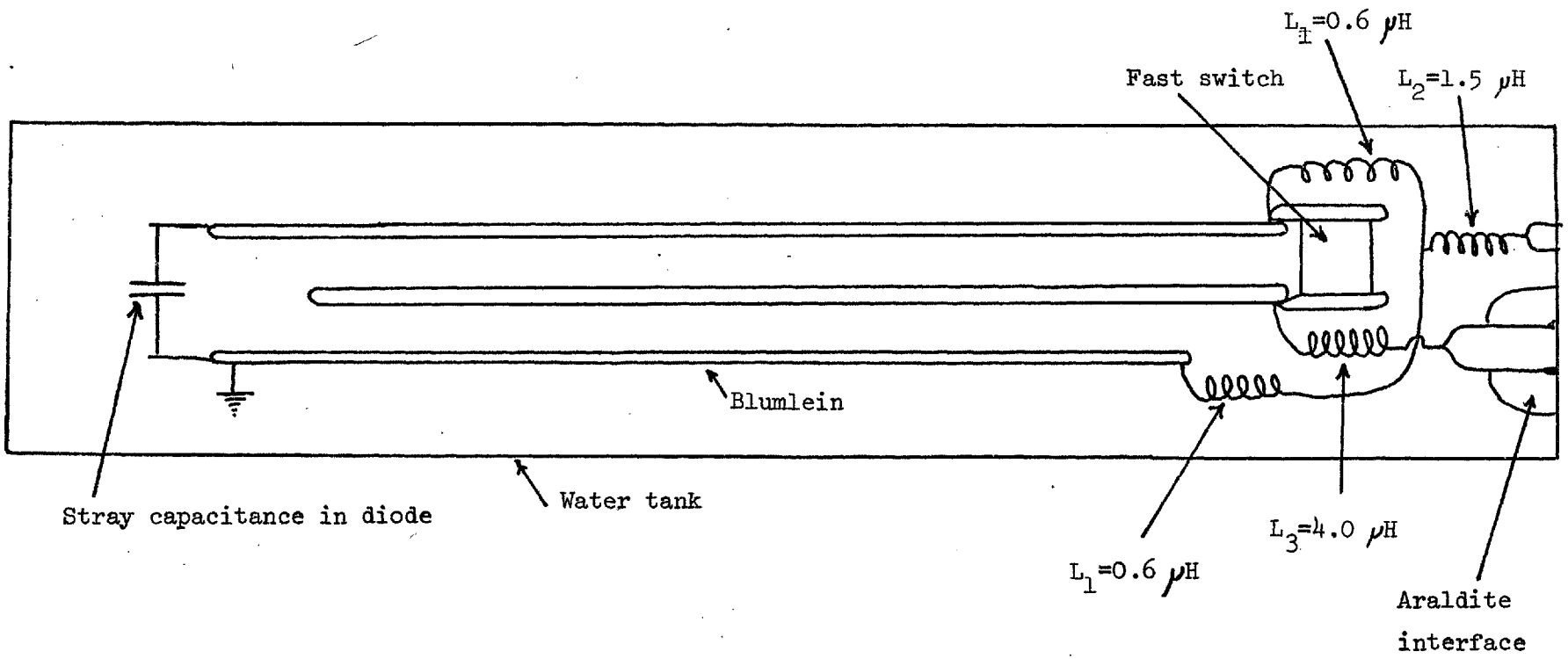

Figure 13. Relative locations of the components of the charging circuit for the Blumlein.

Blumlein's fast switch fired. The inductors to the earthy sides of the lines kept the voltage at the water-air interface sufficiently low to prevent tracking through the tank's water liner and to isolate the two sides of the Blumlein when the fast switch fired. The inductor to the center line (1) provided some isolation for the Marx when the fast switch fired, (2) slowed the charging to reduce the charging imbalance (which produced a voltage prepulse on the diode) of the two halves of the Blumlein and (3) provided some voltage ring-up through resonant charging.

For a line of impedance Z_o, the criterion for the isolation between adjacent ends of the folded Blumlein is that the impedance between the ends is large (a factor of ten) compared to the line impedance for the double transit time (T = 100 ns) of the line. For two equal inductors L_1 in series this gave

$$\omega = 2\pi/T$$

$$\omega(2L_1) = 10\ Z_o$$

$$L_1 = \frac{5TZ_o}{2\pi} \approx 0.6\ \mu H \text{ each for } T = 100 \text{ ns.}$$

The voltage that appeared at the water/air interface when the fast switch fired for the arrangement shown in Figure 8, was

$$V_{interface} = V_{line}\left(\frac{R}{R+\omega(L_1+L_2)}\right) = V_{line}/4$$

which assisted in preventing tracking through the water liner at the earthy interface.

The interface for the high-voltage input into the water was a two-inch diameter stainless-steel tube potted in a six-inch-diameter cylinder of araldite. The large diameter conductor reduced the electric field $\sim(V/r)$ on its surface, and the epoxy helped reduce

the dielectric mismatch in the high-field region. The dielectric mismatch is 80 to 3 for water to araldite and then 3 to 1 for araldite to water. Even with this precaution, tracking could occur from the high voltage input to ground in air or between the water liner and the wood, especially if there was a ridge or crease in the liner near that region. If the track then re-entered the water and punctured the liner, the water drained out. Such a "disaster" is illustrated in Figure 9a.

When all of these things are avoided, the Blumlein charging wave form is as shown in Figure 14. This waveform was analyzed with the charging circuit given in Figure 12 to find the series resistance R_s and the total inductance L for the system. The parallel resistance R_p was neglected in this analysis since the $R_p \cdot C$ time for systems of this size was much greater than the charging time, where C was the total capacitance of the circuit.

The differential equation for the charging circuit is

$$-\frac{Q_m}{C_m} + L_m \frac{\partial I}{\partial t} + IR_s + L_b \frac{\partial I_b}{\partial t} + \frac{Q_b}{C_b} = 0 \qquad (3\text{-}6)$$

where the circuit elements are defined in Figure 7 and

$$Q_m + Q_b = Q_o$$

$$Q_m(t=0) = Q_o$$

$$Q_b(t=0) = 0$$

$$L_b = L_2 + L_3 + \tfrac{1}{2}L_1.$$

Let

$$L = L_m + L_b \text{ and } C = \frac{C_m C_b}{C_m + C_b},$$

and assume a solution of the form

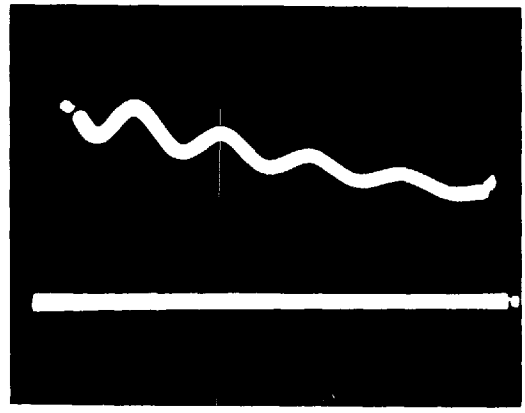

Figure 14. Voltage waveform of the Marx charging the Blumlein through an inductor. The sweep speed is 16 usecs full sweep.

$$Q_b = A \sin(\omega t + \phi) + Q_{20}.$$

The solution for $\sqrt{\frac{L}{C}} \gg \frac{R_s}{2}$, is

$$Q_b = \frac{Q_o C_b}{C_m + C_b} \times \left(1 - \exp\left(-\frac{R_s t}{2L}\right) \cos(t/\sqrt{LC}) \right) . \qquad (3\text{-}7)$$

The voltage V_b across the Blumlein is given by

$$V_b = \frac{Q_b}{C_b} . \qquad (3\text{-}8)$$

Let $V_o = Q_o / p\, C_m$, the charging voltage on each of the p capacitors in the Marx. The gain of the system is defined as

$$G \equiv \frac{V_{b\ max}}{p\, V_o} = \frac{C_m}{C_m + C_b} \left(1 + \exp(-\pi R_s \sqrt{C}/2\sqrt{L})\right) \qquad (3\text{-}9)$$

at $t = \pi \sqrt{LC}$ for the maximum voltage $V_{b\ max}$ on the Blumlein.

If the voltage V'_2 is measured across the charging inductors L_b in series with the Blumlein, the measured voltage is reduced, since the capacitative and inductive reactances have opposite signs.

The ratio of $V'_{2\ max}$ to $V_{2\ max}$ is given by

$$\frac{V_{2}'_{max}}{V_{2\ max}} = \frac{V_{2\ max} + L_b\, {}^2Q_b / t^2}{V_{2\ max}} \simeq 1 - \tfrac{1}{2} \frac{L_b C_b}{LC} \qquad (3\text{-}10)$$

Consequently, this effect (usually $\sim 30\%$) must be considered in the measurement of the gain.

The total inductance L of the circuit is found from the frequency β of the ring of the waveform with

$$\beta = \frac{1}{\sqrt{LC}}$$

$$C = \frac{C_m C_b}{C_m + C_b}$$

$$L = \frac{1}{\beta^2 C} .$$

From the period of the ring in Figure 14, $\beta = \frac{2\pi}{T} = 2.3 \times 10^6$ sec^{-1}. The Marx and Blumlein capacitances are 62 nF and 27 nF respectively, so C = 19 nF. Thus L is 10.3 μH for the charging circuit.

The series resistance R_s is obtained from the slope of the differences $|V-V'|$ between the waveform extrema for each half cycle of the ringing waveform, as shown in Figure 15.

$$R_s = \frac{2 L \beta}{\pi} \times (\text{slope of } |V-V'| \text{ plot})$$

$$= \frac{2 L \beta}{\pi} \times (0.17) = 2.7 \text{ ohms.}$$

The Marx inductance $L_m = 5\,\mu$H, since

$$L_3 = 4\ \mu H \qquad \text{(calculated)}$$

$$L_2 + \frac{L_1}{2} = 1.3\ \mu H \qquad \text{(calculated).}$$

The measured resistance in the series resistor is 1.5 ohms, so there is 1.2 ohms (0.12 ohms/gap) in the Marx's spark gaps.

With these values of the circuit elements, the gain calculated with equation (3-9) is 1.2. Consequently, a Marx charging voltage of only 63 KV will charge the Blumlein to 8 x 1.2 x 63 KV = 600 KV.

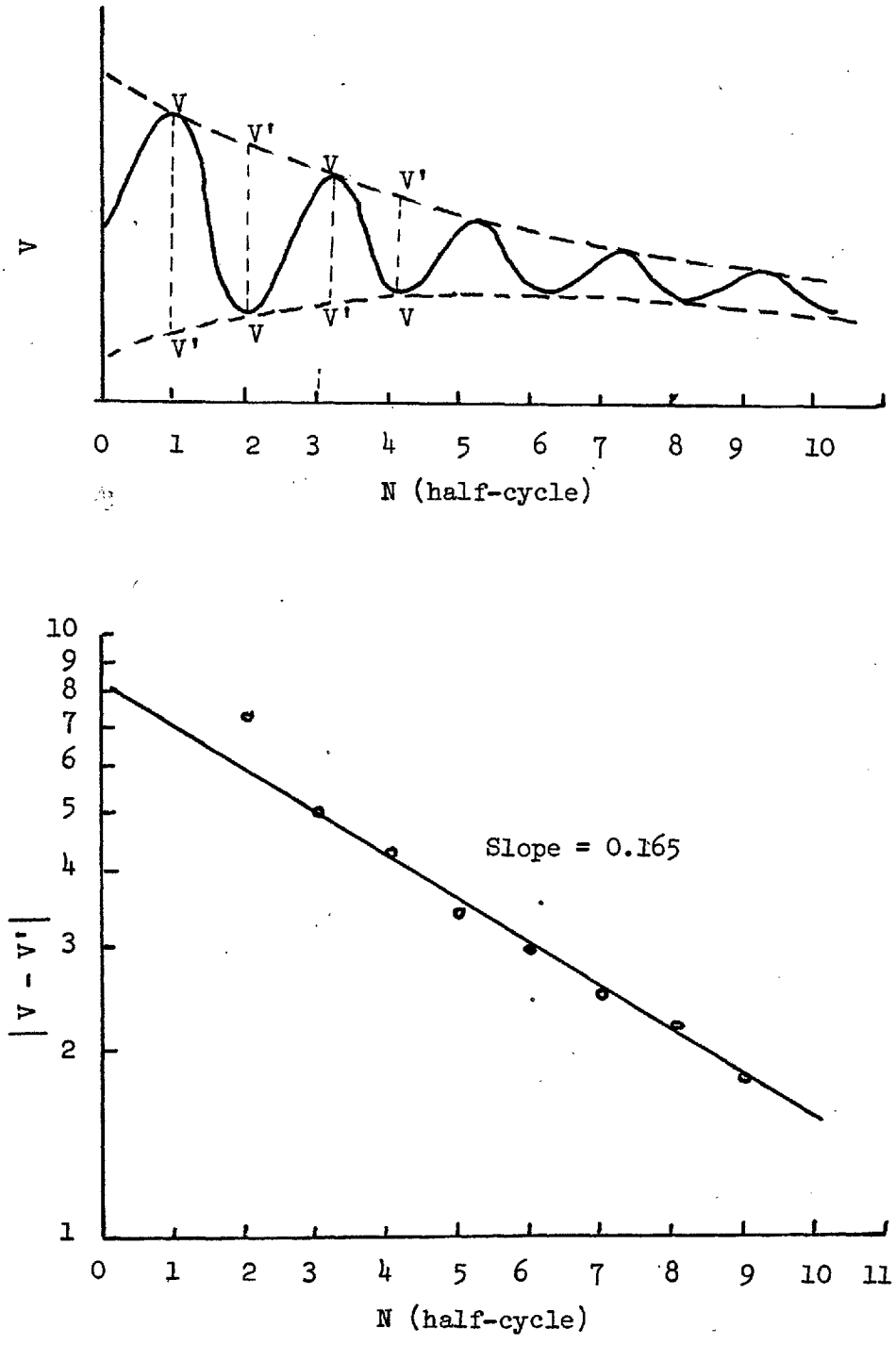

Figure 15. Plot of the differences $|V - V'|$ of the voltage extrema for analysis of the charging waveform. $|V - V'|$ is defined in the top figure and is plotted on a semi-log scale in the bottom figure.

3.5 The Diode

Initially the diode consisted of three perspex sections separated by aluminum rings as shown in Figure 16. The aluminum rings divide the perspex segments to form capacitors along the length of the diode. The capacitance per unit length is made uniform in this manner, so the voltage drop along the interface is uniform. This technique of capacitively grading the diode is commonly used to distribute the electrical stress and, thereby, to prevent flashover.

The inductance of the diode is proportional to the length of the current channel in the diode, and the rise time of the current is the L/Z_L time of the diode for a fast rising voltage pulse from the Blumlein. To reduce the rise time of the beam current, one of the three segments of the diode was removed.

The voltage for interface flashover under vacuum is given by Martin (1971) as

$$E_{flashover} = \frac{178}{t^{1/6} A^{1/10}} \quad kV/cm \qquad (3\text{-}11)$$

for a pulse of t μsec and a surface area of A cm^2 with the electric field at approximately 45° to the surface. The 45° inclination of the inside surface prevents electrons that leave the perspex from striking the surface to cause avalanching and flashover. The angle of inclination is not very critical. For the diode in the present experiment, $E_{flashover}$ = 700 KV for each section for a 100 ns pulse. Since each segment is only stressed to 300 KV, the design is conservative with a safety factor of 2.3.

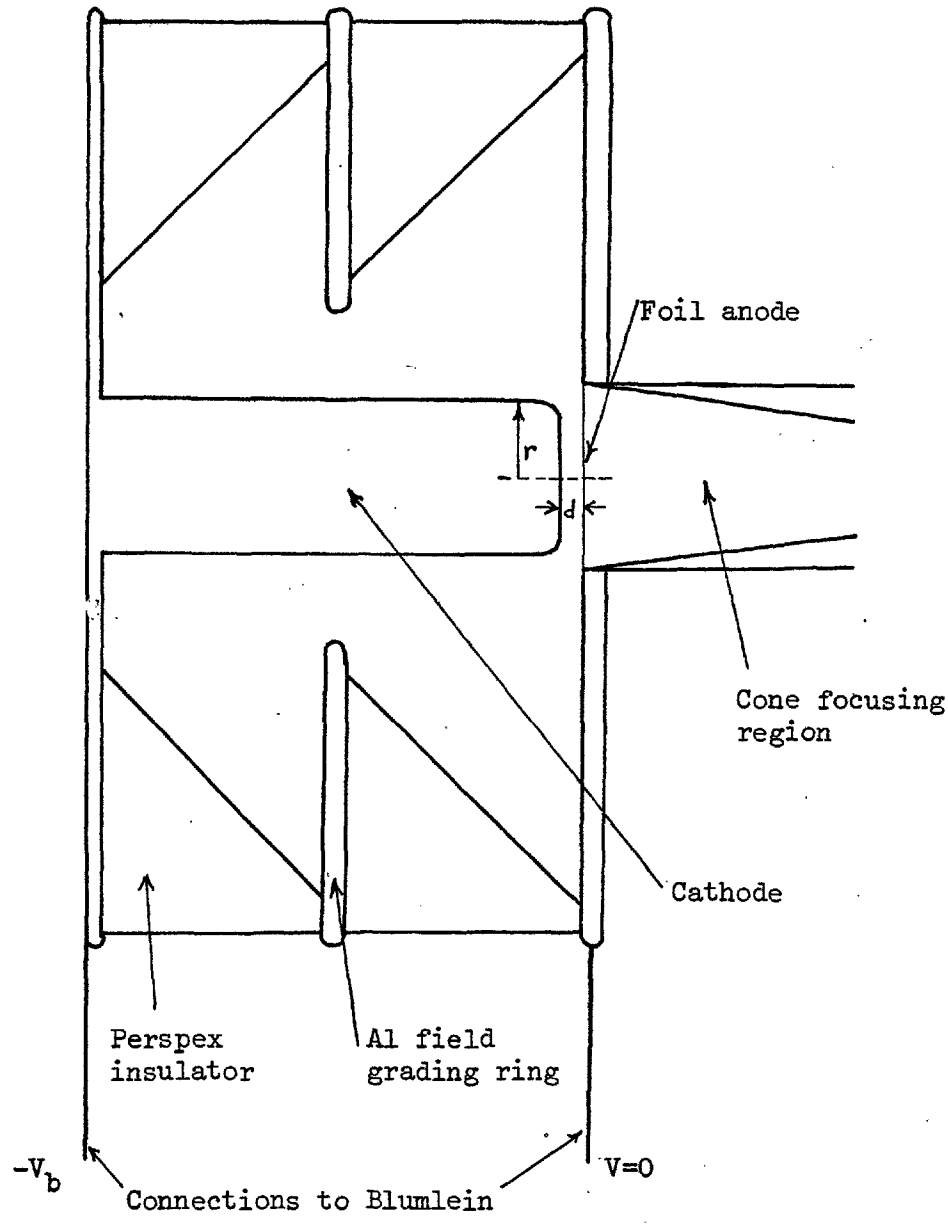

Figure 16. Schematic diagram of the diode. The diode consists of a high voltage envelope (the perspex insulators separated by the field-grading rings), the cathode, and a thin foil anode. The Blumlein produces a voltage pulse across the anode-cathode gap, and the electrons are accelerated from the cathode to the anode and through the foil into the cone focusing region.

After each shot, the surfaces were cleaned with alcohol, wiped with a clean paper, and coated with a thin layer of silicone vacuum oil, which helped prevent flashover.

Various cathodes were used. The dull side of a hacksaw blade worked but emitted very unevenly. Un-coated Gillette Techmatic razor blades gave very uniform emission but had to be replaced after each shot. Finally, a POCO Graphite cathode was adopted following successful use at NRL, Washington, D.C., and Sandia Laboratories, Albuquerque, N.M. A plasma quickly forms over the surface of the cathode and is the source of the electrons for the field-emission process. The work function of the plasma is very low and allows the necessary current to be extracted.

The anode foil is normally aluminized melanex, 0.00125 cm thick, to minimize the scattering of the electrons in their passage through the foil.

The impedance of the diode was consistent with that given by Equation 3-3 for a space charge limited current density. However, since the anode-cathode gap closed after the formation of the cathode plasma during the prepulse, the appropriate spacing was determined by trial and error. In the present experiment, an initial gap of 6 mm, a cathode radius of 3.2 cm, and an applied voltage of 350 KV produced an impedance of 6 ohms. This compares with a gap of 5.1 mm given from the Child-Langmuir law, so the gap has closed 0.9 mm during the prepulse.

3.6 Beam Diagnostics

The large stray electric and magnetic fields involved in these

experiments and the fast response times required for the diagnostics, posed considerable difficulties. The stray capacitance of the voltage monitor to its surroundings caused an erroneous output signal if the voltage distribution in the monitor differed from that in its surroundings. Consequently, every effort was made to place the voltage monitors along field lines to reduce this effect. The resistor chain was made uniform so the voltage gradient in the monitor was uniform. Initially, 2 watt carbon resistors were potted in araldite and placed across the diode as shown in Figure 17. The output was taken through the copper pipe serving as the ground conductor to the system, to an oscilloscope. These monitors worked well until they blew up. Since the breakdown voltage of solids is a function of the number of times it is stressed, the monitors eventually tracked through the araldite. An alternative monitor was made with a $CuSO_4$ resistor placed along the electric field lines, as shown in Figure 17. For a resistive load, the voltage and current waveforms matched to 10%, and the value of the voltage signal was consistent with the line voltage to $\sim 8\%$. The LdI/dt contribution to the signal was measured with a short in the diode and subtracted from the signal.

The Marx voltage monitor is shown in Figure 18 and was placed between the Marx and the water tank in a region with a nearly uniform field. It was calibrated with a 10 ampere, DC current source with both polarities, as well as a 1 μsec, 7 kV pulse. These calibrations agreed to 5%.

The current monitor was a single loop of wire with cross-sectional area approximately equal to 4 cm^2 terminated with a stainless-steel foil resistor 0.0025 cm thick, which is approxi-

Figure 17. Diode diagnostics: current and voltage monitors.

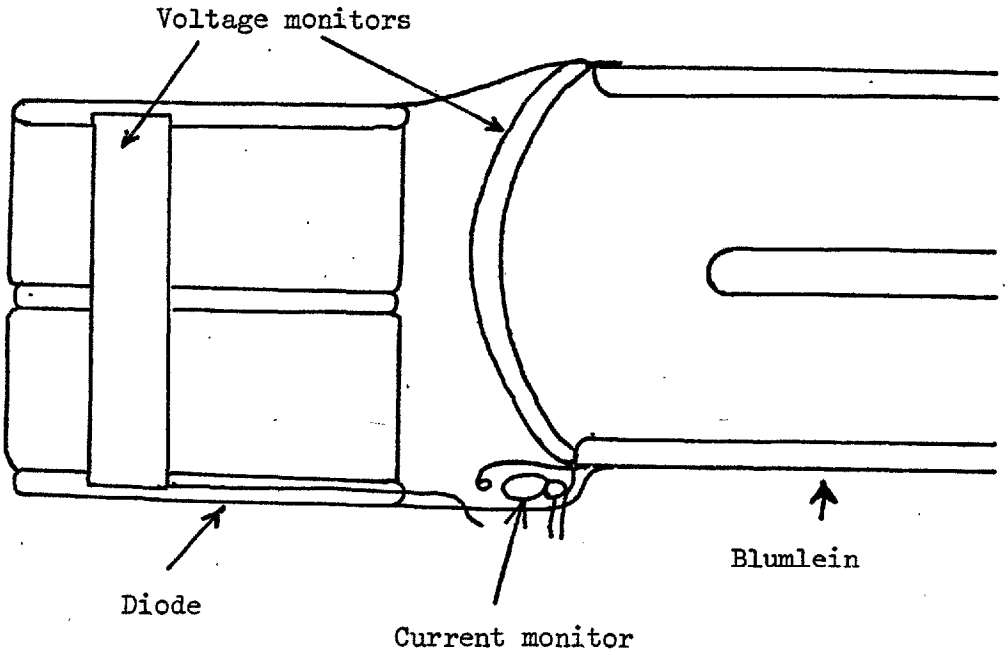

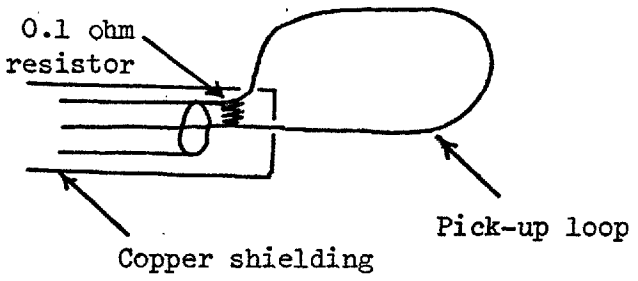

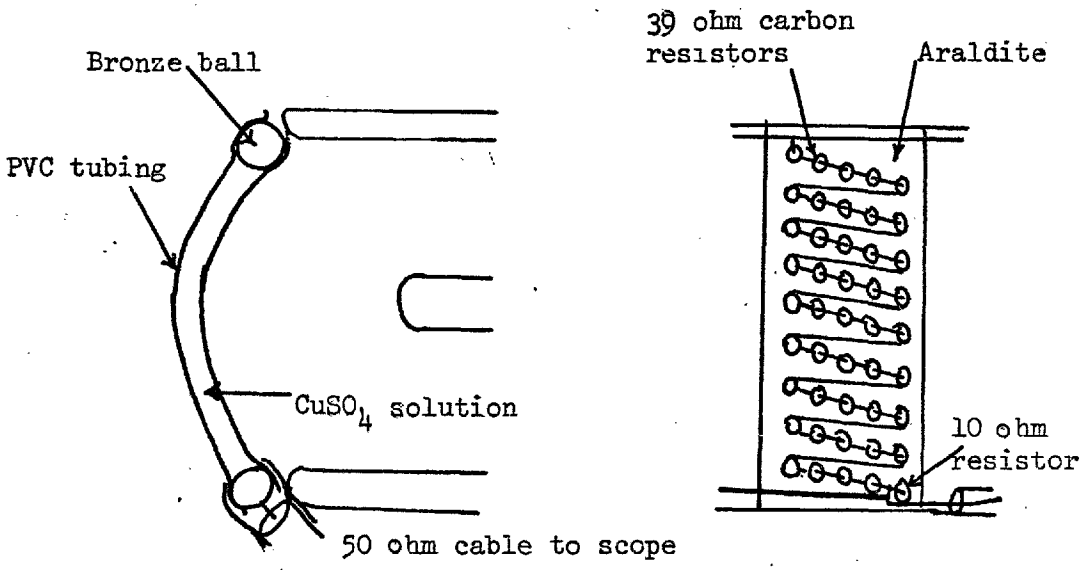

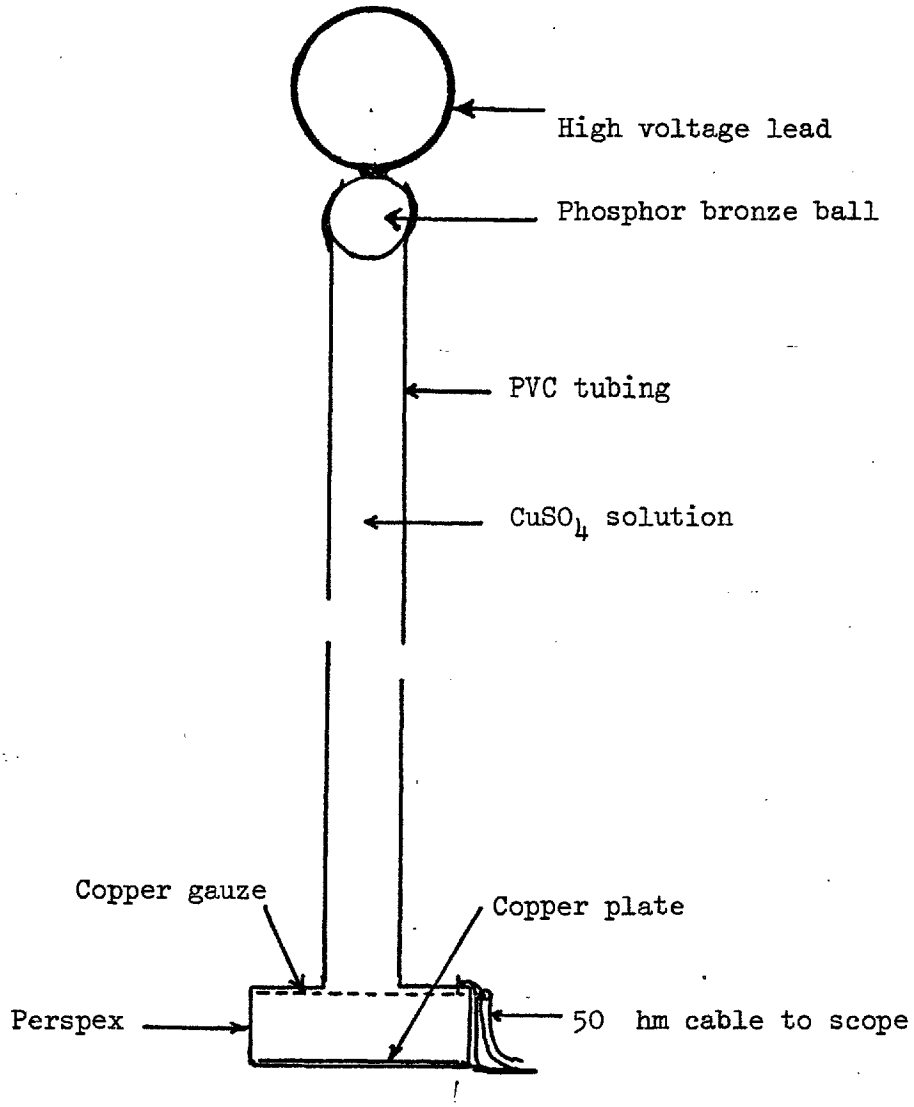

Figure 18. Voltage monitor for the Marx generator. The monitor was placed parallel to the Marx column and in an approximately uniform field to minimize the effect of stray capacitance between the resistor and its surroundings. The total resistance of these monitors was 5 to 10 kohms. Each monitor was calibrated with a sufficiently large DC current to burn away the capacittive film at the electrodes and with a 7 kV pulse.

mately the classical skin depth for the rise-time of the current signal. This gives an L/R self-integrating, pick-up coil that has been described by Pellinen and Spence (1971). The coil is shown schematically in Figure 17. The coil was calibrated in position by firing the Blumlein into a resistive load and calculating the current from the signal of the voltage monitor across the load. This procedure corrected for the unknown current distribution in the feeds from the Blumlein to the diode.

The signal with the Blumlein fired into a short circuit with a known line voltage and line impedance gave a check on the linearity of the monitor and on the effect of the stray electric fields. A plot of a typical signal vs. current calibration for both arrangements is given in Figure 19. Typical voltage and current waveforms are given in Figure 20.

These monitors measure the voltage across the diode and the current through the feeds from the Blumlein to the diode. One would like to measure the voltage across the anode-cathode gap and the current of beam electrons that enters the experimental chamber. A check on the relevance of the measured quantities to the desired quantities is provided by calorimetry and x-ray data. Total stopping calorimetry measures the integral of IVdt, and the total x-ray dose measures the integral of $IV^{2.8}dt$ as discussed by Forster, et al. (1971). An evaluation of both quantities gives an adequate check on both the current and voltage monitors. The calorimeter was built of graphite which could absorb the beam energy with a minimum of vaporization and spalling. Several have been made of the same design, which is shown in Figure 21. Five thermocouples were wired in series to give an average temperature of the calorimeter.

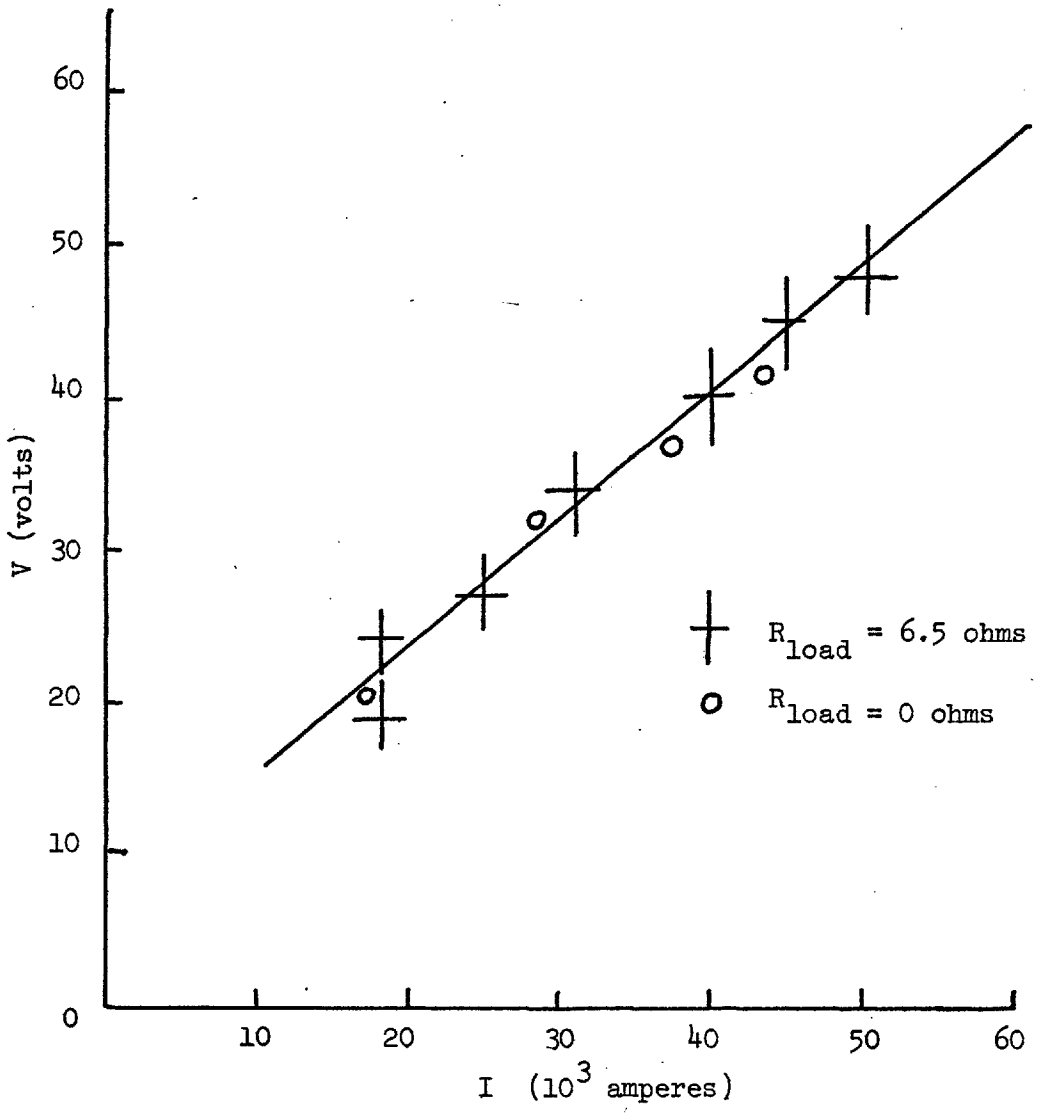

Figure 19. Calibration curve for the diode current monitor. The output V in volts into 50 ohms is plotted as a function of the diode current. Shots were taken with either a resistive load or a shunt in the diode.

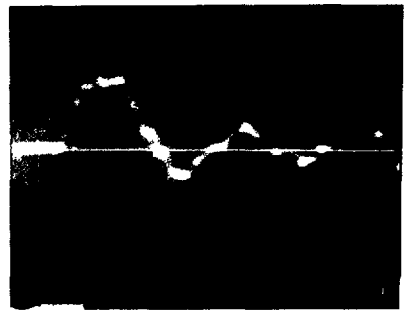

Voltage

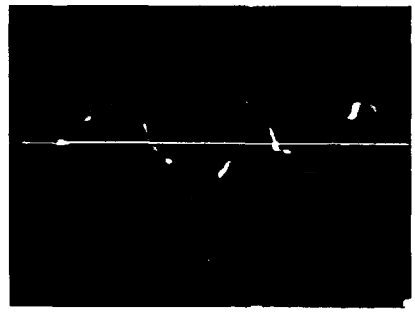

Current

100 ns

Figure 20. Voltage and current waveforms from the diode diagnostics.

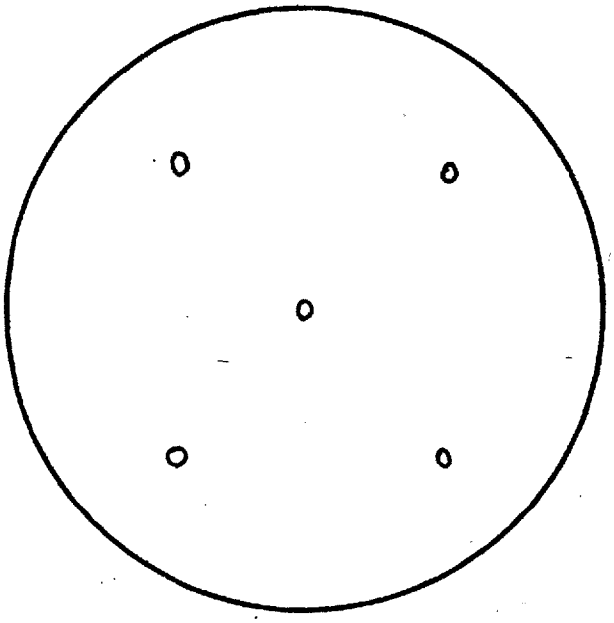

Top view showing location of thermocouples

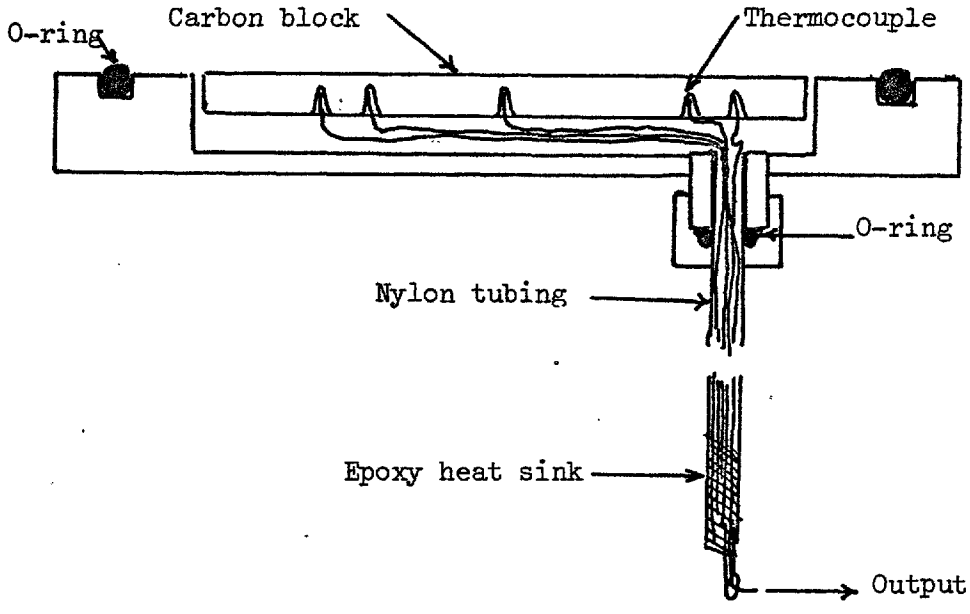

Side view showing construction

Figure 21. Construction of the carbon calorimeter used to measure the beam energy.

The thermocouples were copper-constantine and were calibrated in the usual way with a mercury thermometer in a water bath, with the output taken on a ballistic galvonometer. The calibration curve is shown in Figure 22. The heat capacity of the carbon (POCO Graphite) was measured by the temperature rise following a known energy deposition from a resistance wire (from the integral of IVdt). The calorimeter was insulated with cotton wool and the readings were taken either with the heater between two plates of carbon or with the heater between carbon and cotton wool. The measured heat capacity was 0.8 joules/g C^{o} compared with 0.71 joules/g C^{o} for pure graphite. Thus the calorimeter was absolutely calibrated. The rise time of the signal for uniform energy deposition was ~10 sec and the decay time of the signal was ~150 sec to decay by 10%. Since the measurement of the calorimeter required approximately 15 to 20 seconds after the experiment, the response time of the calorimeter gave a systematic error of ~ 10%.

The spalling of the carbon and the possibility of elastic reflection of high energy electrons from the surface (which may be as high as 10% for a 350 keV beam into a metal plate from a Monte Carlo calculation reported by Miller and Kuswa (1973)) may cause a low reading if the calorimeter is far away from the diode. If the calorimeter is very near to the anode, reflected electrons are returned to the calorimeter after passing twice more through the anode. With the calorimeter one centimeter from the anode, the reading and the integrated power agreed to within 10% under the experimental conditions. This agreement was the best check on the adequacy of the diode monitors.

The x-ray measurements were taken in the experimental arrange-

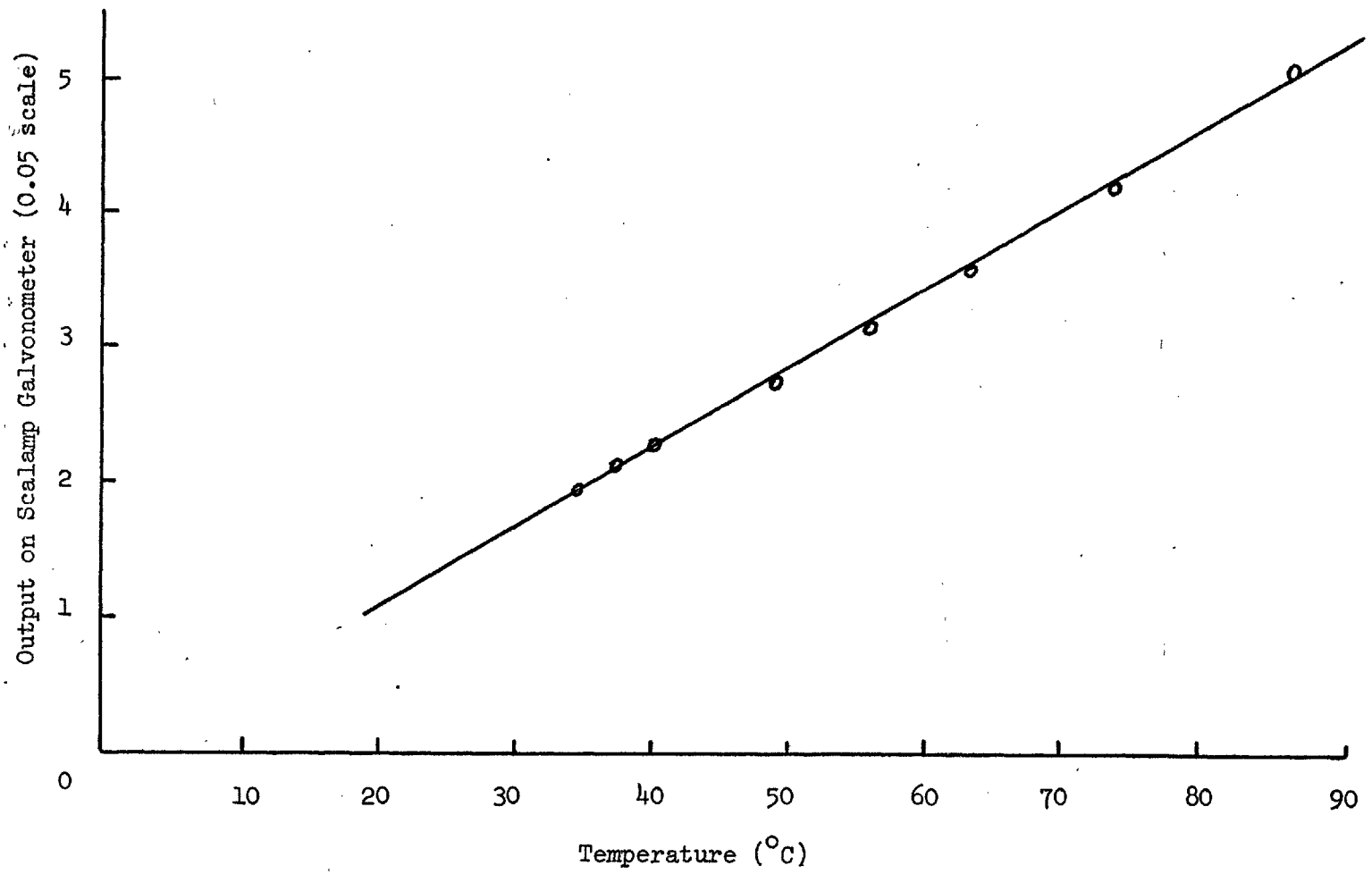

Figure 22. Calibration curve for copper-constantine thermocouples used for the calorimeter.

ment shown in Figure 23. The dose registered with quartz fibre dosimeters at the angle to the axis of the diode is given in Table 1 with the correction for self-absorption for the target and intervening material of the vacuum chamber. The primary absorption was from Compton scattering and was therefore only mass-dependent. The effective mass-absorption co-efficient for the bremsstrahlung x-ray spectrum was obtained by measuring the dose on either side of the same quantity of absorber that was present during the experiment. A filter of 0.45 g/cm^2 copper around each dosimeter absorbed x-rays below 40 keV and filtered the spectrum to reject low-energy Compton-scattered x-rays from the background. The resulting x-ray polar diagram is given in Figure 24 with the expected polar diagrams for various half-angles. The polar diagrams for a given half-angle were generated by computer code ETRAN from a distribution of electrons that uniformly fill a cone to an angle Θ_{max}. The average half-angle is $\Theta_{\frac{1}{2}} = 0.65\Theta_{max}$ as described by Forster et al. (1971). The average angle $\Theta_{\frac{1}{2}}$ is seen to have been approximately zero degrees.

The dose on axis at one meter was 143 mr. The expected dose on axis for the carbon target is given by Forster, et al. (1971) as

$$D = 3.7 \times 10^2 V^{2.8} Q \text{ rads} \qquad (3\text{-}12)$$

for V in megavolts and Q in coulombs. The calculated dose for the 60 kA current and 400 kV voltage for 85 ns agrees with the measured value of 143 mr. The agreement is fortuitiously good for the data is only $\pm$ 10%.

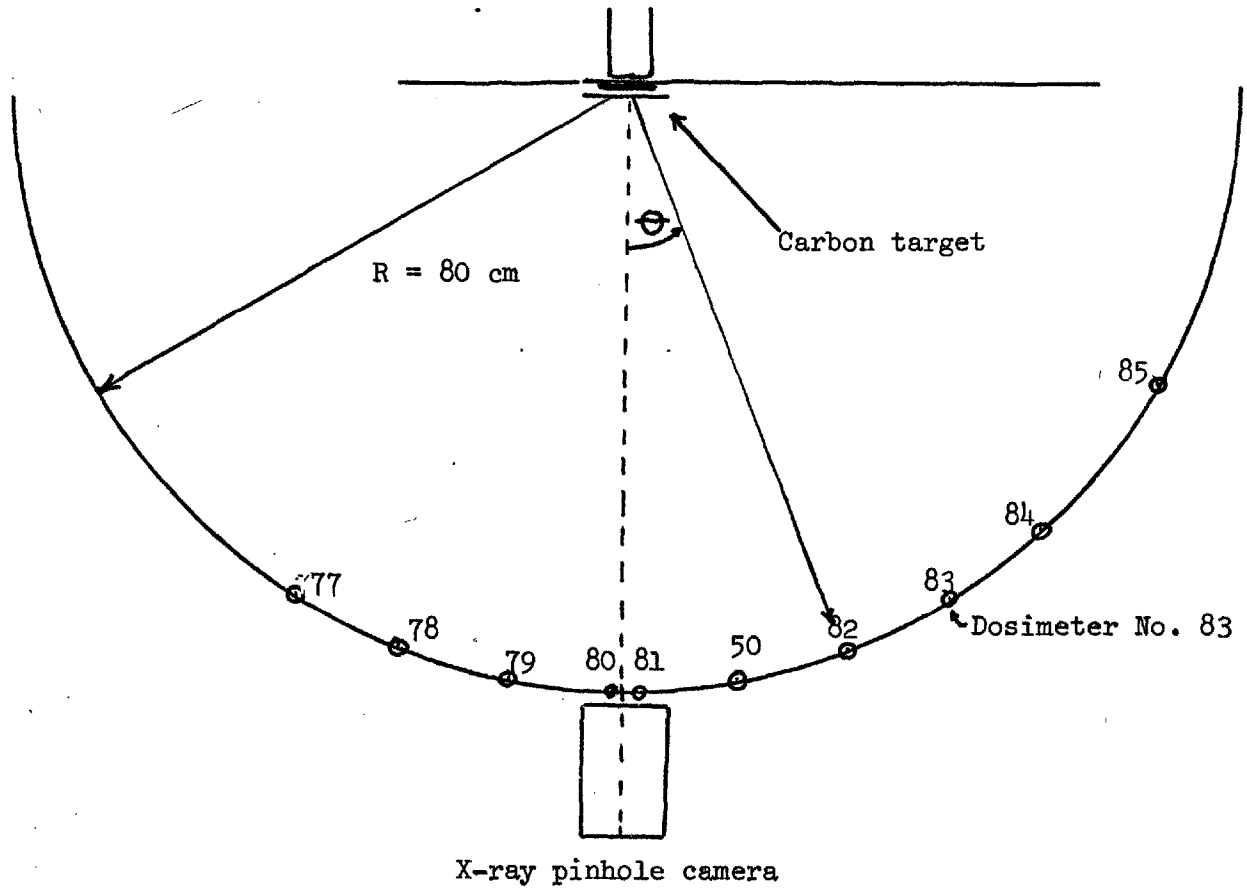

Figure 23. Arrangement for x-ray dosimetry of the electron beam at the anode. The polar diagram of the bremsstrahlung was measured from the x-ray dose as a function of the angle θ from the axis of the beam. The four aperture camera gave an indication of the uniformity of the beam.

Table 1. Data from the x-ray polar diagram measurement. The radiation dose at one meter is given by

$$R = X \cdot \exp(\mu_c l_c/\cos\theta) \cdot \exp(\mu_b l_b/\cos\theta) \cdot r^2$$

where

μ_c = absorption co-efficient for carbon = 0.24/cm

μ_b = absorption co-efficient for brass = 2.54/cm

X = the dosimeter reading at position (r, θ)

l_c = thickness of carbon in target = 0.30 cm

l_b = thickness of brass in target = 0.32 cm

r = the distance from the target to the dosimeter in meters

θ = the angle between the dosimeter and the beam axis

θ (degrees)	X (mr)	R (mr)	R/R_{max}
-31.5	58	96	0.67
-21.	95	143	1.
-10.	102	142	1.
0.	98	137	0.95
0.	99	139	0.99
10.	87	122	0.90
21.	69	104	0.73
31.5	55	91	0.64
42.	52	96	0.67
52.5	34	71	0.50

The x-ray data is plotted in Figure 24 and is compared with the theory to find the beam's half-angle.

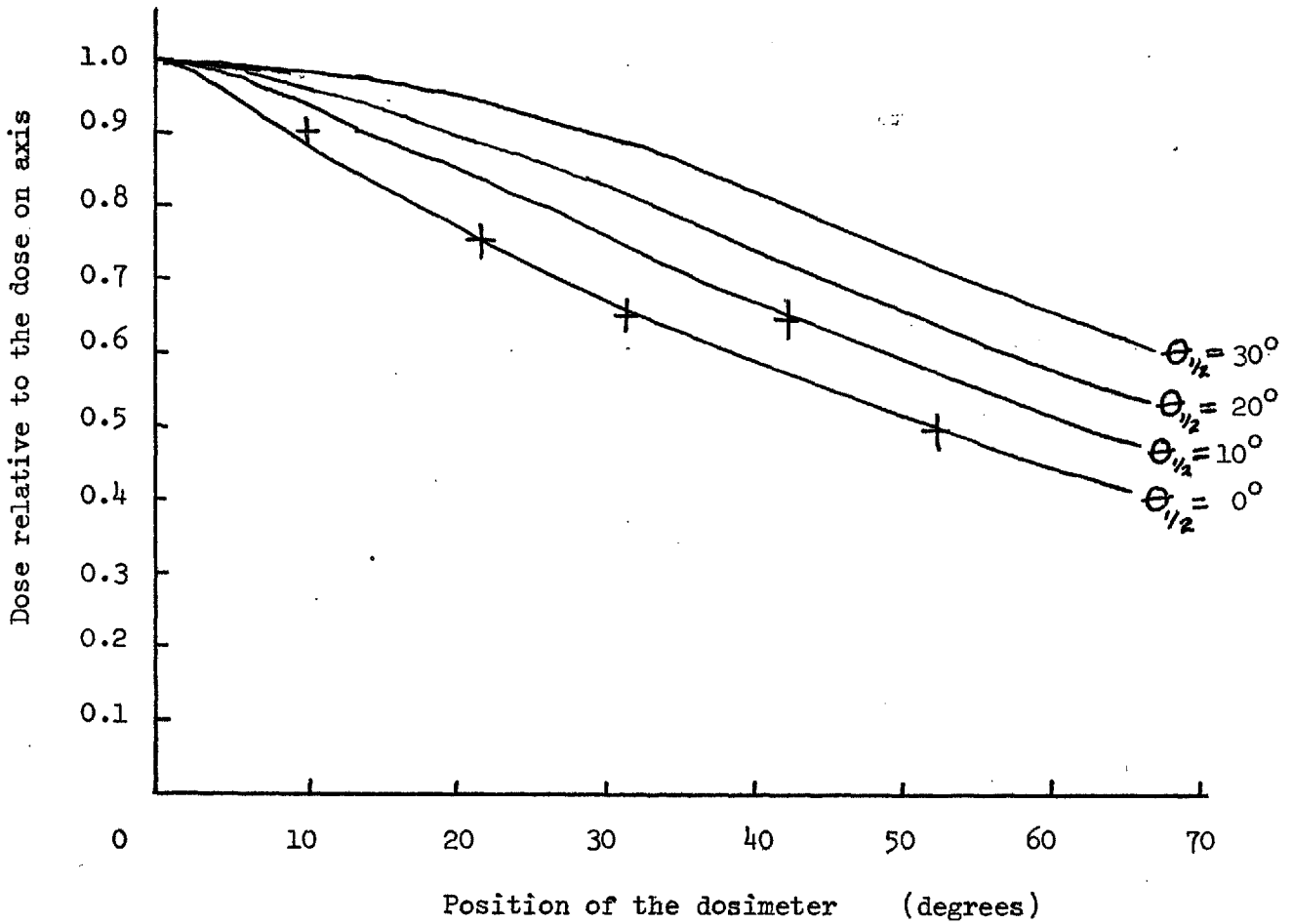

Figure 24. X-ray polar diagram of the bremsstrahlung from the carbon target at the anode. The calculated polar diagrams for various beam-electron half-angles are shown for comparison. The beam electron energy was 350 keV. The measured half-angle was less than 10°.

The uniformity of the beam was measured through x-ray pinhole photography. Two lead pinhole cameras were constructed as described in Figure 25. The four-aperture camera showed that the beam was approximately uniform as shown in Figure 26, although the linearity of the Kodak RP-Royal and Blue Brand x-ray film with image intensifier plates was not ideal. Nevertheless, the beam was not grossly one-sided and the cathode was emitting nearly uniformly. The exposure with the second largest pinhole in Figure 26 shows a more intense spot on the axis, although the photographic reproduction of the original x-ray film enhances the appearance of the central spot. This spot is consistent with a pinch in the diode at late times or on a second, lower energy pulse after the main pulse. The x-ray polar diagram shows that the perpendicular energy of the beam electrons was small, which would not be the case if a large fraction of the beam were pinched in the diode. Consequently, the beam emission was uniform during the main beam pulse.

The usual method for checking for uniformity on lower current machines is to use radiation-sensitive blue cellophane that bleaches under beta radiation. Beams with the present integrated energy density vaporize the material, thus making that technique impractical as a direct measure of uniformity.

From the measurement of the beam's cross section in Figure 26, the beam current density was calculated as 1.9 kA/cm^2. Thus the beam density was 5×10^{11} cm^{-3}. This gives a ratio of n_b to n_p less than 0.005, which was too small for the experiment. Since I was really interested in heating a volume with 1 cm^2 cross section, allowing the e-beam to have a 30 cm^2 cross section was a waste of most of the beam energy. In principle, by reducing the cathode diameter but keeping the same aspect ratio (cathode radius to gap

Figure 25. Construction of the x-ray pinhole cameras. The cameras used RP-Royal or Blue Brand film by Kodak with regular Kodak x-ray intensifier screens.

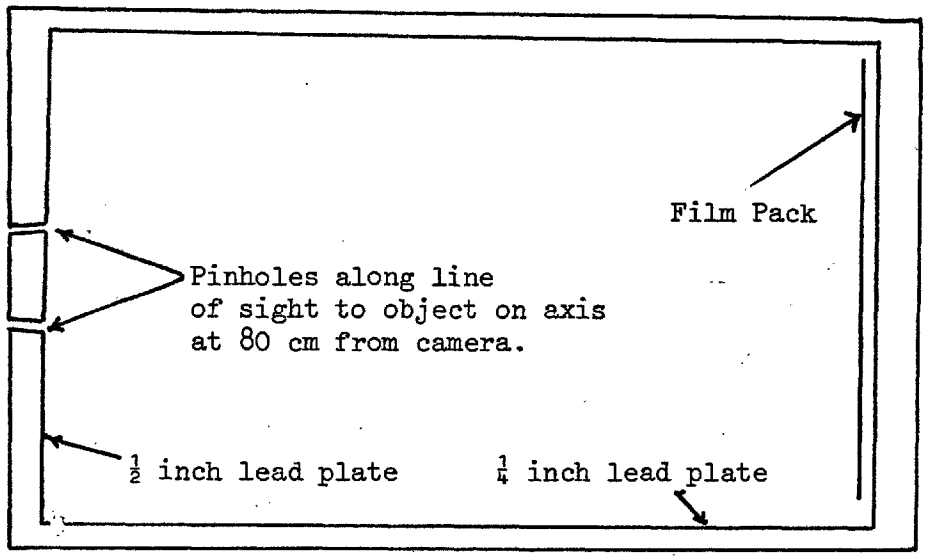

Four Aperture Camera

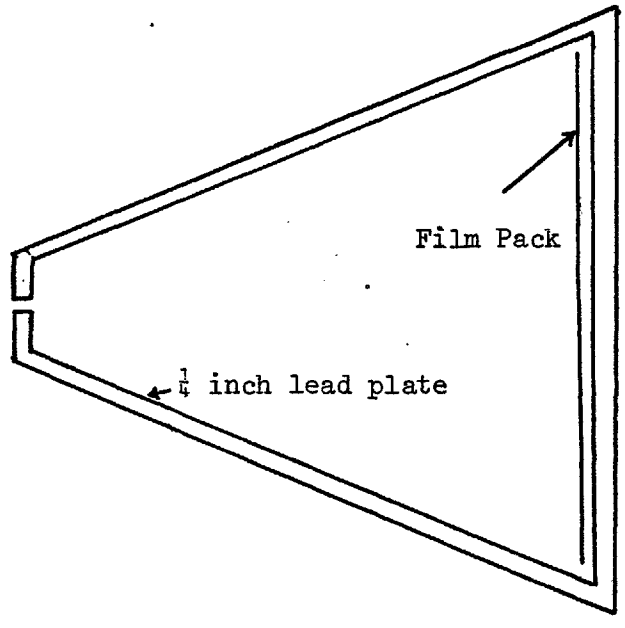

Single Aperture Camera

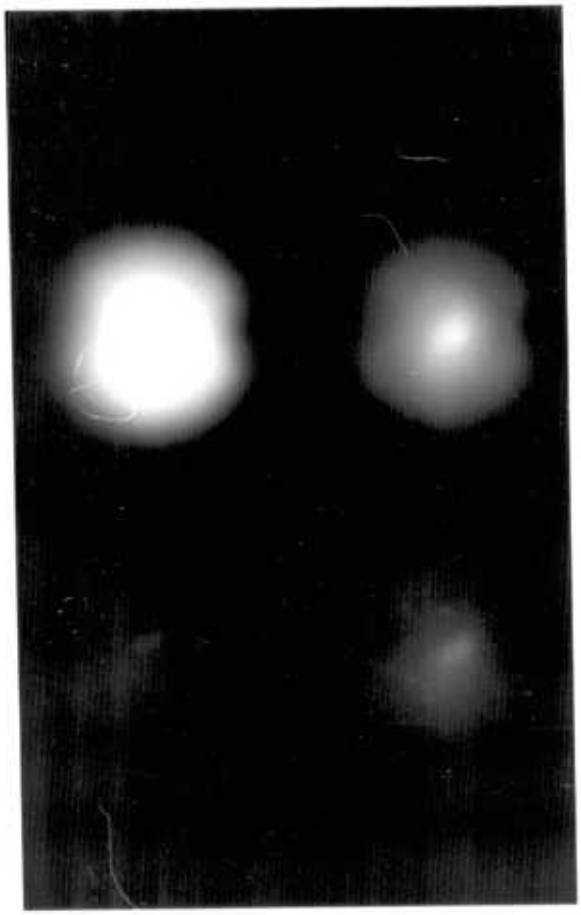

Figure 26. X-ray pinhole photograph showing the beam distribution on a carbon target at the anode. The magnification is 0.38. The four images are from the four pinholes, each of which has a different aperature.

separation), one could obtain a higher beam density and keep the same diode impedance. However, this procedure caused the diode gap to close faster, and the impedance changed significantly during the pulse. To go to a smaller area with the same gap separation led to beam-pinching in the diode under the beam's self-magnetic field, which produced a hot beam (one with a large value of $\Theta_{\frac{1}{2}}$). Such hot beams were found to head to the nearest wall when they were propagated.

3.7 Cone Focusing

The beam was focused by firing it into a 10% half-angle copper cone as shown in Figure 27. The rationale was to use the currents induced in the wall of the cone to reflect the electrons, towards the center of the cone. The focusing worked, but possibly for the wrong reasons. Olson (1973) has subsequently published a theory on cone focusing that argues that the focusing is caused by non-uniformity in the breakdown process in the cone (See Section 3.1). The net current then increased with axial distance from the anode to self-focus the beam. Experiments by Davitian (1971) revealed that if the beam did not pinch in the diode, Olson's mechanism explained his data for cone focusing. If the beam pinched in the diode from the beam's self-magnetic field, the pinched beam propagated without additional focusing to the cone exit.

My observations were that the beam was not pinched at the anode; the evidence came from the x-ray photographs and from the damage pattern (or lack of it) on the carbon calorimeter 1 cm from the anode foil, and from the diode impedance (calculated from the voltage and

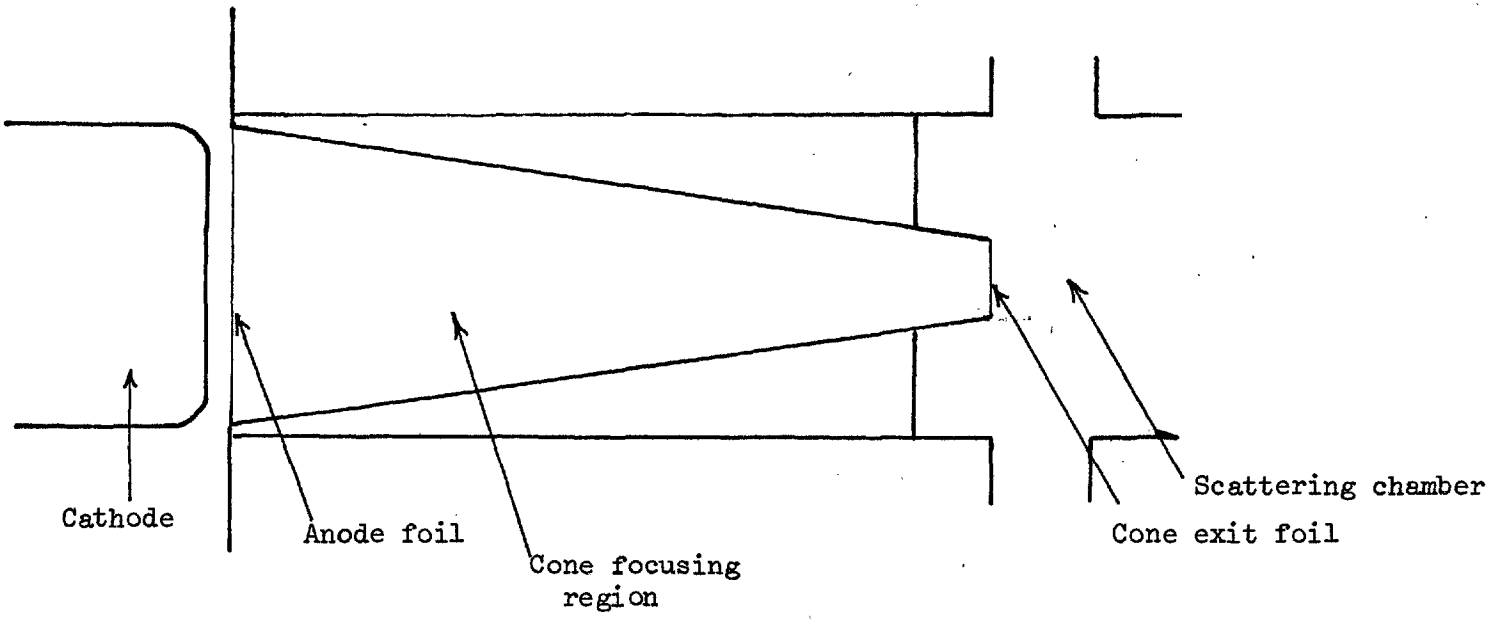

Figure 27. Schematic diagram of the cone-focusing system. The electron beam is injected through the anode foil and into the copper cone. The cross section of the cone at an axial position z determines the net current in the axial direction. The axial net current and the associated azimuthal magnetic field increase with increasing z. The beam electrons are focused by the azimuthal magnetic field as they travel down the cone.

current traces). However, more than 60% of the energy reached the cone exit, and the beam's cross-sectional area at the exit was less than that of the cone's aperture. The beam distribution at the cone exit was not uniform, and the center of the beam was shifted away from the Blumlein, as measured from the damage pattern on the calorimeter at the cone exit.

X-ray photography was not very useful for measuring the angular distribution of the beam electrons at the exit since the x-rays from the cone walls were found to contribute significantly to the x-ray flux. (Approximately 50% of the total dose could be attributed to electrons hitting the walls.) Consequently, the beam diameter was measured in three ways: (1) the damage pattern on the carbon calorimeter, (2) the Al-foil/blue-cellophane dosimeter package, and (3) the diameter of the luminosity of the plasma channel taken with an image-converter streak camera. These measurements gave an effective beam diameter of 1.5 cm and a current density of 20 kA/cm^2. Examples of each type of measurement are shown in Figure 28. The length of the streak camera photograph corresponds to the full 100 ns (with 20 ns resolution and a 30 ns beam rise time), so the energy and current must be lost throughout the pulse as opposed to only at the beginning or end of the beam pulse. Since the heating is a function of the plasma current squared, knowledge of the beam's current distribution is very important.

The transmission of the cone did not appear to be critically dependent on the pressure, in contrast to lower current measurements taken by the author on other machines in the past. The energy transmitted remained 60 ± 6 percent as the pressure in the cone was varied from 300 mTorr to 1.4 Torr of air. There was usually damage

(a)

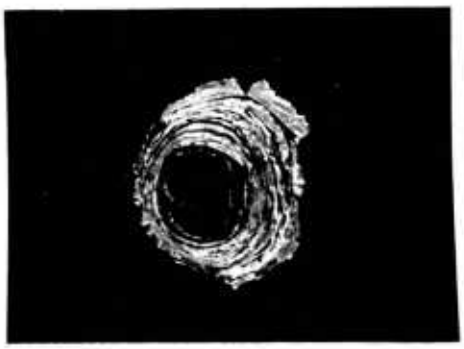

(b)

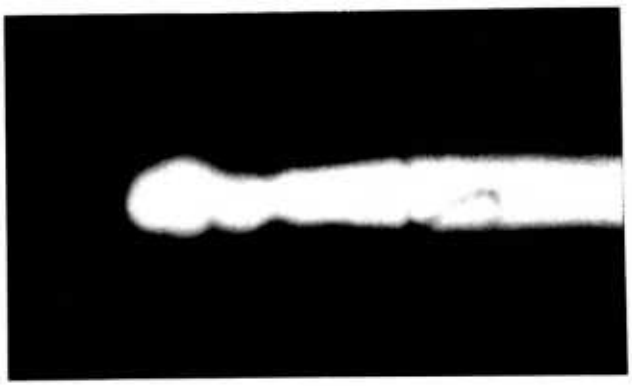

(c)

Time sweep is 100 ns/cm. Radial magnification is .5.

Figure 28. Measurements of the beam diameter at the exit from the focusing cone. The diameter of the beam was measured by a) the damage pattern on the carbon calorimeter placed at the cone exit, b) the damage pattern on the Al-foil/blue-cellophane dosimeter packet at the cone exit, and c) the luminosity of the plasma channel observed with a streak camera.

to the side of the cone about 15 cm from the anode at a cross section of 9.6 cm^2, which was fairly reproducible. The mechanism that leads to this damage and the associated energy loss is not understood.

Attempts were made to measure the half-angle of the beam electrons which was expected to have increased as the beam was focused. However, the x-ray technique failed because of the x-rays from the copper walls of the cone. However, the x-ray pattern on the walls of the experimental chamber during injection into plasma with rapid charge and current neutralization was a measure of the beam's half-angle, as discussed in Section 4.2. The energy collected on the calorimeter at 20 cm was also a measure of the half-angle, assuming the beam filled a cone to the angle θ_{max}, as discussed in Section 4.5. These two measurements gave the angle θ_{max} as 30°, so $\theta_{\frac{1}{2}} = 0.65 \times \theta_{max} = 20^\circ$. Consequently, the transverse velocity of the beam electrons apparently increased during the focusing process.

3.8 Summary of the Beam Parameters

The electron beam has been diagnosed as having the following characteristics as it left the cone:

Electron energy eV_b: 375 ± 40 keV

Total current I_b: 36 ± 6 kA

Effective cross-sectional area: 1.8 cm^2

Average current density j_b: 20 kA/cm^2

Average beam density n_b: 5×10^{12} cm^{-3}

Average electron half-angle $\theta_{\frac{1}{2}}$: 20°

$\beta = 0.8$

$\gamma = 1.7$

$\frac{\nu}{\gamma} = \frac{I}{I_A} = 1.6$

3.9 Experimental Chamber

In the experimental chamber, the beam interacted with the plasma. A laser beam was admitted, and the scattered light was observed through suitable ports.

During the course of the experiment, the experimental chamber and plasma source evolved through several stages. Originally, a z-pinch was constructed from a perspex cylinder (15 cm diameter and 2 meters long) with the anode foil of the diode as one electrode and an aluminum plate the other end electrode. A hydrogen plasma which formed on axis was observed spectroscopically, and no impurities were observed. However, the electron beam did not reach more than 30 cm from the anode (as determined with the calorimeter), and the laser scattering ports were at 40 cm. Examination of the damage to the perspex walls indicated the beam was defocusing and hitting the walls.

Consequently, the tube was shortened and the laser scattering region was placed at 20 cm from the anode. At filling pressures sufficiently low to get a reasonable fraction of ionization and a sufficiently large ratio of n_b/n_p, the complicated joints in the scattering ports tracked under the voltage applied with the z-discharge (before the gas was ionized) and the voltages associated with the dI_{net}/dt of the beam. These discharges repeatedly destroyed the drift tube.

Then a glass scattering chamber of length 40 cm and inside diameter of 7.5 cm was built with the scattering region 15 cm from the anode. Several of these chambers were destroyed by the high voltages in the experiment and the occasional pinched-beam hitting the wall near the end of the tube.

Consequently, a brass scattering-section was constructed with a replaceable z-discharge section attached to the end, as shown in Figure 29. The scattering region was now only 4 cm from the entrance foil and the construction of the water tank blocked the optical path from the laser to the scattering volume. To make the scattering volume accessible to the line of sight for the laser, a drift section was installed to drift the beam 20 cm from the anode foil, through a second foil and into the experimental chamber. The drift efficiency was found to be nearly 90%, and the beam was uniformly distributed across the 7.5 cm diameter, as observed by the x-ray photographs and calorimetry. The use of the drift region also ensured that the anode-cathode gap was independent of the pressure in the experimental chamber since the drift section was held at the constant pressure of 500 mTorr air, while the pressure in the experimental chamber was altered for various initial conditions. Experiments with this arrangement indicated very little additional plasma heating or ionization, because the beam number-density was too low.

The cone focusing technique described in Section 3.7 was introduced to increase the beam density and also to bring the scattering region to within 8 mm of the entrance foil. This version of the experimental chamber was used in the final experiments, and is shown in Figure 30.

Before each shot, the diode was cleaned, the cathode was

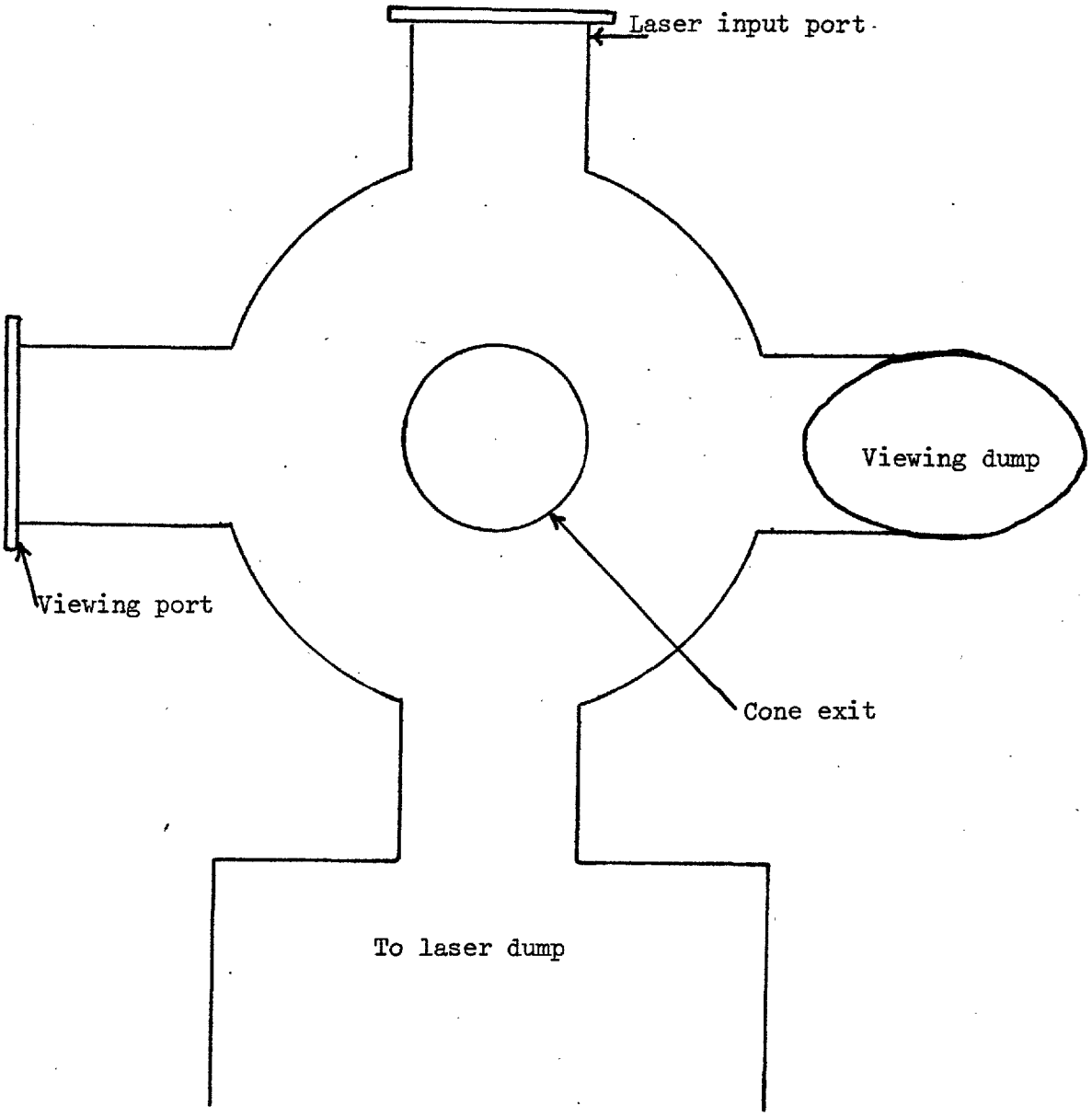

Figure 29. Construction of the brass experimental chamber for the laser scattering experiments. The light dumps were OB-10 glass mounted at the Brewster angle for the laser light.

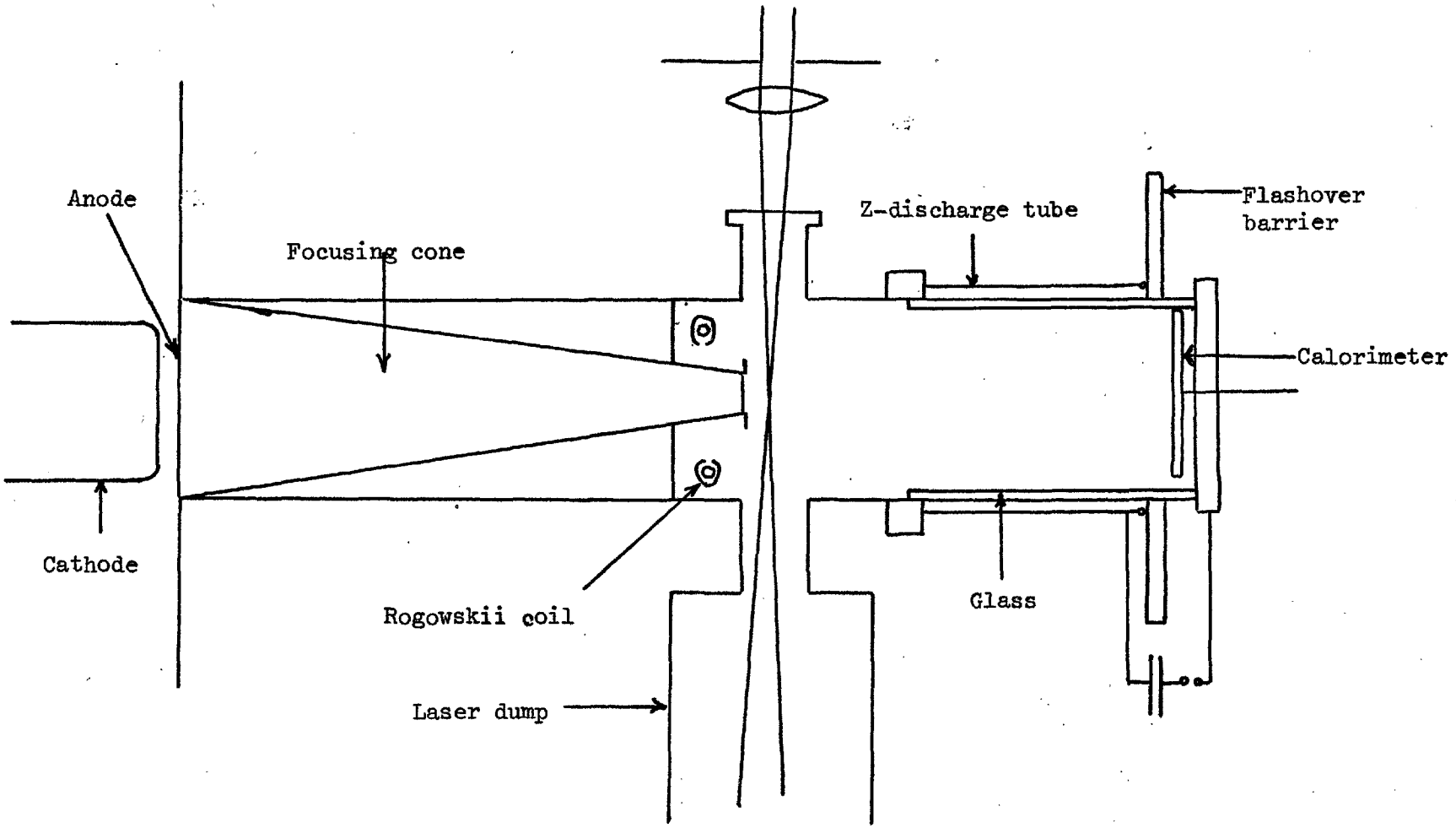

Figure 30. Diagram of the experimental arrangement for the experiments with the focused beam.

resurfaced, the anode and cone-exit foils were replaced (they were completely vaporized during the experiment), the windows and light dumps were cleaned, the scattering system was re-aligned and re-calibrated, and everything was pumped down.

In the new arrangement, the breakdown of the gas in the z-discharge was not as satisfactory as it was in the perspex tube. Although the breakdown was assisted by a spark discharge in the chamber, at low pressures (less than 10 mTorr H_2) the breakdown was through an arc along the wall. Nevertheless, Rogowskii coil measurements of the current flowing through the cone exit (and away from the walls of the pinch) indicated a plasma current flowed through the experimental volume. The time integrated spectrum of the plasma light taken through the laser-input window showed many impurity lines as well as the hydrogen lines. It was found that the wall material arrived in the scattering region approximately 30 μsec after the z-discharge. The arrival of wall material was measured by the increase in the Rayleigh scattered light at 6943 A^{o} after 30 μsec as shown in Figure 31. Thus the technique of varying the initial plasma conditions by simply waiting for the plasma to recombine and cool could not be used.

The proximity of the entrance foil to the scattering region intially caused concern because the closure velocity of the anode-cathode gap was typically 1 to 3 cm/ μsec. If the gap closure were caused by the foil velocity and if that same velocity were applicable to this foil, the material would arrive in the scattering region in 0.3 to 1.0 μsec. The gap closure in the diode was expected to be primarily from the expansion of the exploded whiskers on the cathode. The anode velocity was expected to be much slower. However, a

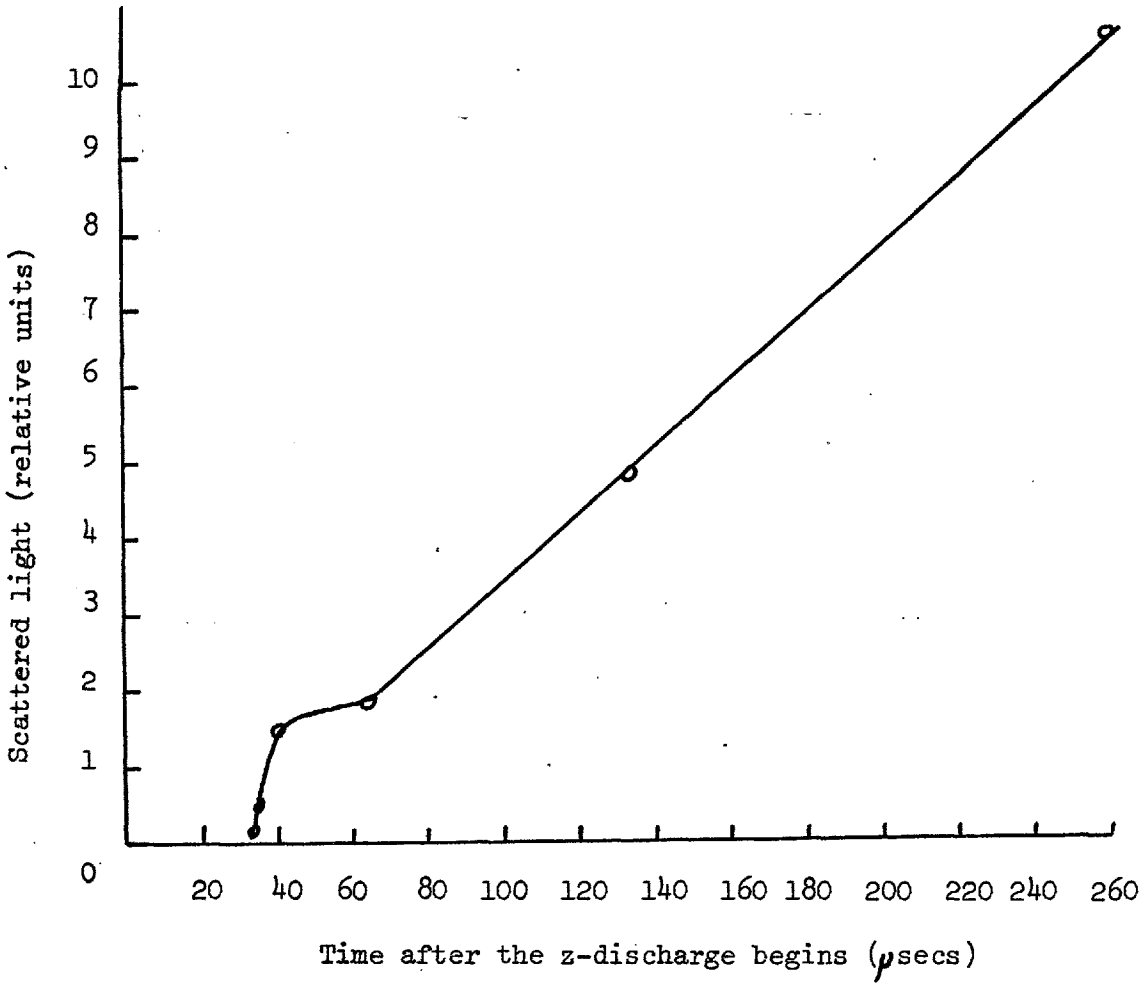

Figure 31. Contamination of the plasma by wall material. The arrival of the wall material in the scattering region was observed from the increase in the Rayleigh scattered light at 6943 A° as a function of time after the beginning of the z-discharge. The contamination limited the useful lifetime of the decaying afterglow for the experiment.

check was made for contamination by the foil material by measuring the Rayleigh scattered laser light after the beam. There was no indication of the arrival of foil material 2 μsec after the beam.

This result is understandable from the energy deposition of the electron beam in the foil. From the data by Berger and Seltzer (1964), the energy deposition for 350 keV electrons is

$$\frac{dE}{dx} = 2.21 \text{ MeV per g/cm}^2 \text{ of foil material.}$$

For a foil of $\rho \approx 1 g/cm^3$, and dx = .00125 cm,

$$\Delta E \approx 2.21\ (.00125)\ (1) = 3 \times 10^{-3} \text{ MeV}$$

$$\approx 3 \text{ keV}.$$

The beam contained $\sim 2.2 \times 10^{16}$ electrons, so the total energy deposited was $\sim 7 \times 10^{19}$ eV ≈ 10 joules. For a mass of 2.5×10^{-3} grams, $V \approx 3 \times 10^5$ cm/sec, which is approximately the expansion velocity of the foil since the thermal equilibration time at solid densities is so small. The foil should have arrived in the scattering region at t = 4 μsec. It was observed to be 3.5 μsec for the increase in luminosity for injection into 1.6 mTorr neutral gas, in reasonable agreement with this calculation. Consequently, the foil material did not contaminate the plasma during the experiment.

CHAPTER 4

EXPERIMENTAL RESULTS

4.1 Introduction

The understanding of high-current, relativistic electron beam-plasma interaction is still in its infancy as evidenced by the fact that the present experiment was the first to measure the number density and temperature of the plasma during and shortly after the beam pulse. Very few assumptions could safely be made about the beam-plasma system. Consequently, a wide range of diagnostics were employed to determine the parameters needed to compare the theory with the experiment. To interpret the plasma-heating experiment, one must know the number density, temperature, and current density distribution of the plasma and the current distribution of the beam electrons. Since the energy transfer via the ion-acoustic instability depends on the ion temperature, one must also estimate or measure T_i.

The accepted model for the beam plasma system presented in Section 2.2 has several features relevant to the interpretation of this experiment: (1) the predicted charge neutralization time for injection into a low pressure gas exceeds the beam duration in the present experiment, (2) the beam and plasma current channels are coincident, and (3) the ion motion (radial expansion or contraction) can be neglected. These three points must be investigated experimentally.

The diagnostics employed and the type of information obtained

are summarized in Table 2.

The experiments fall into two categories: either the beam was injected into a preformed plasma or into a neutral gas. Table 3 contains a summary of the experimental conditions. Cases I through IV are the experiments with a preformed plasma and cases V through VIII are those with a neutral gas, as shown in Table 3.

The experimental limitations on the range of systems studied were defined by the following experimental difficulties:

(1) For injection into neutral hydrogen below 60 mTorr filling pressure, no scattered light was observed.

(2) For injection into neutral hydrogen above 10 Torr filling pressure, the background plasma light was too large to allow data to be taken.

(3) For sufficiently short delay between the beginning of the z-pinch and the beginning of the beam pulse to have a high initial plasma temperature ($T_e \geq 2$ eV), the plasma was not very reproducible, and the z-discharge current was still flowing significantly.

(4) The excessive plasma light and the relatively low plasma number density during the beam made observation of laser scattered light impossible during the beam pulse, except in a few cases.

Each diagnostic will be discussed and its results given. The information will then be interpreted in Chapters 8 and 9.

Since the measurement of the gross plasma position and beam position set the stage, so to speak, for the more detailed measurements, they will be described first.

Table 2. Summary of the diagnostics employed in the present experiment.

Diagnostic	Description	Type of information acquired
Laser scattering	Analysis of the spectral distribution and absolute intensity of ruby laser light scattered by the plasma electrons	Plasma electron number density and velocity distribution
Net current	The waveform of the beam current minus the plasma current at the exit from the focusing cone	Self-magnetic field, mass motion of the plasma channel, breakdown time of the gas for injection into neutral hydrogen at low pressure
X-ray pinhole photography	X-ray photography of the x-ray pattern produced by the beam electrons as they strike the walls of the chamber	Gross beam behavior, half-angle of the beam electrons
Calorimetry	Total stopping calorimetry of the beam energy transmitted to the calorimeter at the end of the experimental chamber	Beam energy transmitted through the focusing cone, half-angle of the beam electrons, force neutralization time t_f of the beam electrons
Streak camera photography	Image-converter streak photography of the radial extension of the plasma light emission versus time	Radius of the plasma channel versus time, duration of the beam pulse, diameter of the beam, charge neutralization time of the beam at low filling pressures
Plasma light	The waveform of the background emission in a band about 6943 A°. Data was taken with the laser scattering collection system.	Data on reproducibility of the plasma, time scale for expulsion of plasma from the scattering region, energy loss through vibrational excitation of H_2
Witness plate	Target composed of layers of Al foil and radiation sensitive blue cellophane was placed in front of the beam and the damage was recorded	Time integrated spatial distribution of the beam's energy density
Electrostatic energy analyzer	Waveform of charge collected on a plate behind biased grids to exclude slow electrons	Charge neutralization time for injection of the beam into low pressure hydrogen

Table 3. Summary of the initial experimental conditions.

Case No.	Filling Pressure (Torr)	Electron Number Density (cm^{-3})	Electron Temperature (eV)
I	0.01	$3 \times 10^{13} \pm 40\%$	<1
II	0.003	$7 \times 10^{14} \pm 50\%$	$1.5 \pm 30\%$
III	0.2	$2 \times 10^{15} \pm 50\%$	$0.6 \pm 20\%$
IV	0.1	$5 \times 10^{13} \pm 40\%$	$2.5 \pm 20\%$
V	0.06	--	--
VI	0.1	--	--
VII	1.0	--	--
VIII	10.0	--	--

4.2 X-Ray Pinhole Camera Measurements

The construction of the cameras and the film package have already been described in Figure 25. The basic information obtained from this diagnostic was the co-ordinates (r, z) at which the beam electrons struck the walls. The plasma case and the neutral gas case gave two distinctly different types of x-ray patterns on pinhole photographs. X-ray photographs for these two types of experiments are shown in Figure 32, with the features of the experimental chamber overlaid. All photographs of the plasma case gave similar photographs to Figure 32a, and all of the neutral gas shots produced photographs similar to 32b. The loss of electrons in the cone exit, the x-ray flux from the exit foil, the main wall radiation within the solid angle subtended by the dotted lines, and the spot at the calorimeter can be seen in the photographs. Clearly the beam defocused in the plasma and had an apparent half-angle θ_{max} of 30°, and therefore $\theta_{\frac{1}{2}} = .65\ \theta_{max} = 20^{\circ}$. This is understandable from the nearly complete magnetic neutralization $I_{plasma}/I_b \approx 0.95$ for injection into the plasma. Consequently, the force on a beam electron was very small, and its Larmor radius r_L was larger than the chamber radius; for example, $r_L \sim 12$ cm compared to a chamber radius of 4 cm for injection into a preformed plasma.

For the neutral gas cases, the ratio I_{net}/I_b varied from 0.6 to 0.25. The maximum magnetic field, calculated from the measured values of I_{net}, varied from 5000 to 2100 Gauss, and the Larmor radius for the beam electrons varied from 4 mm to 1 cm. Consequently, the beam electrons were constrained to a channel of nearly constant radius.

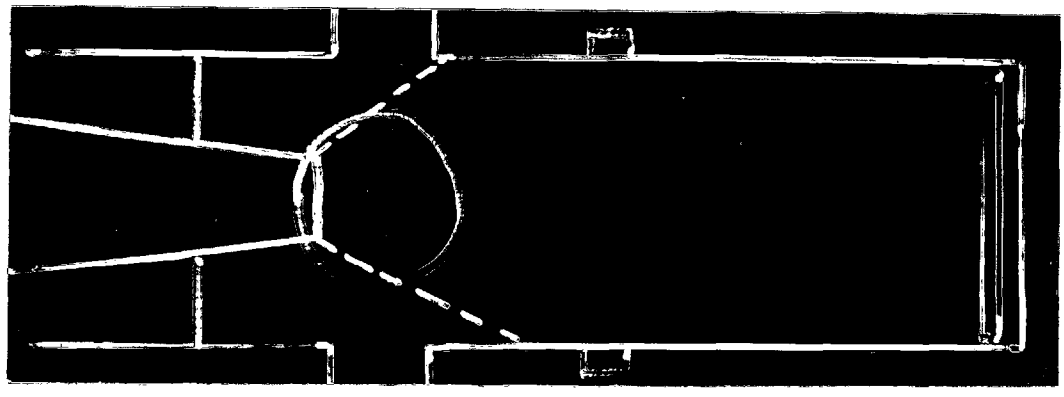

Cone Scattering Chamber Z-discharge Chamber

a) X-ray pattern for injection into plasma with $n_e = 8 \times 10^{13}$ cm^{-3} and $T_e = 2$ eV

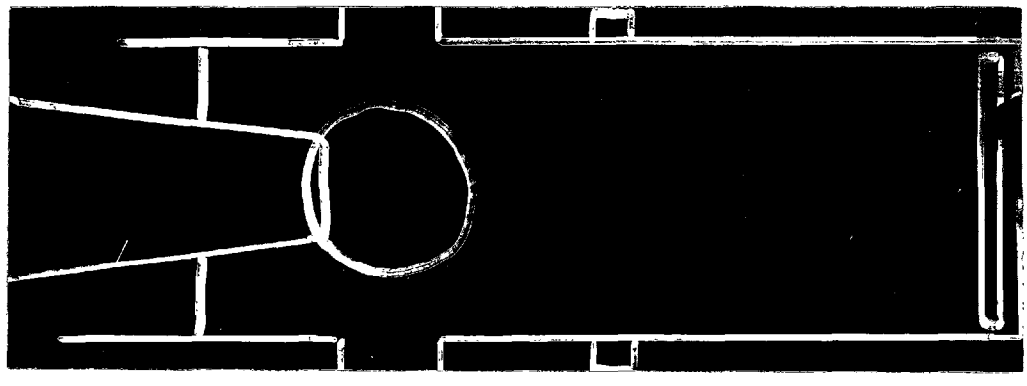

Cone Scattering Chamber Z-discharge Chamber

b) X-ray pattern for injection into neutral hydrogen at 3 mTorr

Figure 32. X-ray pinhole photograph of the experimental chamber. The film recorded the x-rays from the walls of the chamber. When the beam was injected into a preformed plasma, it apparently defocused and struck the walls. However, the beam remained focused with less loss to the walls for injection into a low pressure gas.

The implications of these measurements are that for injection into a preformed plasma, the beam number density decreased rapidly with z (the distance from the entrance foil) and that the resistance and inductance per unit length of the net current channel were strong functions of the axial position. This z-dependence complicated the interpretation of the results. In contrast, the beam-plasma system for injection into a neutral gas was essentially independent of z.

4.3 Witness Plate Measurements

The damage done to a solid target (the witness plate) as the beam electrons were stopped in the material was used to determine the dimensions and position of the beam channel. Basically, the energy per unit volume absorbed by the target material is a function of the beam's energy density and the range of the beam electrons. The melted and vaporized material is blown away before it solidifies. The resulting cavity then defines the volume that was heated above the threshold for melting and/or vaporization. If the material is brittle, like carbon, it may spall and produce a crater that is difficult to interpret. If the mass of the target is small, it can move appreciably during the beam by the rocket effect. If these difficulties are avoided, the witness plate can reveal the beam's spatial distribution.

The witness plate used in these experiments consisted of layers of aluminum foil (0.059 g/cm^2 areal density), periodically separated by sheets of radiation-sensitive blue-cellophane. The aluminum sheets absorbed and attenuated the beam to the point that

the blue cellophane survived the shot and could be read with a microdensitometer to give a relative dose distribution within the beam. The blue-cellophane analysis gave the same pattern of energy deposition as observed by the damage pattern on the foils. Figure 33 shows a typical damage pattern taken at one centimeter from the cone exit foil in 100 mTorr initially neutral hydrogen. This is a typical profile. The energy deposition at the entrance foil is centered on the side away from the Blumlein.

The position of the laser-scattering volume is shown relative to the beam profile in Figure 44. The volume of the plasma sampled is approximately 3 mm off the beam axis.

A very large dose of beam electrons on the POCO graphite of the calorimeter was found to discolor the material. The discoloration of the graphite placed at the end of the experimental chamber was nearly circular and centered slightly off the chamber axis away from the Blumlein. With 100 mTorr H_2 and 60 mTorr H_2 in the experimental chamber, the spot size was 10 mm and 6 mm, respectively. Above 100 mTorr the beam density was insufficient to discolor the carbon. The damage on the calorimeter was evidence that the pinched beam remained well defined and approximately of constant radius for injection into neutral gas at these pressures.

4.4 Image-Converter Streak Photography

The x-ray measurements and witness plate work established the dimensions of the beam-current channel. The accepted model for injection into a neutral gas specifies that if the breakdown time

Blumlein →

Witness Plate

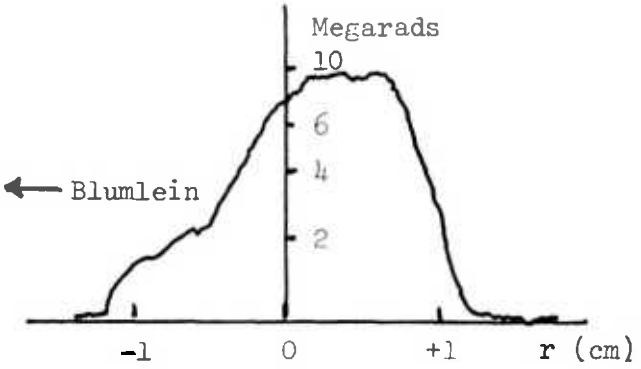

Microdensitometer Trace

Figure 33. Typical witness plate measurement of the beam's energy distribution at the scattering volume. The blue-cellophane behind the foil was bleached by the electrons, and the electron dose was measured from the change in the transmission of the cellophane. The distribution of dose is shown on the microdensitometer trace of a piece of blue cellophane behind 0.95 g/cm^2 of aluminum. The scattering volume was at r = 0.

of the gas is much less than the beam's rise time, the beam and plasma currents flow in the same channel, as discussed in Section 2.2. Nevertheless, after the system is established, the $\underline{v}_e \times \underline{B}$ forces on the plasma electrons and the beam electrons are in the opposite directions since their axial velocities are in the opposite directions. The beam and plasma current channels could conceivably depart from co-incidence during the pulse.

An image-converter streak-camera was used, as shown in Figure 34, to photograph the time history of the radial profile of the light emitted when the beam was propagated into neutral gas at 10 Torr, 1 Torr, 100 mTorr, and 60 mTorr hydrogen. The camera was focused on a position 1.5 cm from the entrance foil. The camera aperture was fully open on all shots. The results are shown in Figure 35. The light emission in a band around 6943 A° was recorded with the laser scattering system on other shots under the same experimental conditions reported here. The light emission measurements are described in Section 4.9. The plasma current $I_b = I_{beam} - I_{net}$ was recorded under the same experimental conditions, as described in Section 4.7.

The waveforms for the light emission and the plasma current waveforms are shown for comparison with the photographs.

For the 1 Torr and 10 Torr cases, the plasma channel is relatively stationary. The luminosity recorded on the photographs follows the plasma current waveform, as does the continuum emission from the plasma during the beam.

The sudden rise in the plasma emission at 10 Torr after the plasma current has decayed, is recorded in the photograph and in the continuum emission. The light was emitted from the plasma, not from fluorescence of the walls. This was the first indication that the molecular excitation of the gas was important at high pressures,

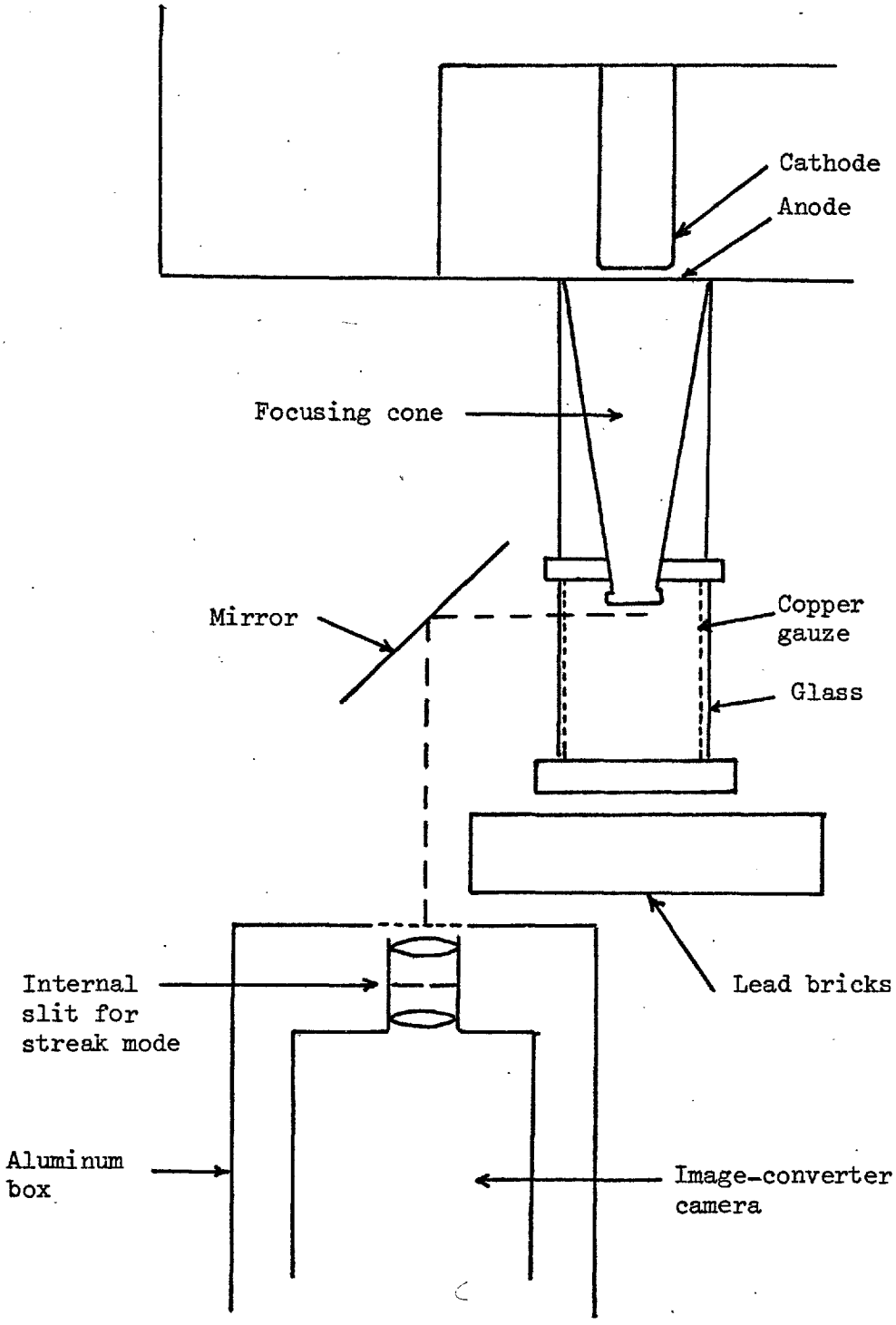

Figure 34. Experimental arrangement for image-converter streak photography to measure the radius of the plasma channel as a function of time.

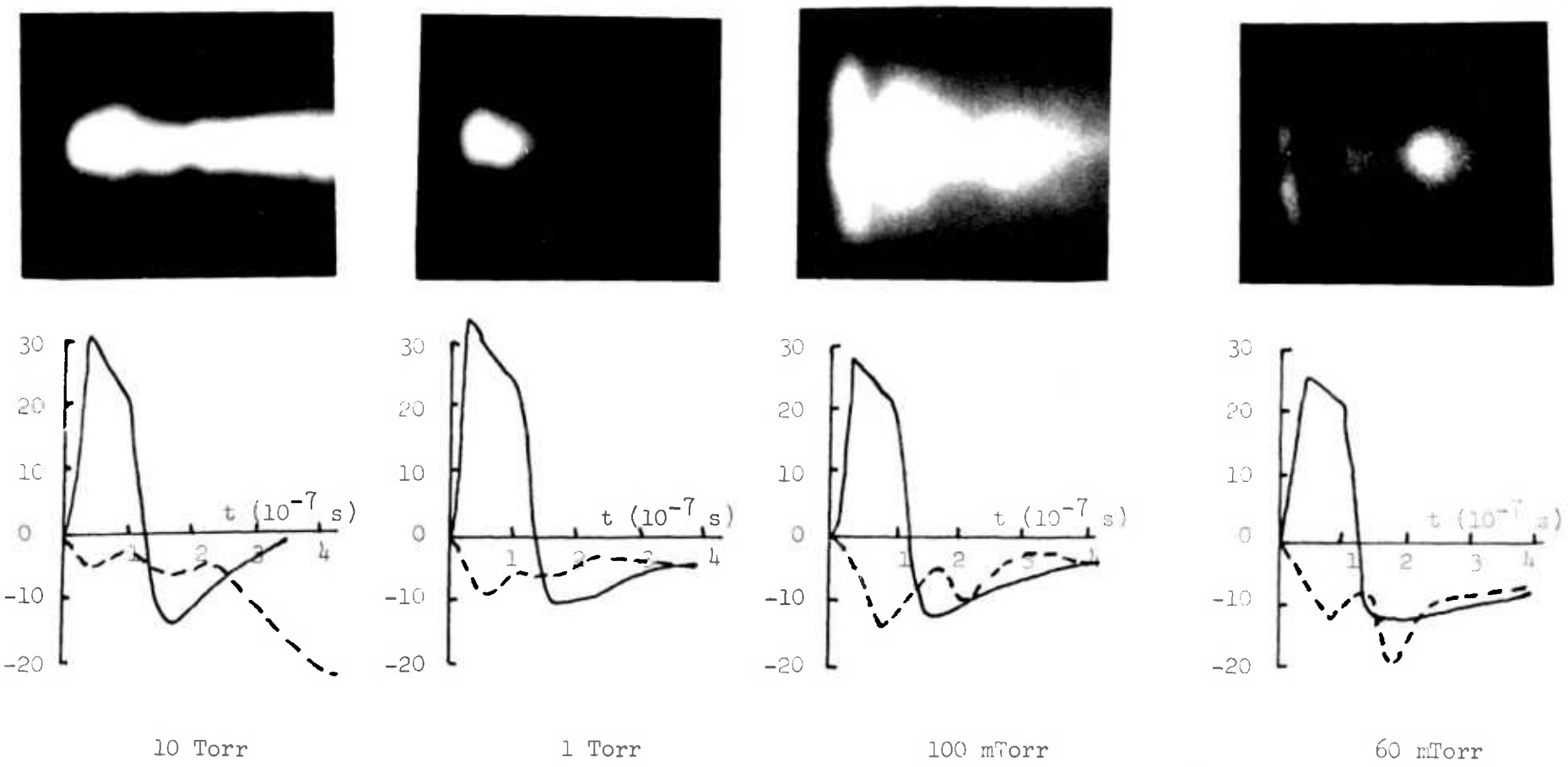

Figure 35. Streak photographs of the radius of the plasma channel as a function of time. The plasma channel had a nearly constant radius when the beam was injected into 1 Torr and 10 Torr hydrogen. However, for injection into 100 mTorr and 60 mTorr hydrogen, the channel expanded during the beam pulse. The plasma current profiles and the intensity of the continuum around 6943 A° are shown for comparison with the luminosity recorded by the photographs. The plasma current is given in kilo-amperes by the solid lines. The luminosity is given in relative units by the dashed lines.

as will be discussed in Section 7.6.

The radial profiles of the 100 mTorr and 60 mTorr cases were quite different from those at higher pressures. The initial burst of luminosity shown in the photographs was associated with secondary electrons escaping to the wall and causing it to fluoresce. The light emitted by high energy electrons colliding with glass is primarily Cherenkov radiation and is mainly in the blue region of the spectrum. This was visible on the image-converter camera photographs and not on the photo-multiplier signals because (1) the bandwidth of the former was approximately 80 times that of the photomultiplier channels and (2) the spectral sensitivity of the S-20 phosphor in the streak camera peaks in the blue,while the region of the spectrum monitored by the photo-multipliers was in the red. The Cherenkov radiation is emitted in a cone about the direction of the electron velocity, so it is not observed at the top and bottom of the drift tube. The duration of this light was small compared to the 20 ns resolution of the photographs. At higher pressures, the secondary electrons did not reach the walls with sufficient energy to cause fluorescence.

For the 60 mTorr and 100 mTorr cases, the plasma light became sufficient to expose the film at about 70 ns after the beam began. At this time the luminosity reached at least a radius of 2 cm. The apparent radius continued to increase until $t \approx 120$ ns and then decreased as the discharge pinched to the axis at 200 ns.

Finally, the correlation of the plasma light trace with the photographs established that the photo-multiplier recorded light from the plasma, not from the walls. Consequently, interpretation of the plasma light trace should be a meaningful exercise.

4.5 Calorimeter Measurements

The construction and calibration of the calorimeter has already been described in the Section 3.6. The same or a similar calorimeter was placed at the end of the z-discharge region for the experiments with a preformed plasma or at the exit from the scattering section for the experiments with neutral gas. The energy transmitted as a function of initial conditions for the experiments with a neutral gas is given in Figure 36. The energy transported to the calorimeter in the experiments with a preformed plasma varied from 15 to 300 joules for 1 kilo-joule injected energy.

The half-angle $\theta_{\frac{1}{2}}$ of the beam velocity can be estimated from these data. Assume the beam expands uniformly into a cone with a half-angle θ_{max} and with its apex at the entrance foil to the experimental chamber. The ratio of the energy that will be collected by the calorimeter to the injected beam energy (W_c/W_b) is the ratio of the solid angles subtended by the calorimeter and the cone.

$$\frac{W_c}{W_b} = \frac{\pi r_c^2/l^2}{\pi l^2 \cot^2(\theta_{max})/l^2} = \frac{r_c^2}{l^2 \cot^2(\theta_{max})}$$

where r_c is the radius of the calorimeter and l is the distance between the calorimeter and the entrance foil. Consequently,

$$\theta_{max} = \cot^{-1}(r_c^2 W_b / l^2 W_c)^{\frac{1}{2}} \qquad (4\text{-}1)$$

if the expansion is not hindered by the self-magnetic field of the net current, which is the case when the net current is at a minimum. For W_b = 1 KJ, W_c = 0.015 KJ, l = 20 cm, and r_c = 4 cm, $\theta_{max} = 31^o$. The

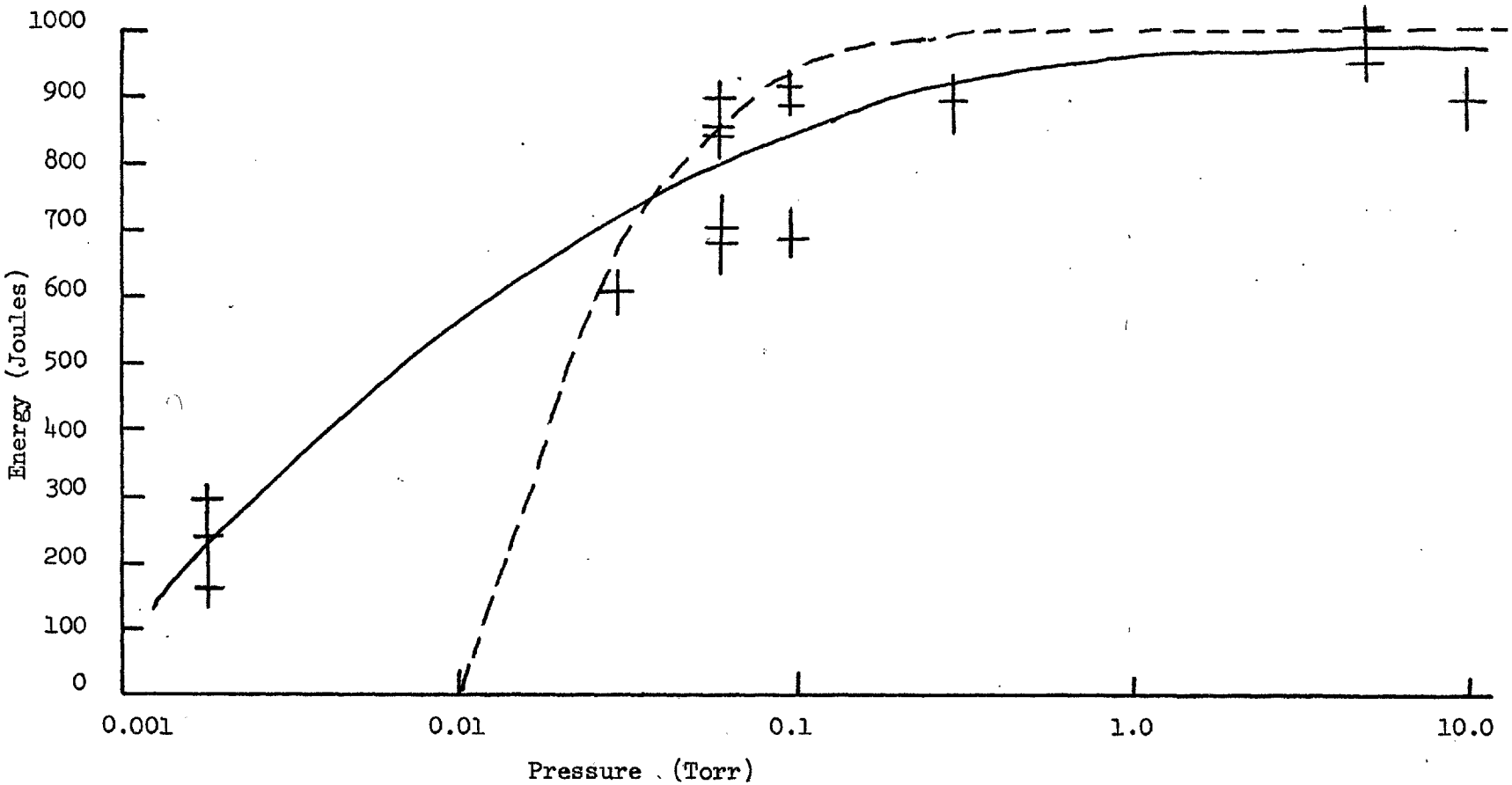

Figure 36. Plot of the energy transmitted to the end of the scattering chamber as a function of the initial pressure of hydrogen for injection into a neutral gas. The broken line gives the energy expected under the assumption that all the energy is lost until t_f when the beam is force neutralized by ionization by primary electrons.

average half-angle is $\theta_{\frac{1}{2}} = 0.65 \times \theta_{max} = 20^{o}$.

The calorimeter data can also be used to investigate the force neutralization time t_f for the beam electrons when the beam is injected into neutral hydrogen. Let the beam have a current I and an electron energy eV_b given by

$$I = I_o\, t/t_r, \quad \text{and} \quad eV_b = eV_o\, t/t_r \qquad \text{for } t<t_r$$

$$I = I_o, \quad \text{and} \quad eV_b = eV_o \qquad \text{for } t_b>t>t_r$$

$$I = I_o\left(1-\frac{t-t_b}{t_r}\right), \text{ and } eV_b = eV_o\left(1-\frac{t-t_b}{t_r}\right), \text{ for } t_b+t_r>t>t_b$$

where t_r and t_b are the beam's rise time and duration respectively. For the cases for injection into neutral H_2 at a pressure P, the time t_f is given by equation (2-5) for 350 keV electrons as

$$t_f = \frac{2.1}{P}\ \text{ns} \qquad \text{for } t_f< t_r$$

$$= \frac{1.05}{P} + t_r/2 \qquad \text{for } t_b> t_f> t_r$$

where P is the initial gas pressure in Torr. The total beam energy W_{bT} that has passed the anode foil at time t for t_b = 100 ns is

$$W_{bT}(t) = \int_0^t I(t)V_b(t)\, dt$$

$$= \frac{I_oV_o}{9 \times 10^{-8}}\,(t^3/3t_r^2) \qquad \text{for } t<t_r,$$

$$= \frac{I_oV_o}{9 \times 10^{-8}}\,(t - 2t_r/3) \qquad \text{for } t_r<t<t_b$$

$$= \frac{I_oV_o}{9 \times 10^{-8}}\,(t_b - t_r/3 + (t - t_r - t_b)^3/3t_r^2)$$

$$\text{for } t_b<t<t_b+t_r.$$

If one assumes that all the beam energy is lost for $t < t_f$, and then

after t_f all the beam energy reaches the calorimeter, then the transmitted energy is

$$W_{transmitted} = W_{bT}(t=130ns) - W_{bT}(t=t_f) \qquad (4-2)$$

and is plotted in Figure 36 for comparison with the experimental measurements.

The reading on the calorimeter was used with the diode diagnostics to ensure that a shot was a good one, i.e. that there was not an equipment failure such as a charging inductor becoming discontinuous or the Blumlein falling off its supports.

4.6 Electrostatic Energy Analyzer Measurements

H. Chuaqui had built an electrostatic energy analyzer to analyze the ion energy spectrum of the Polytron plasma at Imperial College. The analyzer proved unsuitable for his experimental geometry, and he kindly offered to let me adapt it to my experiment. An apparatus was constructed as shown in Figure 37 and 38.

The experimental arrangement caused several problems that limited the use of the analyzer. The particles that entered the analyzer were moving perpendicular to the magnetic field of the net current so ions were likely to hit the wall before reaching the collector. The distance from the plasma to the collector was approximately 3 cm, which corresponded to the charge-exchange mean free path for H_2 at 16 mTorr. Above that pressure, few energetic ions would arrive at the collector. The secondary electrons expelled by the beam during space-charge neutralization were sufficient to ionize the gas in the analyzer and to cause current to flow from the third grid to the collector. These

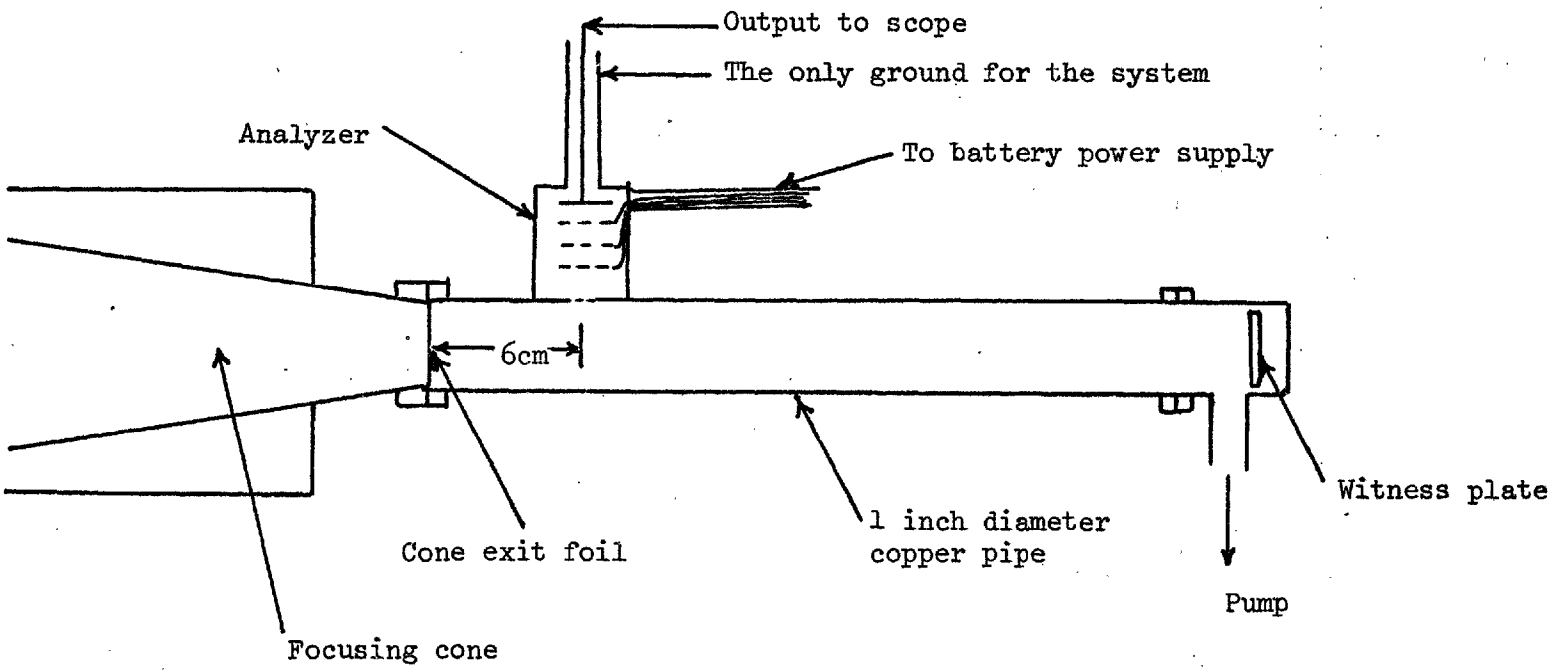

Figure 37. Experimental arrangement for experiments with electrostatic analyzer. The time history of the secondary electrons expelled from the beam was measured.

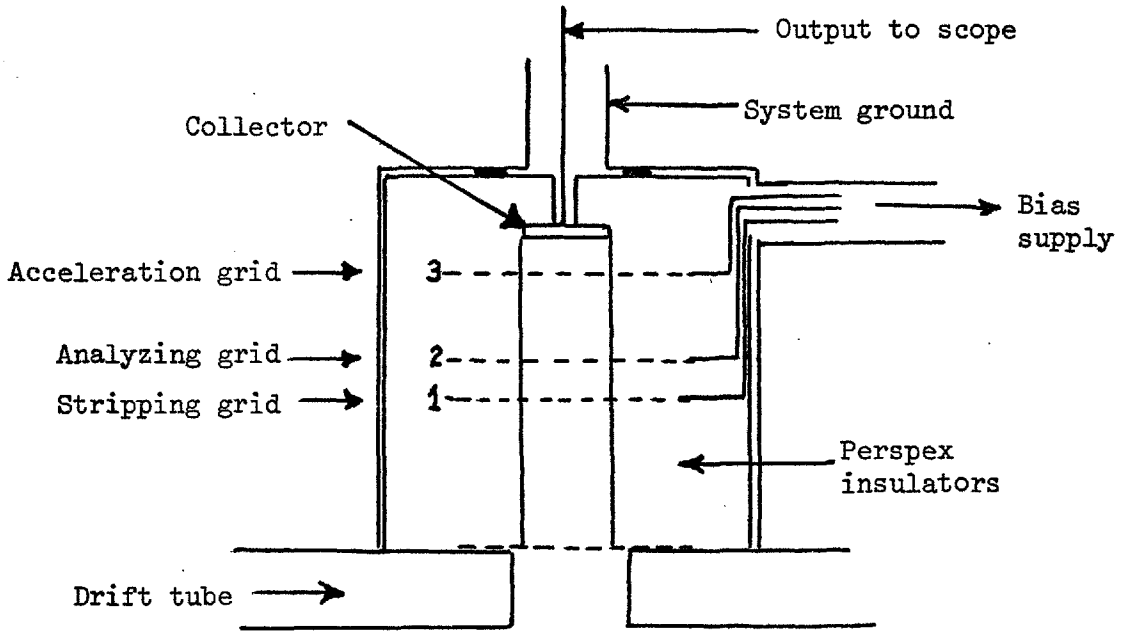

Analyzer construction

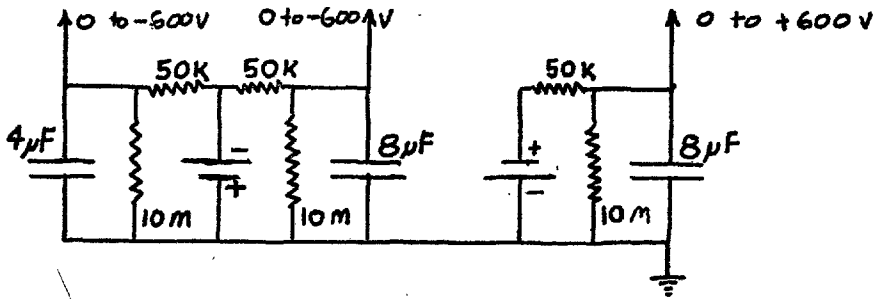

Bias supply

Figure 38. Construction of the electrostatic energy analyzer.

difficulties made the analyzer useful to measure only the secondary fast electrons expelled from the beam during the charge neutralization process. The retarding potential on the first grid was -250 V to reject low energy electrons. The signals reaching the oscilloscope from the collector are shown in Figure 39.

Since the signal at 40 mTorr decreased after 35 ± 5 ns, the charge neutralization time at 40 mTorr must have been approximately 40 ns which should be compared with the theoretical value of 90 ns, calculated from Equation 2-4.

The trace at 10 mTorr showed that electrons were expelled throughout the beam pulse. Consequently, at this pressure and in this experimental geometry, the beam might not be space-charge neutralized.

At higher pressures, the secondary electrons caused additional ionization of the background gas. The cross section for ionization of H_2 by an electron with energy between 30 eV and 20 eV is approximately $Q_{ioniz} = 8 \times 10^{-17}$ cm^2 from Massey (1969). Consequently, the mean free path for ionization is

$$\lambda = \frac{1}{3.54 \times 10^{16} Q_{ioniz} P(\text{Torr})} \text{ cm} = 0.35/P \quad \text{cm}.$$

At 1 Torr, the secondary electrons produce additional ionization in the beam-channel to reduce t_{cn} below the 6 ns value calculated from Equation 2-4. The small charge meutralization time would not be observed with this apparatus. The bump after the main pulse is consistent with a discharge from the third grid (at -250 V) to the collector after the gas in the analyzer was ionized by the fast electrons.

4.7 Net Current Measurements

The present experiment used a self-integrating Rogowskii coil placed behind the nozzle of the cone exit to measure the net current in the plasma channel near the cone exit as shown in Figure 40.

The construction of the coil is shown in Figure 41. The coil was

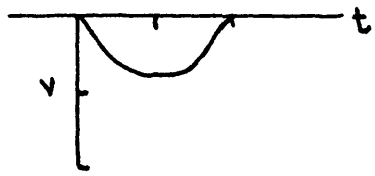

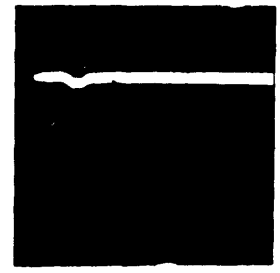

12.5 v/cm, 100 ns/cm

5.5 v/cm, 550 ns/cm

a) 1 Torr H_2

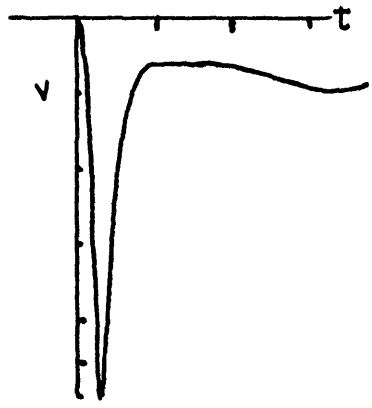

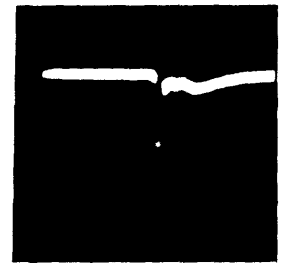

25.0 v/cm, 100 ns/cm

5.5 v/cm, 550 ns/cm

b) 40 mTorr H_2

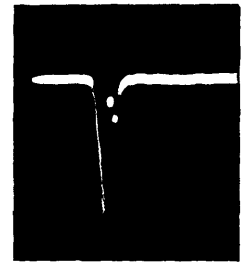

50. v/cm, 100 ns/cm

5.5 v/cm, 550 ns/cm

c) 10 mTorr H_2

Figure 39. Time histories of the secondary electron emission from the beam during charge neutralization.

Net current flow for injection into a preformed plasma

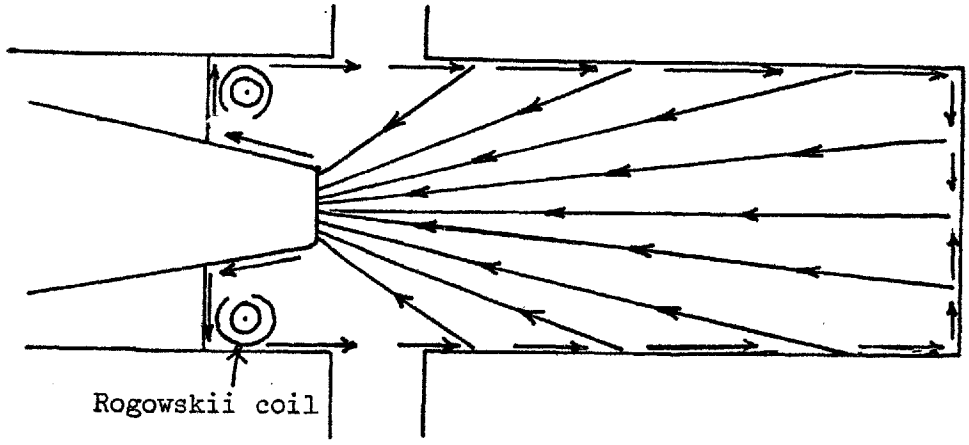

Net current flow for injection into neutral H_2

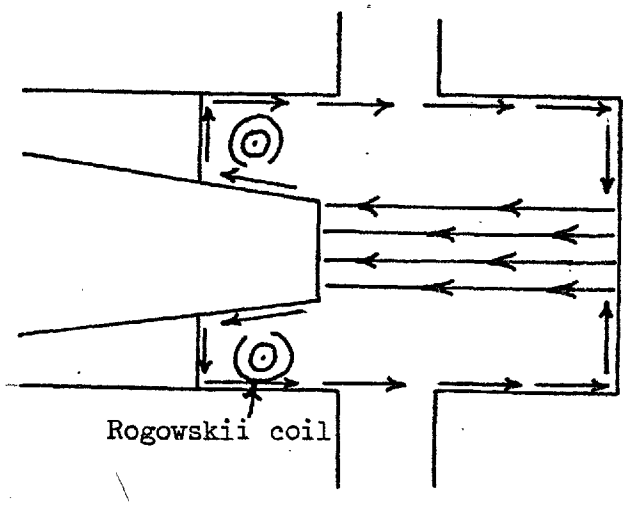

Figure 40. Net current flow for injection into a preformed plasma and into a neutral gas. The z-dependence of the problem could be neglected for injection into a neutral gas, but not for injection into a preformed plasma. The Rogowskii coil measured the net current, i.e. the current with a return path outside the beam channel.

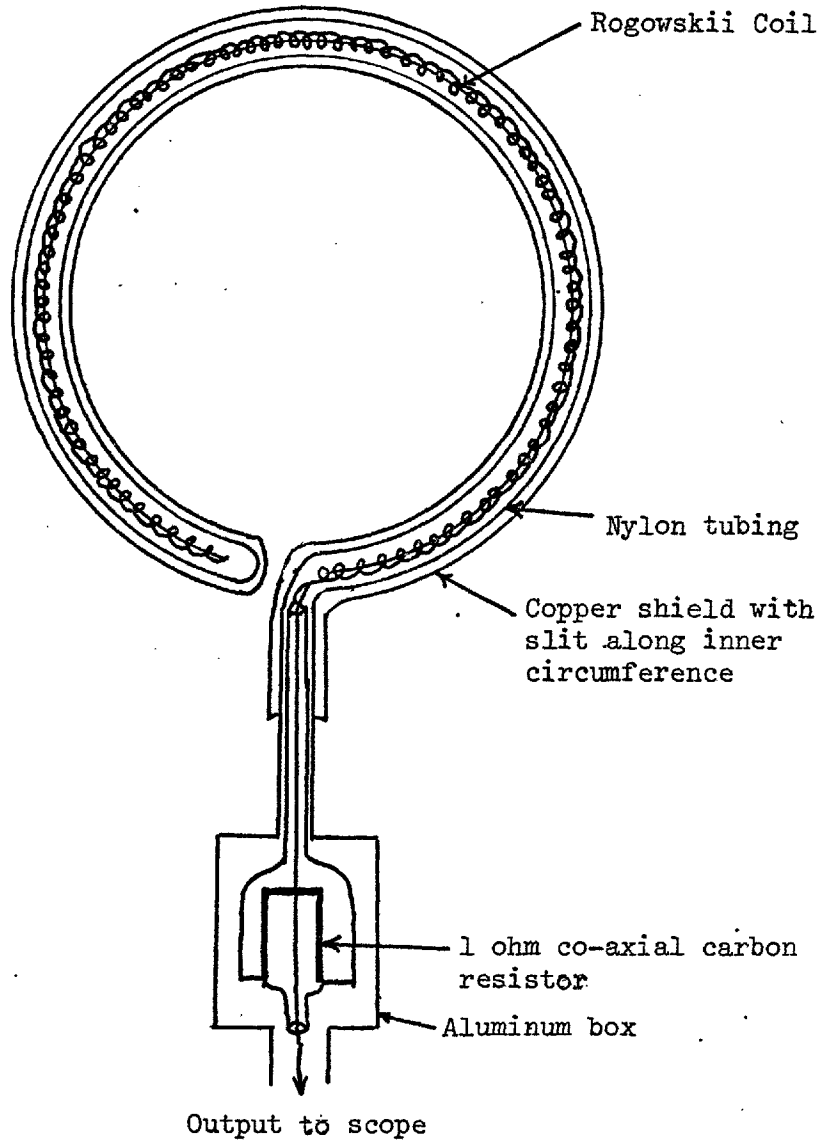

Figure 41. Construction of the Rogowskii coil to measure the net current. The coil was wound on 50 ohm mini-coax, stripped of its outer conductor, with polypropelene insulated copper wire. The coil was at atmospheric pressure to prevent flashover and was shielded inside a copper tube with a slit running around the inner circumference.

calibrated with a 100 ns, low amplitude current pulse from a pulse generator. The L/R decay time of the observed signal for a 10 μsecs current pulse was 2.0 μsec. The net current monitor was then cross-calibrated with the diode current monitor by shunting the Blumlein current through the net current monitor and firing the Blumlein at a low voltage. The two current monitors agreed to within 10%.

The information obtained with the x-ray camera, the streak camera, and the witness plates indicated that the beam and plasma currents flowed in the patterns shown in Figure 40 for the cases with a preformed plasma and for those with neutral hydrogen. The net current measured by the Rogowskii coil was the beam current minus the plasma current in the region of interest, which included the scattering volume. It was axially independent for the neutral gas cases, except weakly dependent at 1 Torr (the pressure for maximum magnetic neutralization).

The value of the net current at 100 ns after the beginning of the beam is given in Table 4 for the various experimental conditions.

Sample waveforms for the net current under different experimental conditions are given in Figure 42. The noise was often excessive in spite of the shielding and has been reported by other experimenters, e.g. McArthur and Poukey (1973). Shots with the beam stopped before it reached the scattering chamber showed the high-frequency pick-up was symmetric about the baseline of the trace and could, therefore, be averaged out.

In Figure 43 the net current waveforms versus time are plotted for initial conditions. The net current actually increased after the beam pulse. The dotted line is the expected L/R decay after the beam.

4.8 Laser Scattering Measurements

The measurement of the plasma number density and temperature in the presence of a high-current, relativistic electron beam required a technique that would not perturb the plasma and an apparatus that was not destroyed

Table 4. Net current for various experimental conditions.

Case No.	Pressure (Torr)	Number Density (cm^{-3})	I_{net} (t=100ns) (10^3 amps)	Max I_{net} (10^3 amps)
I	0.01	$3x10^{13}$	1.8±20%	2.2±20%
II	0.003	$7x10^{14}$	---	---
III	0.2	$2x10^{15}$	1.7±15%	3.0±15%
IV	0.01	$8x10^{13}$	1.8±15%	2.2±15%
V	0.06	--	11.±15%	12.±15%
VI	0.1	--	13.±15%	14.±15%
VII	1.0	--	5.±20%	8.5±20%
VIII	10.	--	11.±20%	13.±20%
--	0.002	--	15.±15%	20.±15%

(a)

13 kA/cm, 550 ns/cm

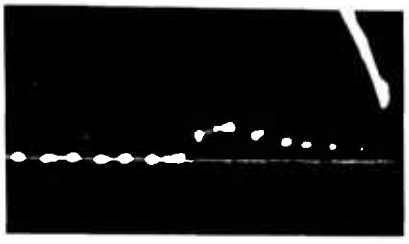

(b)

35 kA/cm, 160 ns/cm

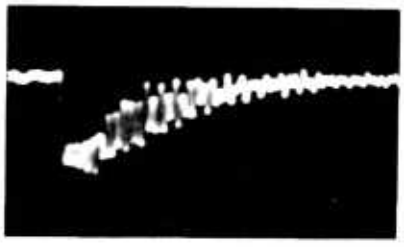

(c)

6 kA/cm, 500 ns/cm

Figure 42. Net current waveforms for selected experimental conditions: a) 2 mTorr neutral H_2, b) 100 mTorr neutral H_2, and c) $n_o = 2 \times 10^{14}$ cm^{-3} and $T_{eo} = 1$ eV.

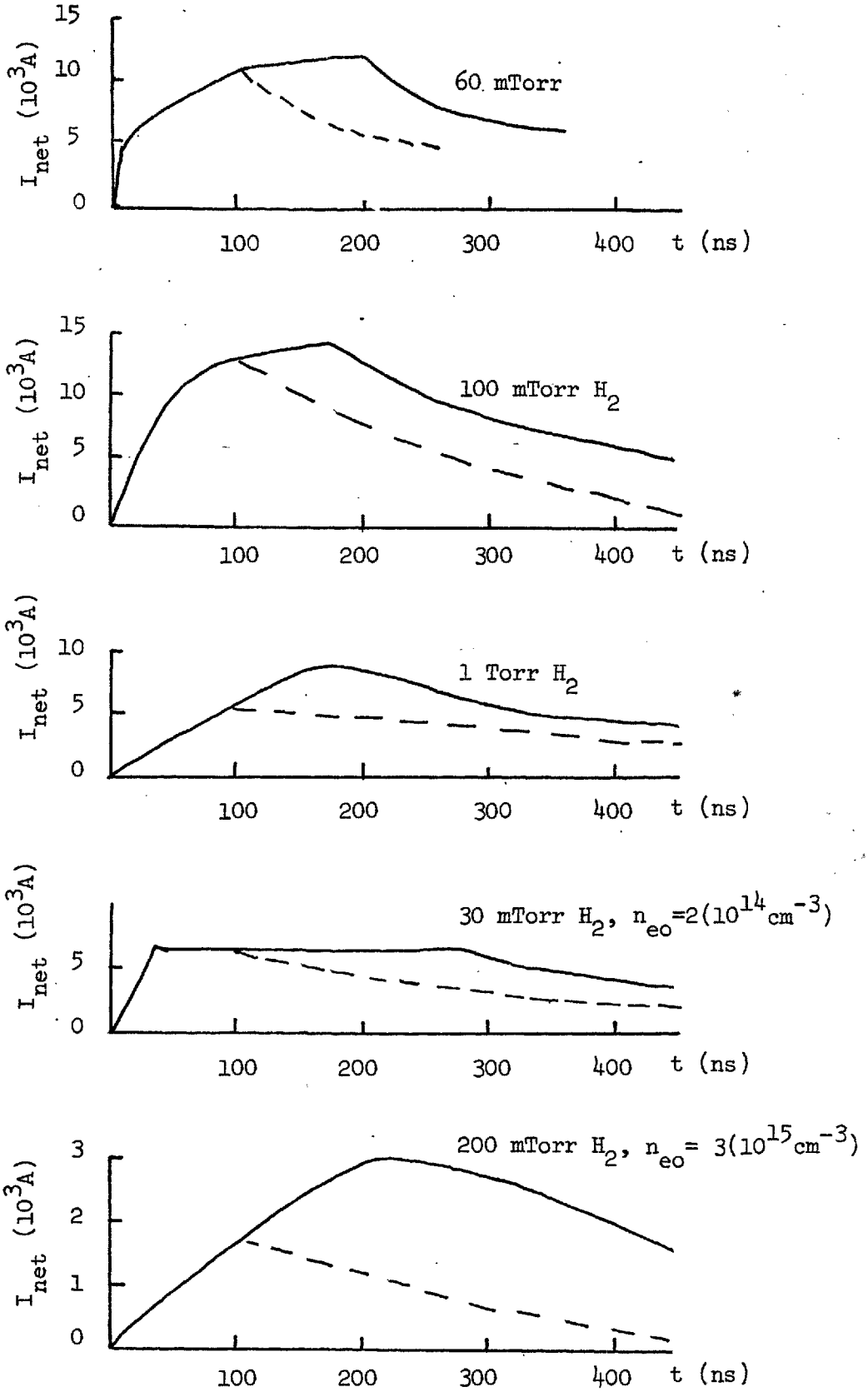

Figure 43. Net current waveforms for selected experimental conditions. The waveform is compared to that expected from a simple L/R decay of the plasma current after the beam (broken line).

by the beam. Thomson scattering of laser light offered the possibility of measuring the number density of the plasma and the electron velocity distribution projected along a particular direction in a small volume of plasma, as described by several authors, for instance Evans and Katzenstein (1969). Laser scattering was the principal diagnostic in the present experiment. The time resolution was approximately 20 ns and was limited by the laser pulse width and the rise time of the collection system.

The laser light was focused on a spot in the plasma,and the scattered light was collected along a line perpendicular to the laser beam as shown in Figure 44. The collected light was directed through a spectrometer to photomultiplier tubes. The photomultiplier tube signals were recorded on an oscilloscope, and the peak of the signal on all channels was measured from the resulting photograph. Since the photomultiplier channels were cross-calibrated and since the sensitivity of the system was calibrated absolutely, the number of electrons in the velocity interval observed by each photomultiplier was then known. The plot of that number versus the velocity (wavelength) interval is the electron velocity distribution, along the direction of the scattering vector $\bar{k}_s = \bar{k}_{in} - \bar{k}_{out}$, as shown in Figure 44.

The significance of the scattering vector arises from the fact that the observed light has been Doppler shifted twice in the scattering process: once from the lab frame to the electron frame along the vector $\underline{k}_{in}$ and again from the electron frame to the lab frame along the vector $\underline{k}_{out}$. The net result is a single Doppler shift along the scattering vector $\underline{k}_s$. If this scattering vector corresponds to the wave vector of plasma waves, the spectrum of the scattered light yields the frequency distribution of the plasma turbulence with the selected $\underline{k}$-vector, and the intensity yields the strength of the fluctuations. Since plasma waves with wavelengths less than the Debye length λ_D are quickly damped, the criterion of

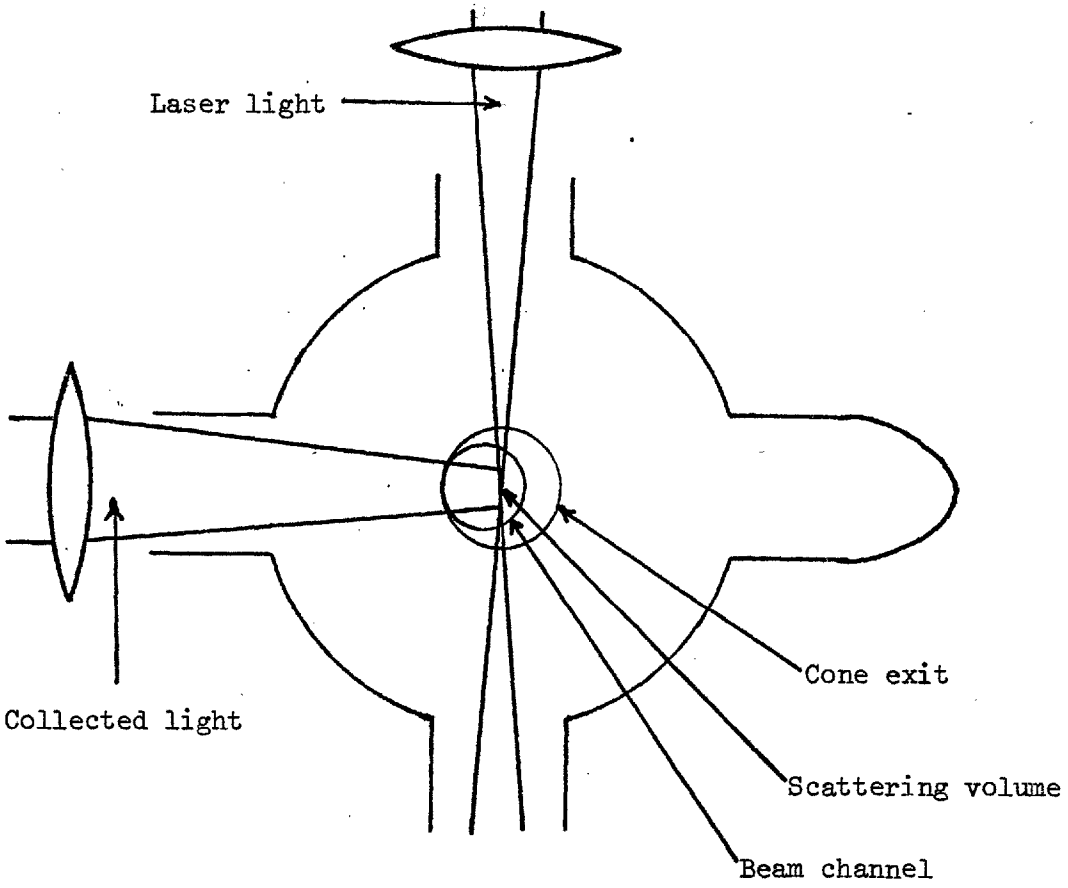

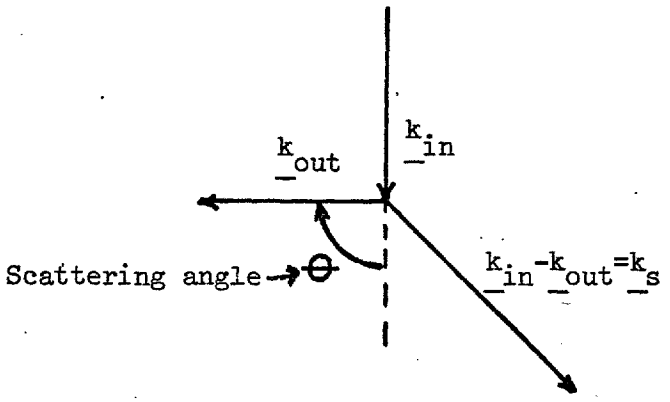

Figure 44. Schematic view of the laser scattering chamber. The center of the beam-plasma channel was displaced horizontally by $\approx$3 mm from the center of the scattering volume. The direction of the scattering vector $\underline{k}_s$, i.e. the direction along which the electron velocity distribution was measured, is shown in the bottom drawing.

$$\underline{k}_s = \underline{k}_{wave} \text{ implies that } \alpha \cong \frac{1}{k_s \lambda_D} > 1 \qquad (4\text{-}3)$$

for the regime of collective scattering. For the opposite case, $\alpha < 1$, there are no plasma waves with the appropriate $\underline{k}$ and the scattering is done by free electrons. In the present experiment the value of α was 0.2, so the interpretation of the spectrum followed that of free-electron scattering; i.e. the shift in the wavelength was given by $\frac{\Delta\lambda}{\lambda_o} = \frac{\underline{k}_s \cdot \underline{v}_e}{c} \frac{\lambda_o}{2\pi} = \frac{2v_s}{c} \sin(\theta/2)$ where v_s was the component along $\underline{k}_s$ and θ was the scattering angle. The location of the scattering volume and the direction of the scattering vector for this experiment is shown relative to the measured beam channel in Figure 44.

The experimental difficulties of performing a laser scattering experiment in the environment produced by currents with dI/dt of 2×10^{12} amps/sec and by x-ray fluxes of 10^9 rad/sec were formidable. The physical layout of the scattering system is shown in Figure 45. The ruby laser was either a Laser Associates Model 501 or one built by Mr. John Westlake of our research group. Both were rated at 100 MW with pulse widths of 50 ns and 20 ns (full width at half maximum), respectively. The divergences were $\sim$3 milliradians and $\sim$2.5 milliradians, respectively. To assist in aligning the system, a HeNe laser was aligned with the cavity of the ruby laser through a beam splitter, so the light reflected from the faces of the laser rod was colinear with the ruby laser light. Since the scattering chamber had to be dismantled before each shot, a quick and accurate method of re-alignment was necessary, and this method was adopted.

A small fraction of the ruby laser's light was deflected to a photodiode to monitor the laser output of each shot. This signal

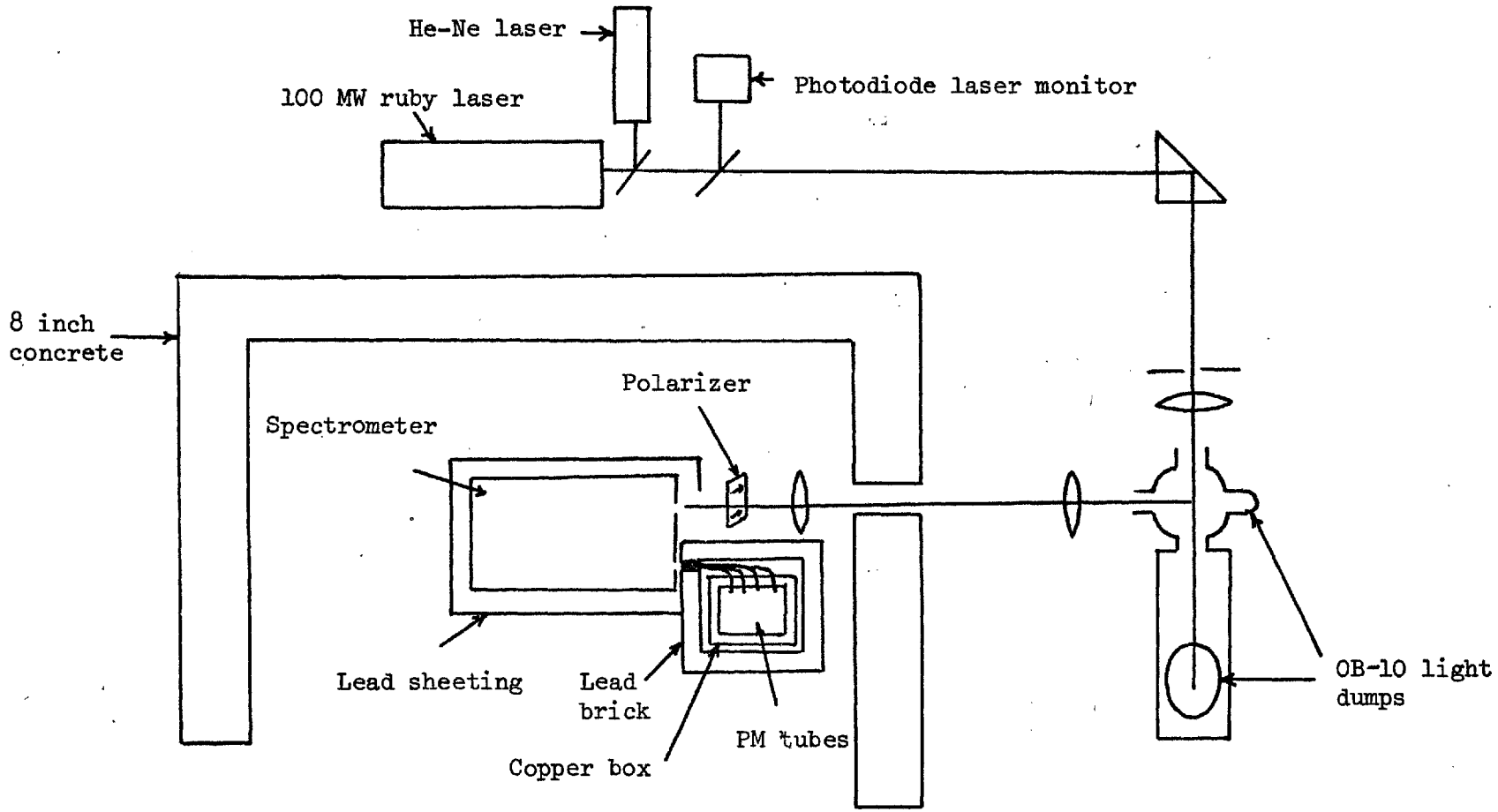

Figure 45. Physical arrangement of the scattering system. The effect of the large x-ray flux was overcome with massive concrete and lead shielding.

was used to normalize the data to the laser output. The assumption that the distribution of power within the laser beam's cross section was reproducible was verified by the reproducibility of the calibration shots taken before each experimental shot. The scatter in the calibration shots was typically 10%.

The laser light was first focused with a 3 m focal length lens to reduce light loss from the laser divergence. The light was then sent through a 90° prism and focused by a second lens of focal length 15 cm to a spot approximately 1 mm diameter at the center of the scattering chamber. The unscattered light was absorbed by blue OB-10 glass at the Brewster angle in the laser dump.

The scattered light was viewed against another OB-10 light dump to minimize the parasitic light at the unshifted wavelength. The light collection system had an overall f number of f/4.5, which was limited by the aperture and focal length of the first field lens. The light collected by the field lens was relayed through a hole in the 20 cm thick concrete wall of the x-ray shielding to a second lens that focused the light onto the spectrometer slit. A polarizer was used to attenuate the plasma light by rejecting the component perpendicular to the laser light's polarization.

The spectrometer had a grating with 1200 lines/mm and gave a dispersion of 13 A°/mm in first order. The entrance slit to the spectrometer was set at 0.75 mm. The output slits were formed by light pipe bundles 1 mm wide. The resolution was 13A°. The collection system had a magnification of 1.3, so the 0.75 cm high and 0.075 cm wide scattering region was imaged onto the 1 cm high and 1 mm wide light pipes. The arrangement of light pipes and photomultipliers permitted simultaneous observation of four wavelength intervals.

The light pipes and photomultiplier tubes were contained in a

lead box with 5 cm thick walls to give an attentuation of $\sim 10^{80}$ to the x-rays. This was found to be necessary to prevent the x-rays from causing fluorescence in the light pipes.

RCA 7265 photomultipliers were used. They have S-20 cathodes, a rise time of ~ 3 ns, and a quantum efficiency of 2% at $\lambda = 6943$ A°. They were contained in a copper box with 0.044 inch thick walls with doubly shielded high-voltage and signal leads from a screened room, which housed the oscilloscopes and high voltage supplies. This arrangement produced no observable x-ray pulse and a pick-up signal of less than 20 mV, which was adequate for the experiment. The wavelength interval monitored by each of the four photomultipliers is shown in Figure 46. Each experiment observed either the red- or the blue-shifted light. The photomultipliers were checked for their response time and linearity, and they were cross-calibrated with a fifth RCA 7265 (looking at 6943 ± 6.5 A°) with a 100 ns pulse from inside the spectrometer. The pulse had a 250 A° bandwidth centered on 6550 A°. The diode emitted light uniformly onto all of the light pipe channels. The cross calibration was checked periodically to ensure that it remained constant. The system was absolutely calibrated with the fifth photomultiplier by observing the scattered light from a known pressure of CO_2 in the scattering chamber just before the experiment. Normally three calibration shots were taken with the CO_2 in the chamber, and then three were taken with the chamber pumped out. The parasitic signal (signal with chamber evacuated) was subtracted from the signal observed during the shot. The ratio of the Rayleigh scattering cross section to the Thomson scattering cross section provided the calibration for the electron number density of the plasma, from the relation

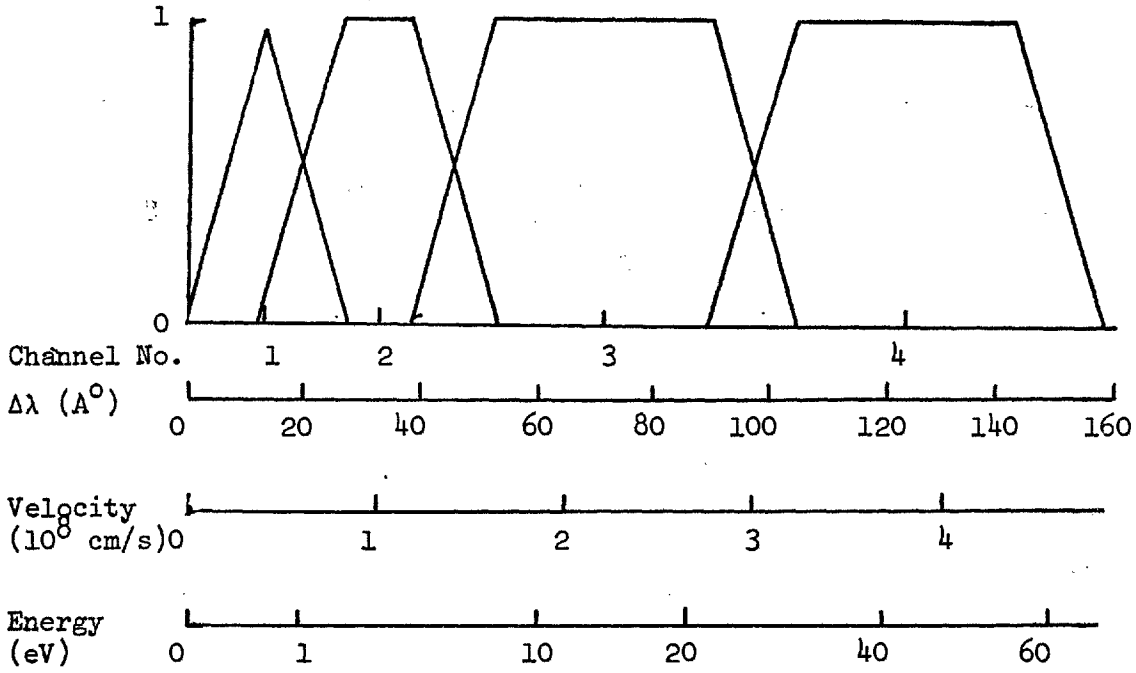

Figure 46. Diagram showing the wavelength, velocity and energy intervals monitored by each of the photomultipliers in the light collection system.

$$1 \text{ Torr } CO_2 = 2.1 \times 10^{14} \text{ cm}^{-3}$$

in total scattering power. This procedure had to be repeated for each shot.

Sample data is shown in Figure 47. For the data taken after the beam, the signal was usually sufficiently above background to make the correction for the plasma light negligible. However, during the beam the plasma light often changed on the same time scale as the laser pulse, and the reproducibility of the plasma light was used when possible to subtract the plasma light and recover the scattered signal. This was rarely possible and even when it was, the estimated error was approximately $\pm$ 30%. Nevertheless this method showed reproducibility of the number density to within 20% which gives confidence in the results and in the reproducibility of the phenomena.

The intrinsic error from the photon shot noise is 10% from Poisson statistics with the noise given by $\sqrt{n}/n$, where n is the number of photons counted. The shot noise of the plasma light, the pickup from the currents in the system, the uncertainty in the plasma light, and systematic errors involved in cross-calibration and the energy distribution in the laser pulse were used to arrive at a realistic estimate of the error, which is shown in the error bars of the data. The fact that the measurements were reproducible to an accuracy of less than the indicated errors justifies this procedure. It was not possible to take a large number of shots for each case at each time because of the experimental difficulties.

The basic datum for the experiment was the number density Δn_{ej} that corresponded to the amount of light scattered into the j_{th} channel monitored a velocity interval ΔV_{ej} centered at a velocity

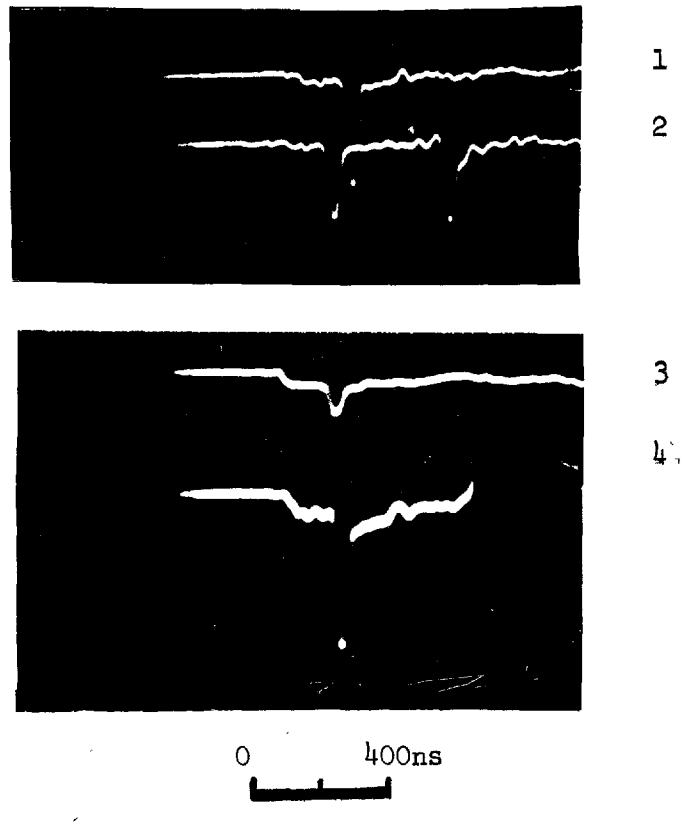

Figure 47. Sample data from the laser scattering experiment. This shot was taken 190 nsec with 100 mTorr H_2 in the scattering chamber. Traces 1-4 were centered at wavelengths -39 A°, -13 A°, -123.5 A°, and -71.5 A°, respectively, from 6943 A°. The laser monitor and x-ray signals were also displayed on traces 2 and 4 with known time delays inserted in the signal cables.

V_j. The electron velocity distribution was obtained by plotting the ratio of $\Delta n_{ej}/\Delta V_{ej}$ at the velocity V_j for each of the four channels.

The data taken for the various cases and at the various times are given in Figure 48. The data was reduced to give the number density n_e, the electron energy per unit volume nkT_{eff}, and the average energy per electron kT_{eff} (since the distribution was non-Maxwellian). These quantities were defined as follows:

$$n_e \equiv 2\int_0^\infty \frac{\Delta n_e}{\Delta v_e}\, dv_e = 2\sum_{j=1}^{4} \Delta n_{ej} \tag{4-4}$$

$$n_e kT_{eff} \equiv 2\int_0^\infty \frac{n_e}{v_e}\left(\tfrac{1}{2}m_e v_e^2\right) dv_e$$

$$= 2\sum_{j=1}^{4} \left(\Delta n_{ej} \cdot \tfrac{1}{2}m_e v_{ej}^2\right) \tag{4-5}$$

$$kT_{eff} \equiv n_e kT_{eff}/n_e \,. \tag{4-6}$$

Figures 49 through 51 give n_e, kT_{eff}, and nkT_{eff} respectively for the neutral gas experiments, and Table 5 gives these reduced quantities for the experiments with a pre-formed plasma.

A Maxwellian electron velocity distribution would produce a Gaussian spectral distribution of the scattered light. Many of the observed spectra in Figure 48 are inconsistent with Maxwellian velocity distributions. In particular, the distributions do not monotonically decrease with increasing velocity.

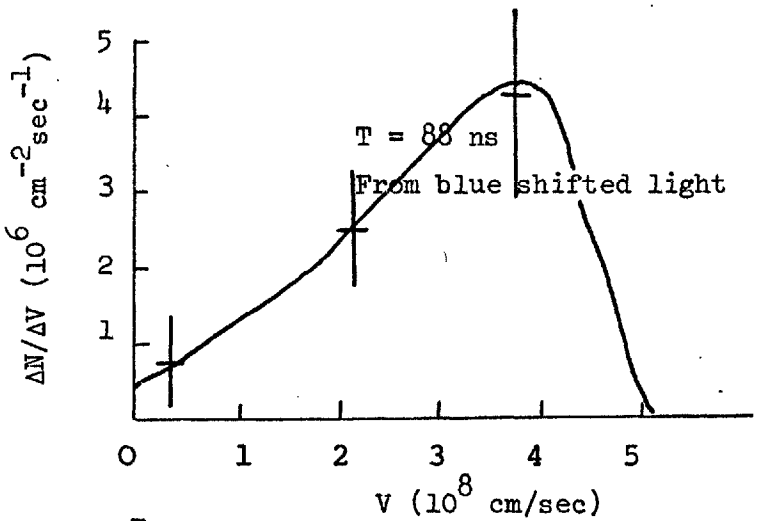

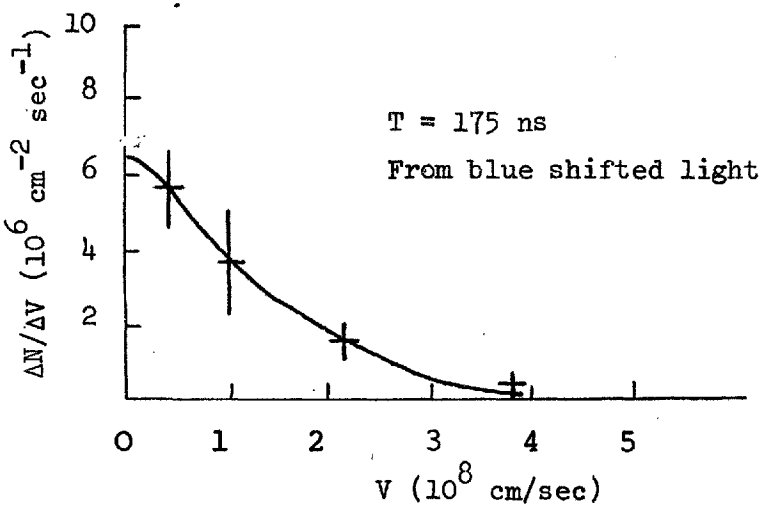

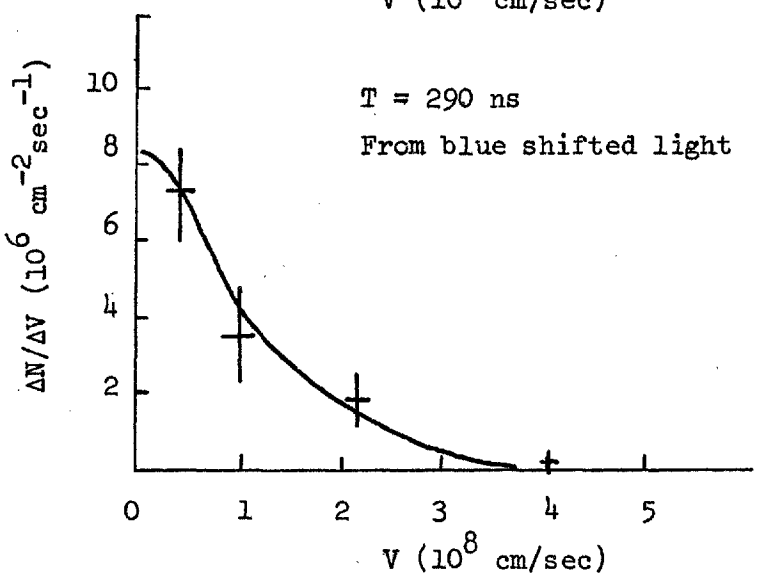

Figure 48a. Electron velocity distributions along the scattering vector for the various initial conditions and at various times (T) after the beginning of the beam pulse. Figure 48a gives the distributions for injection into a plasma at $n_e = 3 \times 10^{13}$ cm^{-3} and $T_e < 1$ eV with P = 10 mTorr (Case I).

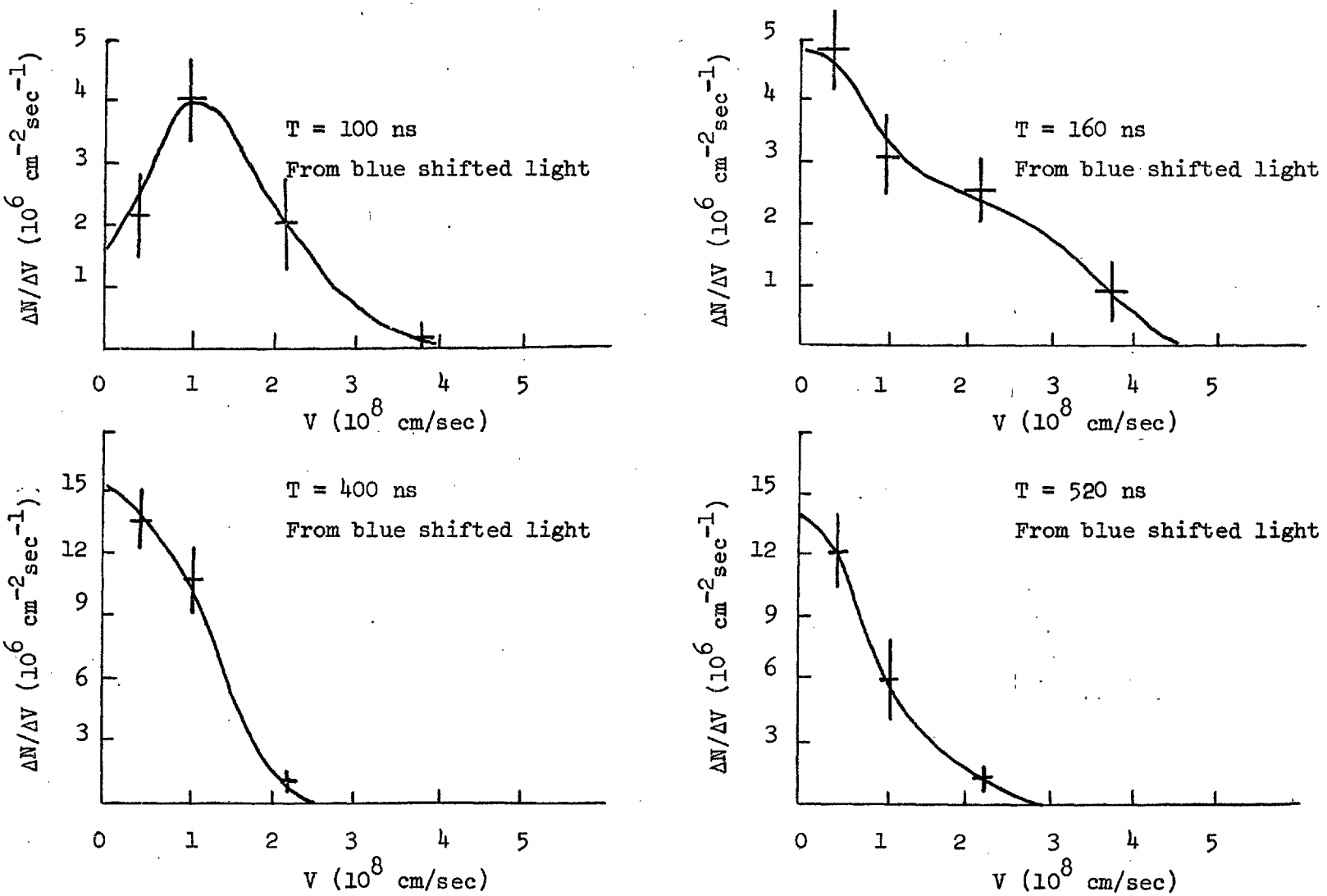

Figure 48b. Electron velocity distributions for injection into plasma at $n_e = 7 \times 10^{14}$ cm^{-3} and $T_e = 1$ eV with P = 2 mTorr (Case II).

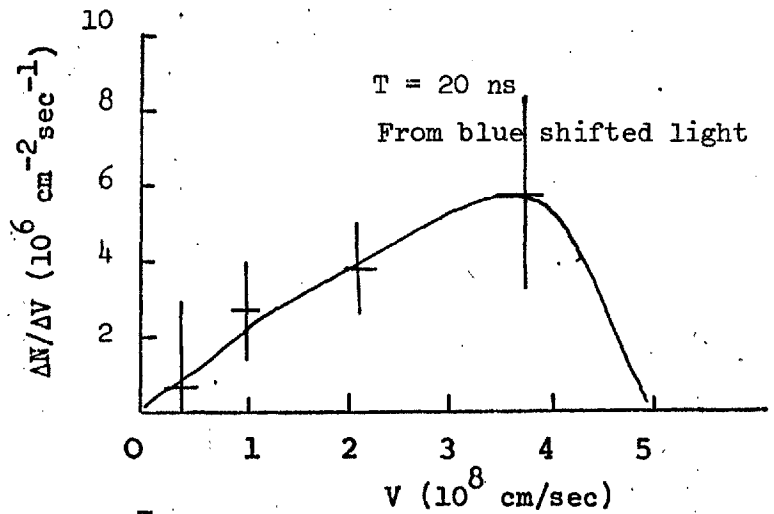

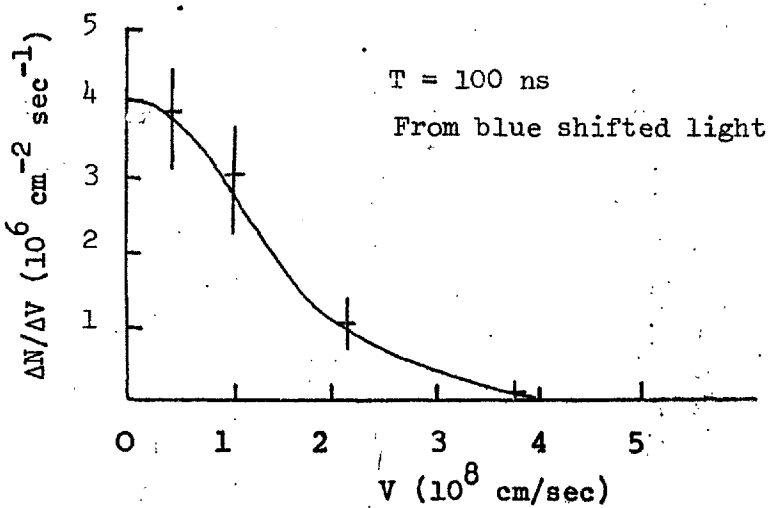

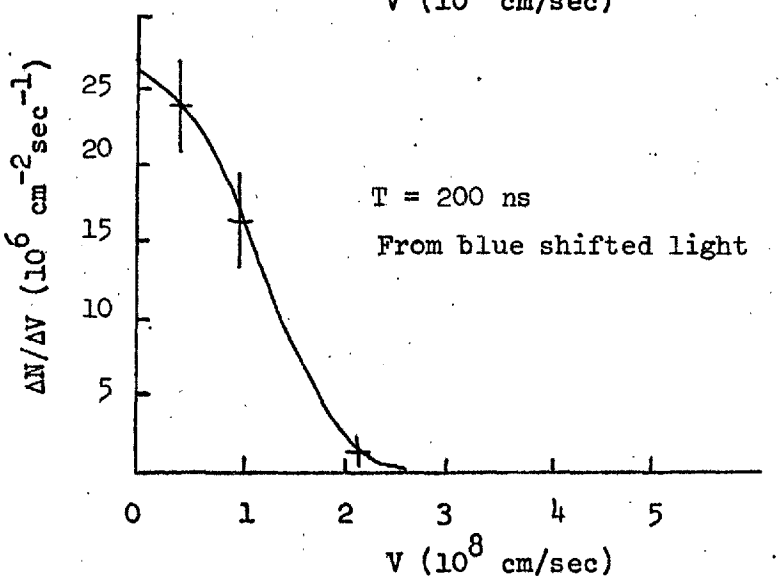

Figure 48c. Electron velocity distributions for injection into plasma at $n_e = 3 \times 10^{15}$ cm^{-3} and $T_e = 0.6$ eV with P = 0.2 Torr (Case III).

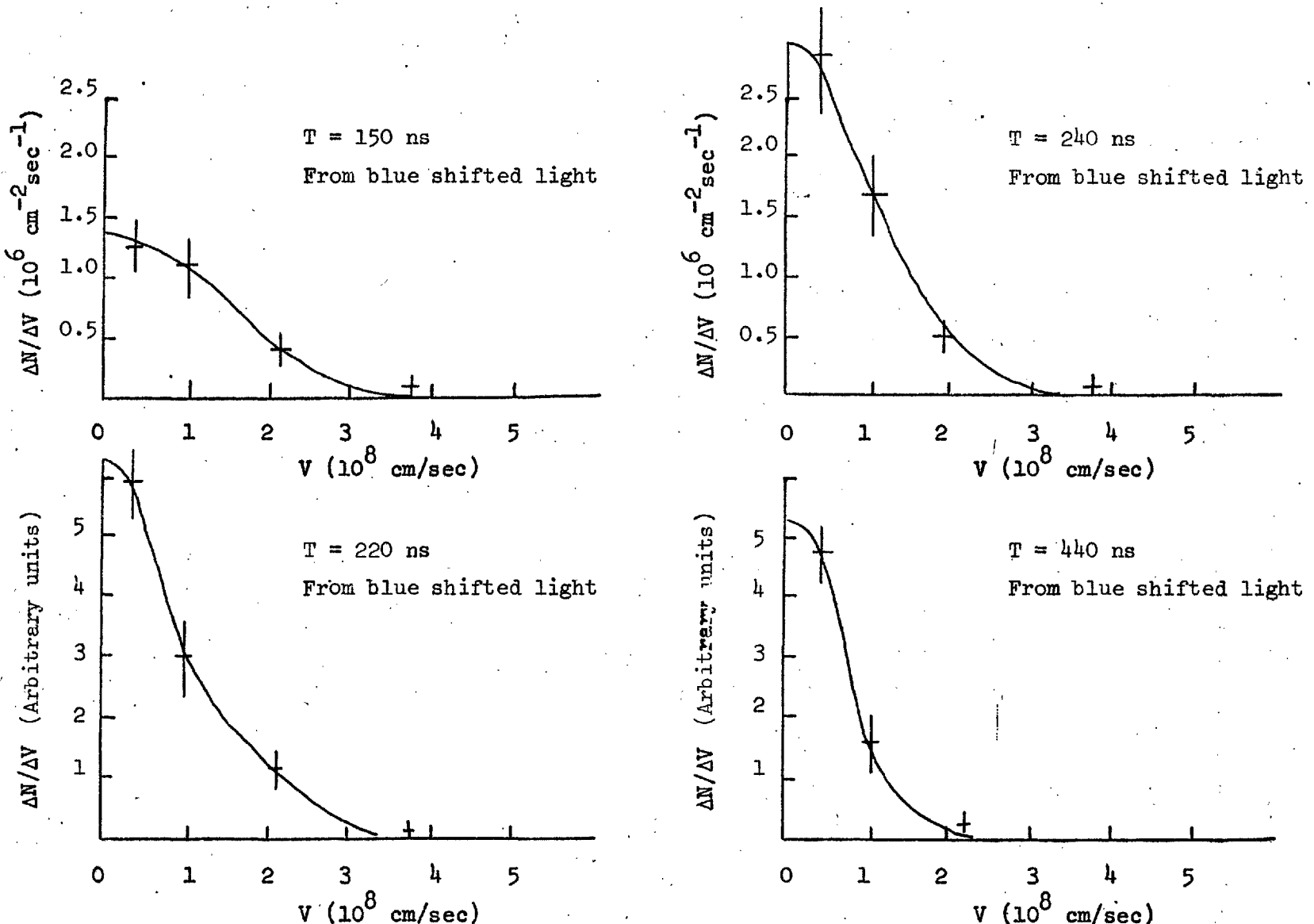

Figure 48d. Electron velocity distributions for injection into a plasma with $n_e = 5 \times 10^{13}$ cm^{-3} and $T_e = 3$ eV with P = 10 mTorr (Case IV).

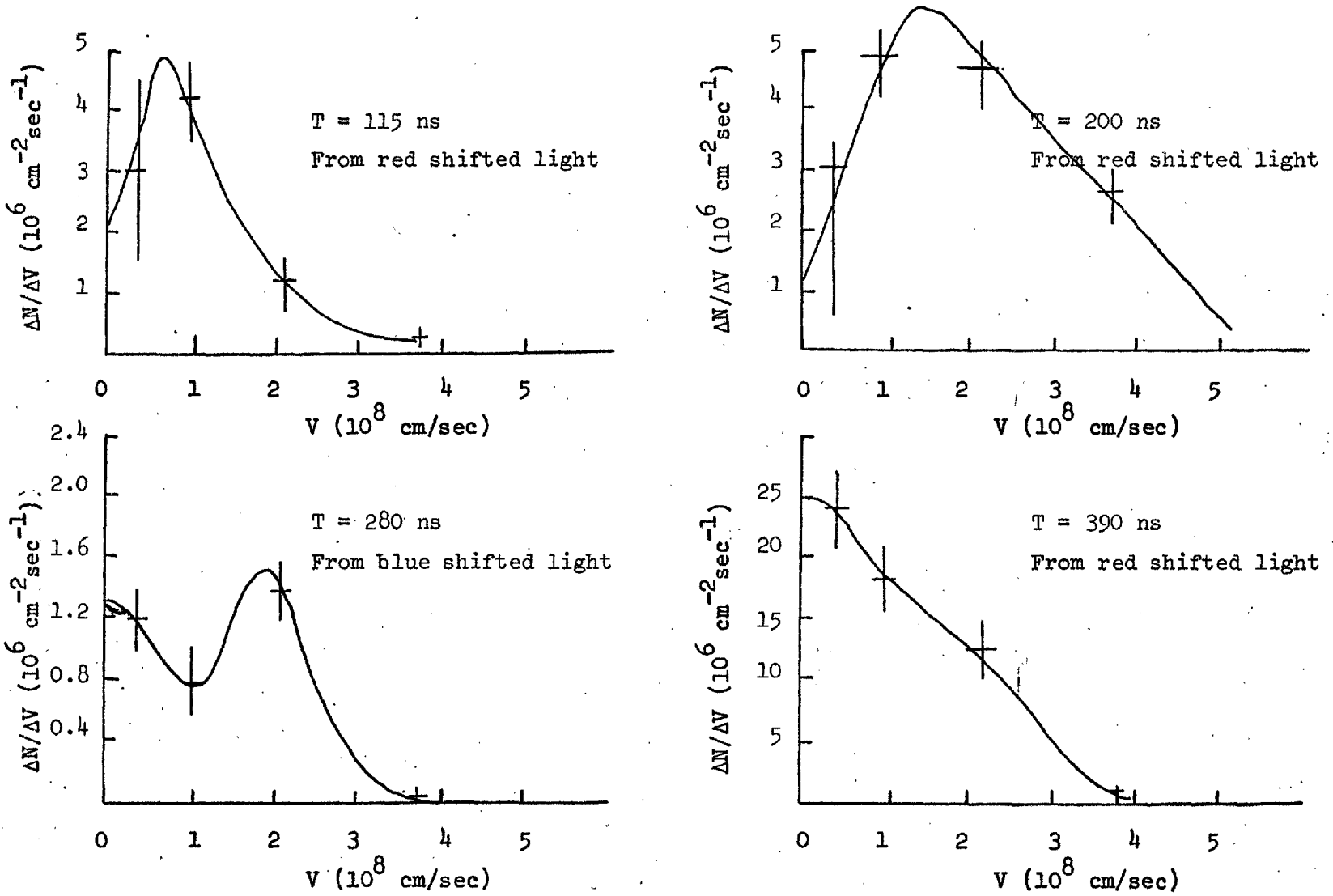

Figure 48e. Electron velocity distributions for injection into 60 mTorr neutral hydrogen. (Case V).

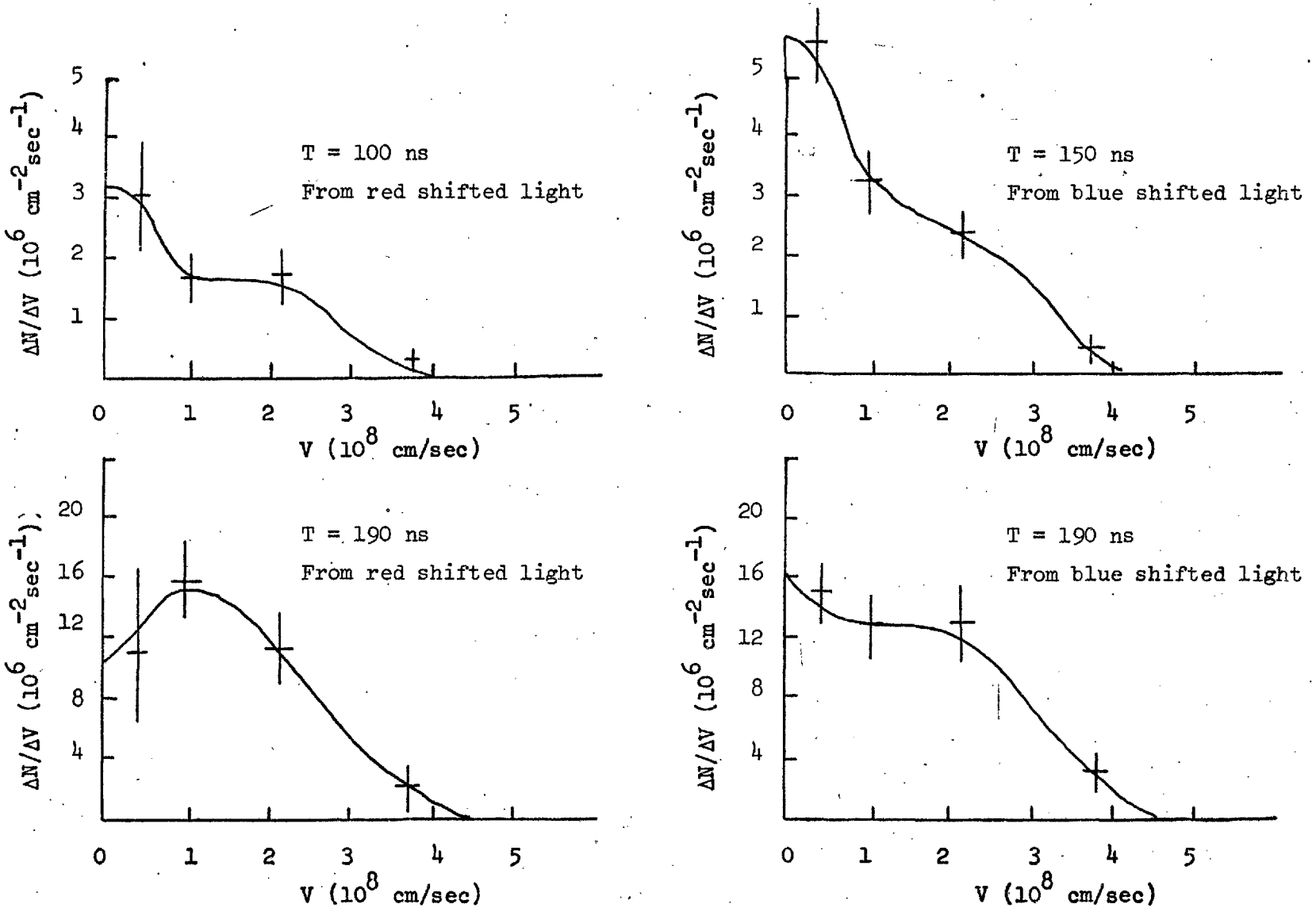

Figure 48f. Electron velocity distributions for injection into 100 mTorr neutral hydrogen (Case VI).

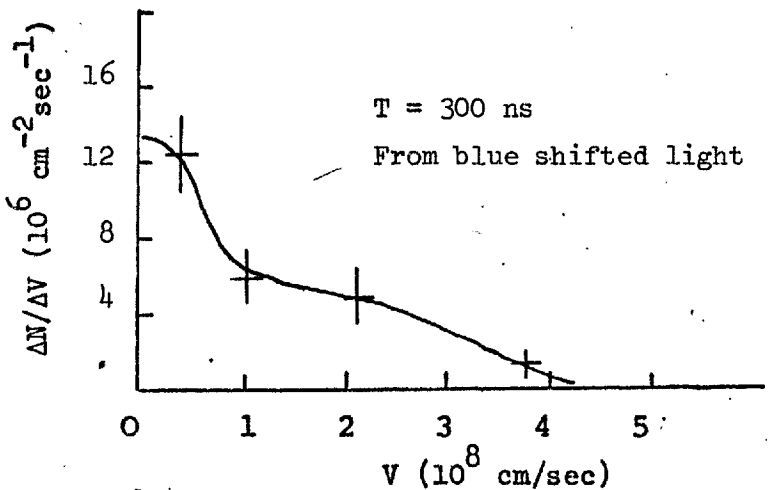

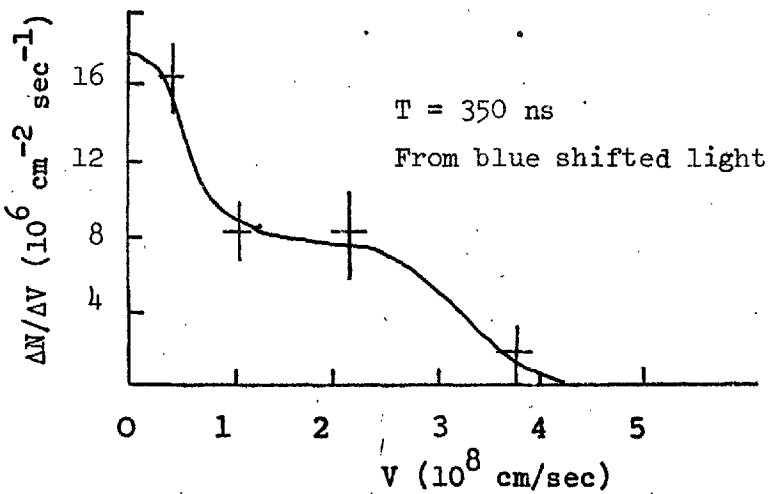

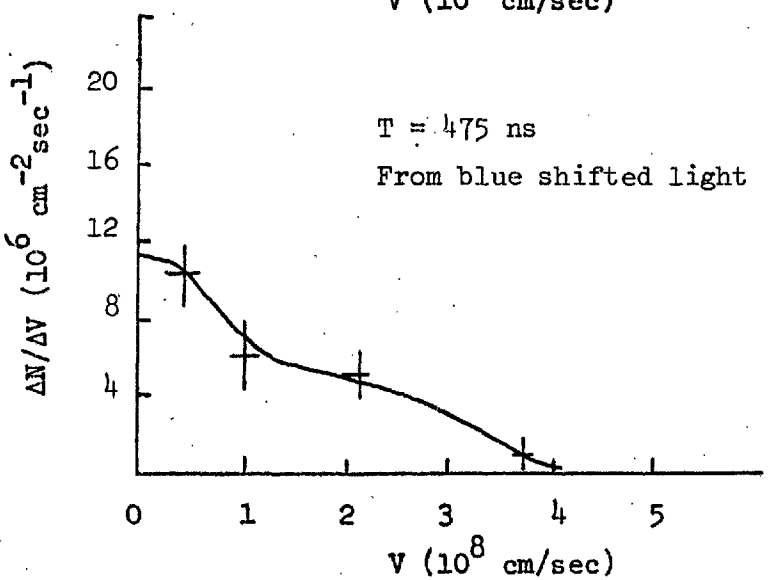

Figure 48g. Electron velocity distributions for injection into 100 mTorr neutral hydrogen (Case VI, cont.).

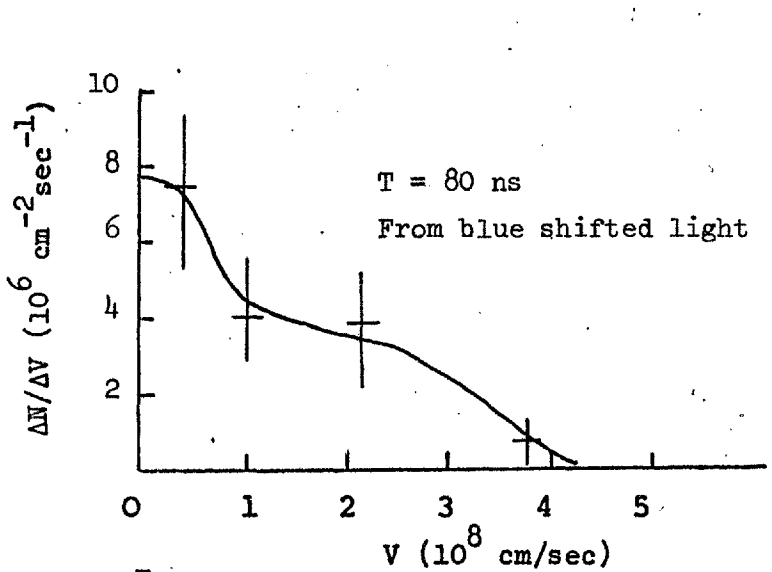

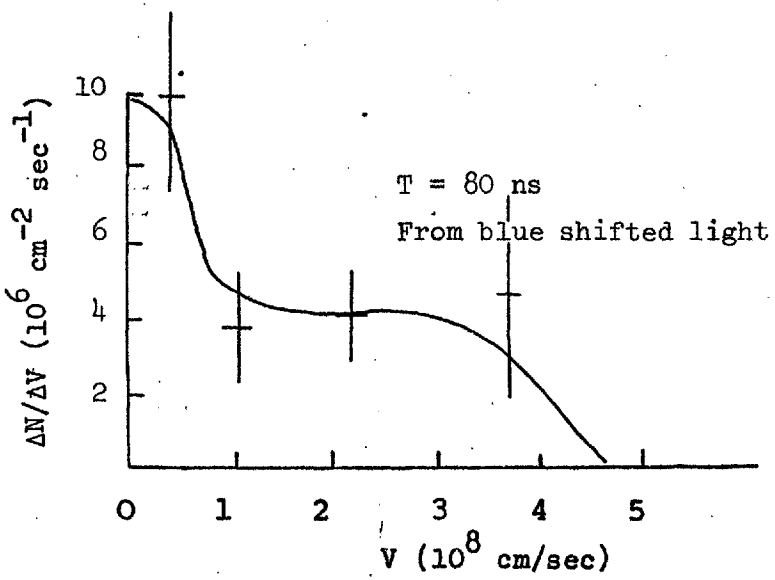

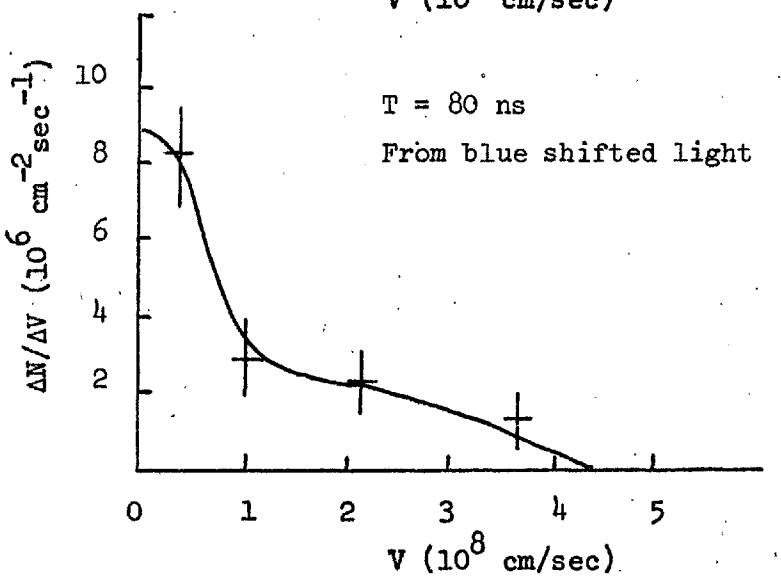

Figure 48h. Electron velocity distributions for injection into 1 Torr neutral hydrogen (Case VII).

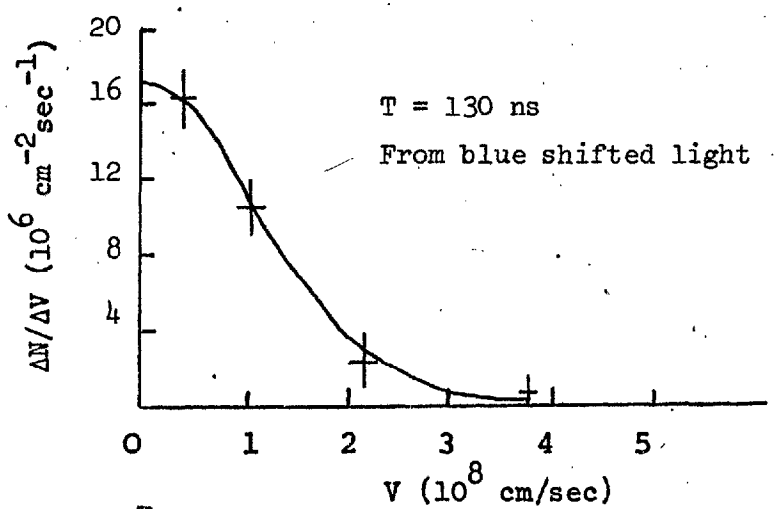

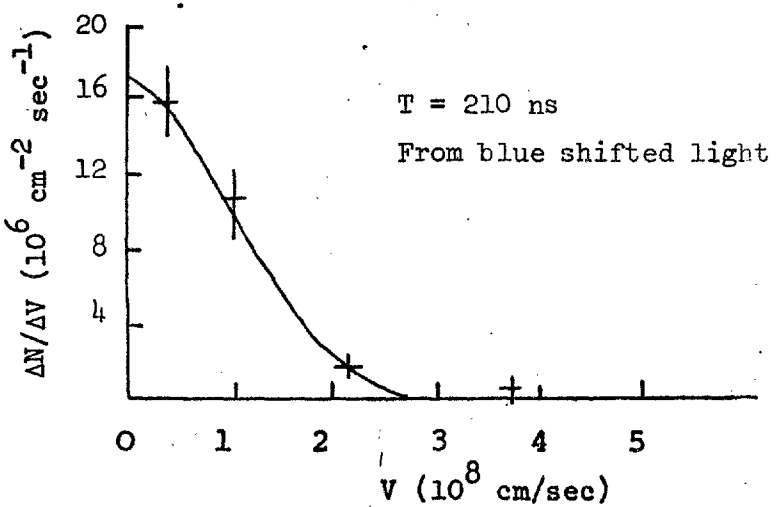

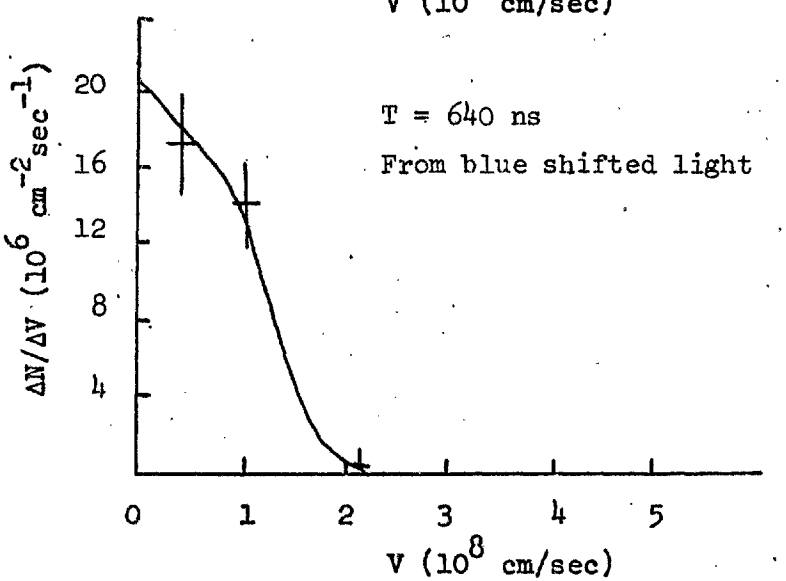

Figure 48i. Electron velocity distributions for injection into 1 Torr neutral hydrogen (Case VII, cont.).

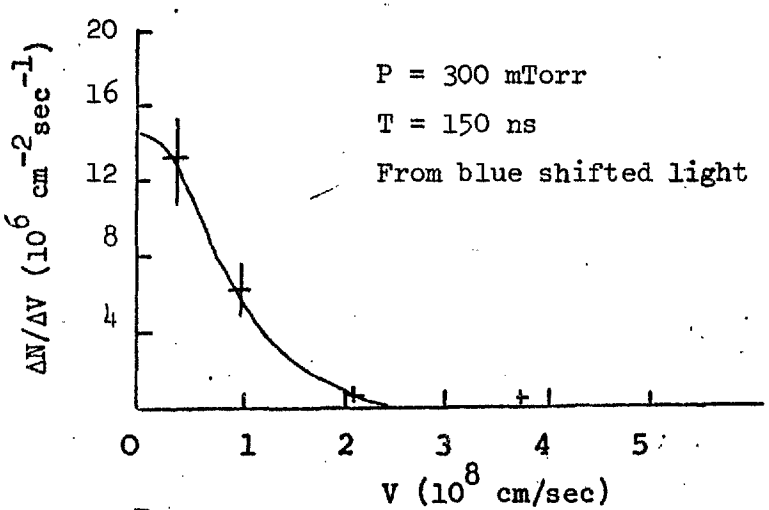

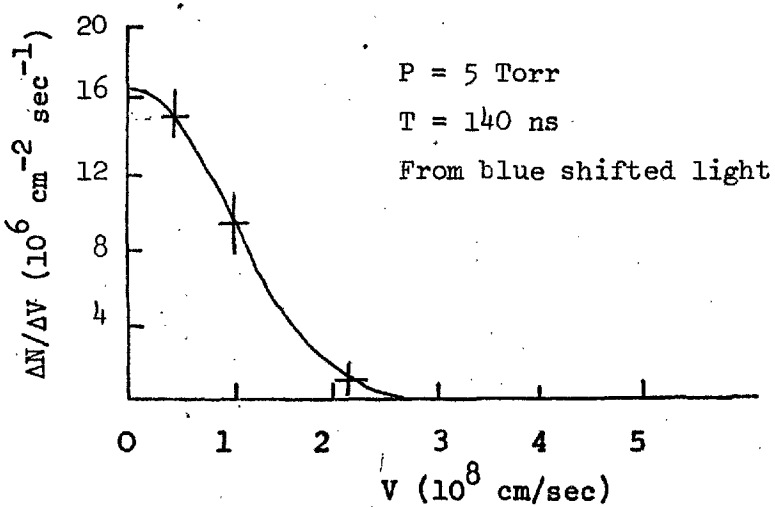

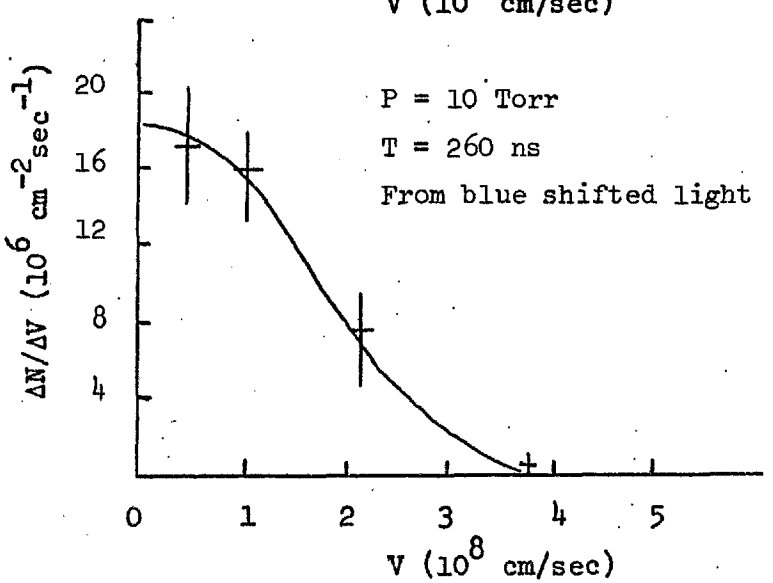

Figure 48j. Electron velocity distributions for injection into 0.3 Torr, 5.0 Torr, and 10.0 Torr neutral hydrogen.

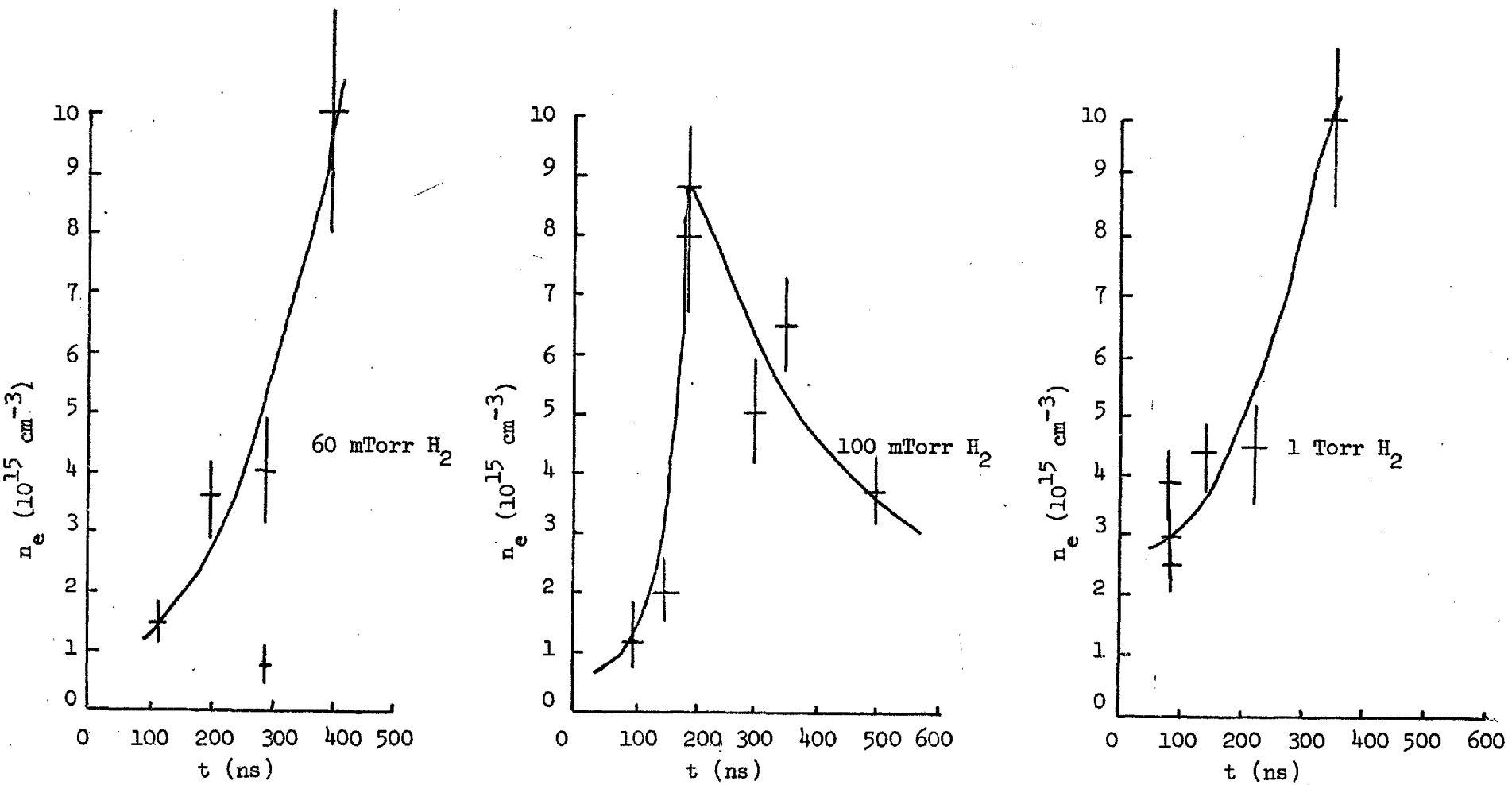

Figure 49. Time histories of the electron number density for injection into neutral hydrogen at 60 mTorr, 100 mTorr, and 1 Torr.

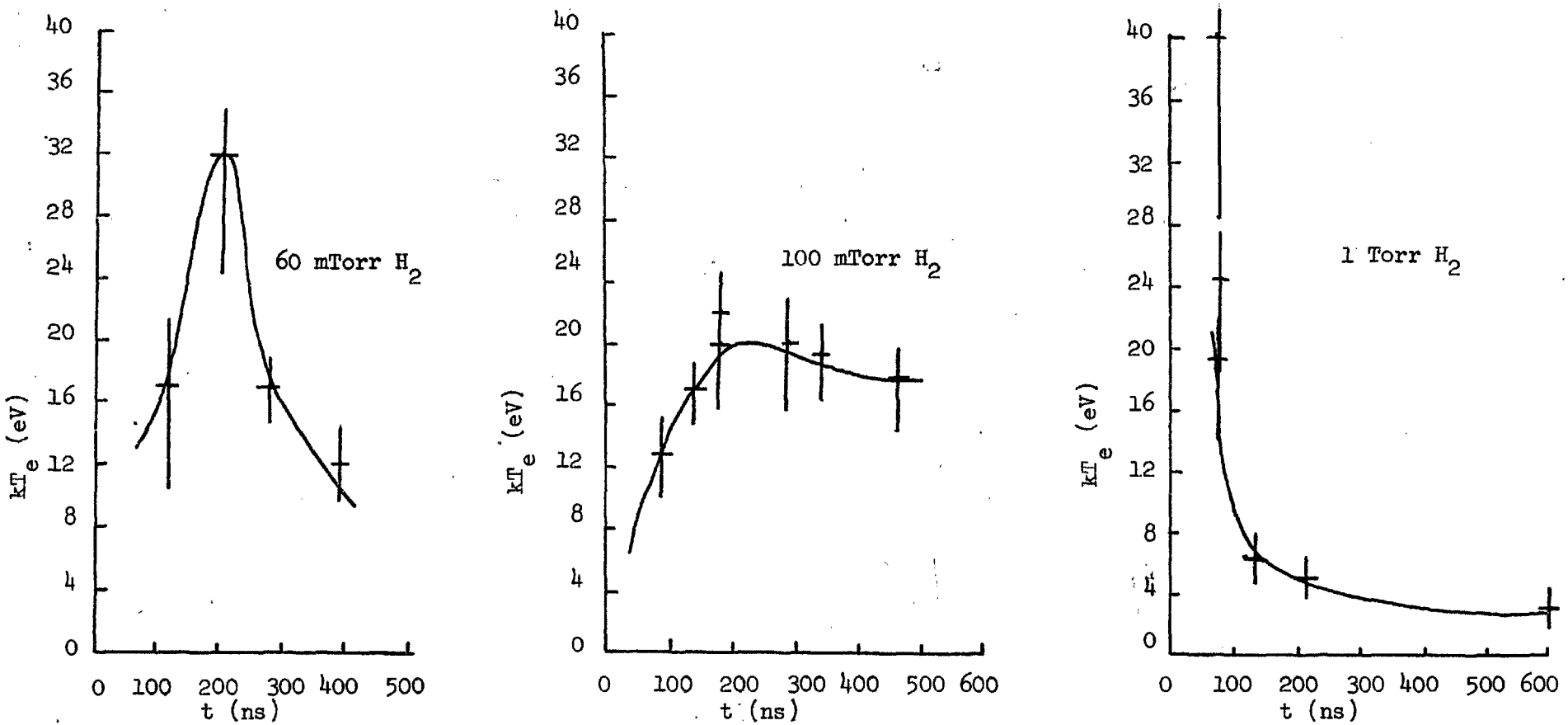

Figure 50. Time histories of the average electron energy kT_e for injection into neutral hydrogen at 60 mTorr, 100 mTorr, and 1 Torr.

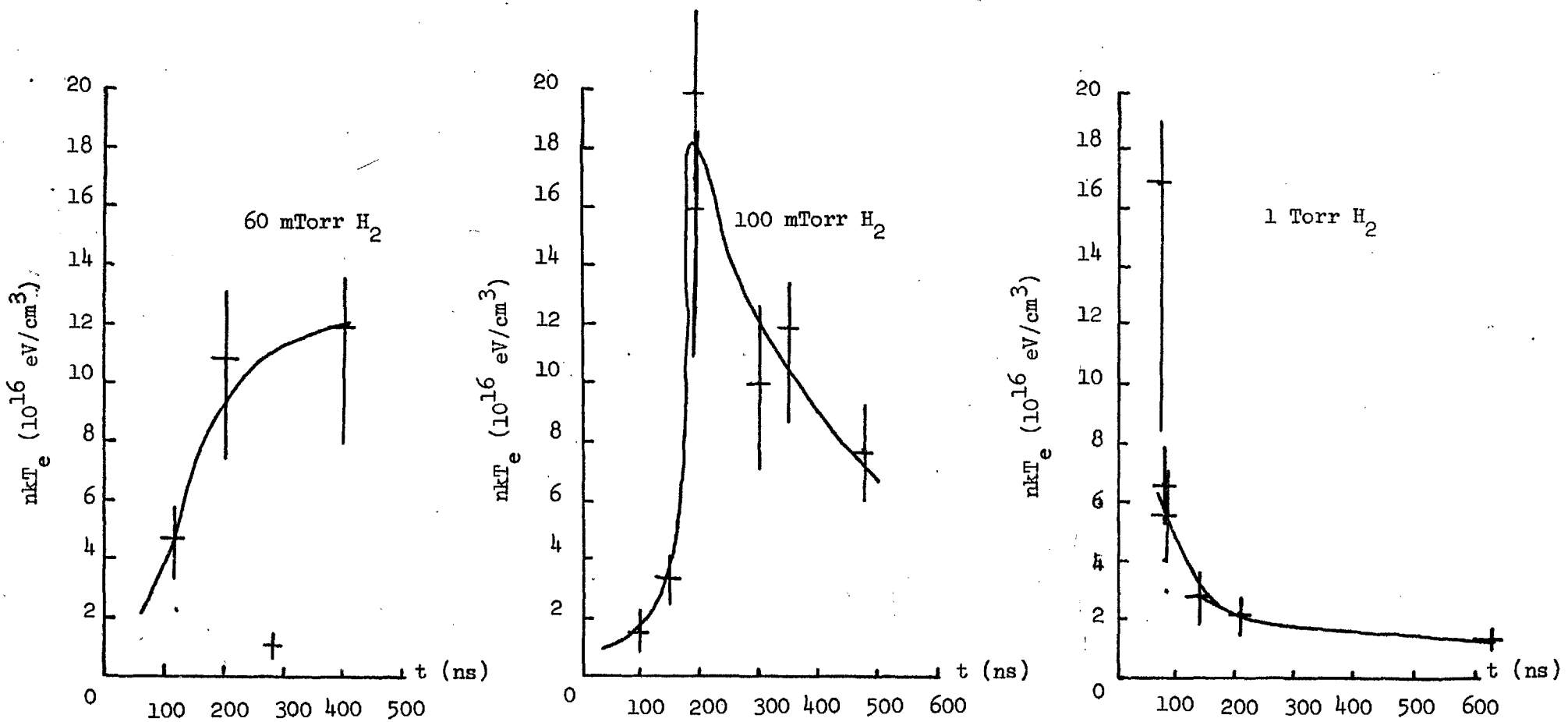

Figure 51. Time histories of the electron energy density nkT_e for injection into neutral hydrogen at 60 mTorr, 100 mTorr, and 1 Torr.

Table 5. Summary of the electron number density, average electron energy and electron energy density for injection of the beam into a preformed plasma.

Case No.	Time (ns)	Number Density (10^{15} cm^{-3})	Average Electron Energy (eV)	Electron Energy Density (10^{16} eV cm^{-3})
I	88	4.0±20%	$35.^{+30\%}_{-100\%}$	$14.^{+30\%}_{-100\%}$
	175	3.5±20%	5.2±30%	1.8±30%
	290	2.4±20%	8.0±30%	1.9±30%
II	100	1.2±20%	20.±40%	2.4±40%
	160	1.8±20%	28.±30%	5.0±30%
	400	2.9±20%	5.9±30%	1.7±30%
	520	2.4±20%	8.4±20%	2.0±20%
III	20	3.7±30%	$4.9^{+30\%}_{-100\%}$	$18.^{+30\%}_{-100\%}$
	100	1.2±20%	10.±20%	1.2±20%
	200	4.2±20%	5.7±20%	2.4±20%
IV	150	0.44±20%	14.±20%	0.6±20%
	240	0.54±20%	11.5±20%	0.6±20%
	220	---	11.±20%	---
	440	---	2.±30%	---

4.9 Plasma Light Measurements

4.9a Introduction

Since the plasma light limited the use of laser scattering in the beam, understanding the source of this light is important. Analysis of the plasma light also assists (1) in interpreting the streak photographs, and (2) in identifying the ion species in the plasma.

The collecting system for laser scattering and the background-light dump described in Section 4.8 allowed the continuum emission from the plasma to be measured. Since the system was calibrated absolutely for the laser scattering measurements, the absolute values for the light emission from the plasma were measured.

4.9b Analysis of the Level of Plasma Light

If the plasma light were from free-free bremsstrahlung, and if the theory of fluctuations were valid for the scattered light intensity, the ratio of scattered light to plasma light would be

$$\frac{I_s}{I_p} = 4.1 \times 10^{13} I_o(\lambda/n_e \sin(\theta/2)) \frac{V_s}{V_p}$$

for low alpha (free electron) scattering [Evans and Katzenstein (1969)]. In this expression, I_o = laser power in watts/cm^2, θ = scattering angle, n_e = electron number density in cm^{-3}, λ = wavelength in cm, and V_s/V_p is the ratio of the scattering volume to the emitting volume. For this experiment, $I_s/I_p \simeq 700$. However, the observed value was approximately 1 during the beam. This excessive plasma light limited the number densities that could be investigated.

The spectral distribution of the continuum from 6943 A^o to 6807 A^o for one case is given in Figure 52. The spectrum was

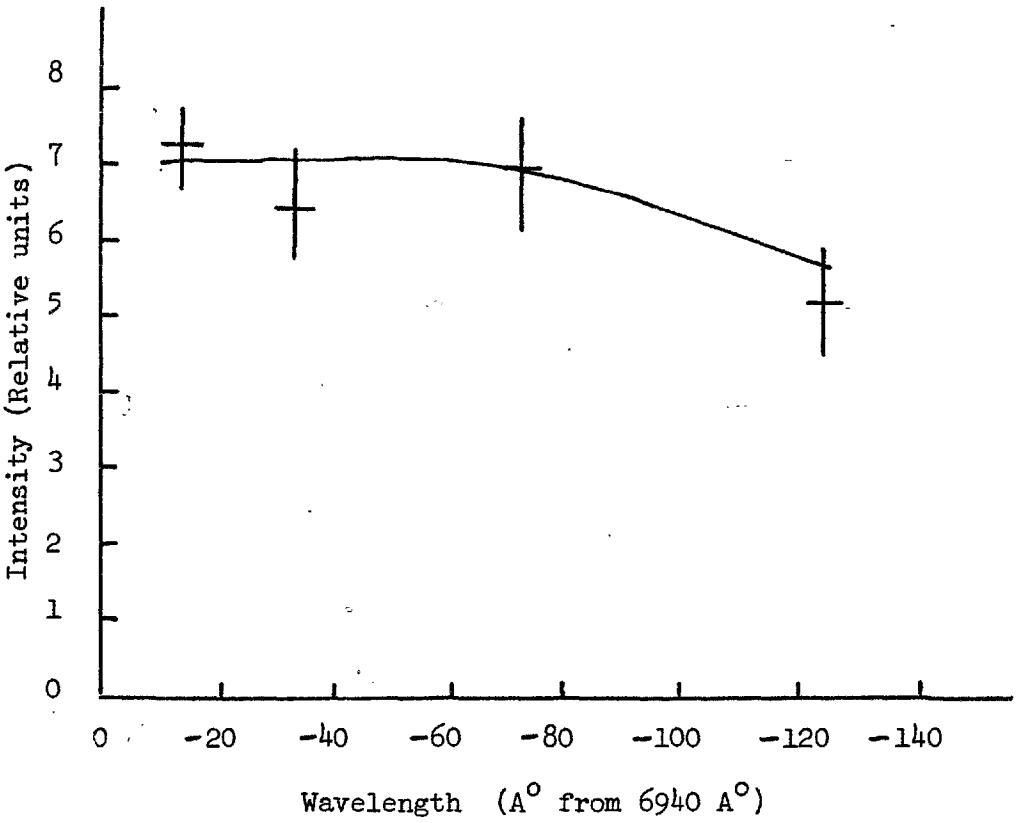

Figure 52. Spectral distribution of the plasma light between 6940 and 6790 A°. The beam was injected into 2 mTorr neutral hydrogen, and the peak of the light emission was recorded.

reasonably flat from 6800 A° to 7080 A°, i.e. over the bandwidth covered by the laser scattering measurements. Consequently, the emission was broad band.

Waveforms of the plasma emission for several experimental conditions are given in Figure 53. The rapid increase in the plasma light (following a time delay after the beam that decreased with increasing pressure) is shown for the 1 Torr and 10 Torr cases. This delayed increase is characteristic of the pumping of excited molecules by collisional excitation or of dissociative recombination often observed in molecular gases. The excited molecule undergoes radiative decay and emits light at wavelengths determined by the energy gap between the initial and final states at the given inter-nuclear separation. The bandwidth of the observed continuum was 1.74 eV to 1.8 eV and appeared to fall off slowly toward the blue. Figure 54 gives the energy level diagram for molecular H_2 from Massey (1969) and transitions between State VI, i.e. H_2^+, and excited levels of IV, III, and II would account for the light emission. The pumping and decay scheme necessary to give the emission has not been worked out, but it is believed to explain the origin of the delayed pulse and the initial broad band emission during the beam.

A similar phenomenon was reported by Hinnov and Hirschberg (1962) in the afterglow of a hydrogen plasma in the B-1 Stellarator. They observed a P^{-1} dependence in the delay between the excitation and the peak afterglow emission. They also observed an increase in the emission as the pressure was increased. They tentatively attributed the behaviour to dissociative recombination of residual H_2^+ ions. However, O'Malley (1969) noted in his paper on the theory of dissociative recombination that H_2^+ has no dissociative state crossing the H_2^+

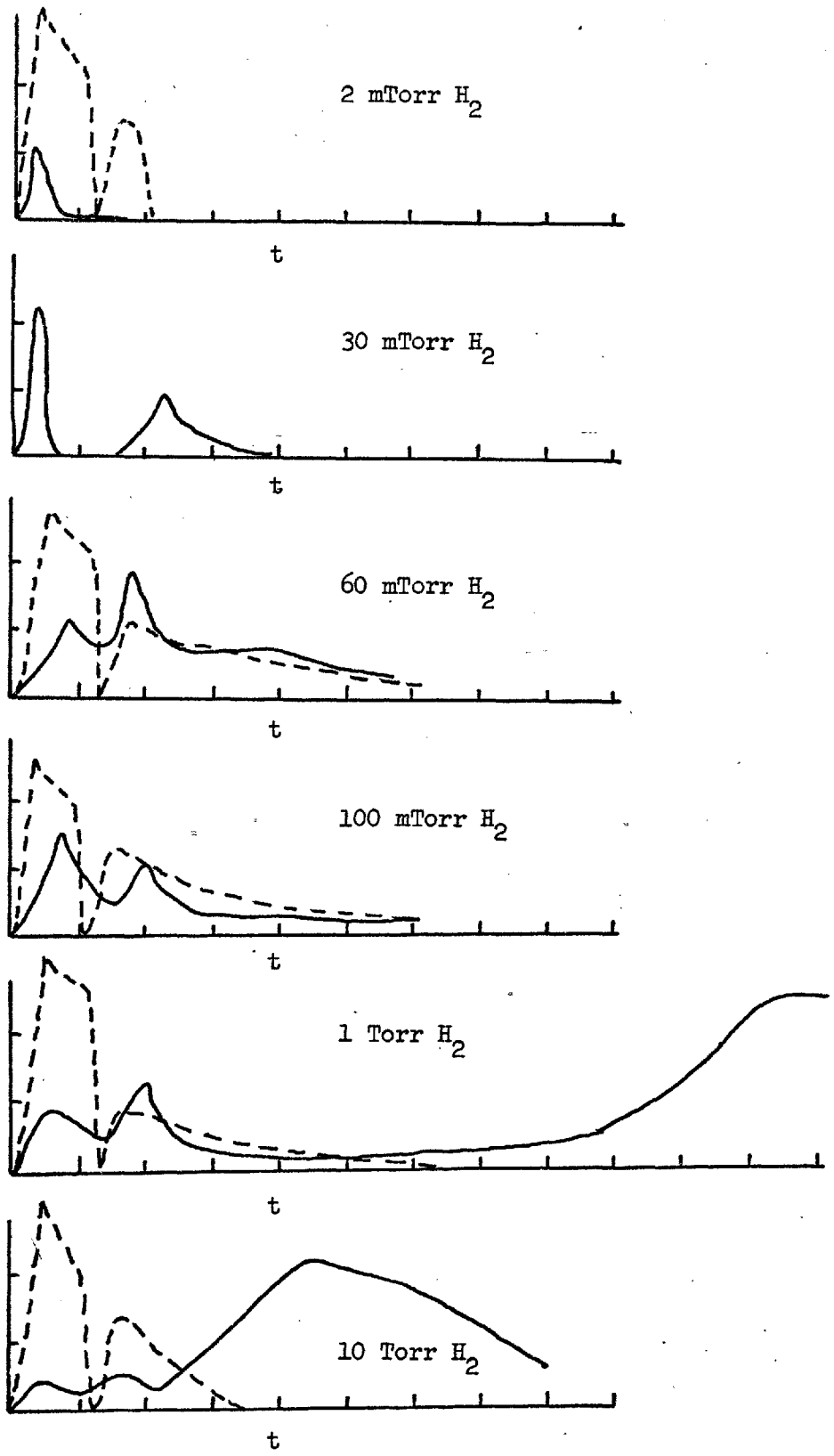

Figure 53. Time histories of the plasma light near 6940 A° as a function of the initial pressure of hydrogen. The solid line gives the plasma light emission in arbitrary units. The broken line gives the plasma current waveform for comparison, with one division equal to 10 kA. The time scale is 100 ns per division.

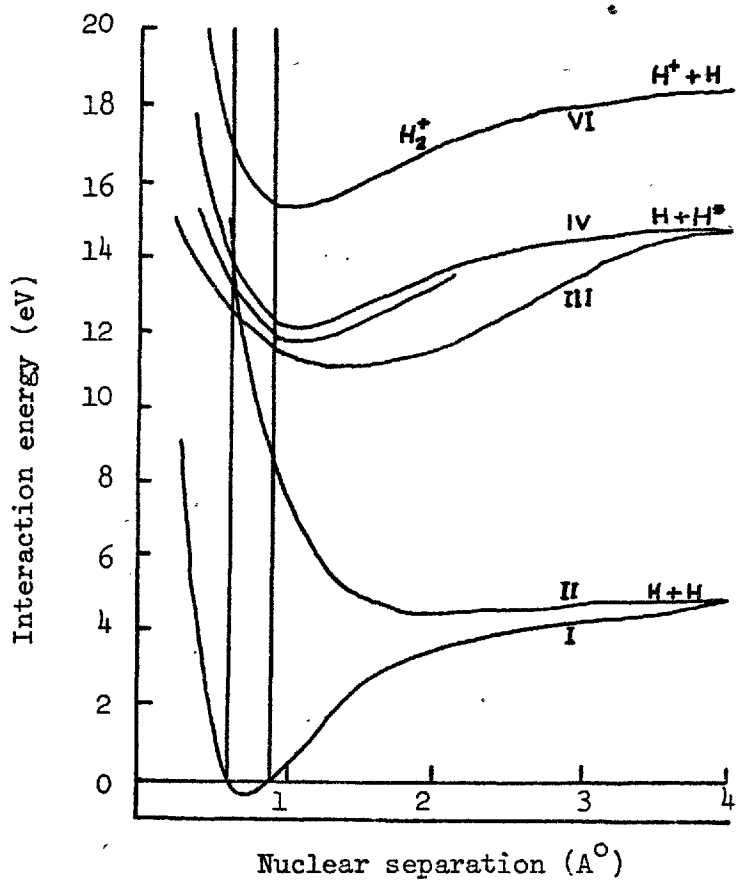

Figure 54. Energy level diagram for the H_2 molecule. Transitions between VI and the excited levels of IV and III would produce emission in the observed bandwidth of plasma light.

potential curve in the Frank-Condon region, so dissociative recombination of H_2^+ is not expected. Consequently, the excessive emission is probably from the decay of excited vibrational states.

4.9c Correlation of the Plasma Luminosity with the Plasma Current

The absolute value of the plasma current (derived from I_b minus I_{net}) are also shown in Figure 53 with the waveforms of the luminosity. Above 60 mTorr initial pressure the intensity of the light emitted during the beam followed some monotonic function of the plasma current. Below that pressure, the light increased and then quickly decreased during the beam, although the plasma current remained high.

CHAPTER 5

UNUSUAL FEATURES OF THE EXPERIMENTAL RESULTS

5.1 Introduction

Under some experimental conditions, several unexpected features of the data became apparent:

(1) The charge neutralization time was much less than the theory in Section 2.2 predicted.

(2) The electron distribution functions were non-Maxwellian.

(3) The net current increased during the beam at a rate greater than that predicted by theory.

(4) The net current increased after the beam had ended.

(5) The ion motion was significant during the beam.

These observations are discussed in this chapter.

5.2 Charge Neutralization

Any interpretation of the results of the present experiment relies on a model of the beam-plasma system. The accepted model was developed and substantiated for beams of considerably lower current densities and may not be appropriate to the beam-plasma system in the present experiment.

The model presented in Section 2.2 describes (1) the time required for charge neutralization t_{cn} from ionization by beam electrons, (2) the time t_f required for force neutralization of the beam

electrons, and (3) the time t_{bd} required for the breakdown of the neutral gas. The model specifies that $t_f < t_{cn} < t_{bd}$ for injection of the beam into neutral gas. The times t_f, t_{cn}, t_{bd} were inferred from the calorimeter measurements, the electrostatic energy analyzer measurements, and the net current measurements, respectively.

The comparison of the calorimeter data with that predicted from t_f was described in Section 4.5. The results are reproduced in Figure 55 for convenience. The calorimeter data for the energy transmission to the end of the scattering chamber agreed quite well with that expected from the calculated value of t_f for pressures above 20 mTorr hydrogen in support of the theory. The agreement was surprising because of the assumption of radial beam equilibrium for $t < t_f$, i.e., the beam electrons were assumed to travel down the drift tube for $t < t_f$ in spite of the strong radial force to expel them to the wall. At very low pressures, the energy transferred was significantly higher than was predicted with the model.

The charge neutralization time t_{cn} was measured for a much smaller diameter tube with the electrostatic energy analyzer. The results were described in Section 4.6 and were reproduced in Figure 55 in tabular form for convenience. The theoretical values of t_{cn} were calculated from Equation (2-4) with $\beta = 0.8$ and are shown with the experimental values for comparison. The measured charge neutralization times for the 40 and 10 mTorr cases were significantly less than that predicted by the theory.

The information needed to find t_{bd} from the calculated electric field E and the filling pressure P was not available for hydrogen at the values of E/p required in the present experiment. Nevertheless, t_{bd} must be greater than t_{cn}, and these two quantities were compared.

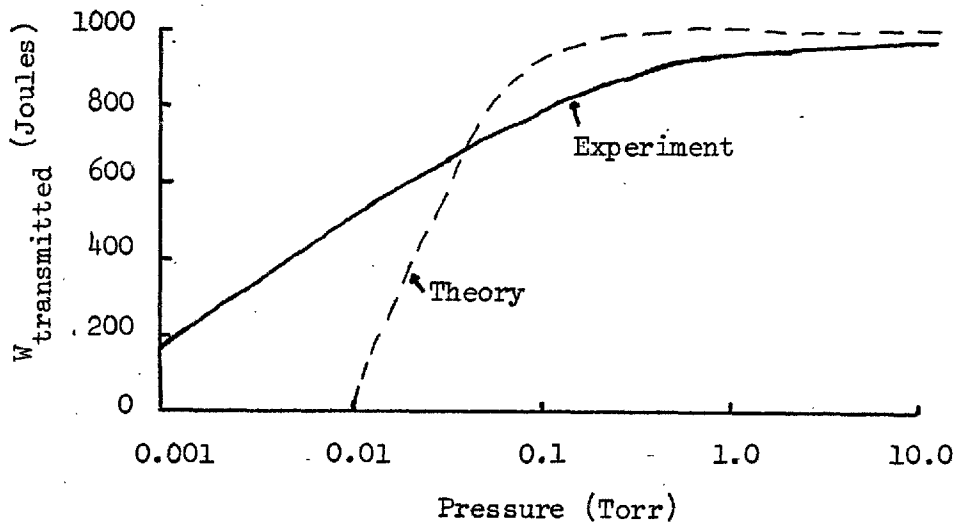

a) Comparison of calorimetry data (solid line) with that expected from t_f calculated from the model in Section 2.2.

Pressure (Torr)	t_{cn}(calc.) (ns)	t_{cn}(exp.) (ns)
1	<6	<3
0.04	90	35±5
0.01	>>100	>100

b) Comparison of t_{cn} from theory with t_{cn} inferred from the measurements with the electrostatic energy analyzer

Pressure (Torr)	I_{net} (10^3 amps)	t_{bd} (ns)	t_{cn}(calc.) (ns)
1	<3	<3	<6
0.1	<3	<3	45
0.06	5.7	4.8	65

c) Comparison of $t_{bd} = I_{net} t_r / I_b$ at t=30 ns with the calculated charge neutralization time t_{cn}

Figure 55. Comparison of the experimental and theoretical quantities relevant to the ionization of the background gas by the beam electrons.

From the discussion of the breakdown process in the formation of the net current in Section 2.2, the breakdown time was given by

$$t_{bd} = \frac{I_{net} \times t_r}{I_{beam\ max}} \qquad \text{for } t_{bd} < t_r, \tag{5-1}$$

for a beam with a rise time t_r. From the data for I_{net} given in Section 4.7, the time t_{bd} was calculated and listed in Figure 55. Comparison of the t_{bd} (experimental) and t_{cn} (theory) shows that t_{bd} (experimental) $< t_{cn}$(theory), which is less than t_{bd}(theory).

Consequently, the charge neutralization occurred more rapidly than the simple theory predicted. The source of the ionization process has not been identified.

5.3 Non-Maxwellian Velocity Distribution of the Plasma Electrons

The origin of the bump (or dip) in an otherwise Maxwellian velocity distribution was intially thought to be instrumental. However, checks on the linearity and cross-calibration of the photomultipliers failed to show any irregularities in the system. The bump was not always on the same channel, and the distribution relaxed to a Maxwellian when the plasma current decayed. The non-Maxwellian feature was qualitatively correlated with the presence of large net currents and large plasma currents and was more prominent when the plasma number density was low.

The distributions were approximately symmetric about the axis after the beam except for the injection into 60 mTorr neutral hydrogen, where the spectral distribution of the scattered light was shifted to the red.

These features were qualitatively consistent with a large azimuthal electron drift velocity. The program "SPECT" was written to calculate the spectral distribution of laser light that was scattered from a plasma with a constant uniform electron angular velocity (i.e. the rigid rotor model). The axis of the rigid rotor electron distribution was displaced from the center of the scattering volume by a distance 1, as shown in Figure 56. The scattering volume was divided into 1000 equal segments, and the velocity $\hat{k}_s \cdot \underline{V}_\theta = \omega r \hat{k}_s \cdot \hat{\theta}$ was calculated for the electrons at the center of each segment. The resulting distributions for $\hat{k}_s \cdot \underline{V}_\theta$ are shown in Figure 56. For $1 \approx 4$ mm, the distribution resembles that observed at 60 mTorr hydrogen with an electron drift in the minus $\hat{\theta}$ direction. Such a drift would produce an axial magnetic field in the + z direction. The apparent shift in the spectrum at t = 115 ns for injection into 60 mTorr neutral hydrogen corresponds to a velocity of approximately 10^6 m/sec. The distance 1 was measured as 3×10^{-3} m, as discussed in Section 4.3, so the angular velocity would have been 3×10^8 rad/sec. For a plasma with $n_e = 10^{21}$ m^{-3} and with a constant electron angular velocity of $\omega = 3 \times 10^8$ rad/sec to a radius $r_o = 0.02$ m, the axial magnetic field on axis is given by Ampere's Law as

$$B_z(0) - B_z(r_o) = -\mu_o \int_0^{r_o} j_\theta dr = \mu_o n_e e \omega \int_0^{r_o} r \, dr$$

$$= \mu_o n_e e \omega \, r_o^2 / 2$$

$$= 0.12 \text{ Tesla}$$

which is equal to the maximum azimuthal magnetic field B_θ calculated from $I_{net} = 12$ kA at t = 100 ns for $r_o = 0.02$ m (the conditions appropriate for injection into 60 mTorr neutral hydrogen). The origin of such an azimuthal electron drift and the associated magnetic field is not apparent.

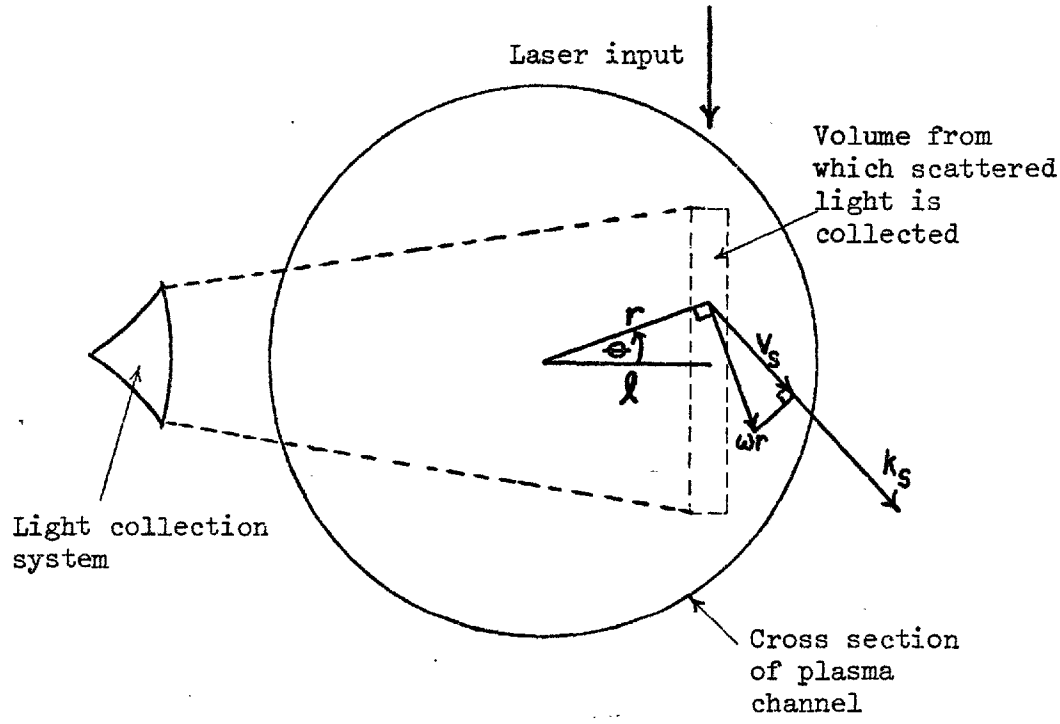

The component of the azimuthal electron velocity ωr along the scattering vector k_s is given by

$$V_s = \frac{\omega}{\sqrt{2}}(r\cdot\cos(\theta) + r\cdot\sin(\theta))$$

for an electron at (r,θ).

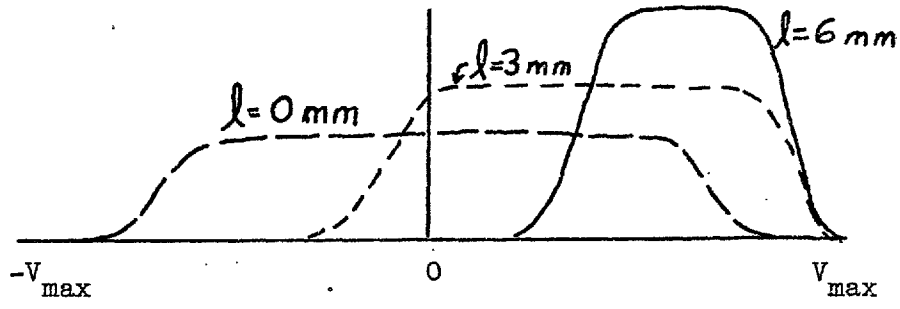

Figure 56. Calculated velocity distributions along the scattering vector as a function of the distance ℓ between the center of the plasma channel and the center of the scattering volume. The electron density is assumed to be uniform, and the angular velocity ω of the plasma electrons is also assumed to be uniform. The scattering volume was divided into 1000 square segments, and the component of the azimuthal velocity along the scattering vector was calculated for each segment. The distribution of the resulting velocity V_s is shown in the lower drawing for three values of ℓ .

If the electron thermal velocity were large compared to this drift velocity, the non-Maxwellian feature would be obscured. Thus, the presence of the feature at 60 and 100 mTorr indicates that nkT_{eff} defined by Equation (4-5) was greater than the actual value of the electron "thermal" energy density. The shift in the spectrum at 60 mTorr indicates that the electron number density at 60 mTorr as defined by Equation (4-4) was approximately twice the actual value of n_e. However, since the experiments with initially neutral hydrogen cannot be used to analyze the plasma heating process (the energy loss rate from vibrational excitation of the neutrals was too great in those experiments, as discussed in Section 7.6), the correction to nkT_{eff} does not interfere with the analysis of plasma heating via the streaming instabilities.

5.4 The Rise of the Net Current during the Beam

The model states that the decay of the plasma current and the rise of the net current are governed by the L/R decay of the plasma current during the beam. This feature of the model can be tested from the data for t_{decay} (as defined in Section 2.2c) of the plasma current presented in Figure 57. The inductance L of the net current channel (which was assumed to be uniform) of radius r_o = the beam radius and length l is given by

$$L = \frac{l\mu_o}{2\pi}\left(\frac{1}{4} + \ln(r_w/r_o)\right) \quad \text{Henries} \qquad (5\text{-}2)$$

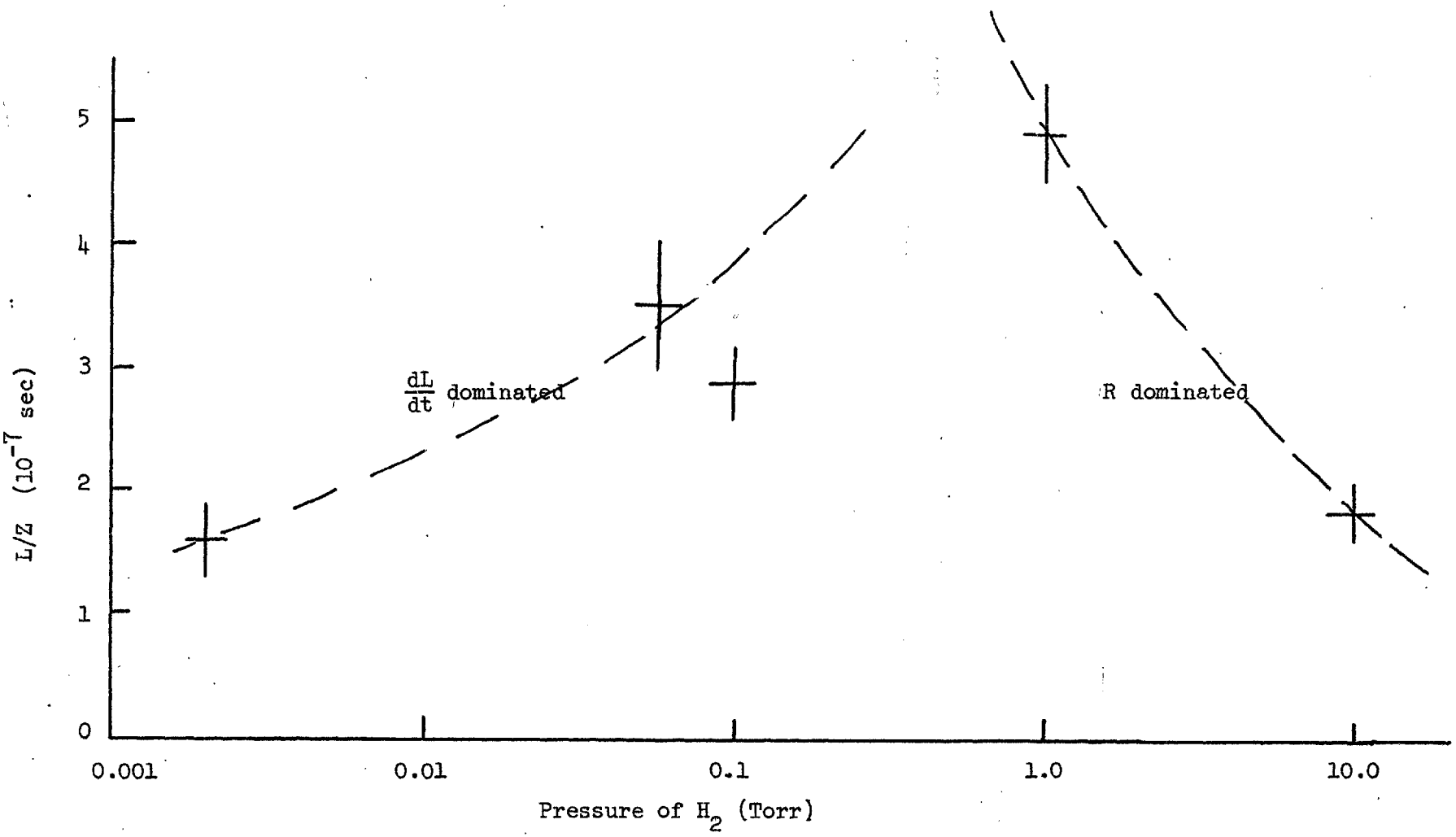

Figure 57. Apparent L/Z decay times of the plasma current from the rise of the net current for injection into neutral hydrogen. At high pressures the resistive term dominates Z. At low pressures the dL/dt term dominates.

and the resistance R of the plasma current channel is given by

$$R = \frac{\eta l}{\pi r_o^2} = L / t_{decay} \qquad \text{ohms} \qquad (5\text{-}3)$$

where η is the resistivity of the plasma. As discussed in Section 2.2, the value of η inferred with such an analysis have been compared to the Spitzer value (presumably for a strong magnetic field) given by Spitzer (1962) for hydrogen as

$$\eta_{Spitzer} = \frac{1.75 \times 10^{-3}}{T_e^{3/2}(eV)} \qquad \text{ohm-m} \qquad (5\text{-}4)$$

for $\ln\Lambda = 10$. The electron temperature kT_e and the dimensionless parameter $\omega_{ce}\tau$ (where ω_{ce} is the electron cyclotron frequency and τ is the electron collision time for momentum transfer) were inferred from

$$\eta = \eta_{Spitzer}$$

$$kT_e = \left(\frac{1.75 \times 10^{-3}}{\eta}\right)^{2/3} \qquad eV$$

$$\omega_{ce} = \frac{eB}{m_e}$$

$$B = \frac{\mu_o I_{net}}{2\pi r_o}$$

$$\tau = \frac{m_e}{\eta n_e e^2}$$

Usually, the plasma electron number density was estimated from α, the first Townsend co-efficient for the E and P (electric field and pressure) of the experiment. Since the coefficient α is not known for the values of E/P in the present experiment, n_e was taken from the laser scattering data at t = 100 ns, given in Section 4.8.

For the beam radius $r_o = 0.008$ m, the wall radius $r_w = 0.04$ m, and the channel length $l = 0.11$ m, the inductance is given by

Equation (5-2) as $L = 4 \times 10^{-8}$ H. The values of R, kT_e, n_e, and $\omega_{ce}\tau$ are given in Table 6 for injection into neutral hydrogen at P = 1 Torr, 100 mTorr, and 60 mTorr. The laser scattering measurement of kT_{eff} at 100 ns is given for comparison with kT_e. The value of τ can also be calculated (as τ') from the laser scattering data of n_e and kT_{eff} for electron-ion and electron-neutral collisions as discussed in Section (2-4):

$$\eta' = \eta_{ei} + \eta_{en} = \frac{1.75 \times 10^{-3}}{kT_{eff}^{3/2}} + \frac{6.6 \times 10^{-6}\, n_o}{n_e} \quad \text{ohms-m}$$

where kT_{eff} is in eV, n_o is the neutral number density and equals $3.54 \times 10^{22} \times P\ m^{-3}$ for the pressure P of neutrals in Torr. Consequently,

$$\tau' = \frac{m_e}{\eta' n_e e^2}$$

which is listed in Table 6 for comparison with τ.

The analysis of the net current waveform does not give the experimentally measured kT_e, and the $\omega_{ce}\tau'$ calculated from the data for n_e and kT_{eff} does not agree with $\omega_{ce}\tau$ calculated for the net current waveform. The calculated resistance from electron-ion and electron-neutral collisions is much less than the resistance inferred from the net current waveform during the beam.

Table 6. Analysis of the net-current waveforms for the plasma parameters

Pressure (Torr)	n_e ($10^{15}cm^{-3}$)	I_{net} (10^3amps)	Decay Time (10^{-7}s)	R (ohms)	kT_e (eV)	$\omega_{ce}\tau$	R' (ohms)	kT_{eff} (eV)	$\omega_{ce}\tau'$
0.06	1.4	10	3.5	0.11	4.0	6	0.02	16	30
0.10	1.2	12.5	3.	0.13	3.7	7	0.04	12	26
1.0	3.0	6.5	5.	0.08	5.0	2.3	0.06	20	3.5

5.5 Net Current Waveform after the Beam Pulse

The net current waveforms shown in Figure 43 showed that the net current increased after the beam pulse under some experimental conditions. If the inductance of the current channel remained constant or increased after the beam, the total energy W_{fT} in the magnetic field given by

$$W_{ft} = \tfrac{1}{2} L I_{net}^2$$

also increased. The image converter camera photographs in Figure 35 showed that the radius of the current channel decreased after the beam pulse for $120 < t < 200$ ns. The increase in the electron number density on axis (shown in Figure 49) also indicated that the radius of the plasma channel decreased after the beam. The inductance of the current channel given by Equation (5-2) shows that the inductance increases as the radius of the plasma channel decreases, so the energy in the magnetic field must have increased after the beam. Since the experimental chamber was isolated from the rest of the universe after the beam pulse, there must have been a source of energy in the plasma that was converted to magnetic field energy after the beam pulse. Alternatively, the inductance of the plasma current channel actually decreased after the beam, in apparent conflict with the simple interpretation of the streak photographs.

5.6 Plasma Motion

The accepted model assumes that the ions do not move during the beam pulse. However, streak photographs in Figure 35 showed that

the plasma current channel did expand during the beam pulse for the injection of the beam into 60 and 100 mTorr neutral hydrogen.

No completely satisfactory hypotheses have been found to explain the reduced charge-neutralization time or the origin of the non-maxwellian velocity distributions. However, the unusual features of the net current waveforms and the apparent mass motion during the beam pulse have led to a model for the mass motion that is discussed in Chapter 6.

CHAPTER 6

PROPOSED ADDITION TO THE BEAM PLASMA MODEL

6.1 Introduction

Much of the disagreement between the accepted model for the beam plasma system after charge neutralization and the observations made in the present experiment can be reconciled by postulating that the plasma is accelerated by the $\underline{j}_p \times \underline{B}$ force on the plasma during the beam.

This postulate is made to explain the following: (1) the expansion of the plasma channel during the beam, (2) the rapid rise in the net current during the beam at low filling pressures, (3) the increase in the net current between t = 100 and 200 ns, i.e. after the beam is over, (4) the failure to observe any plasma with laser scattering for injection into neutral hydrogen below 30 mTorr H_2 and (5) the rapid decrease in the plasma light intensity after an initial burst for injection into neutral hydrogen at 2 mTorr.

6.2 Beam Dynamics

Consider the case of a relativistic electron beam with number density $n_b << n_p$ the plasma number density. The radius r_o of the plasma is comparable to the Larmor radius of the beam electrons in the magnetic field of the net current. The mean free path for momentum transfer between the beam electrons and the plasma particles is very much longer than the dimensions of the plasma. Under these conditions,

the beam dynamics can be described with a particle model and the plasma dynamics with the fluid model through the generalized Ohm's law. The ions have a number density $n_i = n_e + n_b$ and provide quasi-charge neutrality for the system. The plasma and beam systems interact only through the magnetic field of the net current.

The electric fields in the system under consideration produce a weak perturbation on the motion of the beam electrons. The radial force F_b on a beam electron is

$$F_b = -eE_r + ev_b B_\theta \hat{r} \tag{6-1}$$

The radial electric field arises from the force-free criterion for the plasma electrons drifting with a velocity $v_p \hat{z}$:

$$F_p = -e(E_r - v_p B_\theta) = 0, \tag{6-2}$$

so $$E_r = v_p B_\theta.$$

The relative magnitude of the two terms in Equation (6-1) is

$$\frac{-eE_r}{ev_b B_\theta} = \frac{-ev_p B_\theta}{en_b B_\theta} = -\frac{v_p}{v_b} \tag{6-3}$$

Since the ratio of the plasma current density to the beam current density is the fractional magnetic neutralization $f_m \approx 1$,

$$\frac{j_p}{j_b} = \frac{n_e v_p}{n_b v_b} \cong f_m \approx 1$$

then $$\frac{v_p}{v_b} \approx \frac{n_b}{n_e} = \left| \frac{E_r}{v_b B_\theta} \right| << 1.$$

Consequently, the motion of the beam electrons is dominated by the magnetic field term in the Lorentz force.

The beam electrons lose their kinetic energy at a rate

$$\frac{dW_{beam}}{dt} = \int_V \underline{j}_b \cdot \underline{E}\, d^3R$$

which is the source of the energy to heat and accelerate the plasma. However, since the beam electrons lose only $eE_z l$ energy in traversing the length l of the experiment and since $eE_z l \ll eV_b$, the initial kinetic energy of a beam electron, the effect of this loss can be neglected in describing the beam dynamics.

6.3 Plasma Dynamics

Since the ratio

$$\frac{\nabla P_e}{\underline{j} \times \underline{B}} \approx \frac{(n_e k T_e / r_o)}{\underline{j} \times \underline{B}} < 0.02$$

during the beam pulse for the present experiments, the ∇P_e term in fluid equations can be neglected for the description of the plasma dynamics. Then the self-consistent motion of the plasma is described by the cold-plasma fluid equations:

Ohm's Law: $$\underline{E} = \eta \underline{j}_p - \underline{v} \times \underline{B} - \frac{\underline{j}_p \times \underline{B}}{n_e e} \qquad (6\text{-}6)$$

Ampere's Law: $$\nabla \times \underline{B} = \mu_o (\underline{j}_p + \underline{j}_b) \qquad (6\text{-}7)$$

Faraday's Law: $$\nabla \times \underline{E} = -\frac{\partial \underline{B}}{\partial t} \qquad (6\text{-}8)$$

Equation of Motion: $$\rho \frac{\partial \underline{v}}{\partial t} = \underline{j}_p \times \underline{B} \qquad (6\text{-}9)$$

and a description of the beam equilibrium as a function of the magnetic field $B_\theta(r)$:

$$j_{bz}(r) = f(B_\theta(r)). \tag{6-10}$$

The axial component of Ohm's Law is

$$E_z = \eta j_{pz} - v_r B_\theta, \qquad \text{for } j_{pr} = 0, \tag{6-11}$$

and the θ component of Faraday's Law is

$$-\frac{\partial E_z}{\partial r} = -\frac{\partial B_\theta}{\partial t}, \qquad \text{for } \frac{\partial}{\partial z} = 0. \tag{6-12}$$

Combining Equation (6-11) and (6-12) gives

$$\begin{aligned}\frac{\partial E_z}{\partial r} &= \eta \frac{\partial j_{pz}}{\partial r} - \frac{\partial}{\partial r}(v_r B_\theta) \\ &= \frac{\partial B_\theta}{\partial t}\end{aligned} \tag{6-13}$$

The axial component of Ampere's Law is

$$\frac{1}{r}\frac{\partial}{\partial r}(rB_\theta) = \mu_o (j_{pz} + j_{bz}) \text{ for } \frac{\partial}{\partial z} = 0,$$

so

$$j_{pz} = \frac{1}{\mu_o r}\frac{\partial}{\partial r}(rB_\theta) - j_{bz} \ . \tag{6-14}$$

Combining Equations (6-13) and (6-14) gives

$$\frac{\partial B_\theta}{\partial t} = \frac{\eta}{\mu_o}\frac{\partial}{\partial r}\left(\frac{1}{r}\frac{\partial}{\partial r}(rB_\theta)\right) - \frac{\eta}{\mu_o}\frac{\partial j_{bz}}{\partial r} - \frac{\partial}{\partial r}(v_r B_\theta) \tag{6-15}$$

where v_r is given by the integral of Equation (6-9) as

$$v_r = \int_0^t \underline{j}_p \times \underline{B}\cdot\hat{r}\, dt = -\int_0^t \left(\frac{1}{\mu_o r}\frac{\partial}{\partial r}(rB_\theta) - j_{bz}\right) B_\theta dt. \tag{6-16}$$

So if $j_{bz}(r, B_\theta)$ can be specified, the equations reduce to a system of two coupled equations for B_θ. However, to date, a self-consistent analytical expression for $j_b(r)$ for a given distribution of $B_\theta(r)$ has not been reported. In computer simulations, such as the one by McArthur and Poukey (1973), the time-integrated radial beam distribution was measured with total stopping colorimetry and was assumed to be constant during the pulse. This assumption is not necessarily appropriate for experiments which have significant plasma motion during the pulse. Consequently, the function $j_b(r, B_\theta(r))$ is not available to complete Equation (6-15) and (6-16).

6.4 Zeroth Order Description of the Mass Motion Model

When the beam and plasma channels are formed, the beam and plasma currents are coincident, as discussed in Section 2.2. For a uniform beam, the net current density is then uniform throughout the beam channel to r_o, i.e.,

$$\begin{aligned} j_{net} &= j_b + j_p \qquad \text{for } r \leq r_o \\ &= 0 \qquad\qquad \text{for } r > r_o. \end{aligned} \tag{6-17}$$

The magnetic field at radius r is then

$$\begin{aligned} B_\theta(r) &= \frac{\mu_o}{2\pi r} \int_0^r (j_p + j_b) \cdot \hat{z}\, 2\pi r\, dr \\ &= \frac{\mu_o\, r\, j_{net}}{2} \qquad \text{for } r \leq r_o, \end{aligned} \tag{6-18}$$

and the force on a fluid element at r is

$$\underline{F}_p = \rho \frac{\partial \underline{v}}{\partial t} = - j_{pz} B_\theta \hat{r}$$

$$= - \frac{\mu_o \pi}{2} j_{pz} j_{net} r \hat{r} \qquad (6\text{-}19)$$

For a beam current in the minus z direction, j_{net} is less than zero and j_p is greater than zero, so the force is radially outward. At $r = 0$, the force is zero. Under this acceleration, the plasma moves radially outward.

As the plasma moves, one is interested in discovering what happens to the distribution of the plasma and the beam current densities inside and outside the beam channel under the EMFs associated with (1) the induced electric field from the change in the net current distribution caused by the plasma motion, (2) the induced electric field caused by the decay of the plasma current, and (3) the polarization electric field $-\underline{v} \times \underline{B}$ from the local plasma motion. The solution of equations (6-10), (6-15), and (6-16) would provide the time evolution of the current densities. However, in the absence of such a solution, a quantitative comparison of the experimental results and the theory is inappropriate. Nevertheless, the sources of the experimentally observed phenomena can be described qualitatively.

6.5 Increase of the Net Current During the Beam

The expansion of the plasma channel and the associated re-distribution of currents in the experimental chamber causes the inductance to decrease as the channel expands. If the energy W_{field} in the magnetic field remained constant or increased after the beam then the decrease in the inductance would be accompanied by an increase in the net current,

since

$$W_{field} = \tfrac{1}{2} L I_{net}^2$$

$$\frac{\partial W_{field}}{\partial t} = \tfrac{1}{2} I_{net}^2 \frac{\partial L}{\partial t} + I_{net} L \frac{\partial I_{net}}{\partial t} \geq 0,$$

$$\frac{\partial I_{net}}{\partial t} \geq - \frac{I_{net}}{2 L} \frac{\partial L}{\partial t} > 0 \quad \text{if} \quad \frac{\partial L}{\partial t} > 0.$$

For example, if the current distribution is uniform to a radius r_o with the cylindrical current-return at the wall radius r_w, then

$$L \doteq \frac{\mu_o}{2\pi} \left(\tfrac{1}{4} + \ln(r_w/r_o)\right)$$

and

$$\frac{\partial L}{\partial t} = - \frac{\mu_o}{2\pi} \frac{1}{r_o} \frac{\partial r_o}{\partial t} . \qquad (6\text{-}21)$$

For $\frac{\partial r_o}{\partial t} > 0$, $\frac{\partial L}{\partial t} < 0$, and $\frac{\partial I_{net}}{\partial t} > 0$,

so the net current increases even though the plasma resistivity is very small.

6.6 Increase in the Net Current after the Beam

The same argument as that presented in Section (6-5) applies after the beam, since the inertia of the ions ensures that the inductance continues to decrease until the ions are decelerated by the $\underline{j}_p \times \underline{B}$ force on the fluid element.

In practice, the energy in the magnetic field does not remain constant because (1) the net current increases as the plasma current decays during the beam and (2) the kinetic energy of the ions is transferred back to the magnetic field from $\underline{j}_p \cdot (-\underline{v} \times \underline{B})$ after the beam. The situation is further complicated by the fact that some of

the plasma is expanding outward and being decelerated after the beam while the plasma nearer the axis is being pinched toward the axis. This inhomogeneity in $\underline{v}$ is caused by the radial dependence of the azimuthal magnetic field and hence of the plasma acceleration for the initially homogeneous plasma channel. Consequently, the interpretation of the net current signal to deduce the plasma dynamics is not straightforward.

CHAPTER 7

APPLICATION OF THE MODEL TO THE EXPERIMENT

7.1 Introduction

The results of the experiments on the macroscopic behaviour of the plasma indicated that the mass motion could be neglected if the beam was injected into a preformed plasma or into neutral hydrogen at a pressure greater than 1 Torr. The only experiments in which the mass motion could not be neglected were those with injection into 60 and 100 mTorr neutral hydrogen.

7.2 Description of the General Problem

In principle, the general problem of calculating the electron energy density and the ion velocity is to solve (1) the equation of motion and Ohm's Law for the plasma, (2) a particle calculation for the motion of the beam electrons, (3) the rate equations for the production of the various ionic species, (4) the equation for energy balance, and (5) Maxwell's equations for the fields. Some electron distribution function for the plasma electrons must be assumed, and the initial conditions of the problem must be specified.

A similar calculation was made by McArthur and Poukey (1973), and the calculated net current waveform was compared with experiment. The calculation produced the experimental waveform for the net current to within 20% for injection into nitrogen at pressures above 1 Torr. Below 1 Torr filling pressure of nitrogen, their calculations did not

match the experimental waveforms for the net current. Since the present experiments were in this low pressure regime, their calculations (which neglected ion motion) were not appropriate to the present experiments.

The difficulties in performing the detailed calculation and including mass motion lie in (1) the specification of the initial conditions and (2) the choice of the electron velocity distribution. The ionization mechanism for the gas downstream from the beam front is not well known(as discussed in Section 5.2), so the initial conditions for the problem are not known for injection into neutral hydrogen. A more serious difficulty lies in the choice of the electron velocity distribution. Since the heating occurs on a time scale comparable to the relaxation time for the plasma electrons' velocity distribution, the distribution is not Maxwellian. Also, since the ionization rate at high pressures is comparable to the relaxation rate of the distribution, the high energy tail is depleted by ionizing, inelastic collisions.

The energy relaxation time t_E for electrons with velocity w in a distribution with a kinetic temperature kT_e through electron-electron collisions in the plasma is given by Spitzer (1962) as

$$t_E = \frac{1.5 \times 10^{-20}\, w^3}{n_e\, G(\sqrt{\tfrac{1}{2}m_e w^2/kT_e})} \quad \text{seconds}, \qquad (7\text{-}1)$$

where

$$G(x) = \frac{\Phi(x) - x\,\Phi'(x)}{2x^2}$$

and

$$\Phi(x) = \frac{2}{\pi^{\frac{1}{2}}} \int_0^x e^{-y^2} dy$$

for and electron number density n_e in cm^{-3} and a velocity w in cm/sec. This relaxation time should be compared with the time taken for an electron with velocity w to make an ionizing collision

$$t_{ioniz.} = \frac{1}{Q_{ioniz}\, n_o\, w} \qquad (7\text{-}2)$$

For electrons with velocity $w \geq 2.7 \times 10^8$ cm/sec (20 eV electrons), the cross section for ionization is $\approx 10^{-16}$ cm^2, as given by Massey (1969). Below that velocity, the cross section is essentially zero. Consequently,

$$t_{ioniz.} = \frac{0.28}{w\, P} \quad \text{sec}$$

where P is the pressure of neutrals in Torr. The ratio for $w \geq 2.7 \times 10^8$ cm/sec is

$$\frac{t_E}{t_{ioniz}} = \frac{5.5 \times 10^{-20}\, P\, w^4}{G(\sqrt{\tfrac{1}{2}m_e w^2/kT_e})\, n_e} \qquad (7\text{-}3)$$

For $n_e = 5 \times 10^{14}$ cm^{-3}, $w = 3 \times 10^8$ cm/sec, $kT_e = 10$ eV, the factor G is less than 0.12 and

$$\frac{t_E}{t_{ioniz.}} < 1 \quad \text{implies} \quad P < 2.2 \times 10^{18} \frac{n_e}{w^4} \quad \text{Torr} \qquad (7\text{-}4)$$

$$\therefore P < 0.13 \text{ Torr.}$$

Since, t_E/t_{ioniz} varies as w^4, the high energy tail is quickly depopulated for experiments with neutral hydrogen at pressures greater than 100 mTorr. The ionization rate is then determined by the diffusion of the electrons in velocity space. This effect must be considered in a realistic simulation or the calculated ionization rate will be too large.

7.3 Approximate Semi-empirical Calculation of the Plasma Heating and the Ion Motion

Fortunately, the auxiliary measurements for each experiment provide data that made the self-consistent calculation of the energy transfer and mass motion unnecessary. The total net current as a function of time was measured for each set of experimental conditions. The total beam current was inferred from the diode waveform normalized to the energy transmitted through the cone, i.e.

$$I_{beam}(t) = I_{diode}(t) \frac{(\text{total beam energy monitored at cone exit})}{(\text{total beam energy monitored at the anode})} .$$

The plasma current was determined for each set of experimental conditions by

$$I_p = I_{net} - I_{beam}.$$

For experiments with a preformed plasma, the initial plasma number density and temperature were measured with the laser scattering system described in Section 4.8. The cross sectional area of the plasma current channel was inferred from the measured beam divergence of 30°, as described in Section 4.5. Since the self-magnetic field was too small to produce significant mass motion of the plasma during the beam duration, the beam and plasma current channels remained coincident. The cross section of the plasma channel at the scattering volume (at a position 8 mm from the entrance foil) was then

$$\pi \left(r_o(z=0) + 0.8 \cot(30^{\circ})\right)^2 = 4\pi \text{ cm}^2,$$

and the plasma current density was

$$j_p(t) = \frac{I_p(t)}{\text{Area}(z=0.8\text{mm})}$$

$$= \frac{I_{net}(t) - I_{beam}(t)}{4\pi} \qquad \text{amps/cm}^2 \qquad (7\text{-}5)$$

for the experiments with a preformed plasma.

For experiments with injection into a neutral gas, the initial plasma electron number density and temperature are not known. One of two assumptions was made for the initial plasma number density: (1) the plasma electron number density remained constant at the value measured with laser scattering at t = 100 ns or (2) the number density increased linearly from half its final value to its final value at t = 100 ns, i.e.

Assumption 1

$$n_e(t) = n_f, \quad \text{where } n_f = n_e(t=100\text{ns}), \qquad (7\text{-}6)$$

Assumption 2

$$n_e(t) = \tfrac{1}{2}\, n_f \times (1 + t\times 10^7). \qquad (7\text{-}7)$$

For experiments with the neutral gas, the time history of the radius R(t) of the plasma current channel was measured with the image converter streak camera, as described in Section 4.4. The cross section was approximated as

$$\pi R^2(t)$$

where $$R(t) = R_{t=0} + (R_{t=100\text{ns}} - R_{t=0}) \cdot t \cdot 10^7 \qquad (7\text{-}8)$$

for these experiments.

Since the plasma electron number density that was measured at t = 100 ns was used in the calculations, the unspecified quantity that was calculated as a measure of plasma heating was the effective electron temperature

$$kT_{eff} = \frac{2}{3} \frac{(\text{electron kinetic energy per unit volume})}{n_e} \qquad (7\text{-}9)$$

which will be compared with the measured value, defined by Equation (4-6). However, the energy density per unit volume nkT_{eff} was really the experimentally measured quantity and will be used to compare the theory with the experiment. For the calculation of the mass motion, the ion velocity and the radius of the beam channel were the free parameters and were calculated from the equation of motion.

7.4 The Ionic Species

The species of the ion (i.e. whether the ion is H_2^+ or H^+) determined both the ion mass and the charge exchange cross section. Thus knowledge of the ion species was primarily important for the calculation of the ion motion.

Massey (1969) gives a discussion of the ionic species produced by electron bombardment of neutral, diatomic hydrogen. In all reported measurements the relative abundance of H^+ produced by electron bombardment of H_2 was less than 4% of the total number of ions produced. This result is consistent with the measured cross sections for the production of H^+ and H_2^+ by the collision of an electron of known energy with an H_2 molecule. The cross section for producing H^+ never exceeds 6% of the total ionization cross section as discussed in Massey (1969). The threshold for producing H^+ is 18 eV compared with 15.3 eV for H_2^+ [from Cobine (1958)], so the production of H_2^+ is favored over that of H^+.

Once H_2^+ is formed, it can be dissociated by an additional collision with another electron. The maximum cross section for that process is given by Massey (1969) as 5×10^{-16} cm^2 for bombardment of

H_2 by 4 to 10 eV electrons. The time required to produce an H^+ plasma from an H_2^+ plasma is given by

$$\frac{\partial n_{H_2^+}}{\partial t} \leq n_{H_2^+} n_e Q_{diss} w$$

$$\tau_{diss} \leq \frac{1}{n_e Q_{diss} w} \approx 4 \times 10^{-8} \text{ seconds}, \tag{7-10}$$

which is comparable to the duration of the experiment. Consequently, both ionic species are present for the experiments with injection of the beam into a neutral gas. Since the H_2^+ molecule must be produced before it is dissociated, the dominant ion during the beam is assumed to be H_2^+, in agreement with the assumption made by McArthur and Poukey (1973) for injection of a beam into nitrogen.

For experiments with a preformed plasma, the H_2 molecules have sufficient time to dissociate, and the H^+ ion is assumed to be the dominant species.

7.5 Calculation of Mass Motion to Compare with the Experimental Results

The program "IONW" was written to estimate the velocity of the plasma ions and the radius of the plasma channel at t = 100 ns after the beam began. A copy of the program is included in Appendix I.

The program calculated the radial position R and the radial velocity V of a fluid element that was intially at a radius $R_{1,j}$ and had an initial velocity V (t=0) = 0. The program integrated the equation of motion

$$\rho \frac{\partial \underline{v}}{\partial t} = \underline{j}_p \times \underline{B} \tag{7-11}$$

as

$$V = -\int_0^t \frac{j_{pz}}{\rho} B_\theta(r)\, dt \tag{7-12}$$

$$R = R_1 + \int_0^t V(t)\, dt \tag{7-13}$$

under the following assumptions:

(1) The total beam current I_b and the total plasma current I_p were constant from time t = 0 to t = 100 ns.

(2) The beam current distribution remained uniform from t = 0 to t = 100 ns.

(3) The plasma was divided into 10 cylindrically symmetric plasma elements. The j_{th} element initially extended from R = (j-1) ΔR to R = jΔR, where ΔR was one tenth the initial radius of the beam-plasma channel. The total plasma current $I_{p,j}$ and beam current $I_{b,j}$ carried by the j_{th} element were given by

$$I_{p,j} = \frac{I_p}{r_o^2} (j^2 - (j-1)^2) (\Delta R)^2 \tag{7-14}$$

$$I_{b,j} = \frac{I_b}{r_o^2} (j^2 - (j-1)^2) (\Delta R)^2 \tag{7-15}$$

and were assumed to have remained constant during the beam.

(4) The plasma segments did not cross each other during their motion.

(5) The number of ions in the j_{th} element either (a) remained constant, or (b) increased from $N_j = \frac{1}{2}N_{f,j}$ to $N_{f,j}$ from t = 0 to t = 100 ns, i.e. for a final ion number density n_f, and for

$$N_{j.f} \equiv n_f \pi(\Delta R)^2(j^2 - (j-1)^2) \tag{7-16}$$

assumption (a) was

$$N_j(t) = N_{j,f} \tag{7-18}$$

assumption (b) was

$$N_j(t) = \tfrac{1}{2} N_{j,f} (1 + t \times 10^7). \tag{7-19}$$

Calculations were performed for both of these assumptions and the results were compared.

Under assumptions 2 and 3, the azimuthal magnetic field B_θ at R_j was given by

$$B_\theta = \frac{\mu_o}{2\pi R_j} (I'_{p,j} - I'_{b,j}) \tag{7-20}$$

where $I'_{p,j}$ and $I'_{b,j}$ were the plasma and beam currents at a radius less than R_j, the radius of the j_{th} element, i.e.

$$\begin{aligned} I'_{p,j} &= \frac{I_p}{\pi R_o^2} (\pi R_{1,j}^2) \\ I'_{b,j} &= \frac{I_b}{\pi R_o^2} (\pi R_{1,j}^2) \end{aligned} \tag{7-21}$$

where $R_{1,j} = (j-1)\ \Delta R$.

Consequently, under these assumptions, for an ion mass M_i,

$$\frac{\partial V_j}{\partial t} = - \frac{I_{p,j}}{M_i N_j(t)} B_\theta \tag{7-22}$$

$$V_j = \int_0^t \frac{\partial V_j}{\partial t}\, dt \tag{7-23}$$

$$R_j = R_{1,j} + \int_0^t V_j\, dt \tag{7-24}$$

An additional feature of IONW was the approximate inclusion of the effect of charge exchange. The mean free path for charge exchange is

$$\lambda_{ce} = \frac{1}{Q_{ce}\, n_o} \tag{7-25}$$

where Q_{ce} is the charge-exchange cross section, and n_o is the number density of the neutrals. Fite (1959) gives

$$Q_{ce} = 6 \times 10^{-16} \text{ cm}^2 \quad \text{for} \quad H_2^+ + H_2 \longrightarrow H_2 + H_2^+$$

$$Q_{ce} = 3 \times 10^{-15} \text{ cm}^2 \quad \text{for} \quad H^+ + H \longrightarrow H + H^+. \qquad (7\text{-}26)$$

When the element had moved the distance λ_{ce} the ions in the segment underwent a simulated charge exchange. The fluid velocity V was set equal to the velocity of the neutrals, V_n

$$V_n = \frac{2 W_{atom}}{M_i} \qquad (7\text{-}27)$$

where M_i is the ion mass. W_{atom} was the average energy of the neutral molecule from charge exchange and was estimated as

$$W_{atom} = \frac{\text{Total energy lost via charge exchange}}{\text{Number of neutrals in the beam channel}}.$$

The results of the calculations for the ion motion are given in Table 7.

7.6 Calculation of the Plasma Heating to Compare with the Experimental Results

The program HEAT was used to calculate:

$$nkT_{eff} = 2/3 \times (\text{electron energy density per unit volume}) \qquad (7\text{-}28)$$

at time t = 100 ns for the experiments with a preformed plasma. Calculations were made (1) for heating via classical processes only and (2) for heating via the ion-acoustic instability and the classical processes. The following assumptions were made:

(1) The radius R of the plasma channel and the beam channel were coincident and did not expand or contract during the beam pulse. This assumption made the calculation inappropriate for the experiments for

Table 7. Expected ion energy, molecular energy, and plasma channel radius for the experimental conditions. The results of the program "IONW" are given. W_{ion} is the average energy in directed motion of the ions, W_{atom} is the average energy of the atoms (molecules), and R_{max} is the maximum radial excursion of the plasma channel at t=100ns.

Case	Pressure (Torr)	Ion	Initial Channel Radius (cm)	Beam Current (10^3amps)	Net Current (10^3amps)	Initial n_e ($10^{14}cm^{-3}$)	Final n_e ($10^{14}cm^{-3}$)	W_{ion} (eV)	W_{atom} (eV)	R_{max} (cm)
I	0.12	H^+	2	35	2.2	20	40	0.26	0	2.0
II	0.04	H^+	2	35	3.0	6	12	5.	0	2.3
III	0.4	H^+	2	35	3.0	6	12	12.	0.1	2.2
IV	0.02	H^+	2	35	2.2	2.2	4.4	20.	0	2.5
V	0.06	H_2^+	0.75	35	12.	3.5	7	1200.	21	5.0
VI	0.10	H_2^+	0.75	35	14.	6	12	640.	11	3.7
VII	1.0	H_2^+	0.75	35	8.4	20	40	15	0.4	1.2
VIII	10.0	H_2^+	0.75	35	13.	40	80	0.55	0.14	0.9

injection into neutral hydrogen at low pressures.

(2) The total plasma current $I_p(t)$ was given by

$$I_p(t) = I_{p,max} \frac{t}{30} \; 10^9 \quad \text{for } t < 30 \times 10^{-9} \text{ seconds},$$

$$= I_{p,max} \; (1 - t/\tau) \quad \text{for } t > 30 \times 10^{-9} \text{ seconds}, \tag{7-29}$$

where $I_{p,\,max}$ and τ were specified from the net current waveform and the diode current waveform as

$$I_{p,max} = (I_b - I_{net})_{t=30 \text{ ns}} \tag{7-30}$$

and

$$\tau = \frac{10^{-7}}{\left(1 - \frac{(I_b - I_{net})_{t=100 \text{ ns}}}{I_{p,max}}\right)} \text{ seconds}. \tag{7-31}$$

(3) The total plasma current was uniformly distributed from $0 < R < R_o$, so the plasma current density was given by

$$j_p(t) = \frac{I_p(t)}{\pi R_o} . \tag{7-32}$$

(4) The plasma electron number density n_e increased linearly from an initial value n_{eo} to a final value n_{ef} as

$$n_e(t) = n_{eo} + (n_{ef} - n_{eo}) \cdot t \cdot 10^7, \quad \text{for } t < 10^{-7} \text{sec}.$$

The values of n_{eo} and n_{ef} were specified from the laser scattering.

(5) The resistivity η was given by

(a)

$$\eta_{classical} = \eta_{e,i} + \eta_{e,n} \tag{7-33}$$

(b)

$$\eta_{anomalous} = \eta_{I.A.1}$$

$$\eta_{anomalous} = \eta_{I.A.2} \tag{7-34}$$

where $\eta_{e,i}$ is the electron-ion resistivity, $\eta_{e,n}$ is the electron-neutral resistivity, and $\eta_{I.A.1}$ is the anomalous resistivity given by Caponi and Davison (1973) and $\eta_{I.A.2}$ is that given by Sagdeev (1967) for the energy transfer associated with the ion-acoustic instability. These resistivities were discussed in Section (2-4). The calculations were done for $\eta = \eta_{classical}$, for $\eta = \eta_{classical} + \eta_{I.A.1}$, and for $\eta = \eta_{classical} + \eta_{I.A.2}$.

(6) The energy lost through inelastic collisions with neutrals was very much less than the kinetic energy of the plasma electrons. The effective cross section for vibrational excitation of H_2 by electrons with energy between 1 and 20 eV is given by Frost and Phelps (1962) as $Q_v = 3 \times 10^{-17}$ cm^2. For a 10 eV electron, $w = 2 \times 10^8$ cm/sec, so the characteristic time for making an inelastic collision is

$$\tau_v = \frac{1}{Q_v n_o w} = \frac{5 \times 10^{-9}}{P} \text{ seconds.} \qquad (7\text{-}35)$$

For τ_v to be greater than 100 ns, P must be less than 50 mTorr H_2. Consequently, this assumption made the calculation inappropriate for the experiments with a neutral gas, in which $P \gtrsim 60$ mTorr H_2.

(7) The expansion velocity of the plasma channel was zero, so the equation for energy balance was

$$\frac{\partial}{\partial t}\left(\frac{3}{2} nkT\right) = \eta j_p^2 - \frac{\partial}{\partial t} W_{loss}. \qquad (7\text{-}36)$$

where

$$\frac{\partial}{\partial t} W_{loss} = W_{ioniz} \times \frac{\partial n}{\partial t}. \qquad (7\text{-}37)$$

W_{ioniz} was the energy lost from the electron energy distribution for each electron-ion pair produced and was equal to 18 eV. This value should be compared with the ionization energy of 15.36 eV for the production of H_2^+ and to the average energy of 36 eV required to produce

an ion by electron bombardment with 500 to 1000 eV electrons, as given by Cobine (1958). The energy equation was integrated from t = 0 to 100 ns, and the final value of nkT_{eff} was printed out. The results are shown in Table 8.

Plasma Heating with the Electron-Electron Instability

The expected energy transfer to the plasma electrons from excitation of the two stream instability was discussed in Section 2.3. For the experiments with a preformed plasma, the beam energy density at the scattering volume (z = 0.8 cm) was given from the data in Section 3.8. as

$$W_{beam} = n_b(z=0) \cdot \frac{\text{Area}(z=0)}{\text{Area}(z=0.8\text{mm})} \cdot eV_b \qquad (7\text{-}39)$$

$$= 2.8 \times 10^{17} \text{ eV/cm}^3 \quad \text{at } z = 0.8 \text{ mm.}$$

Thus, the expected plasma electron energy density was

$$W_{plasma} = 0.2\, W_{beam} = 5 \times 10^{16} \text{ eV/cm}^3 \qquad (7\text{-}39)$$

when the e-e mode saturated.

Table 8. Expected heating from classical and anomalous resistivities for the experimental conditions.

Case	$I_{p,max}$ (10^3 amps)	Decay Time (10^{-7} s)	Pressure (Torr)	T_{eo} (eV)	n_{eo} (10^{14} cm^{-3})	n_{ef} (10^{14} cm^{-3})	R (cm)	W_{class}	W_{c+cd}	W_{c+sag}	W_{e-e}
								(10^{16} eV cm^{-3})			
I	34	21	0.1	0.8	0.6	10.	2.	0.9	3.4	4.9	5.
II	28	21	0.1	1.5	7.	12.	2.	1.2	2.5	2.3	5.
III	34	12	0.2	0.6	10.	12.	2.	2.0	4.0	3.6	5.
IV	34	19	0.15	2.5	0.8	2.4	2.	0.6	7.0	13.	5.

CHAPTER 8

COMPARISON OF THE THEORY AND EXPERIMENT FOR THE MODEL FOR MASS MOTION

8.1 Introduction

The experimental evidence gives qualitative support to the model for plasma motion by the $\underline{j}_p \times \underline{B}$ forces on the plasma during the beam. In this chapter, the model is applied to the data on the expansion of the plasma channel, the net current waveforms, the time histories of the plasma light, and the failure of the laser scattering diagnostic at very low pressures.

8.2 Expansion of the Plasma Channel

For experiments with injection of the beam into neutral hydrogen, the light emission from the plasma was recorded with an image-converter camera, as described in Section 4.4. Since the recording medium was non-linear, Polaroid film, the apparent radius of the luminosity was a minimum for the actual radius of the plasma channel. The regions of the plasma that emitted less intensely or that lay along a line of sight intercepted by little plasma did not appear on the film.

The photographs alone are not sufficient evidence for the mass motion of the plasma. If the apparatus were used to photograph a stationary plasma column with a uniform light emission per unit volume that increased with time, then the photograph would reveal an expanding channel. The erroneous result would be due to (1) the path of integration through the center of the distribution being longer than that

through off-axis positions and (2) the non-linearity of the film. Thus, the apparent observation of an expanding plasma channel is necessary but not sufficient evidence of plasma motion. However, the witness plate measurements discussed in Section 4.3, showed that the radius of the beam, and thus the initial radius of the plasma channel, was 0.8 cm. Thus the beam channel expanded from r = 0.8 cm at t $\simeq$ 30 ns to r = 2 cm at t = 100 ns. So the camera measurements interpeted with the witness plate measurements support the model for the mass motion.

The program IONW calculated the maximum radial excursion of the plasma channel at t = 100 ns as 3.7 cm, 1.2 cm, and 0.85 cm for initial pressures of 100 mTorr, 1 Torr, and 10 Torr respectively, as shown in Table 7. The corresponding radii measured from the photographs in Figure 35 were 2 cm, 0.8 cm, and 1 cm. The agreement is qualitatively correct and supports the model for mass motion.

8.3 Rise time of the Net Current after Breakdown

As discussed in Section 6.5, the mass motion allows the net current to increase more rapidly than it would through the simple resistive damping of the plasma current. This feature is consistent with the disagreement between the plasma resistance calculated from the decay of the plasma current and the resistance calculated from the measured number density and temperature of the plasma, as shown in Table 6.

8.4 Increase in the Net Current after the Beam

As the inertia of the ions continued to cause the plasma column to expand after the beam, as discussed in Section 6.6, the net current should have continued to increase. The measured net current waveforms in Figure 42 clearly showed the increase, after the beam pulse.

8.5 Radial Velocity Profile

The model for the mass motion implies that the radial velocity of the plasma increased with increasing radius. Consequently, the slowly expanding plasma that was near the axis was stopped and was pinched toward the axis soon after the plasma current had reversed direction after the beam. At the same time, the faster moving plasma near the edge of the plasma channel continued to move radially outward until it was finally stopped or it hit the wall. The image converter photographs (Figure 35) showed such a pinching of plasma near the axis for the 60 and 100 mTorr cases after the beam. The net current waveforms (Figure 45) were consistent with a net expansion of the current channel during the time when the plasma near the axis was pinching. Thus, the apparent contradiction in the plasma motion is consistent with the model.

8.6 Expulsion of the Plasma from the Original Plasma Channel

Since the radial acceleration on the plasma increases as the plasma number density decreases, and since the plasma number density after breakdown decreases as the initial filling pressure is decreased, the plasma is expelled faster at lower filling pressures. Since the

ionization rate is proportional to the electron number density and to the filling pressure of neutrals, the loss rate of plasma by radial acceleration should exceed the ionization rate at some pressure as the filling pressure is lowered. The lack of scattered laser light in experiments with filling pressures below 50 mTorr and the rapid decay of the continuum of plasma light at 2 mTorr filling pressure (as shown in Figure 53) are consistent with the rapid expulsion of the plasma from the channel, as predicted with the model for mass motion.

8.7 Conclusion

In conclusion, the results from a wide range of diagnostic techniques used on the beam-plasma system support the hypothesis that the $\underline{j} \times \underline{B}$ force on the plasma in the present experiment was effective in accelerating the ions during the beam pulse.

CHAPTER 9

COMPARISON OF THE THEORY AND EXPERIMENT FOR THE PLASMA HEATING

9.1 Introduction and Data Summary

The program "HEAT" was used to calculate the electron energy density in the plasma under each of three different assumptions: (1) the heating was by classical electron-ion and electron-neutral collisions only, (2) the heating was by classical collisions and anomalous collisions associated with the ion-acoustic turbulence as described by Caponi and Davidson (1973), and (3) the heating was by classical collisions and anomalous collisions associated with the ion-acoustic turbulence described by Sagdeev (1967). The three assumptions gave the three values of the electron energy density as W_{class}, W_{c+cd}, and W_{c+sag} respectively. These are listed for the various experiments with a preformed plasma in Table 8 and are reproduced in part in Table 9 for convenience. The energy density for the electron-electron two-stream instability was expected to be 5×10^{16} eV/cm^3 as discussed in Section 7.7 and is shown in Table 9 as W_{e-e}.

The measured electron energy density as defined by Equation 4-5, is given in Table 9 as W_{exp}.

9.2 Heating via the E-E Mode

A comparison of the experimental and theoretical values of the electron energy density shows that W_{exp} is always less than W_{e-e}. Consequently, the electron-electron two stream instability either was

Case No.	W_{class}	W_{c+cd}	W_{c+sag}	W_{e-e}	W_{exp}	$kT_e/\frac{1}{2}M_iV_i^2$
	←		(10^{16} eV/cm^3)		→	
I	0.9	3.4	4.9	5.	>1.8±30%	20.
II	1.2	2.5	2.3	5.	2.4±40%	4.
III	2.0	4.0	3.6	5.	1.2±20%	0.9
IV	0.62	7.0	13.0	5.	0.6±20%	0.7

Table 9. Comparison of theory with experiment for plasma heating. The last column gives the ratio of the experimentally observed electron energy to the calculated energy in the directed motion of an ion at t=100 ns from the program IONW.

not excited or did not give the expected energy transfer to the plasma electrons.

From the measurements of the beam half-angle and the electron temperature and number density, the Singhaus criterion, Equation (2-16), for excitation of the e-e mode was applied to the present experiment. The criterion involves the spread ΔV in the velocity of the beam electrons. The average perpendicular velocity defined by

$$v_{\perp} = \beta c \sin(\theta_{\frac{1}{2}}) \tag{9-1}$$

where

$$\theta_{\frac{1}{2}} = 0.65\ \theta_{max},$$

and θ_{max} is the beam divergence for $I_{net} \simeq 0$ was measured, as discussed in Sections 4.2 and 4.5. The theory by Singhaus (1964) assumes an isotropic velocity spread ΔV, which is the rms value of a Gaussian velocity distribution in the beam frame. However, the physical model only requires ΔV to be parallel to the $\underline{k}$-vector of the wave and hence to the beam velocity. Since the measured and theoretical quantities are not the same, an additional assumption must be made to relate the two. The assumption that

$$\Delta v = \beta c \sin(\theta_{max}) = 0.5\ \beta c \tag{9-2}$$

is the least restrictive assumption and errs on the side of over estimating the beam velocity spread. Consequently, if the instability should be excited under this extreme assumption, then it will be excited if the theory is appropriate to the experiment. Table 10 shows the maximum value of the momentum transfer collision frequency ν_{sing} allowed for instability, shows the calculated collision frequencies ν_c from classical collisions and also ν_{c+ia} from classical plus the

Table 10. Application of the Singhaus criterion for instability of the e-e mode to the experimental conditions. The maximum collision frequency for momentum transfer to the plasma electrons that allows the e-e mode to grow is ν_{sing} given by Equation (2-16). The collision frequency given by

$$\nu = \frac{n_e e^2 \eta_{eff}}{m_e}$$

is shown for 1) ν_c calculated with η_{eff} = the classical resistivity only (Equation 2-28 plus Equation 2-30) and 2) ν_{c+ia} calculated from the classical resistivity plus the anomalous resistivity from the ion-acoustic mode (Equation 2-24). The comparison is shown for the beginning of the beam (t=0) and at t=100ns.

Case No.	Time (ns)	n_e (10^{14} cm^{-3})	T_e (eV)	e-e mode unstable ($\nu_{sing} > \nu_{c+ia}$)	e-e mode unstable w/o ion-acoustic instability ($\nu_{c+ia} > \nu_{sing} > \nu_c$)	e-e mode stable ($\nu_{sing} < \nu_c$)
I	0	0.3	0.5	Yes		
	100	30.	6.0			Yes
II	0	7.	1.5			Yes
	100	12.	20.		Yes	
III	0	20.	0.6			Yes
	100	12.	10.		Yes	
IV	0	0.8	2.5	Yes		
	100	4.4	13.	Yes		

collisions associated with the ion acoustic instability (the Caponi and Davidson (1973) value of ν_{ia} has been used). Clearly, the only experiment in which the electron-electron two stream instability should be unstable throughout the beam pulse is Case IV. This is the case in which the observed energy density is only 12% of that expected from the e-e mode. The observed value agrees very well with the calculated value from classical collisions alone. Since the shots in this case were good ones and since the energy densities measured in all shots were consistent with the result in Table 10, I conclude that the laser scattering did not show the expected energy transfer to the plasma from the e-e mode.

The computer simulations on which the theoretical value was based were one dimensional calculations. The presence of the magnetic field transverse to the streaming velocity, makes the experiment a two dimensional problem. Since the threshold for the instability is a strong function of ν (the frequency for momentum transfer for the plasma electrons) even when $\nu << \omega_{pe}$, then the growth may be strongly dependent on ω_{ce}, even when $\omega_{ce} << \omega_{pe}$ for streaming across a magnetic field. The neglect of the transverse magnetic field appears to be on the same order as the neglect of the electron collisions for momentum transfer. Consequently, a treatment for the instability with $0 << \omega_{ce} << \omega_{pe}$, analogous to the Singhaus' treatment for $0 << \nu << \omega_{pe}$, is required.

A second possible explanation is that the high-energy plasma electrons coupling with the wave (which has a phase velocity approximately equal to the axial beam velocity) contain all the energy extracted from the wave. Such a high energy tail with very few electrons in it would not be observed with the laser scattering diagnostic. If the

energy in the tail is distributed to the other electrons, then the energy transfer would be observed. The classical energy relaxation time, Equation (7-1), from electron-electron collisions given by Spitzer (1962) varies as w^3, the cube of the electron velocity. For a plasma with $n_e = 10^{15}$ cm^{-3}, the thermalization time is of the order of 100 ns for $w \simeq 9 \times 10^8$ cm/sec and for $T_e = 10$ eV. Electrons with very large velocities ($w >> 9 \times 10^8$ cm/sec) would not thermalize during the experiment. However, collective effects can cause a much shorter relaxation time through Landau damping and through the excitation of waves with a low phase velocity as discussed by Ramazahsvili, et al. (1963).

9.3 Heating via the Ion Acoustic Mode

A comparison of the electron energy density expected with the contribution of the ion acoustic mode (W_{c+cd} and W_{c+sag}) in Table 9 with the experimentally observed energy density W_{exp} shows that in two of the four cases (Cases I and II) W_{exp} is consistent with the energy transfer from the ion acoustic instability. The electron energy density in Case III was less than expected from the classical resistivity alone. The reduced electron energy density in Case III is consistent with losses through vibrational excitation of neutrals (as discussed in Section 7.6) since the filling pressure of hydrogen is 200 mTorr. The energy observed in Case IV is in good agreement with the value expected from classical heating alone. Case IV differed from the other experiments in that the plasma number density was relatively low (4.4×10^{14} cm^{-3} at t = 100 ns). Consequently, the acceleration of the plasma became significant during the beam pulse. The results of the Program "IONW" shown in Table 7 showed that the

expected ion energy in the directed radial velocity was 20 eV for H^+ ions (or 10 eV for H_2^+ ions) at t = 100 ns for Case IV. The directed motion is not equivalent to thermal ion energy kT_i. However, if the directed motion was very large, the spread in that motion should have become significant as the ions suffered a few long-range collisions. In comparison with the calculated ion energy of 20 eV for H^+, the electron thermal energy was kT_{eff} = 13 eV at t = 100 ns for this case. For the excitation of the ion acoustic mode, T_e/T_i must be greater than~5, as required by theory and experimentally verified by Taylor and Coroniti (1972) in a weak ion-beam experiment. For Cases I and II, the ratio of kT_e to the directed ion energy (calculated with "IONW") was greater than~5, while for cases III and IV, it was not. Consequently, the instability should not have been excited in Case IV.

Thus, the present experiments were consistent with anomalous heating through the ion-acoustic instability. The results agreed with both the theory given by Caponi and Davidson (1973) and that given by Sagdeev (1967), so the results of the present experiment did not support one theory for the energy transfer via the ion-acoustic mode over the other.

9.4 Conclusions

The measured electron energy densities in these experiments supported an energy transfer to the plasma through the anomalous resistivity associated with the ion-acoustic instability. No evidence of energy transfer via excitation of the electron-electron mode was observed.

CHAPTER 10

COMPARISON WITH OTHER EXPERIMENTS

10.1 Introduction

In the present experiment, no evidence of heating by the electron-electron two-stream instability was found. However, an efficient mechanism for energy transfer to the plasma through the acceleration of the plasma ions was observed. Since the experiment began, other experiments have been performed and most of these experiments reported heating consistent with the excitation of the electron-electron instability. In this chapter, I wish to review the results reported by the other experimenters and to examine the hypothesis that their observed energy transfer was from mass motion rather than from heating via the two-stream instability.

10.2 Review of other Experiments

At the time the present experiment was begun, only one experiment had been reported in which electron beams with total currents of a kiloampere or more were used. Altyntsev, et al., (1971) used a 15 kA beam of 3 MeV electrons for 50 ns ($\nu/\gamma = 0.12$) to heat a magnetized plasma with $n_e \leq 10^{14}$ cm^{-3}. The principal diagnostic was a diamagnetic-pickup coil to measure NkT (the line energy density in the particles) and these measurements indicated an electron temperature of 10 to 100 keV, at $n_e = 10^{11}$ cm^{-3}.

Since that time, six other experiments have been initiated, and

preliminary results have been reported. A summary of the experiments is given in Table 11. All these experiments involved an axial magnetic field. In most of these experiments, the measurement of the energy transfer from the beam to the plasma was based on the diamagnetic signal. Additional measurements of the neutral atom energy and the x-ray emission have also indicated an energy transfer that was more than the classical value. In general, all of the other experiments measured an energy transfer that increased as the ratio of n_b to n_p was increased.

The primary diagnostic used in these experiments was the diamagnetic signal from ΔB_z near the wall of the drift tube. Hammer (1974) discusses the interpretation of these signals for application to high current relativistic electron beams. If one neglects the terms of second order in ΔB_z, assumes space-charge neutralization, and assumes that $d/dt = d/dz = d/d\theta = 0$, the diamagnetic signal is given by

$$\Delta B_z = \frac{\mu_o}{B_o R_w^2} \int_0^{R_b} (P_{rr} + P_{\theta\theta})\, r\, dr - \frac{1}{B_o}(\mu_o I_{net}/2\pi R_w)^2 \qquad (10\text{-}1)$$

where B_o is the applied axial field, I_{net} is the net current, R_w is the wall radius, and R_b is the beam-plasma radius. P_{ii} is the ii_{th} component of the momentum flow tensor given by

$$P_{ii} = \sum_j \int_{\underline{p}} p_i v_i\, f_j(\underline{r},\underline{p})\, d^3p \qquad (10\text{-}2)$$

where p_i and v_i are the i_{th} components of the momentum and velocity for the particles of the j_{th} species with the distribution function $f_j(\underline{r}, \underline{p})$. I_{net} is usually assumed to be zero and B_o and ΔB_z are measured to infer NkT_e from

$$P_{rr} = P_{\theta\theta} = nkT_e \quad \text{with } T_i = 0,$$
$$B_z = \frac{\mu_o NkT_e}{B_o R_w^2 \pi}, \qquad (10\text{-}3)$$

Table 11. Summary of experimental results by other workers. In the table, I_b is the beam current, V_b is the beam electron energy, τ_b is the beam duration, ν/γ is the ratio of the beam current to the Alfven current, n_b is the number density of the beam electrons, n_p is the initial plasma number density, T_{eo} is the initial plasma electron temperature, B_z is the applied axial magnetic field, and nkT is the inferred particle energy density.

Reference	I_b (kAmp)	V_b (MeV)	τ_b (ns)	ν/γ	n_b (10^{12} cm^{-3})	Gas	n_p (10^{14} cm^{-3})	T_{eo} (eV)	B_z (Tesla)	Diagnostic	Results
Altyntsev, et al. (1971)	10-15	3-4	50	0.12	--	H_2	0.001-1.	--	0.25	ΔB_z, neutral energy	$nkT \approx 10^{16}$ eV/cm^3 for $n_p = 10^{11}$/cm^3
Smith (1972)	4	2	50	0.05	0.02	H_2	0.02	--	0.03	ΔB_z	$nkT \approx 2 \times 10^{15}$ eV/cm^3
Kapetanakos and Hammer (1973)	40	0.4	50	1.5	1.	He	0.001-3.	<1	0.5	ΔB_z, piezo-electric probe	$nkT \approx 10^{17}$ eV/cm^3 at $n_p = 3 \times 10^{11}$/cm^3
Miller, et al. (1973)	50	0.35	60	2.	1.	H_2	0.01-5.	--	0.15	ΔB_z, x-ray emission	$nkT = 3 \times 10^{16}$ eV/cm^3 at $n_p = 5 \times 10^{12}$/cm^3 $nkT = 6 \times 10^{16}$ eV/cm^3 at $n_p = 10^{14}$/cm^3
Korn, et al. (1973)	60	0.5	60	2.2	1.	H_2	0.8	--	0.5	ΔB_z, neutral energy	$nkT = 2 \times 10^{17}$ eV/cm^3 at $n_p = 8 \times 10^{13}$/cm^3
Goldenbaum et al. (1973)	50	0.5	70	1.7	0.7	He	0.5-50.	5	0.5	ΔB_z, Thomson scattering, HeII intensity	Δn_p and light emission consistent with anomalous heating
Stallings, et al. (1972)	200-350	0.6	50	6-11	---	He	30.	--	0.6-1.	Soft x-ray spectrum	$nkT = 1.1 \times 10^{20}$ eV/cm^3

where $N = n_e \pi R_B^2$, the line number density of plasma particles. If T_i is not zero, then the signal also measures NkT_i.

Some interesting anomalies have accompanied these measurements. Korn, et al. (1973) reported that the diamagnetic signal decayed with discrete steps, which were accompanied by bursts of hard x-rays. This would indicate trapping of primary electrons in the magnetic well to give the large diamagnetic signal. If only 3% of the primary electrons were trapped in the magnetic well, their contribution to NkT would account for the entire signal.

However, when the end mirror was removed from the experiment reported by Korn, et al, the decay time of the signal was too long (2 μsec in a 150 cm long system) to be explained by end losses from fast electrons. They conclude that the signal is not from trapped beam electrons. This unusually long containment time in an open ended system was also observed by Stallings et al. (1972).

Almost everyone has reported that the energy loss from the beam (as measured by calorimetry) was approximately a factor of ten or more times that which was measured in the plasma by diamagnetic signals. Kapetanakos and Hammer (1973) also reported that the energy density measured by a piezoelectric probe was five times that measured by the diamagnetic signal. This disagreement in energy balance cannot be attributed to loss of primary electrons to the walls since lining the drift tube with tantalum produced no measurable rise in the hard x-ray signal, as reported by Stallings et al. (1972).

The long containment times and the discrepancies in the energy measurements can be explained if the energy were deposited in the ions rather than in the electrons.

10.3 Comparison of the Results of Other Experiments with the Mass Motion Model

To investigate the hypothesis that the observed NkT was caused by the ion motion in these experiments, a program called "STRNB" was written and is included in Appendix I. The simple program divided the beam and plasma region into ten concentric cylinders. Each cylinder had a radial thickness Δr. The motion of the ions in each segment was calculated.

The equation of motion for the plasma and the generalized Ohm's Law without the pressure terms and with the resistivity equal to zero gives

$$\frac{\partial \underline{v}_i}{\partial t} = \frac{1}{\rho} \underline{j}_p \times \underline{B} = \frac{ne}{\rho} (\underline{E} + \underline{v}_i \times \underline{B})$$

$$= \frac{e}{M_i} (\underline{E} + \underline{v}_i \times \underline{B})$$

for

$$\underline{E} = - v_{ze} B_\theta \hat{r}, \qquad \text{if } j_\theta B_z << j_z B_\theta .$$

Thus

$$\underline{E} = \frac{- v_{ze} \mu_o j_{net} r}{2} \hat{r}$$

since $\underline{B} = B_o \hat{z} + \frac{\mu_o j_{net} r}{2} \hat{r}$

for a beam with a uniform net current j_{net} and plasma current $j_{ze} = n e v_{ze}$, where v_{ze} is the electron drift velocity in the z direction. The above equation describes the motion of an ion with velocity $\underline{v}_i$ under the Lorentz force

$$\underline{F} = e\,(\underline{E} + \underline{v}_i \times \underline{B}) = M_i \frac{\partial \underline{v}_i}{\partial t}$$

where

$$\underline{E} = \frac{j_{ze} B_\theta \hat{r}}{ne} = \frac{\mu_o j_{ze} j_{net} r}{2\,n\,e}\,\hat{r}$$

and

$$\underline{B} = B_o\,\hat{z} + \frac{\mu_o\, j_{net} r}{2}\,\hat{r}$$

The motion of an ion on the boundary of each plasma segment was calculated. The perpendicular energy at t = 100 ns was then calculated by multiplying the energy in the motion, perpendicular to B_o (the applied magnetic field), of the representative ion by the number of particles in its plasma element and summing over all the elements. The calculation assumed that the net current was 5% of the beam current, unless the experimenter measured it. This value of 5% is a typical value for injection into a plasma. Charge exchange was neglected and all ions were assumed to be contained: i.e. the Larmor orbit did not intersect the wall. The experimenters' usual assumption of no additional ionization was respected. These assumptions were strictly true for the Cornell experiment only, since they had a fully ionized plasma, a sufficiently large vacuum vessel, and a sufficiently strong B_o to contain the ions. The experiment by Smith (1972) in a neutral gas at low pressure also approximated these assumptions adequately.

The results of these calculations are given in Table 12. It is obvious that the two experiments with conditions most appropriate to the assumptions of the calculation agreed quantitatively with the calculation, as well as scaled appropriately with the beam current. For the other experiments, the calculation predicted energy densities many times

Table 12. Comparison of the ion motion model with the heating results of other experiments. The experiments were selected on the basis of availablity of the experimental details with which to make the calculation.

Reference	B_z (Tesla)	I_b (10^3amps)	I_{net} (10^3amps)	R_{beam} (cm)	n_p ($10^{14}cm^{-3}$)	R_{max} (cm)	W_{calc} (Joules/m)	W_{exp} (Joules/m)
Korn, et al. (1973)	0.27	60.	3.	2.	0.1	9.5	60.	60.
		40.	2.	2.	0.1	6.0	18.	20.
		20.	1.	2.	0.1	3.2	1.5	1.3
Smith (1972)	0.06	4.	0.4	3.5	0.02	3.6	0.04	0.013
Miller and Kuswa (1973)	0.15	50.	2.5	1.5	0.1	14.	58.	0.33
					1.0	3.4	19.	0.55
					2.2	2.6	7.4	0.7
Kapetanakos and Hammer (1973)	0.18	40.	2.	2.5 (hollow)	1.	2.6	1.1	2.6
					0.1	4.4	21.	8.

the observed energy densities. The ions in those experiments were predicted to intersect the wall so most of the energy would have been lost from the plasma.

Korn, et al (1973) reported that whenever the diamagnetic loop signals increased, the ion energy measured by neutral particle energy analysis also increased. The energy equipartition time between the electrons and the ions is given by Spitzer (1962) as

$$t_{eq} = \frac{3 \times 10^7 \, T_e^{3/2}}{n_i}, \qquad \text{for } T_e >> T_i$$

for a hydrogen plasma with an ion density n_i cm^{-3} and an electron temperature T_e in eV. For the Cornell experiment, T_e was reported as 10 keV, $n_e \sim 10^{14}$ cm^{-3}, so t_{eq} = 0.3 seconds. It is difficult to understand how the ions acquired keV energies during the 10 μsec experiment if the energy was originally in the plasma electrons. If the energy was transferred directly to the ions, this measurement would be more reasonable.

The presence of the energy in the ions would also explain the anomalously long containment times for the energy in the open ended system, as mentioned in Section 10.2.

Consequently, the other experiments reported for beam-plasma heating with high-current relativistic electron beams in a strong axial magnetic field were consistent with energy transfer from the beam to the ions through the mass motion of the plasma.

APPENDIX I

COMPUTER PROGRAMS

Program SPECT was used to calculate the apparent electron velocity distribution from laser scattering as described in Section 5.3.

```
ØØ1ØØ PROGRAM SPECT (INPUT,OUTPUT)
ØØ11Ø DIMENSION C(2ØØØ)
ØØ12Ø XL=•1
ØØ13Ø YL=•7
ØØ14Ø 5Ø READ,SHIFT
ØØ15Ø DO 7Ø J=1,2ØØØ
ØØ16Ø 7Ø C(J)=Ø•
ØØ17Ø VMAX=((SHIFT+XL*•5)**2+(YL*•5)**2)**•5
ØØ18Ø DX=XL*•1
ØØ19Ø DY=YL*•Ø1
ØØ2ØØ DO 1Ø J=1,1ØØ
ØØ21Ø DO 1Ø K=1,1Ø
ØØ22Ø XX=K
ØØ23Ø YY=J
ØØ24Ø X=SHIFT-•5*XL+(XX-•5)*DX
ØØ25Ø Y=YL*•5-(YY-•5)*DY
ØØ26Ø V=(X+Y)/1•414
ØØ27Ø N=V*1ØØØ•/VMAX+1ØØØ•
ØØ28Ø 1Ø C(N)=C(N)+1•
ØØ29Ø DO 2Ø N=1,2Ø
ØØ3ØØ SPEC=Ø•
ØØ31Ø DO 3Ø K=1,1ØØ
ØØ32Ø 3Ø SPEC=SPEC+C(N*1ØØ-1ØØ+K)
ØØ33Ø 2Ø PRINT 4Ø,N,SPEC
ØØ34Ø 4Ø FORMAT(2X,I4,4X,F1Ø•2)
ØØ35Ø GO TO 5Ø
ØØ36Ø STOP
ØØ37Ø END
READY•
```

Program IONW was used to calculate the mass motion of the plasma as described in Section 7.5.

```
ØØ1ØØ PROGRAM IONW (INPUT,OUTPUT)
ØØ11Ø PRINT 4Ø
ØØ12Ø 4Ø FORMAT (2X,3ØHINPUT: XINET,XIB,RO,XNEO,XMI,P)
ØØ13Ø READ,XINET,XIB,RO,XNEO,XMI,P
ØØ14Ø XNGAS=3·54E22*P
ØØ15Ø XMFP=1·65E19/(XNGAS-XNEO*1·E2Ø)
ØØ16Ø R1=RO
ØØ17Ø R2=RO
ØØ18Ø NF=1ØØ
ØØ19Ø V=Ø·
ØØ2ØØ R=R1
ØØ21Ø DT=1·E-9
ØØ22Ø T=Ø·
ØØ23Ø WATT=Ø·
ØØ24Ø WION=Ø·
ØØ25Ø PRINT 1ØØ
ØØ26Ø DO 3Ø K=1,1Ø
ØØ27Ø WATOM=Ø·
ØØ28Ø M=Ø
ØØ29Ø V1=Ø·
ØØ3ØØ ALPHA=XINET*(XIB-XINET)*R1**2/(2·52E-6*XNEO*RO**4*XMI)
ØØ31Ø DO 1Ø J=1,NF
ØØ32Ø T=T+DT
ØØ33Ø DV=ALPHA*DT/R
ØØ34Ø V=V+DV
ØØ35Ø R=R+(V+·5*DV)*DT
ØØ36Ø IF(J-7Ø) 11Ø,12Ø,11Ø
ØØ37Ø 12Ø R7Ø=R
ØØ38Ø V7Ø=V
ØØ39Ø WI7Ø=·5E-8*XMI*V**2
ØØ4ØØ 11Ø IF(R-R2-XMFP) 1Ø,115,115
ØØ41Ø 115 R2=R
ØØ42Ø V=((XNEO*1·E2Ø*V**2+(XNGAS-XNEO*1·E2Ø)*V1**2)/XNGAS)**·5
ØØ43Ø V1=V
ØØ44Ø 75 WATOM=·5E-8*XMI*V1**2
ØØ45Ø M=M+1
ØØ46Ø 1Ø CONTINUE
ØØ47Ø WI=·5E-8*XMI*V**2
ØØ48Ø PRINT 2Ø,R1,R,V,WI,R7Ø,V7Ø,WI7Ø,M
ØØ49Ø WATT=WATT+WATOM*(XNGAS-1·E2Ø*XNEO)*3·14*(·2*R1*RO-
ØØ5ØØ+·Ø1*RO**2)
ØØ51Ø WION=WION+WI*1·E2Ø*XNEO*3·14*(·2*R1*RO-·Ø1*RO**2)
ØØ52Ø 2Ø FORMAT(2X,7(E1Ø·3),I3)
ØØ53Ø V=Ø·
ØØ54Ø R1=R1-·1*RO
ØØ55Ø R=R1
ØØ56Ø R2=R1
ØØ57Ø 3Ø T=Ø·
ØØ58Ø WATOM=WATT/(3·14*1·6E-3*XNGAS)
ØØ59Ø WION=WION/(3·14E2Ø*RO**2*XNEO)
ØØ6ØØ PRINT 8Ø,WATOM,WION
```

```
ØØ61Ø 8Ø FORMAT (2X,6HATOM=,E1Ø•3,2HEV,3X,5HWION=,E1Ø•3,2HEV)
ØØ62Ø PRINT 5ØØ
ØØ63Ø PRINT 1ØØ
ØØ64Ø 1ØØ FORMAT (5X,2HR1,9X,1HR,9X,1HV,9X,2HWI,8X,3HR7Ø,
ØØ65Ø+7X,3HV7Ø,6X,4HWI7Ø,3X,1HM)
ØØ66Ø R1=RO
ØØ67Ø R=R1
ØØ68Ø R2=R1
ØØ69Ø ALPHA=ALPHA*1ØØ•*XNEO/RO**2
ØØ7ØØ X=NF
ØØ71Ø WATT=Ø•
ØØ72Ø WION=Ø•
ØØ73Ø DO 5Ø K=1,1Ø
ØØ74Ø V1=Ø•
ØØ75Ø M=Ø
ØØ76Ø ALPHB=ALPHA*R1**2
ØØ77Ø DO 6Ø J=1,NF
ØØ78Ø T=T+DT
ØØ79Ø XNE=XNEO*(•5+T*1•E9/X)*1•E2Ø
ØØ8ØØ DV=ALPHB*DT/(R*XNE*1•E-2Ø)
ØØ81Ø V=V+DV
ØØ82Ø R=R+(V+•5*DV)*DT
ØØ83Ø IF(J-7Ø) 21Ø,22Ø,21Ø
ØØ84Ø 22Ø R7Ø=R
ØØ85Ø V7Ø=V
ØØ86Ø WI7Ø=•5E-8*XMI*V**2
ØØ87Ø 21Ø IF(R-R2-XMFP) 6Ø,65,65
ØØ88Ø 65 R2=R
ØØ89Ø V=((XNE*V**2+(XNGAS-XNE)*V1**2)/XNGAS)**•5
ØØ9ØØ V1=V
ØØ91Ø WATOM=•5E-8*XMI*V1**2*(XNGAS-XNE)
ØØ92Ø M=M+1
ØØ93Ø 6Ø CONTINUE
ØØ94Ø WI=•5E-8*XMI*V**2
ØØ95Ø PRINT 2Ø,R1,R,V,WI,R7Ø,V7Ø,WI7Ø,M
ØØ96Ø WATT=WATT+WATOM*3•14*(•2*R1*RO-•Ø1*RO**2)
ØØ97Ø WION=WION+WI*XNE*3•14*(•2*R1*RO-•Ø1*RO**2)
ØØ98Ø V=Ø•
ØØ99Ø R1=R1-•1*RO
Ø1ØØØ R=R1
Ø1Ø1Ø R2=R1
Ø1Ø2Ø 5Ø T=Ø•
Ø1Ø3Ø WATOM=WATT/(3•14*1•6E-3*XNGAS)
Ø1Ø4Ø WION=WION/(3•14*RO**2*XNE)
Ø1Ø5Ø PRINT 8Ø,WATOM,WION
Ø1Ø6Ø STOP
Ø1Ø7Ø 5ØØ FORMAT(2X,37HRESULTS FOR LIN RIS N FROM NF/2 TO NF)
Ø1Ø8Ø END
READY•
```

Program HEAT was used to calculate the energy density of the plasma electrons as described in Section 7.6.

```
ØØ1ØØ PROGRAM HEAT (INPUT,OUTPUT)
ØØ11Ø PRINT 31Ø
ØØ12Ø READ,XNO,XNF,TEO,RO,RF,XIMP,XJ1,TAU1,TAU2,TAU3,PR
ØØ13Ø PRINT 3Ø5
ØØ14Ø GO=Ø.
ØØ15Ø DT=1.E-9
ØØ16Ø AREA=3.14*RO**2
ØØ17Ø XNO=XNO*1.E2Ø
ØØ18Ø XNF=XNF*1.E2Ø
ØØ19Ø XIMP=XIMP*1.E3
ØØ2ØØ XJ1=XJ1*1.E3/AREA
ØØ21Ø TAU1=TAU1*1.E-9
ØØ22Ø TAU2=TAU2*1.E-9
ØØ23Ø TAU3=TAU3*1.E-9
ØØ24Ø 75Ø T=Ø.
ØØ25Ø W=XNO*2.4E-19*TEO
ØØ26Ø MMAX=1
ØØ27Ø M=1
ØØ28Ø TEMP=TEO
ØØ29Ø XNGAS=3.54E22*PR
ØØ3ØØ XNE=XNO
ØØ31Ø 11Ø T=T+DT
ØØ32Ø IF(T-TAU1) 1Ø,1Ø,2Ø
ØØ33Ø 1Ø XJP=XIMP*(T-.5*DT)/(TAU1*AREA)
ØØ34Ø GO TO 3Ø
ØØ35Ø 2Ø IF(T-1.E-7) 21,21,25
ØØ36Ø 21 XJP=XIMP*(1.-((T-.5*DT)-TAU1)/TAU2)/AREA
ØØ37Ø GO TO 3Ø
ØØ38Ø 25 IF(T-1.E-7-TAU1) 26,26,28
ØØ39Ø 26 XJP=-XJ1*(1.-((T-.5*DT)-1.E-7)/TAU3)
ØØ4ØØ 28 CONTINUE
ØØ41Ø 3Ø CONTINUE
ØØ42Ø ETA=1.75E-3/TEMP**1.5+.65E-5*(XNGAS-XNE)/XNE
ØØ43Ø IF (GO) 6ØØ,6Ø1,6ØØ
ØØ44Ø 6ØØ ETA=ETA+5.E6/XNE**.5
ØØ45Ø 6Ø1 CONTINUE
ØØ46Ø DW=ETA*XJP**2*DT
ØØ47Ø W=W+DW
ØØ48Ø WTOT=W*AREA
ØØ49Ø R=RO+T*1.E7*(RF-RO)
ØØ5ØØ AREA1=3.14*R**2
ØØ51Ø WTOT=WTOT*(AREA/AREA1)**1.57
ØØ52Ø AREA=AREA1
ØØ53Ø XN=XNE
ØØ54Ø XNE=XNO+(XNF-XNO)*T*1.E7
ØØ55Ø TRY=(XNE-XN)*3.E-18*AREA
ØØ56Ø IF(WTOT-2.*TRY) 8ØØ,8Ø1,8Ø1
ØØ57Ø 8ØØ XNE=XN+WTOT/(6.E-18*AREA)
ØØ58Ø 8Ø1 CONTINUE
ØØ59Ø WTOT=WTOT-(XNE-XN)*3.E-18*AREA
ØØ6ØØ W=WTOT/AREA
ØØ61Ø TEMP=4.17E18*W/XNE
```

```
ØØ62Ø T=T+DT
ØØ63Ø IF(M-MMAX) 2ØØ,2Ø1,2ØØ
ØØ64Ø 2Ø1 M=Ø
ØØ65Ø MMAX=1Ø
ØØ66Ø XT=T*1.E9
ØØ67Ø XN=XNE*1.E-6
ØØ68Ø XW=W/1.6E-13
ØØ69Ø PRINT 3ØØ,XT,XN,XW
ØØ7ØØ 2ØØ IF(T-1.1E-7)4ØØ,4ØØ,4Ø5
ØØ71Ø 4ØØ M=M+1
ØØ72Ø GO TO 11Ø
ØØ73Ø 4Ø5 IF (GO) 7ØØ,7Ø1,7ØØ
ØØ74Ø 7Ø1 PRINT 76Ø
ØØ75Ø GO=1.
ØØ76Ø GO TO 75Ø
ØØ77Ø 7ØØ STOP
ØØ78Ø 31Ø FORMAT(2X,34HINPUT: XNO,XNF,TEO,RO,RF,XIMP,XJ1
ØØ79Ø+,17HTAU1,TAU2,TAU3,PR)
ØØ8ØØ 3Ø5 FORMAT(4X,1HT,9X,7HN(CM-3),7X,9HW(EV/CM3))
ØØ81Ø 3ØØ FORMAT(2X,F5.1,5X,E1Ø.3,5X,E1Ø.3)
ØØ82Ø 76Ø FORMAT (2X,26HRESULTS WITH IA RES. ADDED)
ØØ83Ø END
READY.
```

The program STRNB was used to calculate the directed ion energy with an applied B_z as described in Section 10.3.

```
ØØ1ØØ PROGRAM STRNB (INPUT,TAPE6,OUTPUT)
ØØ11Ø DIMENSION R(3,1Ø),V(3,1Ø),XNT(1Ø),XL(1Ø),W(1Ø),WP(1Ø)
ØØ12Ø+,RMAX(1Ø),TMAX(1Ø)
ØØ13Ø PRINT 15Ø
ØØ14Ø READ,DT,XINET,XIB,R1,XNE,BZ,TEND
ØØ15Ø DT=DT*1.E-9
ØØ16Ø TEND=TEND*1.E-9
ØØ17Ø XINET=XINET*1.E3
ØØ18Ø XIB=XIB*1.E3
ØØ19Ø XNE=XNE*1.E2Ø
ØØ2ØØ DR=.1*R1
ØØ21Ø XMI=1.6E-27
ØØ22Ø A=1.6E-19/XMI
ØØ23Ø MMAX=1Ø
ØØ24Ø M=1
ØØ25Ø PRINT 155
ØØ26Ø 155 FORMAT (2X,6X,1HT,11X,6HWTOTAL,4X,13HWPERP    (J/M))
ØØ27Ø DO 1Ø J=1,1Ø
ØØ28Ø X=J
ØØ29Ø R(1,J)=DR*X
ØØ3ØØ R(2,J)=Ø.
ØØ31Ø R(3,J)=Ø.
ØØ32Ø V(1,J)=Ø.
ØØ33Ø V(2,J)=Ø.
ØØ34Ø V(3,J)=Ø.
ØØ35Ø TMAX(J)=Ø.
ØØ36Ø RMAX(J)=X*DR
ØØ37Ø WP(J)=Ø.
ØØ38Ø W(J)=Ø.
ØØ39Ø XL(J)=Ø.
ØØ4ØØ 1Ø XNT(J)=3.14*DR**2*(2.*X-1.)*XNE
ØØ41Ø VD=(XIB-XINET)/(3.14*R1**2*XNE*1.6E-19)
ØØ42Ø T=Ø.
ØØ43Ø 2Ø T=T+DT
ØØ44Ø B2=2.E-7*XINET/R1**2
ØØ45Ø DO 3Ø J=1,1Ø
ØØ46Ø IF(R(1,J)-R1) 4Ø,4Ø,41
ØØ47Ø 4Ø BTHET=B2*R(1,J)
ØØ48Ø GO TO 42
ØØ49Ø 41 BTHET=B2*(R1**2)/R(1,J)
ØØ5ØØ 42 ER=VD*BTHET
ØØ51Ø DVR=DT*A*(ER+V(2,J)*BZ+V(3,J)*BTHET)
ØØ52Ø DVT=-DT*A*V(1,J)*BZ
ØØ53Ø DVZ=-DT*A*V(1,J)*BTHET
ØØ54Ø DXR=DT*(V(1,J)+.5*DVR)
ØØ55Ø DXT=DT*(V(2,J)+.5*DVT)
ØØ56Ø DXZ=DT*(V(3,J)+.5*DVZ)
ØØ57Ø V(1,J)=V(1,J)+DVR
ØØ58Ø V(2,J)=V(2,J)+DVT
ØØ59Ø V(3,J)=V(3,J)+DVZ
ØØ6ØØ R(1,J)=R(1,J)+DXR
```

```
ØØ61Ø R(2,J)=R(2,J)+DXT
ØØ62Ø R(3,J)=R(3,J)+DXZ
ØØ63Ø IF(RMAX(J)-R(1,J)) 2ØØ,2Ø1,2Ø1
ØØ64Ø 2ØØ RMAX(J)=R(1,J)
ØØ65Ø TMAX(J)=T
ØØ66Ø 2Ø1 CONTINUE
ØØ67Ø DL=(DXR**2+DXT**2+DXZ**2)**.5
ØØ68Ø XL(J)=XL(J)+DL
ØØ69Ø W(J)=(V(1,J)**2+V(2,J)**2+V(3,J)**2)*.5*XMI
ØØ7ØØ 3Ø WP(J)=(V(1,J)**2+V(2,J)**2)*.5*XMI
ØØ71Ø IF(MMAX-M) 5Ø,5Ø,6Ø
ØØ72Ø 6Ø M=M+1
ØØ73Ø GO TO 2Ø
ØØ74Ø 5Ø M=1
ØØ75Ø WOUT=Ø.
ØØ76Ø WPOUT=Ø.
ØØ77Ø DO 7Ø J=1,1Ø
ØØ78Ø WOUT=WOUT+W(J)*XNT(J)
ØØ79Ø 7Ø WPOUT=WPOUT+WP(J)*XNT(J)
ØØ8ØØ PRINT 8Ø,T,WOUT,WPOUT
ØØ81Ø 8Ø FORMAT (2X,3(2X,E1Ø.3))
ØØ82Ø IF(T-TEND) 2Ø,1ØØ,1ØØ
ØØ83Ø 1ØØ PRINT 115
ØØ84Ø DO 12Ø J=1,1Ø
ØØ85Ø W(J)=W(J)/1.6E-19
ØØ86Ø WP(J)=WP(J)/1.6E-19
ØØ87Ø 12Ø PRINT 11Ø,J,W(J),WP(J),XL(J),RMAX(J),TMAX(J)
ØØ88Ø 11Ø FORMAT (2X,I3,4(3X,E12.4),1X,E1Ø.3)
ØØ89Ø 115 FORMAT (3X,1HJ,7X,5HW(EV),9X,6HWP(EV),11X,
ØØ9ØØ+4HL(M),1ØX,7HRMAX(M),9X,7HTMAX(S))
ØØ91Ø 15Ø FORMAT (2X,32HINPUT: DT,XINET,XIB,RBEAM,XNE,BZ)
ØØ92Ø STOP
ØØ93Ø END
READY.
```

APPENDIX II

OTHER WORK PERFORMED DURING THE COURSE OF THE EXPERIMENT

Preliminary Study of a Blumlein-Driven Z-Pinch

J. Pace VanDevender

Introduction

During the last decade, pulsed power research has lead to systems containing 3 megajoules of energy with the capability of producing an output of 3 (10^{13}) watts for 100 ns. These low-impedance, pulse-charged transmission lines can be used to drive a small z-pinch and produce a plasma similiar to that produced in a plasma focus, but with considerably less energy expended.

The experiment reported below is an attempt to investigate the feasibility of using a transmission line to drive a small unstabilized z-pinch with an existing 6 ohm, 6 kilojoule Blumlein at Imperial College.

The questions to be treated are summarized below.

1) Is the wall time, i.e. the time taken to form the current sheath and move it off the wall, shorter than the 100 ns cureent pulse from these machines?
2) Is a uniform current sheath formed with such a large dI/dt?
3) What is the scaling of sheath velocity with current?
4) Is there a pre-cursor to the sheath (either a shock or a free particle precursor)?
5) How important is asymmetry in the current feeds to the pinch?
6) How severe is high voltage breakdown in these devices?

The experiment is rather crude since the rapid modification of the relativistic electron beam generator necessitated some unfortunate experimental problems. However, the results can be intrepreted to give tentative answers to the above questions.

Experimental Arrangements

Three arrangements were attempted as shown in Figure 1. The first (a) configuration consisted of placing a pinch tube in the diode to replace the cathode

stalk. This resulted in an arc forming along the path of minimum inductance and sweeping away from the Blumlein. Consequently, a more co-axial feed to the pinch tube was required.

Configuration (b) is the one that produced the results in this report. The pinch tube (8 cm diameter by 17 cm long) was taken into a perspex tube 15 cm diameter by 30 cm long, to extend the current return into a more co-axial geometry. The outside of the tube was covered with copper gauze to form the current return. This arrangement increased the inductance of the current feeds considerably and, therefore, severely limited the current obtainable from the Blumlein during the 100 ns pulse. The space surrounding the pinch tube was flooded with SF_6 to prevent high-voltage breakdown. The filling pressure of hydrogen in the pinch tube was approximately 10 mTorr, although the monitoring system made that measurement uncertain. After several discharges, O-ring material was found on the walls; thus the composition of the plasma was in question.

Diagnostics consisted of a current monitor, an image-converter camera in the streak mode for radius vs. time, and a photodiode looking axially at the volume within a centimeter of the axis.

Pre-ionization of the pinch was accomplished by partially charging half the Blumlein through the pinch tube. At these pressures, an arc formed along the wall. Consequently, the pre-ionization was not uniform.

A third arrangement similiar to (b) was used. The pre-ionization was done by a separate capacitor bank (0.5 uf at 30 kV), and the perspex pinch tube was replaced with a pyrex one. This arrangement suffered high-voltage flashover along the outside of the pyrex and no useful information was obtained.

Data

Figure 2 shows the streak photographs for a maximum current of 33, 42, and 54 kA for 2a through 2c respectively. At less current, no luminosity was recorded on the photographs.

Figure 3 shows the photodiode and camera monitor signals for maximum currents of 15, 33, 42, and 54 kA in 3a through 3d respectively. The current waveform is also shown in figure 3e for comparison . Note the voltage scales on 3a and 3b are ten times as sensitive as that on 3c and 3d.

Results and Interpretations

Pre-ionization and Sheath Uniformity: In the streak photographs, the bright line preceding the discharge is the light caused by the arc during the pre-ionization. The arc is located on the side closer to the Blumlein and, consequently, along the path of minimum inductance. Presumably, the current flow during the main pulse has a similiar asymmetry. The side toward the Blumlein shows a shorter wall time, a larger initial sheath velocity, and a more uniform sheath. The problems of wall time and sheath formation may be helped by better pre-ionization and more symmetric current feeds. Nevertheless, the fact that the discharge does not re-strike at the walls when the second large current pulse begins at t = 400 ns indicates that the sheath has swept up most of the gas in its path.

Wall Time: An enlargement of the photographs and correction for the 3 mm slit width gives a wall time of 30 to 50 ns for the side closer to the Blumlein. With adequate pre-ionization, the wall time should be reduced to acceptable limits for a 100 ns pulse.

Initial Sheath Velocity: The sheath velocity during the first 100 ns of the current pulse is 9 (10^6) and 6.7 (10^6) cm/sec for the 54 kA and 42 kA cases respectively. This gives a scaling of $v \propto I^{1.2 \pm .4}$ assuming a $v \propto I^n$ law. After the main current pulse

the sheath velocity drops rapidly.

Precursor Velocity: The axial luminosity indicates arrival of plasma at r = 1 cm in 130 ns from the beginning of the current pulse, as shown in region C from 130 to 400 ns in Figure 3e. This gives a velocity of 2.0 (10^7) cm/sec and is the same for both the 54 and 42 kA cases, although the rise in luminosity is more rapid for the 54 kA case. This velocity is two times the sheath velocity for the 54 kA case and three times that for the 42 kA case. This velocity seems too large to be consistent with either the free particle model or the shock model for the precursor. Note that the peak axial luminosity does not correspond either to peak current or to peak brightness from the streak camera photographs. Wall light is thus excluded as an explanation of the luminosity. The luminosity from the arrival of the sheath in the field of view is shown as region D for $t \geq 720$ ns in Figure 3e.

Conclusions

From these results the following conclusions can be drawn: 1) For adequate pre-ionization and for symmetric current feeds, the wall time can be reduced to an acceptable level for a 100 ns current pulse. 2) A current sheath does form and does sweep up the plasma in the necessary time with a large dI/dt and is expected to be sufficiently uniform with adequate pre-ionization and current feeds. 3) The scaling of the sheath velocity with current is approximately linear. 4) There is a pre-cursor in front of the current sheath with a velocity more than twice the sheath velocity. 5). An improved design for lower inductance, greater symmetry, and greater protection from surface tracking is required to use the generator efficiently. It may be necessary to put the pinch tube in the water for the strip-line systems and to orient the pinch axis along the transmission line's axis of symmetry.

Acknowledgements

I gratefully acknowledge J. C. Martin and his associates at AWRE for their assistance in establishing a pulsed power facility at I. C. and for discussions on transmission-line driven plasma devices. I also wish to thank A. E. Dangor, A. Folkierski, and D. E. Potter of I. C. for helpful discussions related to a Blumlein driven z-pinch and J. D. Kilkenny of I. C. for helpful consultations and assistance with the experiment. I also appreciate the loan of the STL image-converter camera from Culham Laboratory for these measurements.

Figure Captions

Figure 1. Schematic views of two of the schemes used to couple a Blumlein to a z-discharge.

Figure 2. Streak camera photographs showing sheath radius as a function of time for three peak currents of 30, 42, and 54 kA for a, b, and c respectively. The approximate current waveform is given in d.

Figure 3. Photo-diode traces of luminosity on axis as a function of time and the streak-camera monitor for the 15, 30, 42, and 54 kA shots in a through d respectively. Figure 3e compares the luminosity for the 54 kA shot with the current waveform and shows the sources of axial luminosity as follows: A) the wall light during pre-ionization, B) light from the sheath near the wall during the main current pulse, C) the light from the precursor as it enters the axial volume, and D) the light from the main sheath as it enters the axial region.

Figure 1

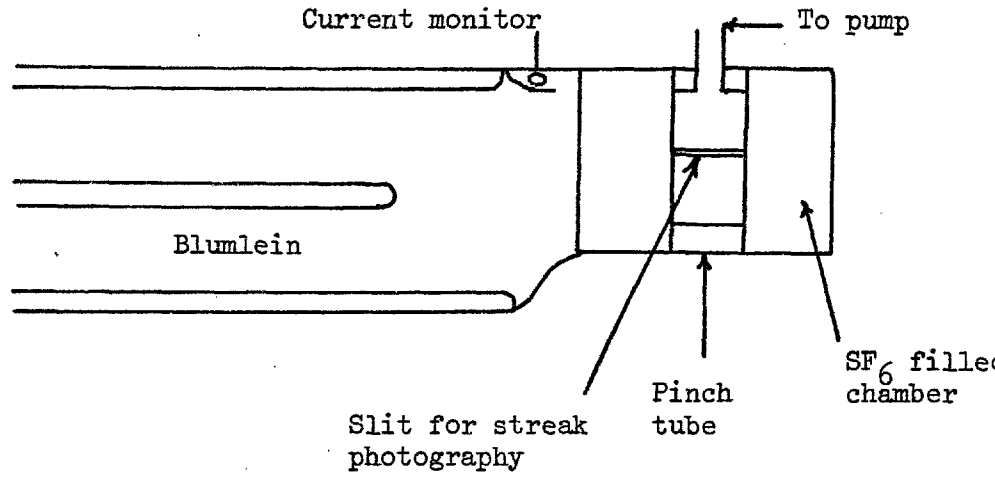

a. Experimental arrangement No. 1

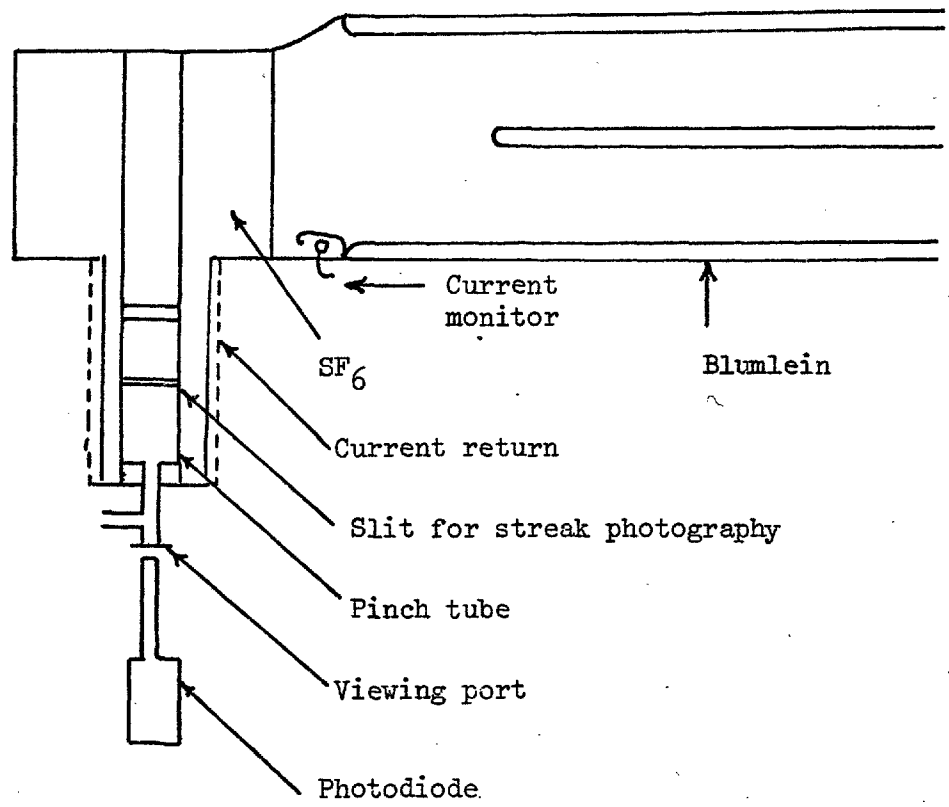

b. Experimental arrangement No. 2

Figure 2

2a

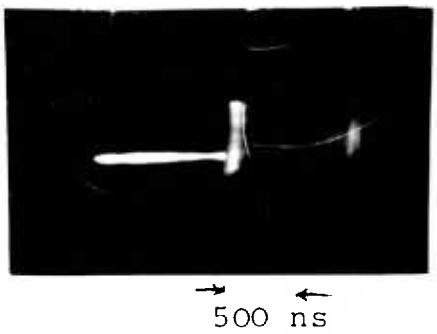

Shot 2
I_{max} = 30 kA

2b

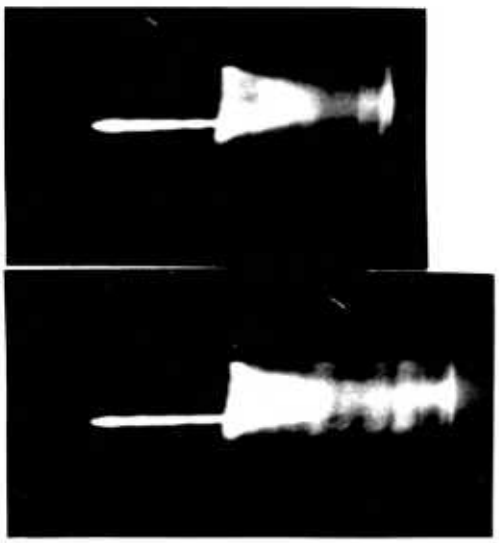

Shot 3
I_{max} = 42 kA

Shot 5
I_{max} = 42 kA

2c

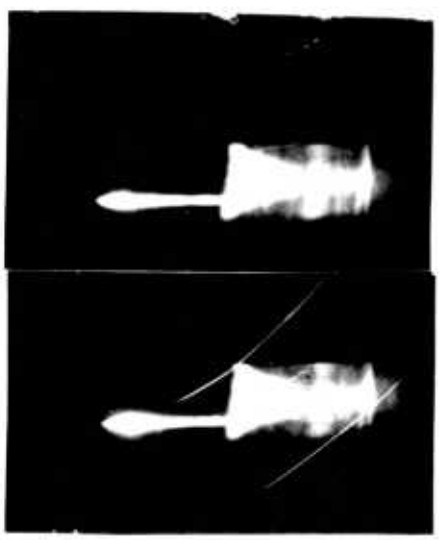

Shot 4
I_{max} = 55 kA

Shot 6
I_{max} = 54 kA

2d

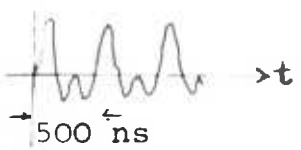

I(t) waveform

Figure 3

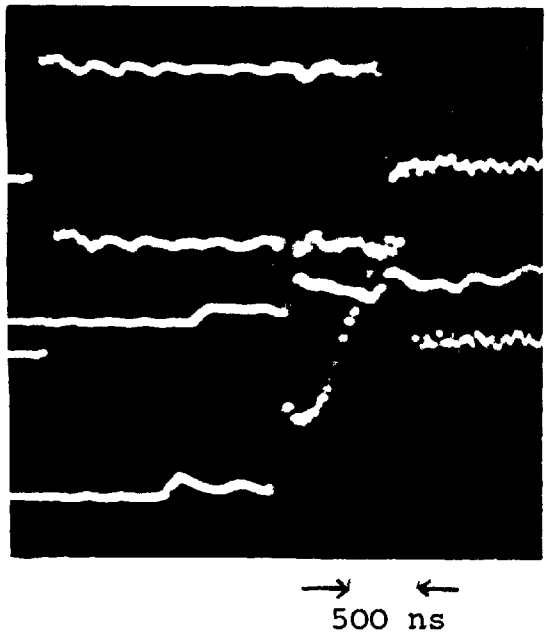

Top traces are from the Streak camera monitor; bottom traces are from the photo-diode on axis.

3a. Shot 1
I_{max} = 15 kA
Photodiode scale: 0.1 v/cm

3b. Shot 2
I_{max} = 30 kA
Photodiode scale: 0.1 v/cm

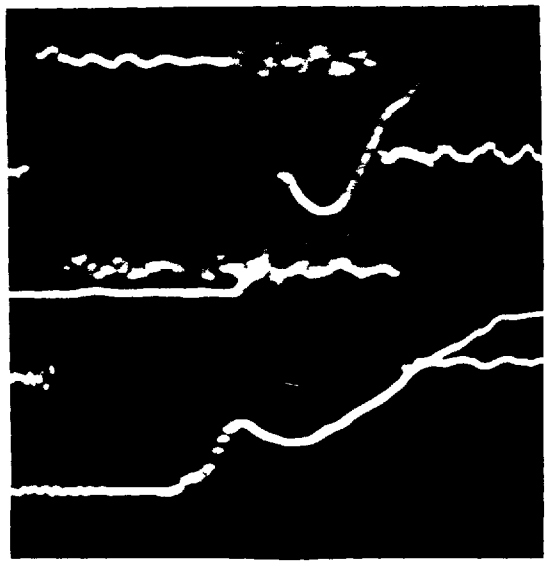

3c. Shot 6
I_{max} = 54 kA
Photodiode scale: 1.0 v/cm

3d. Shot 5
I_{max} = 42 kA
Photodiode scale: 1.0 v/cm

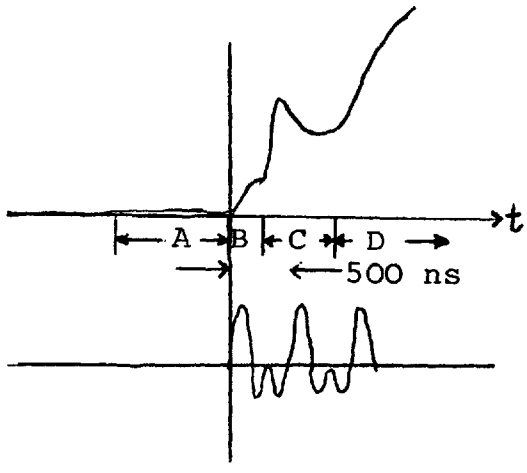

3e. Shot 6 Axial light

I(t) waveform

An Interpretation of the Luminous Halo around a High-Current Relativistic Electron Beam Propagating into a Neutral Gas

J. Pace VanDevender

Abstract

The gross behavior of a 30 kA, 600 keV electron beam is studied as a function of the initial pressure of hydrogen from 60 mTorr to 1 Torr. The luminosity was observed to be composed of a bright column with a radius r_1 approximately equal to the beam radius and a less bright halo extending to r_2. The radius r_1 is interpreted as the radius of the plasma current channel and r_2 as the maximum radius of ions accelerated by $\underline{E}_r = -\underline{v}_d \times \underline{B}$, with $\underline{v}_d$ the plasma electron drift velocity. The radius r_2 gives a maximum ion energy of 270 eV for the low pressure case, in agreement with a simple theory. Ion energies of 10 keV are expected from modest electron beams.

Introduction

During a recent seminar by John Nation on high-current relativistic electron beams, M. G. Haines commented that electrical neutrality cannot be established simultaneously in the rest frames of all particles (i.e. the beam electrons, the plasma electrons, and the ions). John Nation later elaborated upon this idea to show that there is a non-zero radial electric field in the laboratory (ion) frame. Some experimental support for ion acceleration in this radial electric field is obtained from the radius of the luminosity surrounding the beam-plasma channel in beam-propagation experiments. This mechanism offers a promising means of heating ions to energes of several tens of keV with high-current relativistic electron beams, without relying on streaming instabilities.

Theory

When a beam of current I_b is injected into a neutral gas, the gas is ionized by the beam through an avalanche process in the induced axial electric field. Soon after avalanching, the plasma of density n_p is heated to give a magnetic diffusion time long compared to the beam's rise time. The existing current is then maintained as the net current for the system. The plasma current I_p is evidently $I_b - I_{net}$, the beam current minus the net current. The net velocity of the plasma electrons is $v_d = j_p/n_p e$ in the opposite direction from the beam electrons. The force $-e\underline{v}_d \times \underline{B}$ expels the plasma electrons until a radial electric field $\underline{E}_r$ is established to give force neutrality for the plasma electrons.

$$\underline{E}_r + \underline{v}_d \times \underline{B} = 0$$

$$v_d = j_p/n_p e = (I_b - I_{net})/ r_1^2 n_p e$$

$$\underline{B} = I_{net}\, r/2\, r_1^2 \; e$$

for a uniform beam with radius r_1. Consequently, for $r \ll r_1$

$$E_r = \frac{I_{net}(I_b - I_{net})\, r}{2\pi^2 e r_1^4 n_p} .$$

The energy of an ion that has traveled from r_i to r for r much less than an ion Larmor radius is

$$\begin{aligned} W(r_i, r) &= \int_{r_i}^{r} eE_r \, dr \\ &= \frac{e\mu_o I_{net}(I_b - I_{net})(r^2 - r_i^2)}{4\pi^2 e r_1^4 n_p} \\ &= .5 M v^2 . \end{aligned}$$

Therefore, the ion velocity v at r is given by

$$v(r) = \frac{I_{net}(I_b - I_{net})^{.5}}{2\pi^2 M r_1^4 n_p} (r^2 - r_i^2)^{.5}$$

with M the ion mass. For $r_i \ll r$, we have upon integration

$$r(t) = r_i \exp\left[\left(\frac{\mu_o I_{net}(I_b - I_{net})}{2\pi^2 M r_1^4 n_p}\right)^{1/2} t\right].$$

The ions with maximum energy are those that reach r_1 at $t = \tau_b$, the beam duration, since they are accelerated in the largest electric field for the longest time. Consequently,

$$\begin{aligned} W_{max} &= W(r_i(r_1, \tau_b), r_1) \\ &= W_o (1 - \exp(-(8 W_o / M r_1^2)^{.5} \tau_b)) \end{aligned}$$

with $$W_o = \frac{\mu_o I_{net}(I_b - I_{net})}{4\pi^2 r_1^2 n_p}$$

For a modest beam with $I_b = 10^5$ amps, $r_1 = .01$ meters, $I_{net} = .5\ I_b$, $n_p = 5\ (10^{20})\ m^{-3}$, and $\tau_b = 100$ ns (approximately the situation for injection into 100 mTorr neutral hydrogen), $W_{max} = 10$ keV.

The ions leave the plasma region and E_r and continue in the magnetic field B_θ of the net current to a maximum radius equal to the Larmor radius of the ions with energy W_{max}. The ionization produced by these ions causes the luminosity to radius r_2. Consequently, the radius of the halo around the plasma channel is a measure of W_{max} as given by

$$W_{max} = \frac{1}{2} M v^2 \approx \frac{1}{2} M (e r_2 B_{av}/M)^2$$

$$\approx \frac{1}{2M} \left[\frac{e \mu_o I_{net}}{4}\left(1 + \frac{r_2}{r_1}\right)\right]^2 .$$

To compare the two values, one needs to know the number density n_p. From equating the two expressions for W_{max}, the effective average number density is found and can be compared with that obtained from laser scattering.

Experimental Apparatus

Figure 1 is a schematic view of the experimental arrangement. The beam generator is a water dielectric Blümlein with a 20 ohm matched load. A .001 inch thick aluminum foil serves as the anode, which apparently increases the plasma luminosity from that observed with the usual Al-mylar foil. The beam is approximately uniform and has a radius of 3.5 cm at the anode.

The 30 kA, 600 keV, 100 ns electron beam is injected into a drift tube 2 meters long with an inside diameter of 15 cm. It is lined with copper mesh and terminated with an aluminum plate. A shielded Rogowski coil measures the net current and is located 20 cm from the anode.

and is at a radius of 6 cm. The top and side views of the tube are taken on each shot. The x-ray pattern on the end plate is photographed with a four aperature pinhole camera.

Results

Figure 2 shows the open shutter photographs and Figure 3 shows the radii of the central luminosity r_1 and of the halo r_2 as a function of pressure. The x-ray pinhole photographs identify the radius r_1 as the beam radius. Figure 3 is a plot of the net current as a function of pressure.

Using the values of I_{net}, I_b, r_1, and r_2, we have

P_o (mtorr)	W_{max} (eV)	n_p (10^{13} cm^{-3})	$n'/2$ (10^{13} cm^{-3})
60	270	9.3	10
350	70	17	22
500	25	23	28
900	23	29	44

for n_p given from r_2 and n' given by scaling the number density at 100 ns measured for injection at the appropriate pressure for a beam of 12 kA/cm^2. The value is weighted by the energy available for ionization, which is assumed to be proportional to j_p^2. Since the theory gives an average n_p, n' is divided by 2 for comparison with n_p. The agreement is taken to support this explanation for the halo and support the general mechanism for ion acceleration.

The applicability of the theory depends on the ion collision time, which must be greater than or equal to the beam duration. From Spitzer(1), the time taken for the energy of an ion to be lost by collisions is given by

$$\tau_E = 2.5\ (10^{-13})\ v^3/n_p \text{ sec}$$

with v and n_p given in cgs units.

For $n_p = 10^{14}$ cm^{-3} and $\tau_E \geq 10^{-7}$ sec, we have $v = 3.4\ (10^6)$ cm/sec. At 100 ns, $v_{max} = 2\ (10^7)$ cm/sec for the 60 mTorr case, so this criteria is satisfied. Finally, the radial ion current is only a few per cent of the plasma current and need not be considered in the mechanism.

Conclusion

The halo around the beam channel is consistent with ion acceleration in the radial E field in the beam-plasma channel. With more powerful beams of smaller radius, ion energies of 10 to 100 keV may be expected. An experiment to measure the ion energy perpendicular to the beam should be done.

Acknowledgements

Acknowledgement to M. Haines and J. Nation has already been made for pointing out that the radial electric field is non-zero. I also wish to thank J. C. Martin and his colleagues at AWRE for their kind assistance in establishing an electron beam facility at Imperial College, J. Westlake for his technical support, and A. E. Dangor for helpful discussions.

References

1. L. Spitzer, Physics of Fully Ionized Gasses (Interscience, New York, 1962), p. 132.

Figure Captions

Figure 1. Schematic view of apparatus.

Figure 2. Top and side views of experiment for 60 mTorr, 500 mTorr, and 900 mTorr neutral hydrogen taken with open-shutter photography.

Figure 3. Plot of r_1 and r_2, the radius of the plasma channel and the radius of the luminous halo, respectively, as a function of filling pressure.

Figure 4. Plot of net current as a function of filling pressure.

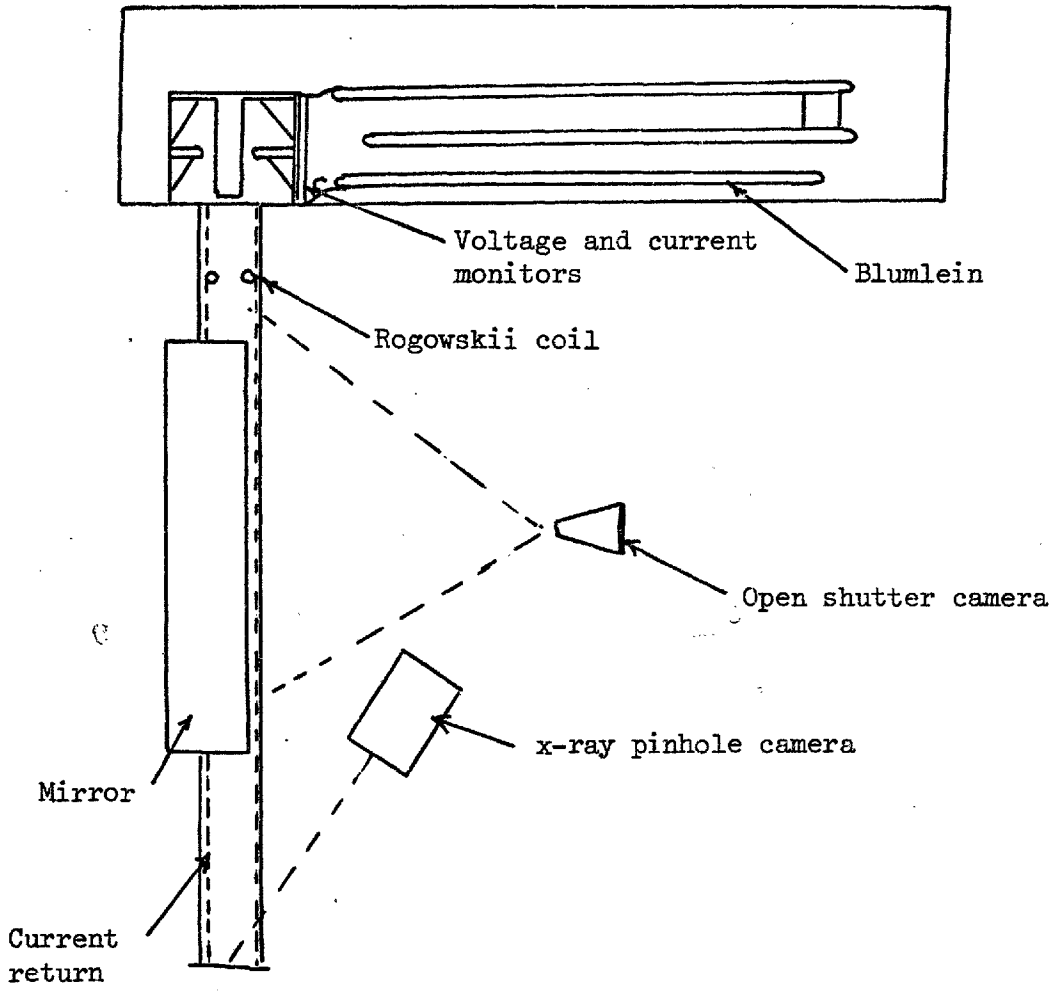

Figure Experimental arrangement.

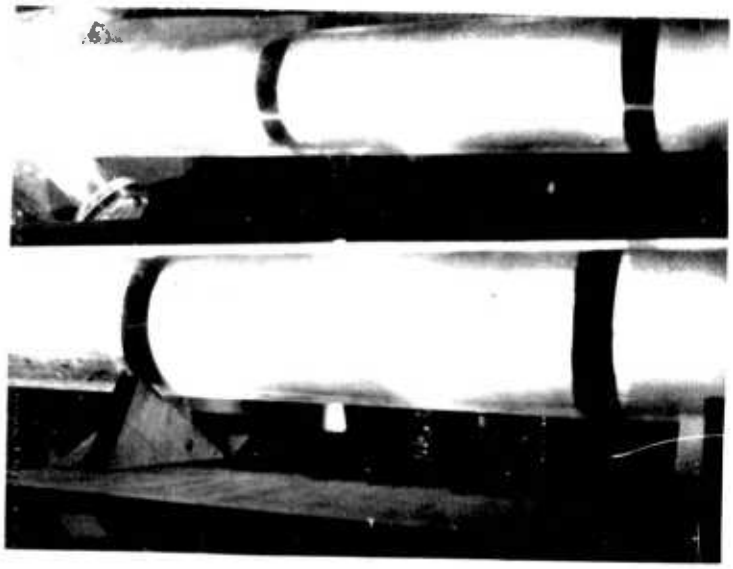

P = 60 mTorr

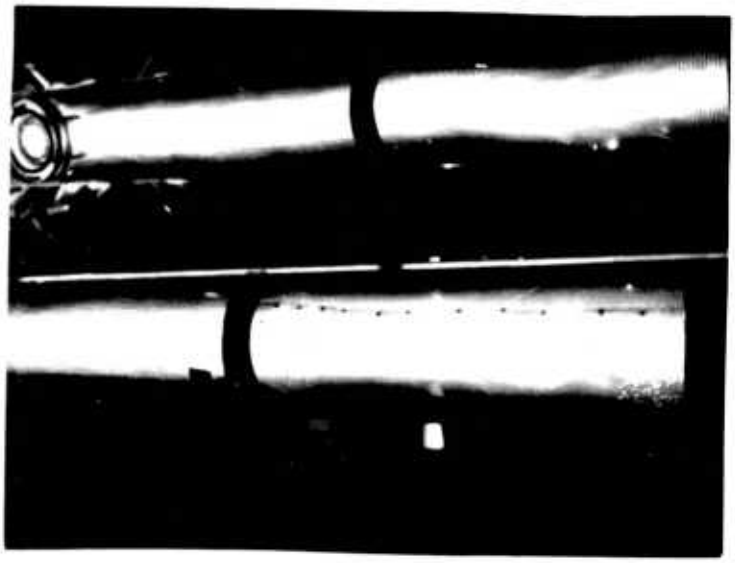

P = 500 mTorr

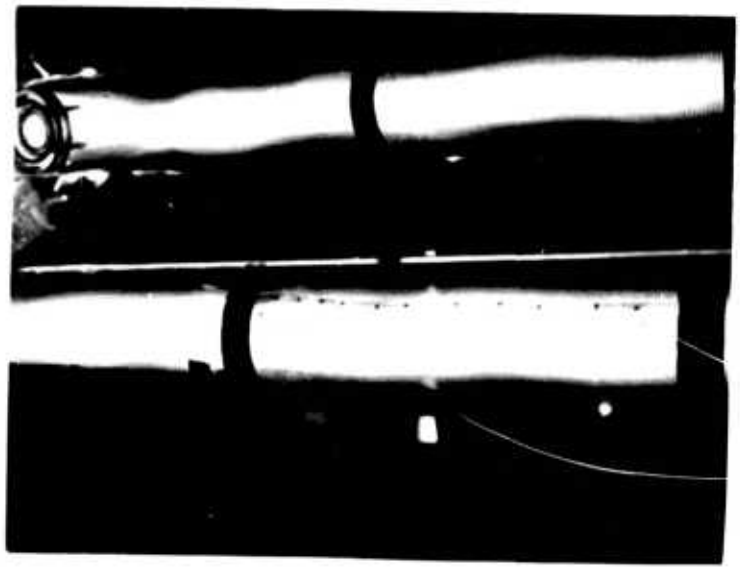

P = 900 mTorr

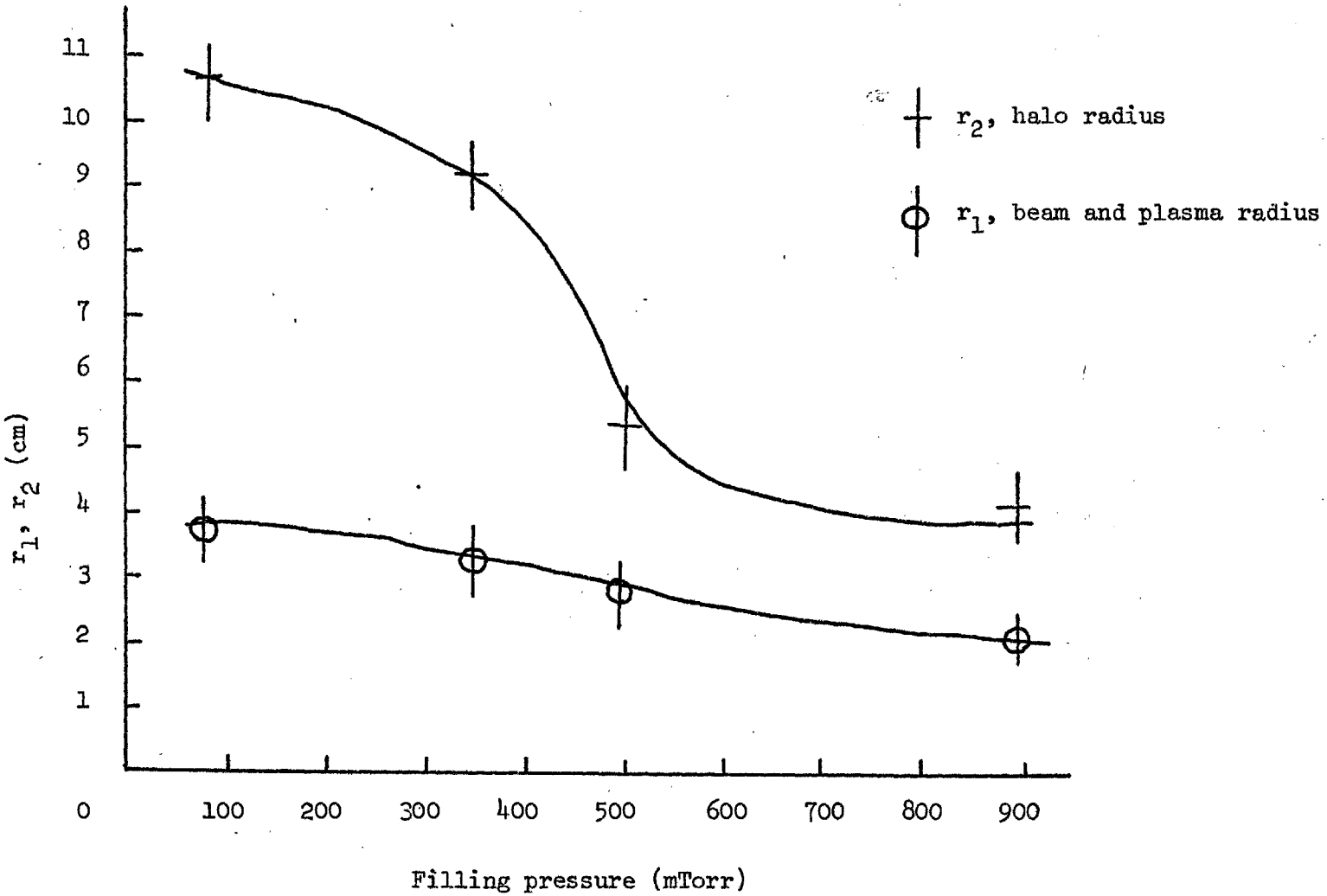
11
10
9
8
7
6
5
4
3
2
1
0
100
200
300
400
500
600
700
800
900
r_1, r_2 (cm)
Filling pressure (mTorr)
r_2, halo radius
r_1, beam and plasma radius

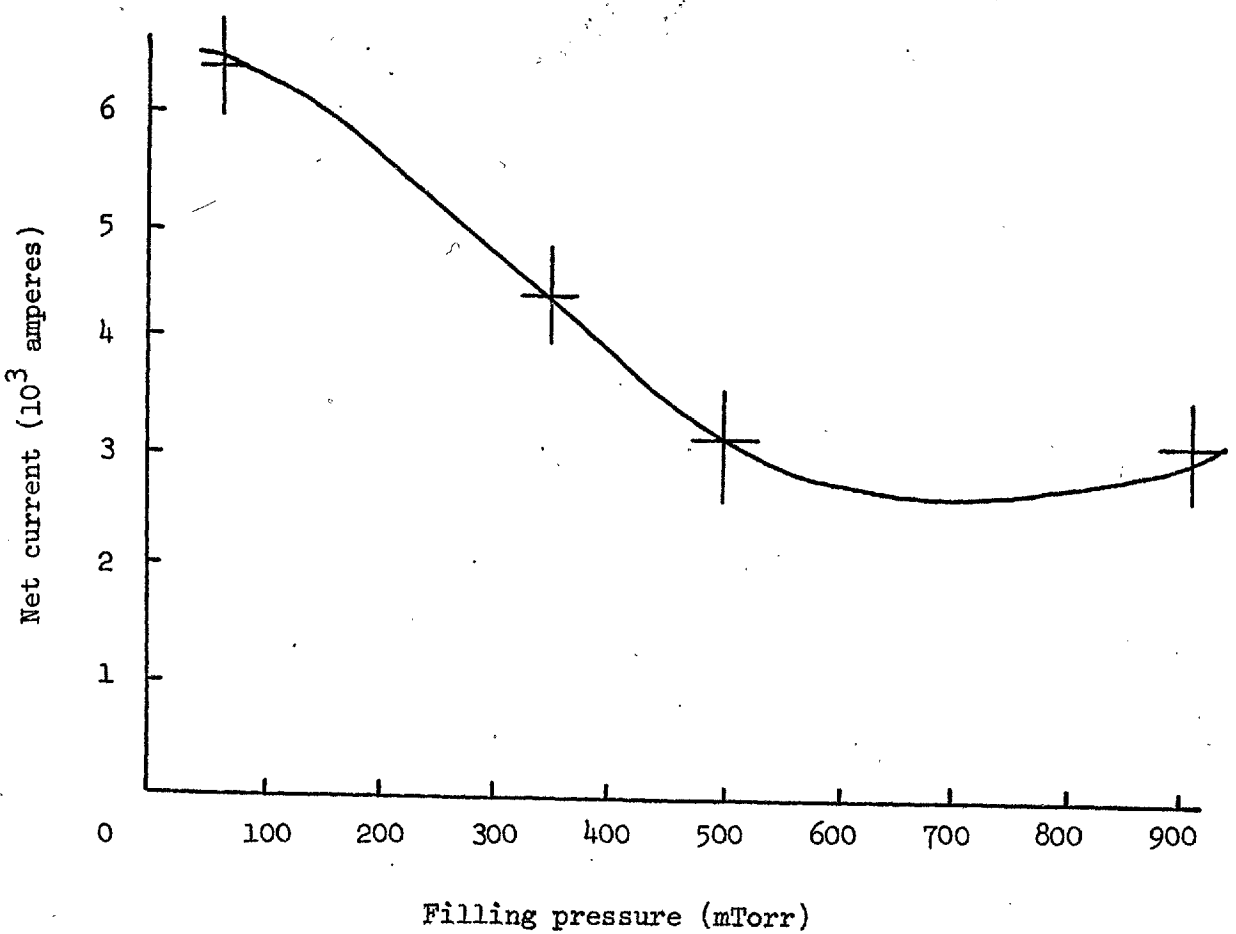
Net current (10^3 amperes)
6
5
4
3
2
1
0
100
200
300
400
500
600
700
800
900
Filling pressure (mTorr)

ACKNOWLEDGEMENTS

The essential element of this experiment, the high-current, relativistic electron beam, would not have been possible without the assistance of J.C. Martin, D.W. Forster, M. Goodman, T. Storr and G. Herbert of AWRE, Aldermaston. I gratefully acknowledge their contributions through the loan of equipment, through advice on pulsed-power technology, and through their encouragement during the experiment.

I am indeed grateful to A.E. Dangor, my supervisor, and J.D. Kilkenny of Imperial College for their essential assistance and support in the experiment and especially for their instruction on the techniques of laser scattering.

Helpful consultations with many other individuals have assisted the progress of the experiment. I am grateful to A. Folkierski, M.G. Haines, R. Latham and C.B. Wheeler of Imperial College, J.A. Nation of Cornell University, and D.A. Hammer of NRL, Washington, D.C. for their discussions and encouragement. It should be noted that the first mention of the presence of the radially outward electric field, which played an important part in the interpretation of these results, was made by J.A. Nation in a colloquium at Imperial College in response to a question by M.G. Haines on the reference frame in which the beam plasma system is charge neutralized.

The successful completion of the experiment was greatly expedited by the work of J. Westlake, T. Cobley, and L. Nyman of our technical staff, and I happily acknowledge their contributions with thanks.

The assistance of A. Dymoke-Bradshaw during the latter portion of the experiment, which he is to continue, is gratefully acknowledged.

The continuous assistance of my wife Nancy throughout the experiment and during the preparation of the thesis has been essential for the successful completion of the research, and I gratefully acknowledge her contribution.

Finally, I wish to note with thanks the loan of image-converter cameras from Culham Laboratory and from the Laser Optics Group of Imperial College.

REFERENCES

Alfven, H. 1939. Phys. Rev. 55: 425

Altyntsev, A.T., A.G. Es'kov, O.A. Zolotovskii, V.I. Koroteev, R.Kh. Kurtmulaev, V.O. Massalov, and V.N. Semenov. 1971. ZhETF Pis. Red. 13: 197. (1971. JETP Lett. 13: 139).

Bates, D.R. 1962. Atomic and Molecular Processes. New York: Academic Press. p. 267.

Benford, J. and B. Ecker. 1971. Phys. Rev. Lett. 26: 1160.

Bennett, W. 1934. Phys. Rev. 45: 890.

Berger, M.J. and S.M. Seltzer. 1964. Tables of Energy Losses and Ranges of Electrons and Positrons. (NASA SP-3012). Washington. D.C.: Office of Technical Service, Dept. of Commerce.

Buneman, O. 1959. Phys. Rev. 115: 503.

Caponi, M.Z. and R.C. Davidson. 1973. Phys. Rev. Lett. 31: 86.

Cox, J.L. and W.H. Bennett. 1970. Phys. Fluids. 13: 182.

Craggs, J.P. and J.M. Meek. 1954. High Voltage Laboratory Techniques. London: Butterworths Scientific Publications. pp. 111-151.

Davitian, H. 1971. Bull. Amer. Phys. Soc. 16: 1250.

Delacroix, J.L. 1960. Introduction to the Theory of Ionized Gasses. New York: Interscience. p. 19.

Evans, D.E. and J. Katzenstein. 1969. Rep. Prog. Phys. 32: 207.

Fainberg, Ya.B., V.D. Shapiro, and V.I. Shevchenko. 1969. Zh. Eksp. Teor. Fiz. 57: 966. (1970. Sov. Phys. JETP. 30: 528).

Fite, W.L. 1959. Proceedings of the Fourth International Conference on Ionization Phenomena in Gases, Uppsala. Amsterdam: North Holland Publishing Co. p. AI-23.

Forster, D.W., M. Goodman, G. Herbert, J.C. Martin, and T. Storr. 1971. Electron Beam Diagnostics using X-rays. (SSWA/JCM/714/162). Aldermaston: AWRE.

Frost, L.S., and A.V. Phelps. 1962. Phys. Rev. 127: 1621.

Goldenbaum, G.C., K.A. Gerber, W.F. Dove, and B.G. Logan. 1973. Bull. Amer. Phys. Soc. 18: 1350. (Also 1974. Phys. Rev. Lett. 32: 830).

Hammer, D.A. and N. Rostoker. 1970. Phys. Fluids. 13. 1831.

Hammer, D.A. 1974. To be published.

Hinnov. E., and J.G. Hirschberg. 1962. Phys. Rev. 125: 795.

Kadomstev, B.B. 1965. Plasma Turbulence. London: Academic Press. p. 68.

Kapetanakos, C.A., and D.A. Hammer. 1973. Appl. Phys. Lett. 23: 17.

Korn, P., F. Sandel, and C.B. Wharton. 1973. Phys. Rev. Lett. 31: 579.
(Also 1973. J. Appl. Phys. 44: 4946).

Lee, R.E., and R.N. Sudan. 1971. Phys. Fluids. 14: 1213.

Levine, L.S., I.M. Vitkovitsky, D.A. Hammer, and M.L. Andrews. J. Appl. Phys. 42: 1863.

Lovelace, R.V., and R.N. Sudan. 1971. Phys. Rev. Lett. 27: 1256.

McArthur, D.A. and J.W. Poukey. 1973. Phys. Fluids. 16: 1996.

McClure, G.W. 1953. Phys. Rev. 90: 796.

Martin, J.C. 1970. Nanosecond Pulse Techniques. (SSWA/JCM/704/49). Aldermaston: AWRE.

Martin, J.C. 1971. Fast Pulse Vacuum Flashover. (SSWA/JCM/713/157). Aldermaston: AWRE.

Massey, H.S.W. 1969. Electronic and Ionic Impact Phenomena. Oxford: Clarendon Press. p. 876-981.

Miller, P.A., and G.W. Kuswa. 1973. Phys. Rev. Lett. 30: 958.

Olson, C.L. 1973. Phys. Fluids. 16: 529.

Olson, C.L. 1974. To be published.

O'Malley, T.F. 1969. Phys. Rev. 185: 101.

Pellinen, D.G., and P. Spence. 1971. Rev. Sci. Inst. 42: 11.

Poukey, J.W., and N. Rostoker. 1971. Plasma Phys. (GB). 13: 897.

Ramazashvili, R.R., A.A. Rukhadze, and V.P. Silin. 1963. Sov. Phys. JETP. 16: 939.

Rukhadze, A.A., and V.G. Rukhlin. 1972. Sov. Phys. JETP. 34: 93.

Sagdeev, R.Z. 1967. Proc. of the 18th Symposium in Applied Mathematics. Providence, R.I.: American Mathematical Society. p. 281.

Singhaus, H.E. 1964. Phys. Fluids. 7: 1534.

Smith, D.R. 1972. Phys. Lett. 42A: 211.

Spitzer, L. 1962. Physics of Fully Ionized Gases. New York: Interscience Press. pp. 120-143.

Stallings, C., J. Benford, and R. Schneider. 1972. Bull. Amer. Phys. Soc. 17: 1031. (Also 1973. Bull. Amer. Phys. Soc. 18: 1350).

Storr, T.H. 1969. Mini-B, Design and Operation. (SSWA/THS/692/9). Aldermaston: AWRE.

Taylor, R.J. and F.V. Coroniti. 1972. Phys. Rev. Lett. 29: 34.

Thode, L.E. and R.N. Sudan. 1973. Phys. Rev. Lett. 30: 732.

Toepfer, A.J. and J.W. Poukey. 1973. Phys. Lett. 42A: 383. (Also 1973. Phys. Fluids. 16: 1546).

Yonas, G. and P. Spence. 1969. Record of the Tenth Symposium on Electron, Ion and Laser Beam Technology. San Francisco: San Francisco Press. p. 143.